Seismic Performance Assessment and Probabilistic Repair Cost Analysis of Precast Concrete Cladding Systems for Multistory Buildings

by

Jeffrey Patrick Hunt

A dissertation submitted in partial satisfaction of the

requirements for the degree of

Doctor of Philosophy

in

Engineering - Civil and Environmental Engineering

in the

Graduate Division

of the

University of California, Berkeley

Committee in charge:

Professor Bozidar Stojadinovic, Chair
Professor Stephen A. Mahin
Professor Douglas S. Dreger

Spring 2010

Seismic Performance Assessment and Probabilistic Repair Cost Analysis of Precast Concrete Cladding Systems for Multistory Buildings

Abstract

Seismic Performance Assessment and Probabilistic Repair Cost Analysis of Precast Concrete Cladding Systems for Multistory Buildings

by

Jeffrey Patrick Hunt

Doctor of Philosophy in Engineering – Civil and Environmental Engineering

University of California, Berkeley

Professor Bozidar Stojadinovic, Chair

Analytical and experimental tests have shown that the seismic response of multistory moment-frame structures with precast concrete cladding in moderate to severe earthquakes is significantly influenced by the cladding system. Moreover, considerable damage to the cladding system components from recent earthquakes has been reported. The cladding system can account for a significant portion of the initial cost of a building, often as much as 20%. However, in seismic analysis and design, engineers typically ignore the additional stiffness and damping that the cladding system may provide, which could prove to be beneficial or detrimental to the building's seismic performance. Most of the efforts in nonlinear dynamic modeling focus on representing the behavior of structural elements and do not include the effects of non-structural elements such as cladding systems. The purpose of the research discussed in this dissertation is to study the effect that the cladding system has on the structural response of multistory buildings, to develop analytical equations to estimate the seismic demands in the cladding connections, to calculate the probability of failure of typical cladding connections, and to determine the post-earthquake repair costs and repair times of typical cladding systems.

The nine-story LA SAC steel moment-frame building is selected as the study building, and a two-dimensional, nonlinear model is developed of the bare-frame structure in OpenSees. The steel moment-resisting frame of the bare-frame structure is modeled using nonlinear force beam-column line elements capable of representing distributed plasticity along their length. The frame connections are reduced-beam section (RBS) moment connections, and their modeled cyclic moment-rotation behavior is based on experimental test results of the connection. Analytical models of three different precast cladding designs are applied to the bare-frame structure to study their effect on the building's seismic response. The three cladding designs represent common systems used in regular multistory buildings in modern construction. The first cladding design, cladding type C1, consists of alternating horizontal bands of spandrel panels (covering the exterior floor beams) and glazing. The spandrel panels extend the full width of the bay. The second cladding design, cladding type C2, consists of spandrel panels that extend the full height of the story with rectangular window openings "punched" into their surface. The third cladding design, cladding type C3, consists of the same spandrel panels as in type C1 with column cover panels spanning between adjacent spandrel panels. The force-deformation curves of the connections used in the model are obtained from experimental tests of push-pull

connections and column cover connections. The total seismic mass of the models with the cladding systems is the same as the total seismic mass of the bare-frame model. However; in the models with cladding, the seismic mass is distributed between the beam-column nodes and the nodes of the cladding system according to their respective tributary weights.

The effects of the cladding on the seismic response of the bare-frame structure are studied by performing modal analyses, nonlinear static pushover analyses, and nonlinear dynamic time-history analyses of the analytical models. The inclusion of cladding decreases the fundamental period of the building by only 4%; however, the effects of the cladding on the maximum interstory drifts, floor accelerations, and plastic hinge rotations are significant. Time-history analyses of each model are performed using 140 ground motions. The ground motions in each bin are scaled by a common factor (cloud method with constant scaling) to ensure nonlinear response was captured. The time-history results are plotted in log-log space, and a linear trend line is fitted to the data to represent the mean maximum response values. The time-history results reveal that the addition of cladding reduces the mean maximum interstory drift ratios in the bare-frame model by up to 22%, 28%, and 33% for the 50%-, 10%-, and 2%-in-50 year probability of exceedance levels, respectively. The reductions in interstory drift are the largest for cladding type C3 and smallest for cladding type C1. The mean residual interstory drifts are small for all levels of intensity and were not significantly affected by the cladding. The mean maximum floor accelerations are not significantly affected by cladding types C1 and C2: the mean values of maximum floor accelerations in the bare frame structure are reduced by only 8% for these two cladding types. On the other hand, the mean values of the maximum acceleration at the roof level in the model with cladding type C3 are up to 35%, 63%, and 97% larger than the values in the bare frame structure for the 50%-, 10%-, and 2%-in-50 year probability of exceedance level, respectively.

The finite-element models of structures with cladding are time-consuming to create and computationally demanding to analyze. Thus, analytical equations are derived to describe the mechanisms for deformation in the cladding connectors. The equations are used to estimate the maximum deformations in the push-pull and column cover connectors. The maximum deformations estimated from the equations are compared to the maximum deformations recorded from the time-history analyses. The comparisons of the median values of maximum deformation between the two approaches show that the analytical equations provide good estimates of the maximum deformations up the height of the building. The analytical equations can be used as conservative estimates of deformation for the seismic design of similar cladding connectors.

The time-history analysis results show that significant deformations develop in the column cover connections in moderate earthquakes. The deformations exceed the life-safety, and in some cases, the collapse prevention performance criteria. Thus, the failure probabilities of the column cover connections subject to multiple hazard levels are investigated using structural reliability theory. The analytical equations for estimating the deformations in the column cover connectors are used to construct the limit-state function describing the structural reliability of the connectors. The random variables consist of the maximum interstory drift, the gap width in the slotted connections, and the failure shear deformation in the connectors. The deterministic parameters in the limit-state functions are the panel dimensions and the story height. The correlation coefficients are calculated for the maximum interstory drifts between different stories. The components of the column covers consist of four connectors (one in each corner). The component failure probabilities (calculated using FORM) are as high as 44.2%, 70.0%, and 100% for the 50%-, 10%-, and 2%-in-50 year probability of exceedance levels, respectively. The

maximum interstory drift is found to be the most important (has the largest effect on the results) random variable, and the gap width is the most important capacity or design variable. Regarding the deterministic parameters, decreasing the panel width has the largest effect on decreasing the probability of failure of one panel. The probability of failure can also be decreased by increasing the panel height or increasing the story height. Story system reliability analyses are performed to investigate the probability of failure of multiple panels per story. For each story, the total probability theorem is used to calculate the total probability of failure of 2 panels in the low hazard event, 4 panels in the moderate hazard event, and 8 panels in the high hazard event. The total probability of failure is as high as 48.4% for a lifetime of 50 years of the building, with the largest probabilities at the top three stories of the building.

To gain additional insight on the seismic performance of multistory buildings with cladding, post-earthquake repair cost analyses are performed on the analytical models using the performance-based earthquake engineering (PBEE) methodology developed by the Pacific Engineering Earthquake Research (PEER) Center. The total repair costs of the cladding system represent up to 5%, 26%, and 66% of the replacement cost of the cladding for the 50%-, 10%-, and 2%-in-50 year probability of exceedance levels, respectively. At the 2%-in-50 year probability of exceedance level, the repair costs of the cladding system are up to 30-50% of the repair costs of the complete building and up to 14% of the replacement cost of the complete building. Using the repair cost results, the mean annual total repair costs of the cladding systems are $39,563, $16,213, and $40,824 for cladding types C1, C2, and C3, respectively. Based on the repair cost analyses, it is apparent that cladding type C2 is the most cost-effective cladding design. Because the cladding panels have window punch-outs, the window panes are protected from damage due to interstory drift. In addition, cladding type C2 does not use the highly damageable column cover connections that are expensive to repair.

The results of this research highlight several important issues in cladding design. First, the cladding system should be carefully designed in consultation with the structural engineer to ensure that the cladding system does not significantly impact the structural response of the building structure. As shown by the results of the time-history analyses, the selected cladding type determines how much the cladding affects the structural response of the building. The analysis of the code equations for window glazing systems reveal that windows with narrow aspect ratios (height greater than width) and generous clearances between the glass and surrounding window framing provide significantly better seismic drift capacity before cracking and glass fallout occurs. The results of the post-earthquake repair cost analyses show that the repair costs of the cladding system have a significant contribution to the repair costs of the complete building. Of the three typical cladding types analyzed in this research, the full-story height cladding system with window punchouts (cladding type C2) incurs the lowest repair costs.

Acknowledgments

First and foremost, I would like to thank my advisor, Prof. Bozidar Stojadinovic, for his support and guidance throughout my research and studies at Berkeley. I am very appreciative of his thoughtful mentoring, technical insights, and steady support in the completion of this dissertation.

I would like to thank the principal investigator on this project, Prof. Kurt McMullin, for his recommendations and for providing the experimental data on the push-pull connections, photographs of the test specimens, and drawings of the cladding system.

Thanks to Ed Knowles at Walters & Wolf for taking the time to meet with me about my research on several occasions and for providing the data on the repair methods and unit repair costs of the cladding system components. Thanks also to Mark Hildebrand at Willis Construction for providing the data on the damage states of caulking in cladding systems.

I would like to especially thank my parents, Maurice and Pamela Hunt, for their unconditional love and support throughout the years. I am very grateful for the motivation they have given me during my years at Berkeley. I am fortunate to have them as role models, and I will never stop learning from them. I would also like to thank my parents-in-law, Michael and Carol Santoki, for being there for me, opening up their home to me, and keeping me well fed.

I would like to also thank my family and friends who have provided their support, encouragement, and entertainment. They are my sister Alison Frenzel, my brothers Andrew and Thomas Hunt, my brother-in-law Peter Santoki, my best man Christoph Welz, Lina Albers, Julia Patsch, and Stefan Naumann.

My deepest gratitude goes to my wife Emily, who has given me the strength, support, and love to complete this dissertation. You have been beside me at every step during my research. Your compassion and love encourage me, and your intelligence motivates me. Thanks for being there for me.

This dissertation is based upon work supported by the National Science Foundation under the project NEESR-SG: Experimental Determination of Performance of Drift-Sensitive Nonstructural Systems under Seismic Loading, CMS-0619157. This work also made use of the Earthquake Engineering Research Centers Shared Facilities supported by the National Science Foundation under award number EEC-9701568 through the Pacific Earthquake Engineering Research Center (PEER). Any opinions, findings, and conclusions or recommendations expressed in this material are those of the author and do not necessarily reflect those of the sponsors.

Table of Contents

List of Figures

List of Tables

Chapter 1: Introduction to Precast Cladding Systems

Precast concrete panels have been used for many decades in the United States and Canada to enclose the exterior façade of buildings. There are many buildings dating back to the 1920's and 1930's today that demonstrate the durability and attractiveness of precast panel systems. The use of precast concrete cladding is a practical and economical way to provide the desired architectural expression, special shapes, and uniform finishes (PCI, 2007). Two typical applications of precast cladding are shown in Fig. 1.1; an isometric drawing of a typical cladding system is shown in Fig. 1.2.

Precast panels can be loadbearing or non-loadbearing, depending on the design and intentions of the architect and structural engineer. Non-loadbearing panel designs, which are often termed "precast cladding," are more common in today's construction (PCI, 2007).

This chapter provides an introduction to precast cladding systems and their terminology. Some design recommendations with regard to cladding panels and cladding connections are summarized from the literature.

1.1 INTRODUCTION

The Precast/Prestressed Concrete Institute (PCI, 2007) defines non-loadbearing precast concrete panels (or precast cladding) as a wall unit that resists wind or seismic loads and its own weight, but not the gravity loads from the structural framing. Accordingly, in this dissertation, cladding refers to precast concrete panels that are attached to the structural framing in a way to provide:

1. Protection of the building occupants and contents from the environmental elements (wind, rain, snow, etc.); and
2. Exterior architectural expression.

Precast cladding can be made in a wide variety of shapes and sizes. Usually, cladding panels do not extend beyond the height of one story, and they are normally limited (by transportation and installation constraints) in width to less than or equal to the bay width of the structure. The cladding system for a building may use several different shapes and sizes of panels to create different architectural details. A variety of colors and textures are available by manipulating the aggregate selection, matrix color, finishing process, and depth of exposure of the aggregate (PCI, 2007). The major design and cost considerations for cladding units are the extent of repetition of the cladding mold and the choice of panel sizes, shapes, and finishes.

1.1.1 Definitions

Several industry-specific terms are encountered in cladding system design. The primary source for information on precast concrete cladding is PCI (2007). Several important terms are defined below:

Non-loadbearing precast concrete panels (cladding) refer to precast concrete panels that are not designed to participate in the gravity or lateral resistance of the building structure. Non-loadbearing systems are designed only to resist the panel self-weight, wind forces on the panels, and seismic forces created by the panel self-weight. Cladding units are the most common application of precast concrete panels.

Loadbearing precast concrete panels refer to precast concrete panels that are designed to participate in the gravity and/or lateral resistance of the building structure. Loadbearing cladding units are integrated into the building structure, and depending on the application, the loadbearing panels may reduce or eliminate the need for interior shear walls or a secondary structural system. The small increases in loadbearing wall panel cost (due to reinforcement and connection requirements) can usually be offset by the elimination of a separate perimeter structural frame.

Cladding system is a collective term that refers to the cladding panels, caulking between the panels, connections that attach the panels to the structure, and the window glazing system.

Spandrel panels are cladding panels that cover the beam and floor slab of the building structure and provide horizontal architectural expression. The vertical dimension of the spandrel panels may be small and only cover the beam or they may spam the full height of the story. The horizontal dimension often extends the full-bay width of the structure. Spandrel panels can either be solid panels or include openings for windows.

Column cover panels and mullions are panels that cover the columns of the building structure and provide vertical architectural expression. Both column cover panels and mullions have the same panel design; however, column cover panels cover the columns of the building structure and mullions are spaced between the column cover panels and do not cover any columns. In most cases, these two types of panels are both called column cover panels. Column cover panels are often used in conjunction with spandrel panels. They may be attached to the building structure or the spandrel panels above and below the column cover panel.

Window glazing system refers to the glass panes, framing system that surrounds the panes, and the rubber gaskets or sealant that glazes the panes to the window framing.

Cladding connections, or connectors, are the connections that attach the panels to the building structure or attach a panel to other panels in the cladding system. There are several types of connectors in a cladding system, each designed to resist specific types of forces.

Bearing (direct or eccentric) connections are intended to transfer the vertical loads from the self-weight of the cladding panel to the building structure. Bearing connections are usually provided at no more than two points per panel, and at just one level of the structure. Bearing can be either directly in the plane of the panel along the bottom edge, or eccentric using concrete corbels, haunches, cast-in steel shapes, or attached panel brackets. Eccentric bearing connections are usually used for cladding panels when movements of the support system are possible. The most common types of eccentric bearing connections involve welding an angle or tube steel section to an embed in the panel and using a leveling bolt to adjust the panel to the correct position. The leveling bolt is usually left in place to carry the vertical load.

Push-pull (tieback) connections are primarily intended to keep the precast concrete panel in a plumb position and to resist wind and seismic loads perpendicular to the panel. Tiebacks

may be designed to withstand forces in the plane of the panel, or isolate them to allow frame distortions independent of the panel and allow movement vertically and/or horizontally. Push-pull connections are often used in seismic areas to isolate the panels and keep them from participating in the lateral response of the building. The most common push-pull connections are made of threaded coil rods bolted or welded to angle or tube steel sections attached to the beam or column of the building structure.

Lateral seismic connections, or shear plate connections, are connections that primarily provide restraint for longitudinal forces in the plane of the panel. Because seismic force is the most common in-plane force, these connections are sometimes also referred to as seismic shear plates.

Column cover connections refer to the cladding connections that attach the column covers to the structure or to adjacent spandrel panels. These connections are typically welded or bolted connections at the bottom of the panel and horizontally slotted connections at the top of the panel to allow lateral movement.

Caulking, or sealant, refers to the material used to seal the joints between the edges of adjacent cladding panels and the edges between the cladding panels and the window framing. The caulking can be a one-stage design (one bead of caulking in the joint) or two-stage design (two beads of caulking used to improve the watertightness of the joint). Caulking is usually made of polysulfides, polyurethanes, or silicones and has a life expectancy from 10-20 years (PCI, 2007).

1.1.2 Configurations

According to Arnold (1989) and PCI (2007), there are three characteristic façade configurations, or typologies, that considerably impact the cladding design, based on both the individual shape of the panels and the way in which they are arranged. The first typology is a cladding design that plates the structural framing, vertically and horizontally, with the openings filled with glass. The cladding panels that cover the beams are known as spandrel panels, and the panels that cover the columns are known as column covers. The second typology eliminates the column cover panels from the first typology, so the façade becomes alternating horizontal bands of spandrel panels and glazing. The third typology is consists of large full-bay rectangular panels with window openings punched in the panel. This design reduces the number of joints and allows for efficient erection, which reduces the installation costs. The designer may employ several different typologies within a single building or combine the typologies to create new ones. Photographs of buildings with the three typologies are shown in Fig. 1.3.

A simpler classification is given by Sack *et al*. (1989), who classify cladding panels as either (1) a “window box”, which encloses one bay of the structural frame and acts as one piece or (2) an “articulated panel” which is used to cover individual columns and beams. When individual panels are used, they are often sized to separately cover the beams and columns. Several options exist to arrange precast concrete panels; typical arrangements are shown in Fig. 1.4. Note that cladding panels may span multiple stories and bays.

1.2 CLADDING PANELS

One of the key elements to cost-effective cladding manufacturing is minimizing the number of molds and mold changes and maximizing the number of castings from each mold. Thus, repetition of panel shapes and sizes is often employed in cladding designs. The size of the panels also has an important effect on the economy of the cladding design. Pricing is more dependent on large pieces than on a large project. For example, a 100-piece project of large panels can be less expensive per square foot than a 1000-piece project using much smaller panels (PCI, 2007). The labor functions performed by a precast erector are a large portion of the cost; thus, the more pieces a project has, the more labor hours (and money) it will take to engineer, cast, strip, finish, load, deliver, and install the panels (PCI, 1989). Therefore, it is more economical to clad a larger portion of a building with a fewer number of precast panels. The minimum thickness of precast panels recommended by PCI (2007) is 1/20 to 1/60 of the unsupported length (the least distance between connections that provide lateral support).

As discussed in Section 1.1.2, the main types of cladding panels are spandrel panels that cover the floor beams of the building structure, column covers that cover the columns of the building structure, and full-bay width panels that have window punchouts. Regardless of their shape, cladding panels are typically designed to transfer negligible load from the supporting structure. They primarily close the building in from wind and rain, and the panels generally resist wind forces, seismic forces generated from the panel self-weight, and the vertical forces required to transfer the self-weight to the supporting structure. In most cases, the forces generated in the panel during the manufacturing and erection stages of construction govern the reinforcement design of the panel (PCI, 1989). Visible cracking is undesirable in precast concrete panels, and thus, sufficient reinforcement must be provided. In cases when the expected design loads are relatively small, distributed reinforcement is needed to control cracking that may occur from fabrication, handling, erection, and stresses due to temperature changes of the panel. For larger design loads in the panels, more conventional reinforcement is needed. The types of reinforcement used in precast panels include welded wire reinforcement, bar mats, deformed steel bars, and prestressing and post-tensioned tendons (PCI, 2007). As a general rule, PCI advises that bar sizes be small (No. 3 through 6). The maximum spacing for reinforcing bars recommended by PCI is three times the panel thickness, while the common spacing for welded wire reinforcement is 6 in.

PCI (2007) also recommends that all panels and the joints between panels have the ability to accommodate movements of the supporting frame. In addition, the weight of the panel, volume changes in concrete frames, and rotation of supporting beams must be evaluated to ensure that the deformation compatibility between the panel and supporting structure is maintained.

1.3 CLADDING CONNECTIONS

The cladding connections that attach the precast panel to the building structure play an important role in the safety, performance, and economy of the cladding system. Different types of connections are used depending on the size and shape of the panels, support conditions, and forces and displacements in the cladding system. In any cladding system, several types of connections are used since different connections are designed to withstand different types of

forces. In the non-loadbearing panel systems discussed in this chapter, the connections must resist the gravity loads from the panel self-weight, wind forces on the panel, seismic forces from the panel self-weight, restraint of volume changes, and construction loads (PCI, 2007).

There are three parts of every cladding connection: the body, the fasteners, and the anchorage. The three terms are shown graphically in Fig. 1.5. The body of the connection is the main part of the connector and usually consists of a threaded rod (for a push-pull connector), angle or tube (for a vertical bearing connection), or a steel plate (for a lateral seismic connection). The fastener is the portion of the cladding connection that attaches the body of the connection to the building structure and usually consists of bolts and nuts or welds. The anchorage portion of the cladding connection attaches the precast panel to the body of the connection and usually consists of an embed-in-the-panel or expansion anchors.

Each part of the cladding connection must be capable of transmitting the forces from the panel to the supporting structure. Cohen (1995) summarizes some of the PCI connection design criteria:

1. *Strength*: the connection forces must be safely transferred to the supporting structure. The connection forces include:
    a. Gravity forces
    b. Seismic and wind forces
    c. Forces from restraint of volume change strains
    d. Forces induced due to interaction of wall panels and movement between the panel and the structure.
2. *Ductility*: the connections must be able to undergo large deformation without fracture or failure. At the interface of the panel and the connection, it is desirable to have steel elements yield before concrete crushes.
3. *Strains due to volume change*: the connection should allow some movement due to shrinkage, creep, and temperature change of the panel.
4. *Durability*: the exposed steel elements of the connections should be painted, covered by concrete, galvanized, or epoxy coated. Regarding fire resistance, susceptible connections should be protected to the same degree as the supporting framing.
5. *Constructability*: the designer should keep in mind to standardize connection types and sizes, consider clearances and tolerances, avoid reinforcement congestion, and provide for field adjustment of the panel units.
6. *Seismic considerations*: seismic effects can results in significant interstory drifts in the building structure. Once the panelization of the cladding system is determined, the general seismic design approach for cladding is to determine how the panel will behave in response to drift and then configure the connections to accommodate that behavior. The story drift in the building structure is generally accounted for with connections that flex or slide.

1.3.1 Connection Types

Several types of connections are used in cladding systems. The most common are the vertical bearing connection and the push-pull (tieback) connection. The vertical bearing connection transfers the self-weight of the panel to the building structure. The push-pull connection resists the forces to restrain panels due to eccentric load and forces perpendicular to

the plane of the panel, such as wind loads. In seismic zones, the push-pull connection, which is usually a flexible threaded rod, is often used to isolate the panel from excessive racking forces due to interstory drift, as shown in Fig. 1.6. Generally, there are two bearing connections and four tieback connections per panel. PCI (2007) advises that only two bearing connections should be used to support the self-weight of the panel so that an indeterminate force distribution of the gravity loads does not develop. Sketches of typical bearing connections and a tieback connection are provided in Fig. 1.7. The bearing connection may be a notch in the panel or a leveling bolt attached to the panel; the lateral connection is typically a threaded rod connected to the beam or column. Additional illustrations of panel bearing connections and tieback connections are shown in Fig. 1.8 and Fig. 1.9. In the case of spandrel panels, an additional connection may be used to tie the panel into the floor slab. The lateral seismic connection, or shear plate connection, is used to resist longitudinal forces caused by seismic loading. This connection type alleviates the push-pull connection from taking all of the lateral loads. Some typical examples of lateral seismic connections are shown in Fig. 1.10.

According to McCann (1991), the designer may choose to support the weight of the panel through bearing connections at the panel's bottom, top, or center, as shown in Fig. 1.11. The choice of the location of the bearing support changes both the force directions in the connections and the deformation mode of the panel. Thus, care must be taken to provide adequate joint spacing. Different panel shapes and types may also warrant different placements of the connections. For example, Fig. 1.12 illustrates different panel sizes and the location of the bearing and tieback connections. For square-shaped panels, the bearing connections are placed at the bottom and the tieback connections are placed at the corners. For the slender column cover panels, the bearing connections could be placed at the bottom or center of the panel. In the spandrel panel, the self-weight is supported at the floor level and restrained at a column or vertical member rather than at the underside of the floor member. This prevents potential creep rotation of the edge member from affecting the alignment of the panel (PCI, 2007).

1.3.2 Panel-Structure Interaction

Since the precast panels are connected to the structural frame, the potential arises for the cladding system to interact with the lateral load resisting system of the building structure. If very stiff and high-strength connections are used along with inadequate joint widths, the cladding system may act as an external shear wall and cause significant damage to the cladding. Moreover, the cladding system may shorten the fundamental period of the building and cause an unintended increased in seismic forces. If the cladding is rigidly attached, the panels may induce force redistribution in the lateral force resisting system, causing increased shear or moment forces in the columns or beams. The cladding panels should be designed to translate or rotate when the building structure undergoes interstory drift. Interstory drift can cause several different movements of the cladding panels: in-plane translation, in-plane rotation, out-of-plane rotation, and out-of-plane translation (PCI, 2007). These four different types of panel movement are shown in Fig. 1.13. In-plane translation occurs when the panel is fixed to one level and is subjected to in-plane motion, such as a spandrel panel fixed to a beam. The panel translates laterally with that level, remaining vertical in elevation. In-plane rotation, also known as "rocking," occurs when the panel is supported at two levels and is subjected to in-plane motion, such as a column cover panel. This type of movement requires connections with slotted holes or

gaps. Out-of-plane rotation occurs when the panel is attached to two different levels and is subjected to out-of-plane motion (i.e. interstory drift perpendicular to the plane of the panel). This type of movement creates tension and compression forces in the push-pull connections. Out-of-plane translation is the movement that occurs when a panel is attached to one level of framing, such as a short spandrel panel, and is subjected to out-of-plane motion. The movements that cause the most significant potential for structural interaction are the in-plane translation and in-plane rotation.

When cladding panels are subject to in-plane interstory drift, the cladding connections may cause the panels to rock up on one corner or translate without rocking. For example, a cladding system using full-height spandrel panels (or wall panels) is shown in Fig. 1.14a. The panels are connected with bearing connections at the bottom of the panel and tieback (push-pull threaded rod connections, such as Fig. 1.7b) at the corners of the panel. In this case, the upper tieback connections become isolating connections (since the in-plane stiffness and strength of the threaded rods is very low), preventing the forces due to interstory drift from being transmitted to the panel. The panel is also rigidly fixed to the floor beam with the two bearing connections, creating a vertical couple and shear forces at the bearing connections. Thus, the entire panel translates with the movement of the floor beam. A cladding system with shorter spandrel panels is shown in Fig. 1.14b. In this case, the bearing connections are located towards the top of the panel; however, the mechanics of translation are similar to the wall panel.

In the case of narrow panels, a rocking mechanism may be more feasible. A column cover panel attached to spandrel panels above and below is shown in Fig. 1.15a (PCI, 2007). The panel is attached with rigid tiebacks at the top of the panel and bearing connections that allow liftoff (i.e. vertically slotted connections). Thus, as the spandrel panels translate, the column cover is forced to rock up on one side, and each of the bearing connections must be designed to withstand the force from the entire weight of the column cover panel. The location of the bearing supports influences the forces experienced by the other tieback connectors. McCann (1991) describes three possible locations of the bearing connections for column cover panels, as shown in Fig. 1.11: at the bottom, top, or center of the panel. When bearing connections are provided at the bottom of the panel, the tieback connections experience tension from the eccentricity of the weight of the panel. When bearing connections are provided at the top of the panel, the tieback connections experience compression from the eccentricity of the weight of the panel. For tall column cover panels extending over two stories, bearing connections can also be provided at the middle of the panel with tieback connections at the corners, as shown in Fig. 1.15b.

The connections should be designed to allow the cladding panels to accommodate the movement and deflection of the building structure. Depending on the story height, two inches or more of interstory drift must be accommodated by the cladding system, presenting the main challenge to the cladding designer. To accommodate the interstory drifts, connections may employ bending of steel (bending of long threaded rods) and/or sliding of a bolt through a slotted hole. Bending connections must have sufficient ductility to withstand the interstory drifts, and slotted connections must have slots long enough to account movement without binding or shearing of the bolt. For example, if tolerances were ± ½ inch and the drift allowance was ± 1 inch, the minimum slot length would equal 3 inches plus the diameter of the bolt. The weather and corrosion protection of the slotted connections is essential to ensure their long-term performance.

The two most important qualities of cladding connections are sufficient strength and adequate ductility (Iverson, 1989). Korista (1989) advises the designing engineer to ensure that

the panel-to-structure connection can accommodate the differential movements between the stiff panel and flexible frame under seismic events. Adequate anchorage of the connection to the panel is required to avoid catastrophic failure and ensure stability. Cohen (1995) notes that many designers use "confining hoops, deformed bar anchors, or long reinforcing bars welded to plates" to create sufficient anchorage of the connection to the concrete panel. Typical connection fasteners are illustrated in Fig. 1.16. If headed studs or inserts are used it is recommended that they be enclosed in reinforcement so a sudden tensile failure of the concrete is avoided.

Building codes set the requirements for lateral forces and story drift accommodation. These parameters are too variable and detailed to list in this chapter; however some basic requirements are discussed below. More detailed requirements are given in Section 1.6. The Uniform Building Code requires that the connection body be designed for a force equal to 1.33 times the required panel force, and the connection fasteners should be design for four times the required panel force (1994 UBC section 1631.2.4.2). The UBC also stipulates a serviceability drift limit of 0.005 times the story height for which the framing should be elastic. Given a 12-foot story height, this limit is equal to 0.005*12*12 = 0.72 inches. To ensure that the cladding panel-to-structure connections have enough ductility, the UBC requires that the connections accommodate 3 to 4.5 times this story drift (1994 UBC section 1631.2.4.2, part 5). Therefore, the connector must be able to move up to 2 to 3 inches sideways. Cohen (1995) gives two possible solutions: (1) use gravity connections that can freely slide sideways to accommodate drift movement and lateral connections made of threaded rods which deform to resist the horizontal seismic loads; or (2) use bolted connections with slotted holes.

1.4 CAULKING

Precast panels are relatively impermeable to water, and thus, moisture will not penetrate through them. Therefore, the joints and caulking are very important in keeping the cladding system airtight and watertight. Caulking, a gunable, field-molded sealant, is used to fill the joints between the edges of the panels and between the panels and the window framing. The joints in the cladding system are required to accommodate changes in the panel dimensions and dimensions of the structure caused by changes in temperature, moisture content, or deflection from applied design loads (PCI, 2007).

There are two types of joints: one-stage joints which use a single line of caulking for weatherproofing and two-stage joints which use two lines of caulking (PCI, 2007). Single-stage joints are normally the most economical with regard to initial cost, and they provide adequate air leakage and water penetration control in most climates. A section of a single-stage joint is shown in Fig. 1.17. Two-stage joints are more complex, and they are based on the open rainscreen principle by providing vents or weeps in the first line of sealant. These types of joints are frequently used in Canada and colder climates.

The width of the joints between the precast panels is determined considering the temperature extremes at the building site, appearance, the movement capability of the sealant, panel size, fabrication tolerance of the precast panel, and panel installation methods. Based on this, a minimum joint width of 3/4-inch is the most common (Hildebrand, 2009).

1.5 WINDOW GLAZING SYSTEM

The window glazing system includes the glass panes, the framing system that surrounds the glass, and the rubber gaskets or sealant that glazes the panes to the framing. The window glazing system presents a particular challenge to cladding designer because the windows interrupt the wall system and require special detailing at their interface with the cladding system. One of the greatest challenges in the design of the window glazing system, especially in seismic zones, is protecting the glass from breakage due to excessive interstory drifts. The connection of the window to the opening in a precast concrete wall must be designed to resist wind, vertical live load, seismic load, and thermal loads. General guidelines are given by PCI (2007) for the allowable deflection of the glass framing members under non-seismic design loads. Under vertical loads, the glass framing should not impose bending or concentrated compressive stresses on the glass, and the framing should not deflect more than 3/4-inch or $1/175^{th}$ of the span under loading, whichever is less. For seismic loading, code documents such as ASCE 7 and FEMA 450 should be used when designing the glazing system. More information about the design recommendations in these documents is given in Section 1.6 and Chapter 5.

There are many different ways of detailing windows within a cladding system. For example, three designs are shown schematically in Fig. 1.18. The glass panes may be recessed in the window opening to discourage water runoff (staining) and to provide more shade from direct sunlight. The typical method of window installation is field installment (PCI, 2007). Embeds and hardware, such as ferrule loop inserts, tubes, or slotted inserts, may be cast in the precast panels to provide fastening for the windows. Several installation options are shown in Fig. 1.19.

For cladding designs that use alternating bands of spandrel panels and glazing (the second typology described in Section 1.1.2), the effect of the seismic deflections and rotations of the spandrel panel on the windows should be considered in the design (Arnold, 2008). Using a glazing system between large rigid cladding panels can have a negative impact on the performance of the glass in seismic events. For example, a spandrel panel cladding system with glass between the panels is shown in Fig. 1.20. The story height is denoted as "X" and, in this case, the height of the glass is X/2. Under seismic drifts, the spandrel panels follow the drift of the floor beams, Δ. Since the panels are very rigid, this magnitude of drift Δ is imparted onto the glazing. Therefore, the drift ratio in the glass is equal to $\theta_{glass} = \Delta/(X/2) = 2\Delta/X$; this drift ratio is twice as large as the interstory drift ratio of the story, $\theta_{story} = \Delta/X$.

1.6 CODE RECOMMENDATIONS

The recommendations for designing cladding system components are given in current code documents. The specifications given in building codes, FEMA 356, and FEMA 450 are based on the recommendations given in ASCE 7. Some of the details of the code considerations are discussed below using FEMA 450.

The exterior nonstructural wall elements and connections that are attached to or enclose the structure are to be designed to accommodate the seismic relative displacements and displacements and movements due to temperature changes. The exterior cladding is to be supported by positive and direct structural supports or by mechanical connections and fasteners in accordance with the following specifications:

1. "Connections and panel joints shall allow for a relative movement between stories of not less than the calculated story drift D_p or 1/2 in. (13 mm), whichever is greater." The calculated story drift D_p is the maximum relative interstory drift computed from an elastic analysis, response spectrum analysis, or nonlinear time-history analyses for the design level earthquake.
2. "Connections to permit movement in the plane of the panel for story drift shall be sliding connections using slotted or oversized holes, connections that permit movements by bending of steel, or other connections that provide equivalent sliding or ductile capacity."
3. "Bodies of connectors shall have sufficient deformability and rotation capacity to preclude fracture of the concrete or low deformation failures at or near welds."
4. "All fasteners in the connecting system such as bolts, inserts, welds, and dowels and the body of the connectors shall be designed for the seismic force F_p determined by Eq. 6.2-3, using values of a_p and R_p taken from Table 6.3-1, applied at the center of mass of the panel." The seismic force F_p is determined by the equations below:

$$F_p = \frac{0.4 a_p S_{DS} W_p}{R_p / I_p}\left(1 + 2\frac{z}{h}\right) \qquad \text{Eq. 1.1}$$

F_p is not required to be taken greater than

$$F_p = 1.65 S_{DS} I_p W_p \qquad \text{Eq. 1.2}$$

The value S_{DS} is the design spectral acceleration at the short-period range (plateau of response spectrum), and the value W_p is the weight of the cladding component. The variable z is the height above the base at which the cladding component is located, and h is the total height of the structure. The variable I_p is the component importance factor; cladding components have an importance factor of 1.0. The variable a_p is the component amplification factor, which is taken equal to 1.0, 1.0, and 1.25 for the cladding panels, body of cladding connections (angles, tube sections, etc.), and fasteners of the connecting system (bolts, welds, etc.), respectively. The variable R_p is the component response modification factor, which is equal to 2.5, 2.5, and 1.0 for the cladding panels, body of cladding connections (angles, tube sections, etc.), and fasteners of the connecting system (bolts, welds, etc.), respectively.

The seismic force is applied independently in each of the two orthogonal horizontal directions in combination with service loads. In addition, the cladding component shall be designed for a concurrent vertical force of $0.2 S_{DS} W_p$.
5. "Where anchorage is achieved using flat straps embedded in concrete or masonry, such straps shall be attached to or hooked around reinforcing steel or otherwise terminated so as to effectively transfer forces to the reinforcing steel."

The cracking and fallout capacity of the glass in the exterior cladding system and storefront systems is to be designed to meet the relative displacement requirement of Equation 1.3.

$$\Delta_{\text{fallout}} \geq 1.25 I_p D_p \text{ or } 0.5 \text{ in. (13 mm), whichever is greater} \qquad \text{Eq. 1.3}$$

The value D_p is the maximum relative interstory drift computed from an elastic analysis, response spectrum analysis, or nonlinear time-history analyses for the design level earthquake. The variable I_p is the component importance factor; a conservative value for I_p is 1.5

Three exceptions to satisfying Equation 1.3 are given:

1. Glass with sufficient clearances from its frame such that physical contact between the glass and the frame will not occur at the design drift, as shown in Equation 1.4.

$$D_{clear} > 1.25 D_p \qquad \text{Eq. 1.4}$$

   The 1.25 factor in Equation 1.4 is used to reflect uncertainties associated with calculated inelastic seismic displacements in building structures (FEMA 356, 2000). The value D_{clear} is calculated with Equation 1.5:

$$D_{clear} = 2c_1 \left(1 + \frac{h_p}{b_p}\frac{c_2}{c_1}\right) \qquad \text{Eq. 1.5}$$

   Where h_p is the height of the glass pane, b_p is the width of the glass pane, c_1 is the clearance (gap) between the vertical glass edges and the frame, and c_2 is the clearance (gap) between the horizontal glass edges and the frame. Further analysis and discussion of Equation 1.5 is given in Chapter 5.
2. "Fully tempered monolithic glass in Seismic Use Groups I and II located no more than 10 ft (3 m) above a walking surface."
3. "Annealed or heat-strengthened laminated glass in single thickness with interlayer no less than 0.030 in. (0.76 mm) that is captured mechanically in a wall system glazing pocket, and whose perimeter is secured to the frame by a wet glazed gunable curing elastomeric sealant perimeter bead of 1/2 in. (13 mm) minimum glass contact width, or other approved anchorage system."

The fallout capacity of the glass shall be determined by experimental testing or engineering analysis. Results of fallout experiments of glass are discussed in Chapter 7.

A comparison of the code requirements of the 1997 Uniform Building Code and 1994 NEHRP Recommended Provisions for Seismic Regulations for New Buildings is given in Carpenter (2004).

1.7 DAMAGE TO CLADDING SYSTEMS

During the past several years, the seismic performance of cladding systems has become a greater concern to engineers due to numerous cladding failures. Despite their widespread use, there is a lack of knowledge about how cladding systems and their components truly behave in earthquakes. In addition, the design of cladding systems is often fragmented: the cladding system is usually conceived by the architect, designed and fabricated by the cladding manufacturer, and checked by the structural engineer (Masek and Ridge, 2009). Cladding is an expensive part of a building and can cost as much as 20% of the building's initial cost (Facades, 1980; Taghavi and Miranda, 2003). In addition, if repairs are needed to the cladding system after an earthquake, the true cost of a building's façade can be much more than anticipated.

Considerable damage to cladding systems has been reported from the 1964 Anchorage, 1971 San Fernando, 1978 Miyagiken-Oki, 1985 Mexico City, 1987 Whittier Narrows, 1994 Northridge, and 1995 Hyogoken-Nambu earthquakes (Hareer, 2007). Several photographs of damage to cladding systems are shown in Fig. 1.21. Reports of damage to cladding systems in the 1995 Hyogoken-Nambu earthquake are given in Seike *et al*. (1997). Several examples of the failure of cladding systems in the 1985 Mexico City earthquake are provided in Goodno *et al*. (1989). Goodno *et al*. surveyed the post-earthquake damage to precast cladding systems in 25 buildings that are 10-20 stories tall and found that the overall performance of the cladding was not good. Approximately two-thirds of the buildings had some glass damage and a significant portion of these buildings has serious glass damage to over 25% of the windows.

Due to the sheer number of buildings employing precast cladding systems, the possibilities of glass breakage and fall out and the detachment of heavy concrete façade panels represent a severe threat to life safety. However, very few casualties have occurred due to cladding failure. Arnold (2008) reports that in recent U.S. earthquakes, only three deaths have occurred due to falling concrete cladding panels. Falling panels at the J.C. Penney store in the 1964 Alaska earthquake killed two people (Fig. 1.21d). A student was killed in the 1987 Whittier, California, earthquake by a concrete panel that fell from a parking structure at California State University, Los Angeles while she walked beneath it. (Fig. 1.22).

Several researchers have studied the seismic performance of cladding systems and sources of their damage. It has been shown that the cladding system does in fact interact with the structural system, which causes unexpected damage to the cladding system (i.e. Wolz *et al*., 1992; Henry and Roll, 1986; Goodno *et al*., 1983; Pinelli *et al*., 1995). A literature review of the previous research projects on the seismic performance of cladding is given in Chapter 2.

More research needs to be completed on the subject of cladding so we can better understand their behavior and minimize the life safety and financial risks due to their failure. Some of the unresolved questions concerning the seismic performance of cladding systems are listed below. This dissertation aims to answer all of these questions.

- How can we analytically model a typical cladding system?
- How much does the cladding system influence the modal periods, lateral strength, seismic drifts, and floor accelerations of a bare-frame structure?
- How can we better understand the mechanics of deformation in a typical cladding system?
- How do we estimate the demands in the cladding connectors using analytical equations?
- What are the probabilities of failure of the components in a typical cladding system?
- What are the expected damage states and repair quantities of the components in a typical cladding system?
- How high are the repair costs of a cladding system compared to the repair costs of the rest of the building components?

1.8 DISSERTATION OUTLINE

This dissertation is organized into eight chapters. An introduction to cladding system was provided in this chapter, including cladding typologies, definitions, and code approaches to

designing cladding systems. A literature review of the previous research on the structural response participation of cladding systems is presented in Chapter 2. The literature review summaries the previous analytical and experimental studies on how cladding systems can affect the free vibration and lateral response of multistory buildings to statically and dynamically applied loads. However, these previous studies were conducted using simplistic models and cladding systems with details that were not necessarily realistic of typical systems used today. Thus, new nonlinear analytic models of multistory buildings with cladding are developed in Chapter 3. The nine-story LA SAC building is used as the study structure, and three cladding systems are modeled to investigate their effects on the seismic response of the building. The results of modal analyses, pushover analyses, and dynamic time-history analyses of the models are presented in Chapter 4. Explicitly modeling the building with a cladding system is time-consuming and requires significant computer resources; thus, analytical expressions are derived in Chapter 5 to estimate the maximum seismic demands in the various components of the cladding system using the response quantities of the bare frame structure. The analytical results reveal that the column cover connections are especially susceptible to failure. Therefore, the failure probabilities of the column cover panels are investigated in Chapter 6 using structural reliability theory. Using the results of analytical studies and experimental tests, fragility curves of the performance of the components of the cladding system are developed in Chapter 7. These curves are used along with the analytical results in the Pacific Earthquake Engineering Research Center (PEER) performance-based earthquake engineering (PBEE) methodology to calculate the expected repair costs and repair times of the cladding systems. Finally, the main results and conclusions of the dissertation are summarized in Chapter 8. A description is also given of future experimental tests that will take place at *nees@berkeley* testing site.

(a) Jefferson County Government Center, Golden, Colorado (PCI, 2007)

(b) Four Lakepointe, Charlotte, North Carolina (PCI, 2007)

Fig. 1.1 Typical applications of precast concrete cladding (PCI, 2007)

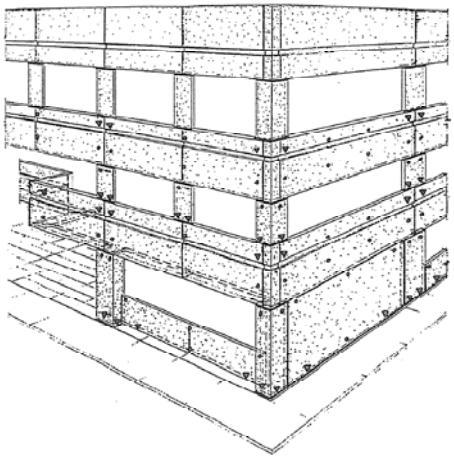

Fig. 1.2 Isometric view of typical cladding system with spandrel panels and column covers (Hegle, 1989)

(a) (b) (c)

Fig. 1.3 Panel configurations: (a) spandrel beams and column covers, (b) spandrel panels and glazing, (c) punched window design (PCI, 1989)

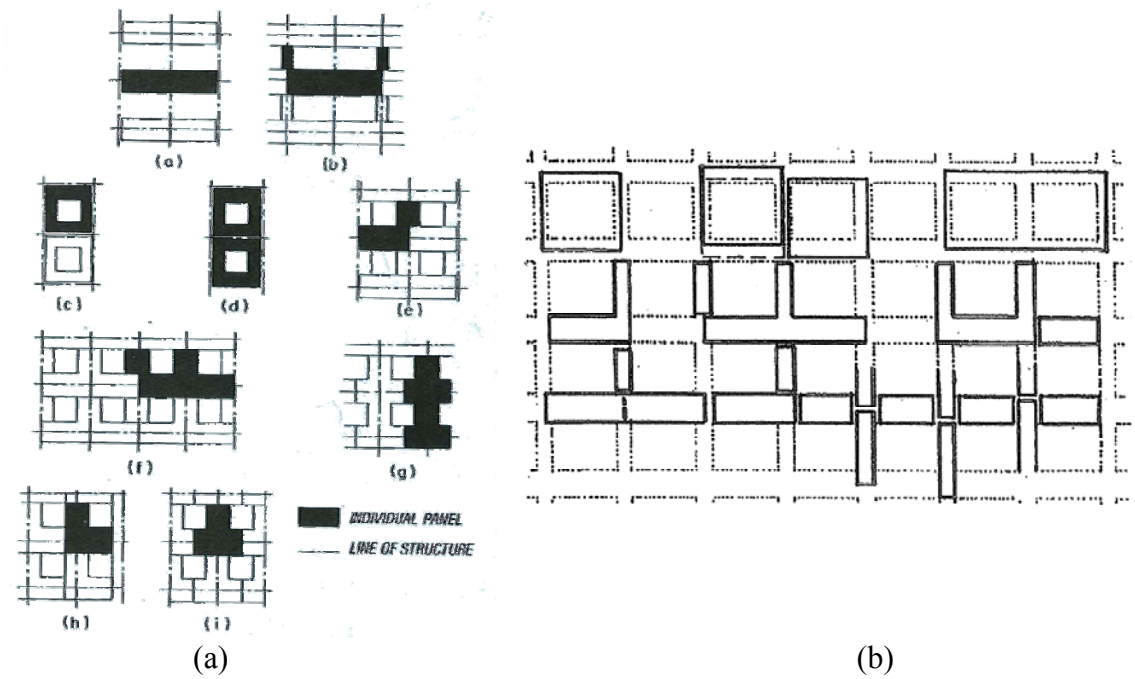

(a) (b)

Fig. 1.4 Cladding panel configurations and arrangements (a) from PCI (1989) and (b) from McCann (1991)

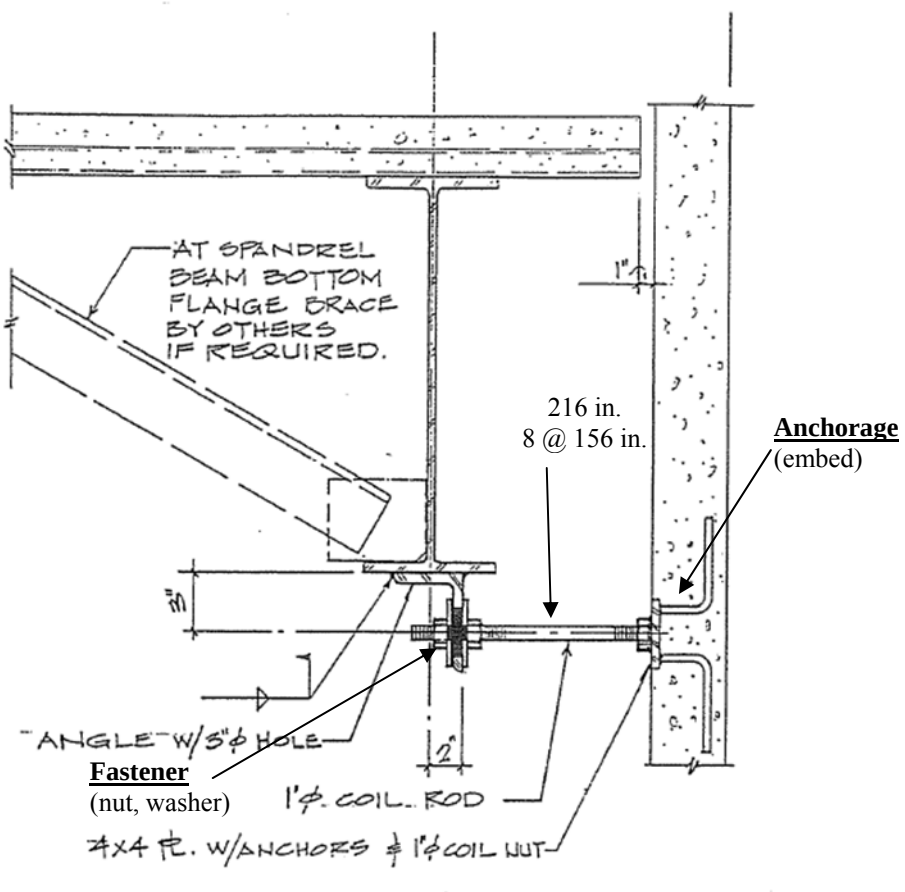

Fig. 1.5 Lateral push-pull connection to beam showing the three distinct parts of the cladding connection (Hegle, 1989)

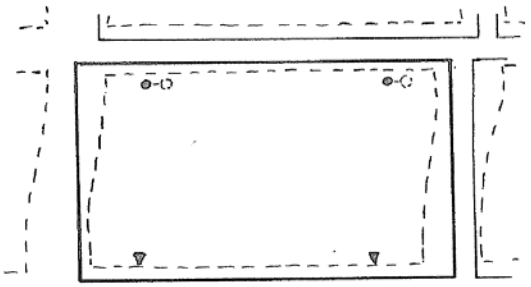

Fig. 1.6 Deformation of supporting frame and cladding connections (McCann, 1991)

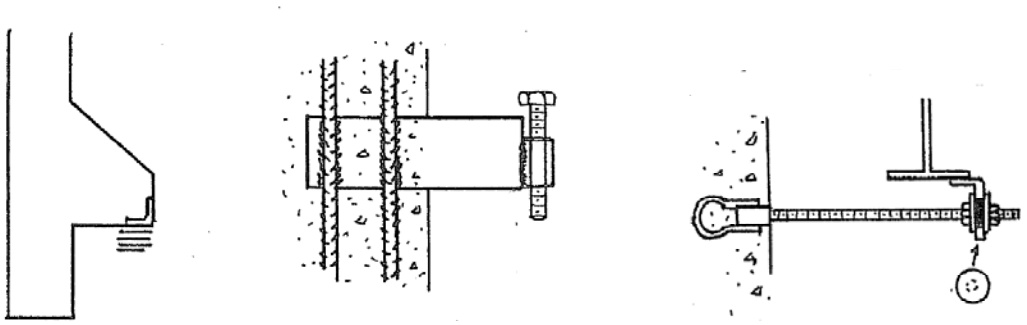

(a) (b)

Fig. 1.7 (a) Bearing connections and (b) push-pull lateral connection (McCann, 1991)

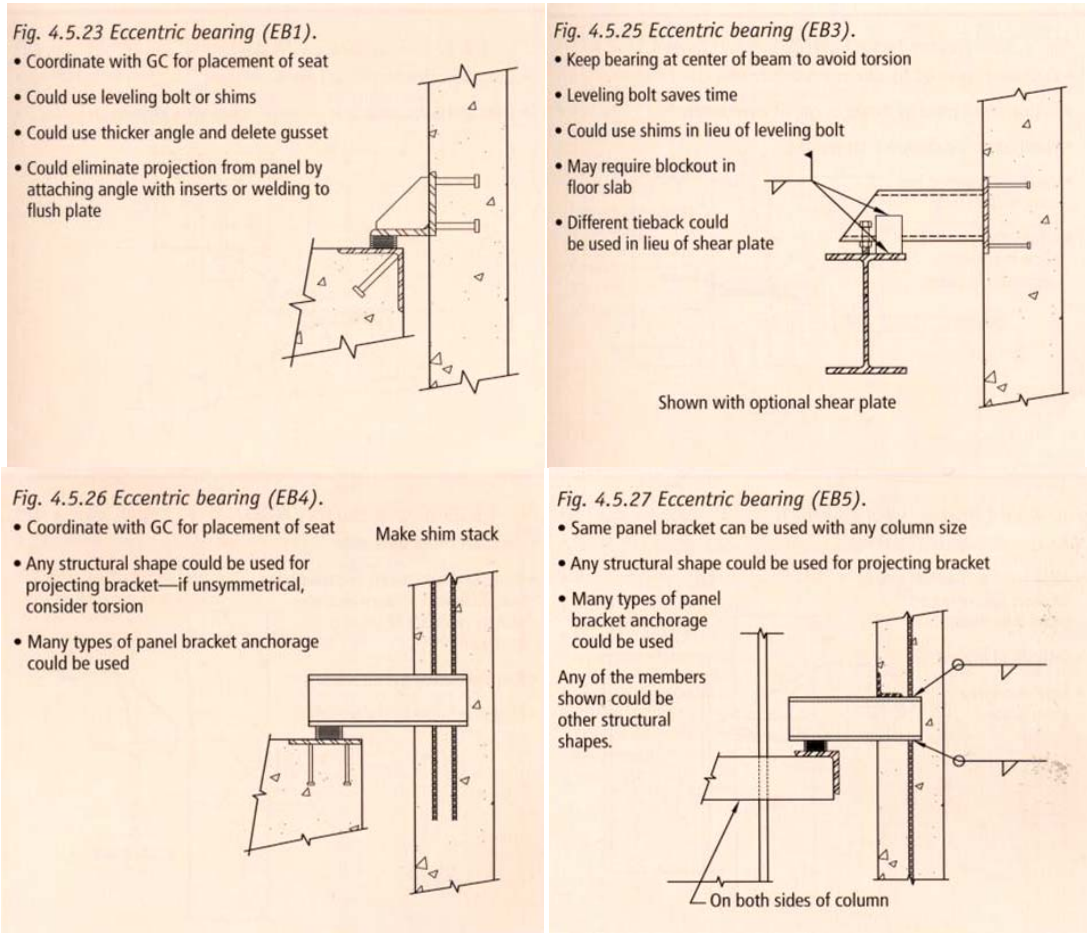

Fig. 1.8 Eccentric bearing connections (PCI, 2007)

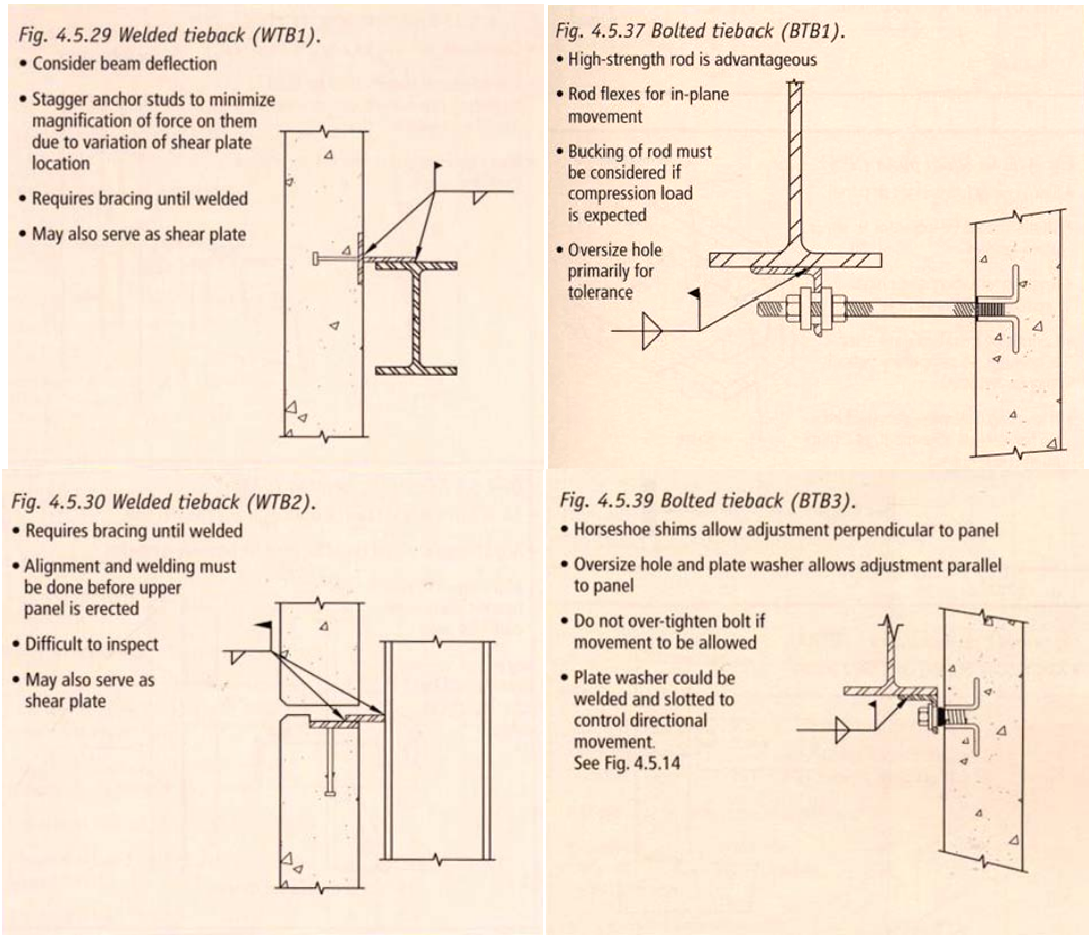

(a) welded tiebacks (b) bolted tiebacks

Fig. 1.9 Push-pull (tieback) connections (PCI, 2007)

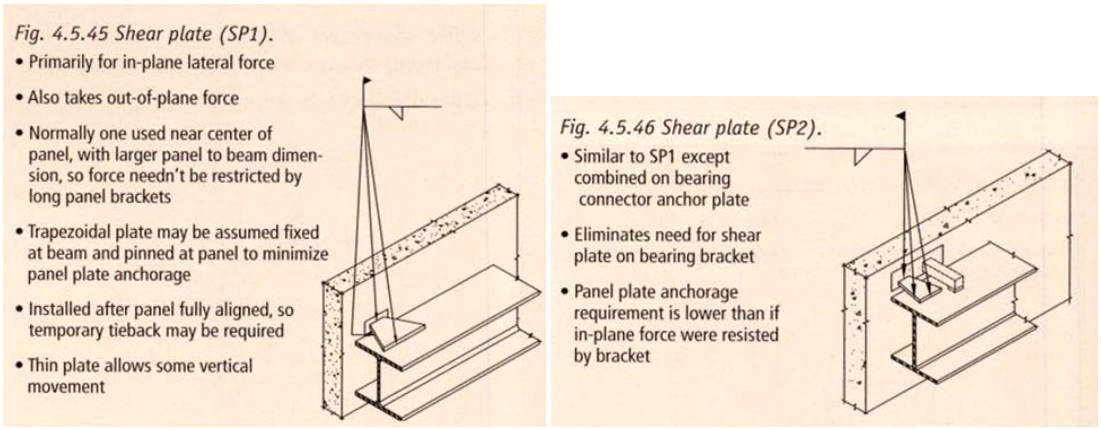

Fig. 1.10 Shear plate connections (PCI, 2007)

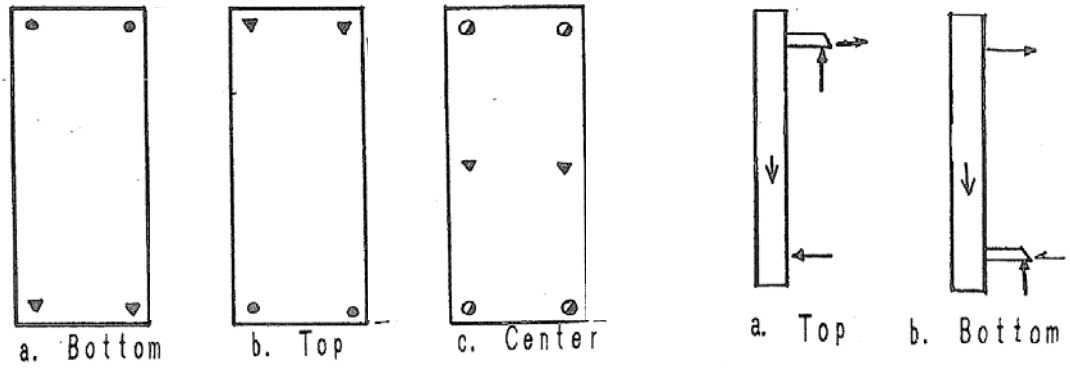

Fig. 1.11 Location of bearing support (McCann, 1991)

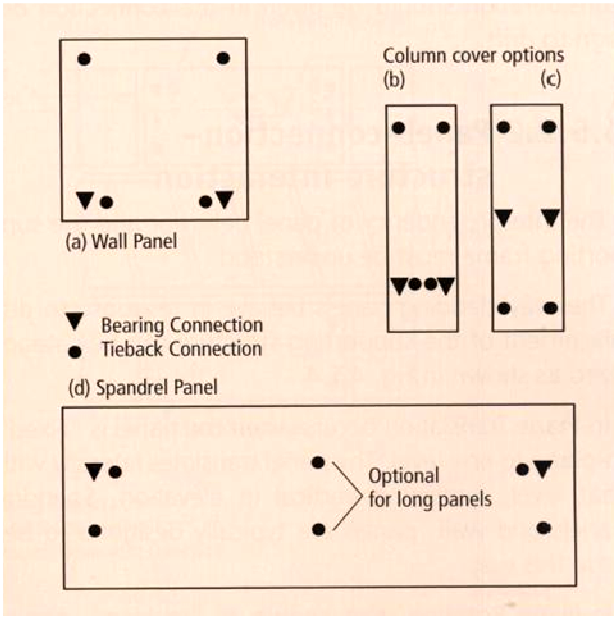

Fig. 1.12 Locations of bearing connections and tieback connections for different panel shapes (PCI, 2007)

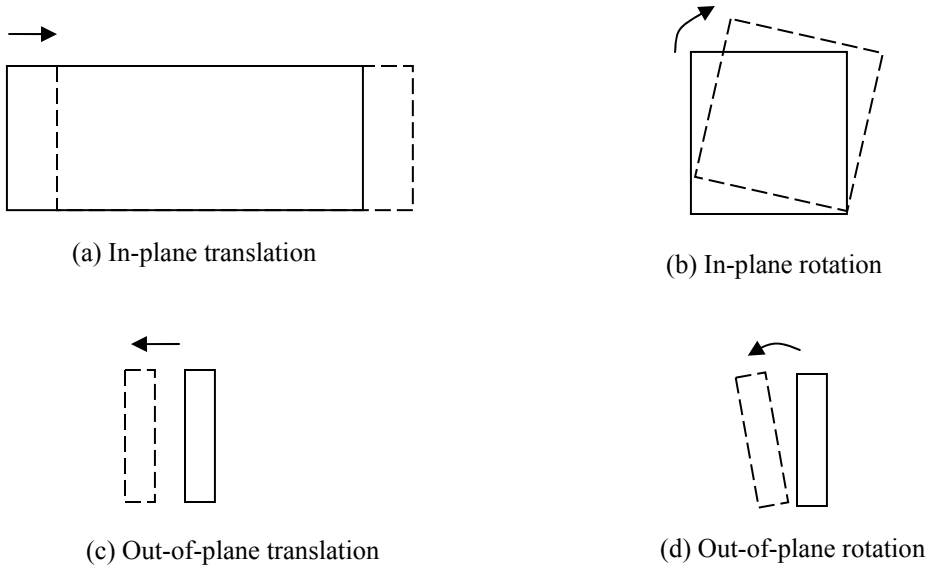

Fig. 1.13 Four different types of cladding panel movements

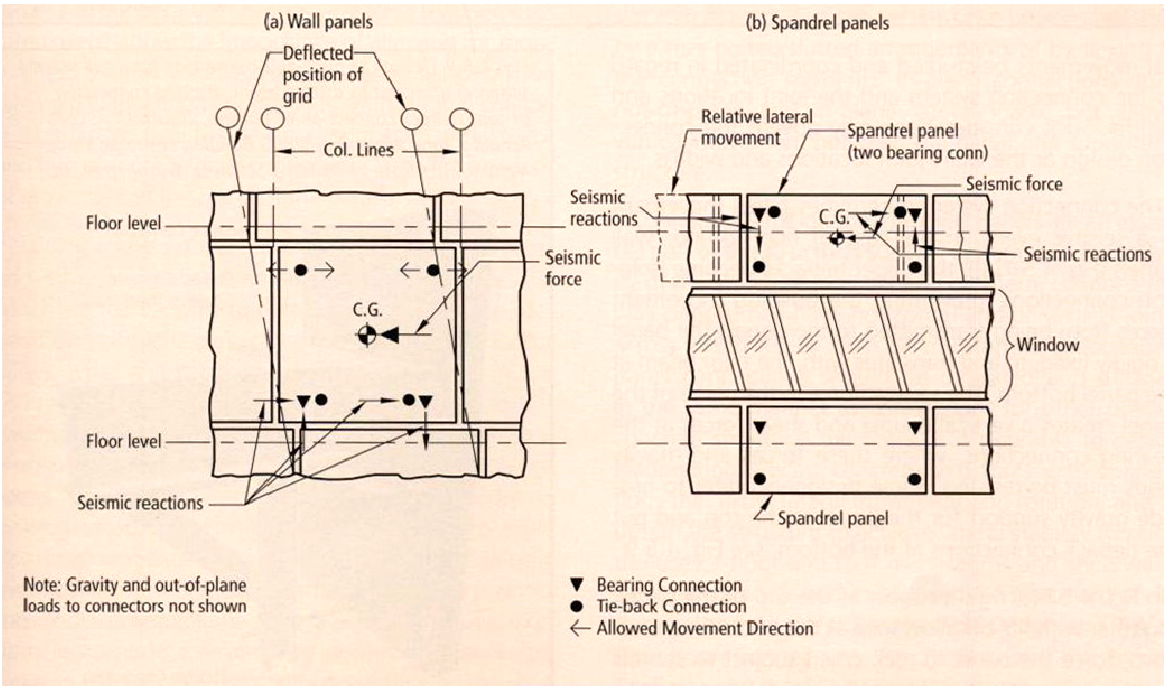

Fig. 1.14 Forces in spandrel panel connections due to interstory drift (PCI, 2007)

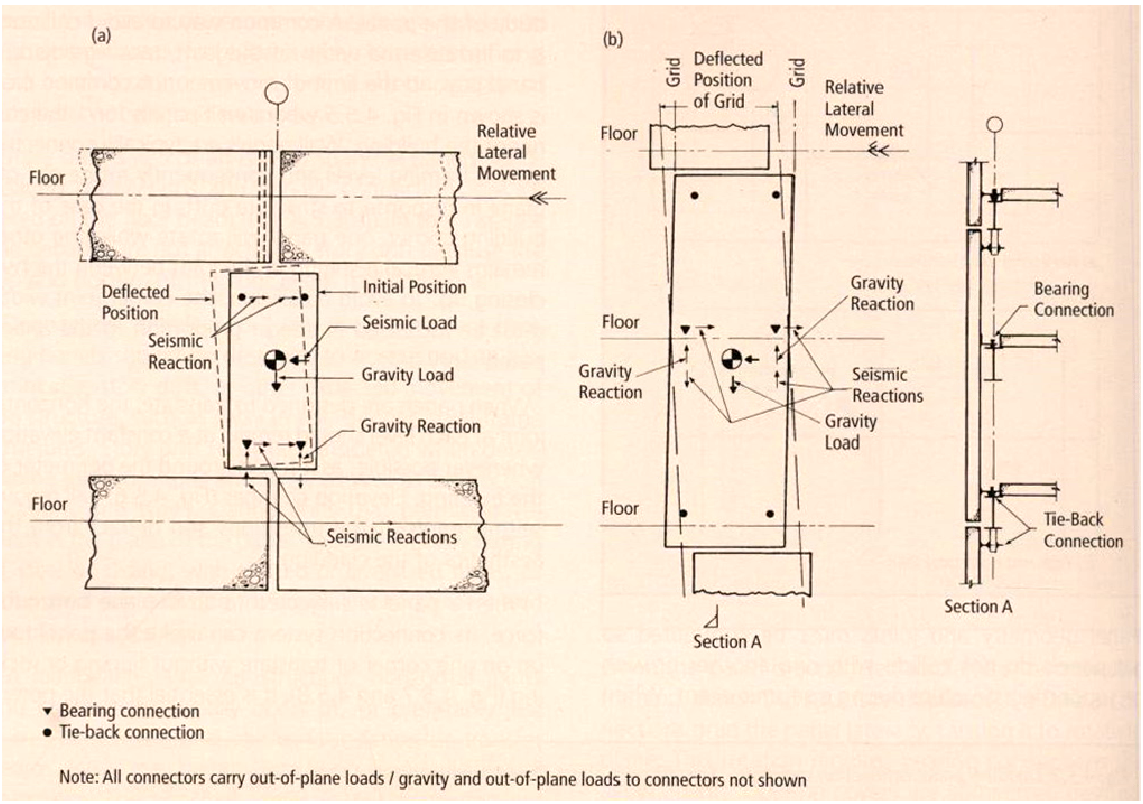

Fig. 1.15 Forces in column cover connections due to interstory drift (PCI, 2007)

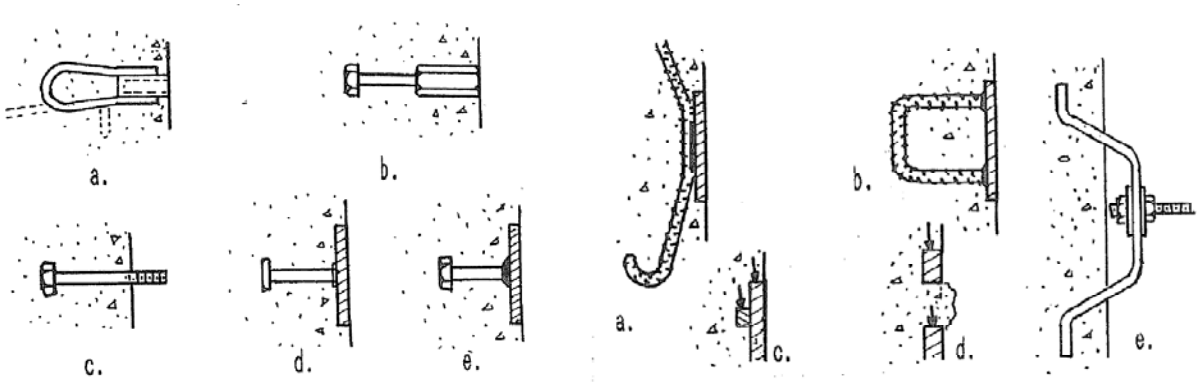

Fig. 1.16 Typical panel embedment connectors (McCann, 1991)

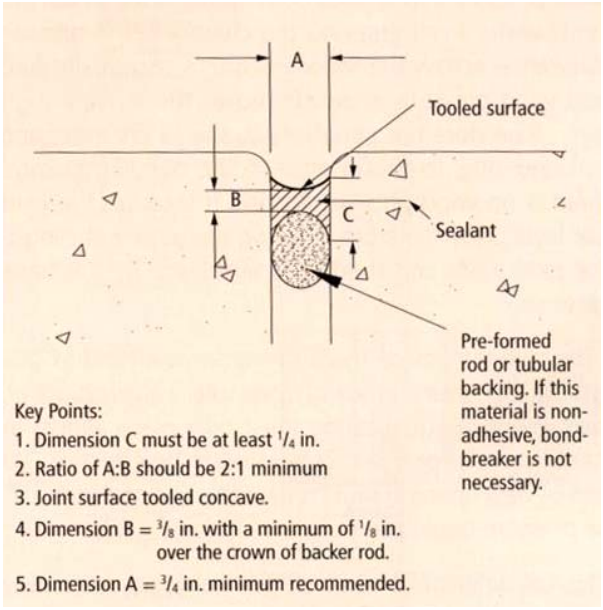

Fig. 1.17 Caulking in joint between panels (PCI, 2007)

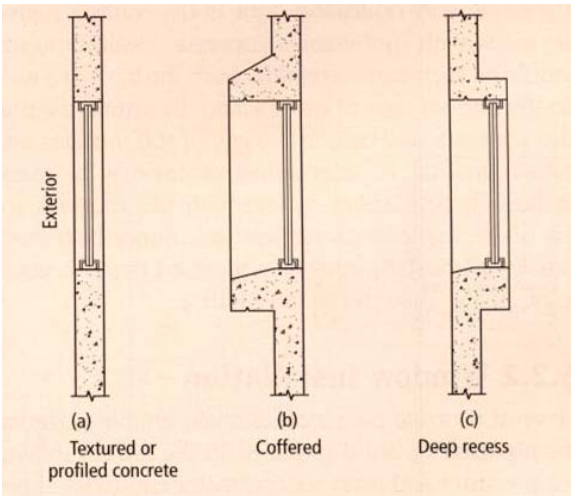

Fig. 1.18 Different recesses for window treatments (PCI, 2007)

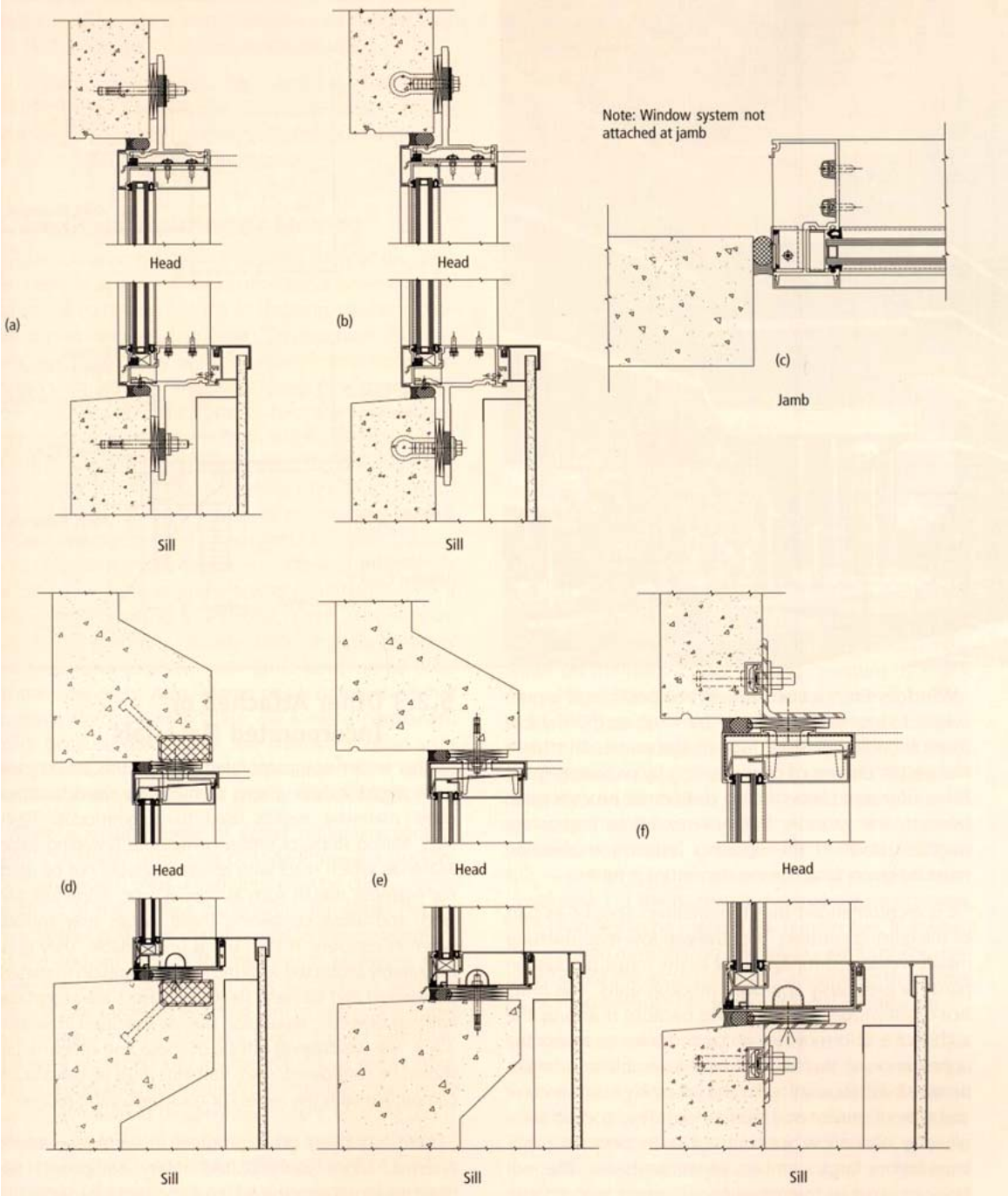

Fig. 1.19 Details of different window framing systems (PCI, 2007)

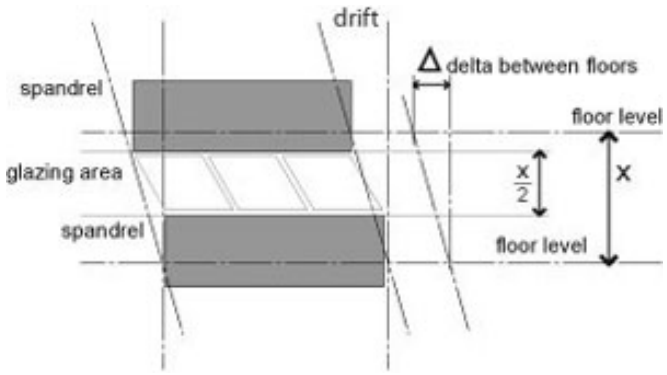

Fig. 1.20 The presence of cladding panels may increase interstory drifts in the window glazing system (Arnold, 2008)

(a) Kobe, 1995 (b) Kobe, 1995 (c) Northridge, 1994

(d) Alaska, 1964 (e) Kobe, 1995

Fig. 1.21 Photographs of cladding damage in past earthquakes (PEER Library)

Fig. 1.22 Parking structure at California State University, Whittier earthquake 1987: left, cladding panels; right, fallen concrete panel, causing fatality (Arnold, 2008).

Chapter 2: Literature Review on the Structural Response Participation of Cladding Systems

A review of the literature was performed to gain insight on how precast concrete cladding can affect the structural response of multistory buildings. Several research groups have performed analytical and experimental studies of the seismic response contribution of cladding.

In Section 2.1, an introduction and historical overview is provided on the contribution of cladding to seismic response. Then, a review of the previous analytical and experimental research on the contribution of cladding to seismic response is presented in Sections 2.2-2.5.

2.1 INTRODUCTION

Typically, nonstructural elements are designed and regarded as separate from the primary structure. This approach simplifies the design process and allows the engineer to focus on one set of nonstructural elements at a time and not worry about their possible interaction with the primary structure. However, many nonstructural elements are connected to different parts of the structure: partitions span between two floors, cladding panels span between two stories, and ceiling systems span across multiple beams (Pinelli *et al*., 1995). Therefore, there is potential for interaction between the nonstructural components and the primary structure, and it has been shown that this interaction may be beneficial or detrimental to the seismic performance of the building (Goodno *et al*., 1983). Engineers try to isolate the nonstructural elements such as exterior cladding from the structure by using connections with flexible elements or slotted holes and placing gaps between the nonstructural and structural elements. However, in seismic events, the connections may be overstrained, the gaps too small, or the slotted holes too short, and interaction between the different elements often occurs, sometimes in the form of cracked partitions, falling cladding panels, or collapsed ceilings (Pinelli *et al*., 1995).

Heavy precast panels that hang from the primary structure provide a link (force transfer) between two adjacent stories. During an earthquake, the connections between the panel and the structure are subjected to shear generated by the interstory drift of the supporting structure. Even when engineers try to isolate the panels from the structure using slotted or flexible connections, analytical and experimental studies have shown that the panels still interact with the supporting structure (Henry and Roll, 1986; Palsson *et al*., 1984; Wang, 1987; Gaiotti and Smith, 1992). The high cost of architectural precast panels, high cost of the wind and seismic resisting systems, high cost of cladding repair, and the lack of understanding of the seismic response of cladding have stimulated several research projects related to the influence of cladding on the seismic

response of buildings (Thiel *et al*., 1986). The following sections summarize some of the relevant previous research projects.

2.1.1 Historical Overview

Interest in the effect of cladding on the structural strength and stiffness of multistory buildings has increased in the last twenty years. One of the first researchers to investigate the effect of cladding on the lateral response of buildings was Weidlinger (1973). He studied the behavior of shear panels and suggested that cladding can be incorporated into the main lateral resistance system to brace against wind. Gjelvik (1973) studied the interaction between the cladding panels and a supporting frame with pinned beam-column connections, and he reported that the panels had an important effect on the lateral resistance of the supporting frame. The dynamic properties of a steel frame with cladding panels were first studied by Oppenheim (1973). The main result was that in designs where the panels have approximately the same stiffness as the supporting frame, the upper-story panels undergo large deformations due to the "whipping effect" (cladding system is in resonance with the structural frame). Goodno *et al*. (1980), Goodno and Palsson (1981), Palsson and Goodno (1982), and Goodno *et al*. (1983) have studied the seismic response of steel frames with cladding panels attached. They compare the modal periods and dynamic response of analytical models with cladding panels to analytical models without cladding. The modal results show that the cladding adds stiffness to the supporting frame, but the results of the dynamic analyses reveal that the effect of cladding on the response of the supporting frame is dependent on the selected ground motion. Thus, it might not always be conservative to neglect the effects of cladding. Goodno and Craig (1989) present a historical summary of the research on the participation of cladding to the lateral resistance of buildings. The early analytical and experimental studies demonstrated that architectural precast cladding systems do in fact contribute to the lateral load resistance of multistory buildings.

More recently, research has focused on designing special panel-to-structure connections to provide additional damping to the structure. Elsesser (1986) stated "We have slowly progressed from masonry construction in 1900 to steel and reinforced concrete framing in the 1920s, to welded steel frame assemblies in the 1950s, to ductile concrete frames in the 1970s, to eccentric braced steel frames in the 1980s, and now we are designing buildings with new concepts using isolation and damping devices." Elsesser projected that by using high-damping cladding connections, the interstory drifts can be substantially reduced under moderate seismic events. The concepts of using ductile, high-damping cladding connections to reduce the seismic response of the supporting structure are summarized well by Pinelli *et al*. (1995).

2.1.2 Contribution of Cladding to Seismic Resistance

The design and detailing of the cladding panels, connections, and structural framing dictate how much the cladding panels and connections participate in the seismic resistance of the building. Four levels of cladding participation are classified by Arnold (1989):

1. "*Theoretical Detachment*: This is represented by the typical push-pull detail for cladding attachment used in California. While, in theory, the ductile rod connection detaches the cladding from the structure, in a building with hundreds of cladding

panels it is likely that the detachment is not complete, and there is some transmission of forces from the structure to the panels and vice versa."

2. "*Accidental Participation*: This occurs with connections such as slotted connections and sliding joints in which, because of deterioration or errors in installation, the separation between the cladding and structure is not effective. This is uncontrolled participation."
3. "*Controlled Stiffening or Damping*: This involves the use of devices to connect the cladding to the structure in such a way that the damping of the structure is modified (usually increased) or the structure is stiffened."
4. "*Full Structural Participation*: The cladding and the structure become a new integrated composite structure in which each element performs an assigned role. The cladding may participate in vertical support, and definitely contributes to lateral resistance."

2.1.3 Architectural and Structural Requirements for Structural Cladding

The configuration or typology of the cladding can determine how much the cladding system participates in the load-resisting capacity of the structure. In Section 1.1.2, three basic cladding configurations were discussed. Arnold (1989) explains how each of these configurations might influence the behavior of the structure:

1. Individual vertical and horizontal panels which cover the beams and columns do not effectively help in lateral resistance, but the panel system might form a composite structure to resist vertical loads.
2. Horizontal or spandrel beams cannot help in resisting lateral forces because they do not brace between the floors. Stronger panels and connections might lead to "short columns" or a strong beam / weak column situation.
3. The full-bay rectangular panels that span between floors provide the greatest chance for contribution to lateral strength.

Arnold also notes that the structural engineer should investigate whether engaging the cladding system in the lateral-resisting system of the building provides significant performance and cost benefits. This information should be communicated by the structural engineer to the building owner. Then, the promotion of architectural cladding as structural cladding would be heard by architects from building owners who are looking for a "functional, cost-effective, and simple building" (Arnold, 1989).

The distribution of the responsibility in cladding design is discussed by Stockbridge (1990) and Sproken (1989). Stockbridge states that the roles of the design engineer and precast cladding contractor should be clearly defined. If the precast cladding contractor has extensive experience in design and selects the details, production, and erection procedures, he/she should be registered to sign and seal the panel shop drawings. On the other hand, Sproken believes that if the cladding is designed to participate in the lateral-load resisting system of the building, then the system must be designed by the structural engineer of record. In this case, the cladding is not simply a non-structural element. Sproken does not think that the precast cladding contractor should be responsible for the behavior of the structure. If the cladding is designed to participate in the lateral resistance of the building, Sproken states that the following information should be investigated:

1. What portion of the lateral load is resisted by the cladding?
2. Does the cladding follow the same deformation as the supporting frame?
3. How are thermal movements accommodated between the cladding and frame?
4. What is the relative long-term creep between the cladding system and frame?
5. What are the damage tolerances and expected repairs in the event that the design limits are exceeded?

These issues require more thought by the structural engineer, and the information must be communicated to the architect in the design process. In any case, more frequent consultations and interaction between the architect and engineer will produce a better and safer design.

2.2 INFLUENCE OF CLADDING ON STRUCTURAL BEHAVIOR

Several research groups have investigated the interaction between precast cladding panels and the supporting framing. Analytical and experimental studies have revealed that cladding may have a significant influence on the seismic response of the building as a whole. In the following sections, the results of previous research on the influence that cladding systems may have on the structural behavior of buildings are discussed. Some of the paper summaries are adapted from the abstract summaries in Cohen (1995).

2.2.1 Free Vibration

The cladding system is attached to the structural framing and may influence the free vibration properties of the building, much like an external shear wall. Several authors have researched the influence that cladding has on the building's modal periods. A large portion of the research that cladding systems have on the vibration properties of multistory buildings was performed by the research team at the Georgia Institute of Technology (Palsson and Goodno, 1982; Goodno *et al*., 1983; Goodno *et al*., 1984; Palsson *et al*., 1984; Goodno and Palsson, 1986; Palsson and Goodno, 1988; Goodno *et al*., 1988). The majority of these papers are summaries of the master report Goodno *et al*. (1983). The research team created analytical models of a 25-story steel-framed office structure to study the effect of cladding on its free vibration properties. The study building used for their models contains a central core with a moment-resisting frame in one direction and a braced frame in the other direction. The core frames were designed for gravity and wind forces only. The precast cladding consisted of two contoured panels per framing bay, with 12 bays on each building face. Three sets of ambient tests and one forced vibration test were performed on the building to determine the first three translational and torsional natural periods (Goodno *et al*., 1983; Palsson *et al*., 1984). A three-dimensional model of the bare frame structure of the building was also constructed to determine the natural periods analytically. The model was constructed as accurately as possible and considered the lateral stiffness of the interior and exterior frames and composite floor beams. When the analytical and measured periods did not agree, the researchers assumed that the difference in the periods was due to the effects of the cladding. The analytical periods of the bare frame structure were up to 34% and 48% greater than the measured translational and torsional periods, respectively. The researchers assigned a constant interstory shear stiffness value V to the stiffness matrix in each story that represented the stiffness of the cladding. The value of the parameter V was found to be

625 kips/in by matching the periods of the analytical model with the measured periods of the actual building. Thus, the researchers stated that the cladding decreased the translational periods by up to 34% and the torsional periods by up to 48%. The disadvantage of this approach is that the analytical model of the bare frame structure may not accurately represent the bare frame of the real building. In addition, it is erroneous to assume that the cladding makes up for all of the difference between the analytical and measured frequencies. Other architectural components may also contribute to the building's lateral stiffness, such as interior partitions, ceiling systems, and stairwells.

The effect of a simple cladding system on the modal properties of a multistory concrete framed building was investigated with analytical models by Henry and Roll (1986). The study building was a two-dimensional, nine-story, three-bay concrete moment-framed structure. The cladding system consisted of spandrel panels attached to the structural frame at the panel corners. Two panels were used to represent one spandrel panel, as shown in Fig. 2.1. The cladding panels were modeled using four-node shear elements, and the stiffness matrices for the cladding connections were modeled as rigid elastic elements with their end conditions fixed. Using this approach, all of the deformations in the cladding system occur in the panels themselves. Several models of the building were constructed to vary different parameters: three variations of bay widths (35 ft, 25 ft, and 15 ft.), five variations of panel heights (0 ft, 3 ft, 5 ft, 7 ft, and 9.5 ft.), and two variations of concrete weight for the panels (150 pcf and 100 pcf). The story height H was taken as 10 ft. Modal analyses were performed on the bare frame structure and the structure with cladding. For the model with 35 ft bay widths, a panel height of 3 ft ($h/H = 0.3$), and normal weight concrete, the fundamental period of the model with cladding is 18% smaller than the fundamental period of the bare frame model. For the model with 35 ft bay widths, a panel height of 6 ft ($h/H = 0.6$), and normal weight concrete, the fundamental period of the model with cladding is 55% smaller than the fundamental period of the bare frame model. The comparison between the bare frame model and the model with cladding for other choices of panel sizes and bay widths is shown in Fig. 2.2. The disadvantage of the Henry and Roll modeling approach is that the authors assumed that all of the deformations in the cladding system occur in the panels themselves. Modeling the cladding system in this manner overestimates the contribution of the cladding to the lateral stiffness of the building. In reality, the shear stiffness of the cladding connectors is much lower than the panels, which can be assumed to act as rigid blocks.

In 1979, a U.S.-Japan testing program was performed on a full-scale steel structure to determine the seismic performance of nonstructural elements (Wang, 1986; Wang, 1987; Wang, 1992). The test building was six stories tall with story heights of 11 feet. There were two bays of framing 25 feet wide in each direction of the building. The three-dimensional test specimen demonstrated the behavior and interaction of cladding which isolated assemblages would not. The test building was constructed with interior partitions, ceilings, doors, and exterior cladding. Both Japanese and U.S. precast cladding systems were attached to the building, as shown in Fig. 2.3. A statically applied loading sequence was applied to the building to determine the seismic performance of the nonstructural elements. However, prior to the static testing of the frame, the Japanese side conducted free vibration and forced vibration tests before and after the installation of the nonstructural elements to ascertain the stiffness and period of the structure. The fundamental periods of the test structure are reported in Foutch *et al*. (1986). The addition of the nonstructural elements reduced the natural period of the building by 30%, which suggests that the overall structural stiffness was increased by more than 100%. The stiffness decreased with damage to these elements. After 8 cycles at a story drift of 1/350 however, most of this

additional stiffness had been lost. Despite these insights from the free vibration tests, it is not possible to separate the contribution of the cladding because the free vibration tests either included all or none of the nonstructural components.

The vibration properties of a two-story structure with and without cladding were experimentally investigated by Rihal (1988, 1989). The test structure was a two-story steel moment-resisting frame structure with one bay in each direction. This test structure is a scaled down version of a larger full-size structure. All beams and columns in the structure are W6x9, A-36 shapes. The structure was connected to a precast concrete base using standard base-plate connections. Precast cladding panels were 4.5 inches thick, and the width and height of the panels were established so that the mass of the cladding panels expressed as a percentage of the mass of the steel test structure is the same as in a full-scale building. The cladding configuration and connection details were developed in consultation with a precast manufacturer who fabricated the cladding system in accordance with current practices. The modal response of the test structure was measured experimentally using random and sinusoidal excitations. The first two translational modal periods of the bare frame structure in the N-S direction were 0.14 sec. and 0.05 sec. With cladding attached, the first two translational modal periods were 0.17 sec. and 0.06 sec. One possible explanation offered by Rihal for the increase in period after adding the cladding is that the effects of the added mass of the precast panels seems to have overcome the additional stiffening offered by the cladding panels and connection assemblies to the test structure.

The vibration properties of a highrise building were measured while construction was in progress in order to trace the changes in the values of the parameters with construction (Meyyappa *et al*., 1981). In particular, the measuring process began after erection of the steel structure when the installation of cladding had just started and continued at seven periodic intervals until cladding was completely in place. The study building was a 24-story steel office tower with a lightweight precast cladding and glazing system. Ambient tests were performed to determine the free vibration periods of the first three translational modes and torsional modes. The test results found that the first translational period in the N-S direction was 2.09 sec. at the beginning of cladding construction and increased to 2.25 sec. when cladding was complete. The first translational period in the E-W direction was 3.11 sec. at the beginning of cladding construction and increased to 3.13 sec. when cladding was complete. The first torsional period started at 1.37 sec. and was 1.45 sec. when the cladding construction was complete. In the higher translational modes, the period first increased after cladding erection began, but then returned to its initial value after cladding construction was complete. The trends of elongated periods at the end of construction is largely attributed to the mass of the cladding and other elements that were moved into the building and stored for later use in construction. In this case, the stiffness of the cladding was not large enough to overcome the effects of the additional mass it provided to the building.

2.2.2 Drifts Due to Statically Applied Loads

The contribution of cladding to the lateral stiffness of buildings was also studied by comparing the drifts of frames with and without cladding. Lateral static forces were applied by Henry and Roll (1986) to their nine-story three-bay model discussed in Section 2.2.1. The equivalent lateral static forces varied linearly up the height of the building and were developed

for an ATC region 7 earthquake. The lateral displacements at the roof were recorded after application of the loads, and the displacements of the frame with cladding were non-dimensionalized with respect to the displacements of the bare frame model. The roof displacement ratios, shown in Fig. 2.4, are plotted for the different bay widths and panel heights. The lateral roof displacement decreased as the height of the panel (height ratio h/H) increased. The model with panels with h/H equal to 0.3 decreased the lateral displacement of the bare frame by 30% for the case of 35 ft. bay widths. The lateral roof displacement of the model with panels with h/H equal to 0.6 decreased the lateral displacement of the bare frame model by 75%. As discussed previously, the drawback to these analyses is that the connectors are modeled as rigid elements and all the deformations in the cladding systems occur in the finite elements of the panels. This approach overestimates the stiffness of the cladding system.

Smith and Gaiotti (1989) and Gaiotti and Smith (1992) studied the potential lateral stiffening effect of precast concrete panels to a bare frame structure. The authors performed an analytical study of a laterally loaded moment-resisting frame with and without cladding panels. Rather than analyzing a multistory multi-bay structure, a single-story module was analyzed, which was designed to behave as a typical end-bay-width story of the frame. The cladding system consisted of one panel (125 mm [4.9 in.] thick precast concrete) that was a full story high and a full bay long with two window openings. The cladding system and connections were described as typical of those used in Montreal and other eastern cities and may not be representative of designs in areas of high seismicity. The panel model and connections are shown in Fig. 2.5: the panel is attached to the frame with two bearing connections, 1 and 5, near the bottom of the panel and four tie-back connections, 2, 3, 4, and 6. The steel moment-resisting frame was modeled with linear elastic elements, and the panel was modeled by a mesh of 240 plane stress elements with a modulus of elasticity of 20 kN/mm^2 (2900 kip/in^2). The stiffness values of the various connectors are shown in Table 2.1. The stiffness values seem to be very large. For instance, the horizontal stiffness of a tie-back connector (connector 2, 3, 4) is 1,167 kN/mm (6,663 kip/in), which is not common for tie-back connectors in the western U.S. The analytical model was subjected to a lateral force at the top, and the displacements of the frame were recorded. The displacements recorded for different analyses are shown in Table 2.2. The displacement of the story-height module decreased from 126.35 mm (4.97 in.) to 3.62 mm (0.14 in.) with the addition of the cladding system. This reduction means that the shearing stiffness of the model with the panel attached is 35 times that of the bare frame. These results are, however, impractical because the stiffness values assigned to the connectors are unrealistically large.

The effect of precast concrete cladding on the lateral response of multistory buildings was investigated by Charney and Harris (1989). They performed analytical studies to determine the effect that a cladding system has on the lateral displacements of a steel moment-resisting frame building. The building, shown in Fig. 2.6, was four stories tall and two bays wide, and the cladding system used was similar to the one in Henry and Roll (1986). The cladding panels were modeled with two four-node shear elements per bay, and the cladding connections were modeled as short beams (with fixed end conditions) four inches in length with a cross section of 0.5 by 6.0 inches. It was assumed the connections were bending about their minor axis. The analytical model was subjected to lateral loads of 20 kips at the first three stories and 10 kips at the roof, and the lateral displacement of the third story was recorded. The primary variable in the analysis was the panel thickness. The effect of the third floor displacement was computed in terms of beam deformation, column deformation, connector deformation, and panel deformation, as shown in Table 2.3. The values listed under “Total” in Table 2.3 are the total lateral

displacements that occurred in the third story. The inclusion of even the 2-inch thick panel decreases the lateral drift from 0.4520 inches to 0.3249 inches, representing a reduction of approximately 28%. For the thin 2-inch panel, the connectors and panels contributed 14.4% and 8.4%, respectively, to the total drift. However, when the panel thickness is increased to 6 inches, the percentages change to 20.3% and 4.3% for the connectors and panels. For the 60-inch thick panel (which represents the infinitely rigid case), the total drift reduced to 0.2921 inches, with the connector being responsible for 24.4% of the total. The total panel-connector contribution was approximately 24% in each of the analyses that included the effect of cladding. This would seem to suggest that in some applications, negligible loss of accuracy would result from modeling panels as infinitely rigid. The authors qualitatively address the effect that cladding panels have on the strength of the supporting frame. As mentioned in Henry and Roll (1986), the panels may redistribute the shear forces and bending moments in the beams and columns. An example structure with cladding panels is shown in Fig. 2.7a. If the panel connections include a slotted hole three inches in width with a 1.0-inch diameter bolt, then there is a maximum of 1.0 inch of "play" in either direction. If the interstory drift in the frame exceeds 1.0 inches during a severe earthquake, as shown in Fig. 2.7b, the effective height of the column is decreased, and the shear force in the column increases drastically. This situation may result in a short-column shear failure mode.

The structural participation of architectural precast concrete cladding was also studied by Sack *et al*. (1989). The authors performed experimental tests on simple cladding connections to determine their force-deformation behavior and energy dissipation characteristics. The test model was a one-story, single-bay frame assemblage containing two precast panels. The panels were connected to the frame with bearing connections at the base and slotted and threaded rod connections at the top. The results of the experimental tests of the connectors were used to model the cladding system analytically. The purpose of the analytical study was to predict the interaction between the structural framing and cladding system. The structural framing was idealized using beam, truss, and spring elements, and the panels were idealized as two-dimensional panel elements. A nonlinear static analysis was performed assuming the structural frame behaved linear elastically and the panel-frame connections behaved with material nonlinearity. The analytical studies showed that the model with cladding had 17% greater stiffness than the bare frame. However, the experimental measurements of stiffness show no appreciable increase in lateral stiffness when the panel is attached, due to the low stiffness of the threaded rod connections and slotted connections.

2.2.3 Drifts Due to Dynamically Applied Loads

The dynamic response of structures with cladding was investigated by several researchers. Thiel *et al*. (1986) studied the effect that the cladding system has on the damping properties of a ductile steel moment-frame. The researchers performed nonlinear time-history analyses of a hypothetical 15-story building of uniform mass and stiffness and four 20 ft. bays. The cladding was modeled as dampers lumped at each floor and idealized as having elastic-perfectly plastic behavior. The building was subjected to a base motion accelerogram consistent with the ATC-3 0.4g spectrum. The roof displacement and equivalent base shear were recorded during the time-history analyses. The main conclusions were that the effectiveness of the dampers, which represented the cladding system, increased with increasing yield level. The

cladding dampers require relatively high stiffness, comparable to the structure's story stiffness to be most effective. For the high yield levels and 2% viscous damping in the frame, the cladding damper reduces the response of the structure by approximately 40% as measured by the maximum roof displacement and 45% as measured by the base shear. In summary, the authors argue that the effective damping of a building can be increased through activation of part of the lateral force resistance capacity of the cladding panels and controlled hysteretic behavior of their connections to the structure. However, as stated in their paper, the cladding connections require very high stiffness to be effective, which is not feasible given the connection details and design approach currently used today.

Most of the studies performed on the dynamic response of frames with cladding are analytical studies by researchers at the Georgia Institute of Technology (Goodno *et al*., 1980; Palsson and Goodno, 1982; Goodno *et al*., 1983; Goodno *et al*., 1984; Palsson *et al*., 1984; Goodno and Palsson, 1986; Palsson and Goodno, 1988; Goodno *et al*., 1988). The researchers performed a limited number of time-history analyses using the analytical model of the 25-story study building described in Section 2.2.1. Four different analytical models of the cladding system were considered. The first involved adding a constant interstory shear stiffness value (calculated by matching the modal periods of the analytical bare frame model and measured period of the actual building) to the stiffness matrix of the bare frame model. As discussed in Section 2.2.1, the drawback in estimating the interstory stiffness of the cladding with this approach is that it assumes that the analytical model of the bare frame is exactly right in determining the modal periods of the building's bare frame. Also, this approach neglects the other important nonstructural contributions to the interstory shear stiffness. The constant interstory shear stiffness of the cladding was selected to be 625 kips/in. In Goodno and Palsson (1986), the researchers performed time-history analyses with two ground motions. The maximum seismic drifts for the two earthquakes are shown in Fig. 2.8. For the El Centro motion, the drifts are slightly higher in the frame with cladding than in the bare frame structure, while for the Parkfield motion, the drifts in the frame with cladding are less than the drifts in the bare frame structure in the upper stories. The results are highly sensitive to the ground motion used. The second modeling approach for the cladding is an incremental failure model. The stiffness of the connectors is reduced in steps as allowable drifts are reached. The simplified force-deformation relationship for the failure model is shown in Fig. 2.9a; failure is defined as a loss of stiffness. The allowable drift was taken to be 0.0025-0.005 times the story height. The results using the failure model were found to lie between the cladded results from the first approach and the uncladded model results, as shown in Fig. 2.9b. The third cladding model is a hysteretic model shown in Fig. 2.10a. The lateral stiffness of the row of panels and connectors is variable and contains both elasto-plastic and shear-slip behavior. The response of the supporting framing is still assumed to be linear. Fig. 2.10b shows the comparison of the hysteretic model with the constant interstory shear model; the overall response was fairly similar. The fourth panel connector model is a slotted connection model. The force-deformation relationship consisted of an initial slip stiffness of $V/10$ followed by a second interstory stiffness of V. The response of the structure using the slotted connection model was bracketed by the response of the models with cladding previously discussed and the bare frame model.

A similar study using the same analytical model was conducted by Goodno *et al*. (1980). The cladding model used in this case was the constant interstory shear stiffness model with V = 725 kip/in. The time-history analyses involved six ground motions, and the maximum roof displacements were recorded for each motion. The maximum roof displacements of the frame

with cladding were less than the maximum roof displacements of the bare frame for three of the ground motions (14%, 22%, and 38% decrease). For the other three ground motions, the maximum roof displacements in the frame with cladding were larger than those in the bare frame (54%, 67%, and 82% increase). These results emphasize the dependence of the effects of cladding on the ground motions selected in the analysis.

Wolz *et al*. (1992) studied the response of a building with cladding using an analytical model and time-history analyses. The study building was a six-story 1:4 scale model of a moment-resisting frame. There were two cladding panels per bay, as shown in Fig. 2.11a. The cladding panels were represented by truss members and were assumed to be rigid in-plane with attachment points located at the beam-column joints and at the midspan of the beams on two successive floor levels. The lower two cladding connectors were assigned to be rigid, while the upper two cladding connectors were assigned to be flexible. The horizontal force-deformation relationship of the flexible connections was assumed to be bilinear with an arbitrarily assigned initial stiffness of 100 kip/in. The model was subjected to one input of ground acceleration, a two-sided pulse with maximum amplitude of 0.3g. The time-history of the roof displacement of the bare frame model and the model with cladding were recorded. The maximum roof displacement of the model with cladding was approximately 33% less than the roof displacement of the bare frame model, as shown in Fig. 2.11b.

2.2.4 Experimental Studies by Wang (1987)

The results of the experimental tests of typical U.S. and Japanese cladding systems are discussed in Wang (1987). A description of the test structure and setup was given in Section 2.2.1. The six-story structure was tested statically with actuators that provided horizontal forces at each story. The structure was displaced so that each story had approximately the same interstory drift (linear shape) with a loading sequence that consisted of alternate positive and negative displacements. The loading sequence started with story drifts of 1/1000, ramping up to 1/125 for several cycles and then finally up to 1/40. Several different cladding systems were attached to the structure, including rocking systems and sway systems with deformable connections. The U.S. cladding was installed on two levels (floors 2 and 4) with several commonly used types of bearing and lateral connections. The panels on floor 2 were connected with angle bearing connections and long-rod lateral connections, and the panels on floor 4 were connected with tube bearing connections and slotted angle lateral connections. Many of the sliding connections were the first to exhibit visible deterioration, which quickly accelerated into total failure at many points. Visible failure of a short-rod slotted connection began at a story drift of 1/250. This early progression of damage was attributed to the fact that some of the slotted connections were incorrectly installed by over-tightening the bolts. The test was stopped and the connections were loosened, after which they started sliding as intended. However, it was found that the slot width was inadequate in accommodating the story drift. The long-rod connections were found to perform much better and possessed significant ductility. Some cracking of the concrete in the cladding panels occurred at the bearing connections because these connections were so stiff. The summary of the main events in the test are given in Table 2.4.

2.3 BEHAVIOR OF CLADDING PANEL CONNECTIONS

The behavior of the panel-to-structure connections has a significant influence on the amount of interaction between the cladding panel system and supporting framing. The stiffness and strength of panel connections vary widely among different buildings (Smith and Gaiotti, 1989). The large variety of cladding and connection configurations limits the ability to collect and document data on how cladding systems affect the response of buildings. This lack of data has makes it difficult to develop realistic models for cladding systems (Goodno *et al*., 1989). In the following paragraphs, previous research on the behavior of panel connections is summarized.

Rihal (1988) undertook a testing program to investigate the earthquake resistance and behavior of precast cladding and connections in medium-rise steel-framed buildings. A cladding panel with bearing connections at the bottom and threaded rod push-pull connections at the top were tested with a cyclic loading pattern. The precast cladding panel was 8 feet wide by 10 feet high by 4.5 inches thick. Two 5/8-inch diameter threaded rods were attached to the top of the panel, and two bearing connections were attached to the bottom. The assembly was attached to a testing frame. The in-plane resistance was controlled by the binding deformation of the top threaded rod connections. The 8-inch long threaded rod failed at an applied load of 1.2 kips and an interstory drift ratio of 0.0117. The in-plane lateral forces in the top connections were approximately 0.25-0.40 times the panel weight at a drift ratio of 0.01. The load capacity of the push-pull connectors decreased with increasing rod length.

Sack *et al*. (1989) tested various basic connection assemblies to obtain the static stiffness properties and a limited amount of low cycle fatigue data. The connection types consisted of ferrule inserts with threaded rods and standard angles with welded inserts and face plates. The results of the test demonstrate that the panel connections perform as ideally elastic perfectly-plastic materials. It was noted that the steel face plates did not enhance the behavior of connections using single inserts and threaded bars, and the energy dissipation characteristics of the connections could be based on the product of the interstory drift and the plastic load limit. During the cyclic tests, the concrete of the panels maintained its integrity.

Craig *et al*. (1986) and Craig *et al*. (1988) investigated the behavior of steel inserts in cladding panels to determine their lateral stiffness, energy dissipation, and ductility. The test specimens were shelf angle inserts placed in a 3 ft. by 3 ft by 6 in. concrete panel, and the inserts were subjected to shear, moment, and pullout tests. The inserts experienced linear strain and displacement up to 10,000 lbs. In the load cycles from 10,000 lbs. to 11,000-12,000 lbs., the inserts exhibited nonlinear behavior with energy dissipation and changing slopes of load versus displacement. The method of failure was the undesirable mode of concrete fracture; a better design would be to integrate the insert with the panel reinforcing steel.

Pinelli and Craig (1989) tested seven concrete panels with steel plate inserts. The embedded inserts were supported with either welded 90-degree rebar J-hooks or welded rebar parallel to the surface of the concrete. The stiffness of the connections was approximately 330,000 lbs/in. The maximum resisted loads were approximately 6,000 lbs., and the inserts showed limited energy dissipation. The cyclic load tests revealed pinching in the hysteretic loops. Low levels of load were resisted primarily by the surrounding concrete, and as the lateral movement increased, the stiffness increased as the rebar engaged the concrete. After failure of the surrounding concrete, the inserts behaved as a hinge. Failure resulted from either failure of the concrete or fracture of the weld between the rebar and plate.

McMullin *et al*. (2004) conducted seven full-scale tests of cladding connections. Push-pull threaded rod connections and welded plate lateral seismic connections were subjected to monotonic loading, and the force-deformation relationships were calculated. The 25-mm diameter (1 in.) push-pull connections were loaded in axial tension and compression, and the performance was very ductile, achieving deformations of 150 mm (6 in.) without a loss of strength. Some of this deformation resulted from bending of the supporting plate connecting the threaded rod to the column. The push-pull connections also exhibited ductile failure when they were loading in bending. The lateral seismic connection failed in a ductile manner under in-plane loading (the intended loading when the connection is in use). However, the connection showed significant stiffness when subjected to out-of-plane loading, and it failed at a limited deformation of 20 mm (0.80 in.).

2.4 PASSIVE CONTROL WITH ADVANCED CLADDING CONNECTIONS

The previous sections have shown that architectural precast concrete panels may influence the lateral stiffness of buildings and alter their predicted response during an earthquake. Cladding damage in the 1985 Mexico City and 1989 Loma Prieta earthquakes showed evidence that the cladding took an active role in participating in the lateral response of buildings (El-Gazairly and Goodno, 1989). Several subsequent research studies have focused on developing conceptual models of advanced panel connections that form an integrated building-cladding system and may offer improved stiffness, energy dissipation, and ductility. Analytical and experimental testing has been performed to quantify the benefits to the response of the building as a whole.

Among the first to propose advanced cladding connections were Kemeny and Lorant (1989) and Pall (1989). Kemeny and Lorant performed experimental testing on elastomeric panel-to-structure connections to determine their effect on interstory displacements and seismic forces. The connections used interlocking keyed steel-rubber isolators and were designed to provide very low stiffness at low excitation and sufficient "delayed stiffness and strength" for larger drifts and forces. The authors stated that the connection system could reduce the seismic forces on the structure by 25-67%. Pall (1989) developed friction-damped connections to attach the cladding panels to the structure. He performed analytical studies to compare the response of a frame using the advanced connections to the response of a bare frame. Time-history analyses revealed that the advanced connections reduced the deflections and column moments to 60-70% of those in the bare frame, and the torsional resistance of the building with the advanced connections was improved by four times compared to the bare frame.

Most of the research on advanced cladding connections and passive control has been carried out by B.J. Goodno, J.I. Craig, and their research team at the Georgia Institute of Technology from 1989-1995 (El-Gazairly and Goodno, 1989; Goodno *et al*. 1991; Pinelli *et al*. 1992; Wolz *et al*. 1992; Pinelli *et al*. 1993; and Pinelli *et al*. 1995). Their work on advanced cladding connections is well summarized in Pinelli *et al*. (1995). Pinelli *et al*. describe analytical studies that were carried out to investigate the stiffening and damping properties of one of their advanced connections. The connections are used as the "connection body" shown in Fig. 2.12a; a sketch of the connection is shown in Fig. 2.12b. The connection provides stiffness and damping through yielding of a tapered section of two plates. The hysteretic behavior of the connection (determined from tests by Pinelli *et al*., 1992) is shown in Fig. 2.12c. The analytical test structure

was a six-story, three-bay moment resisting frame, and two cladding panels were attached per bay. Each panel was attached to the structure with four connections: two bearing connections at the bottom and two advanced tapered connections at the top. The authors also describe an energy-based design methodology to determine the material properties and size of the connections. Several dynamic time-history analyses were performed, and the model using the advanced connections reduced the interstory drifts by 53-58% compared to the bare frame for some earthquakes. For other earthquakes (where the fundamental frequency of the building is lower than the critical frequency of the earthquake), the interstory drift was greater in the model with advanced connections. In most cases, up to 70% of the input energy was dissipated by the connectors.

2.5 COMPARISON OF DIFFERENT MODELING APPROACHES

In Section 2.2, the results of several analytical simulations were presented and discussed. Research groups used different modeling assumptions, element models, and analysis software. This section provides a quick comparison amongst the different modeling approaches. The comparisons are given in Table 2.5 for different researchers. A limited number of nonlinear analyses and dynamic analyses have been performed. However, in a moderate to severe earthquake, both the structure and panel connections are expected to deform in the nonlinear range. Additional nonlinear dynamic analysis will give better insight on how the cladding assemblies interact with the supporting framing in earthquakes.

In summary, previous researchers have used analytical models of buildings with cladding to find that the cladding decreases the fundamental period by 18-48% (Goodno *et al*., 1980; Henry and Roll, 1986). However, forced vibration of a multistory building during different stages of the cladding construction revealed that the cladding had a negligible effect on the fundamental period (Meyyappa *et al*., 1981). In dynamic time-history analyses, the effect that the cladding has is highly dependent on the selected ground motion. The addition of cladding to analytical models has been shown to decrease the maximum seismic interstory drift by 38% or increased the drift by 82%, depending on the ground motion (Goodno and Palsson, 1986; Goodno *et al*., 1980; Henry and Roll, 1986). These discrepancies are thought to be largely due to the fact that the building model with cladding has a smaller period than the bare frame model and, thus, is affected by a different frequency response range of the ground motion. Since most of this previous research was done in the 1980s-1990s, many of the analytical models were overly simplified and did not capture nonlinear response. A limited number of dynamic time-history analyses were performed, so no overall trends can be observed. Therefore, one of the goals of the research in this dissertation is to determine the global and element demand trends of updated nonlinear models using analyses with large suites of ground motions.

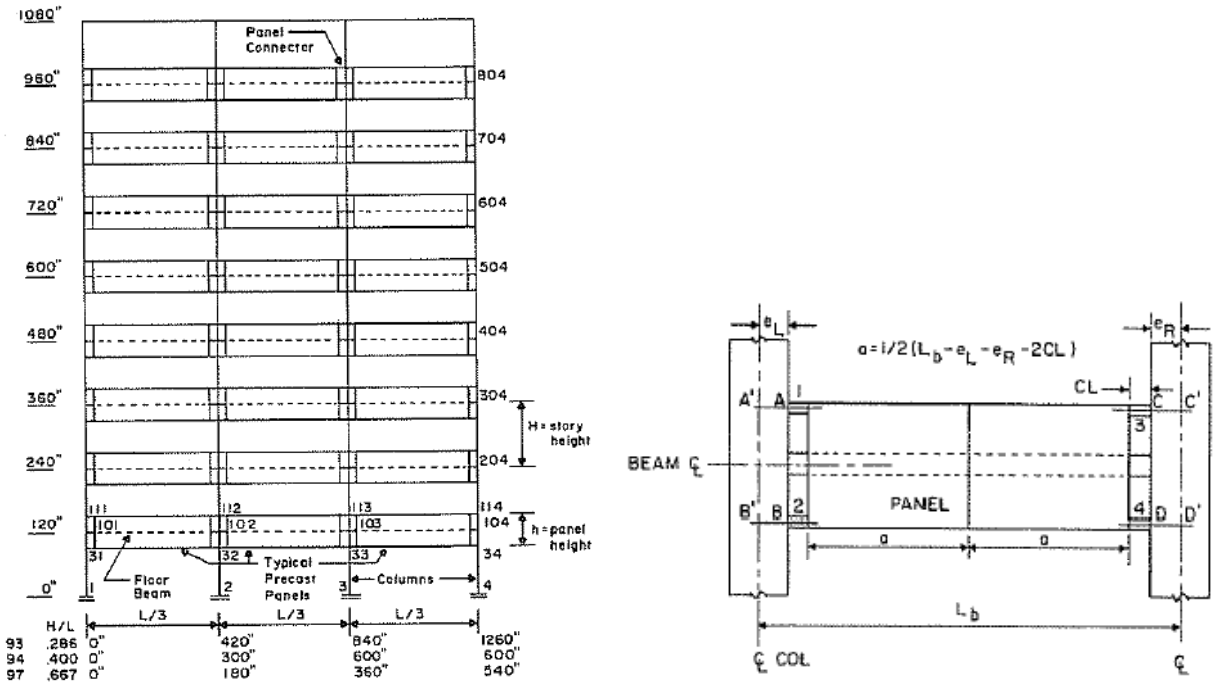

Fig. 2.1 (a) Test model configuration, (b) Typical bay model (Henry and Roll, 1986)

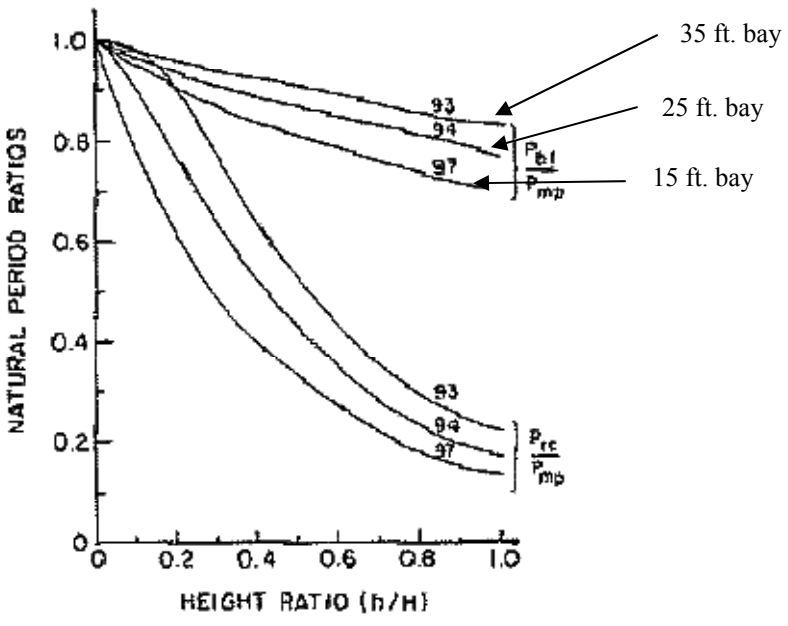

Fig. 2.2 Modal analysis: natural periods of cladded frame normalized with respect to modal periods of bare frame (upper three curves; Henry and Roll, 1986)

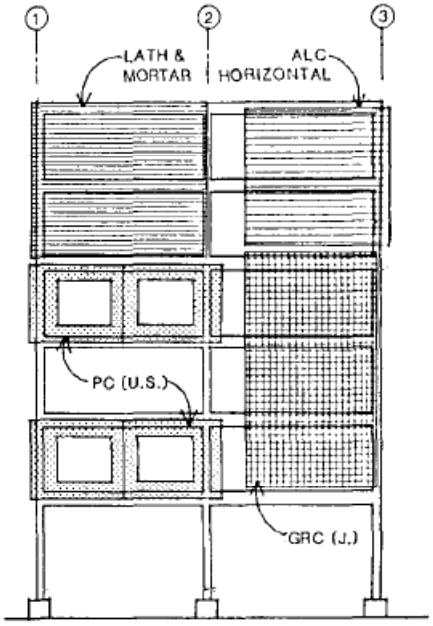

Fig. 2.3 Elevation of one side of test specimen in Wang (1987) with several types of cladding attached

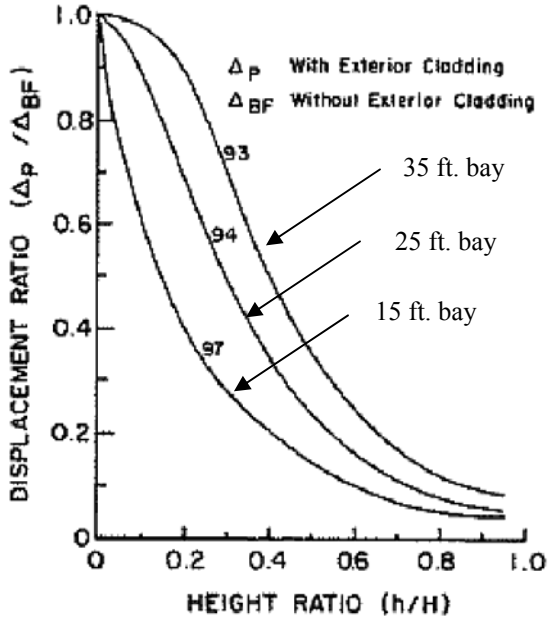

Fig. 2.4 Displacements of roof level of cladded frame normalized with respect to displacements of bare frame (Henry and Roll, 1986)

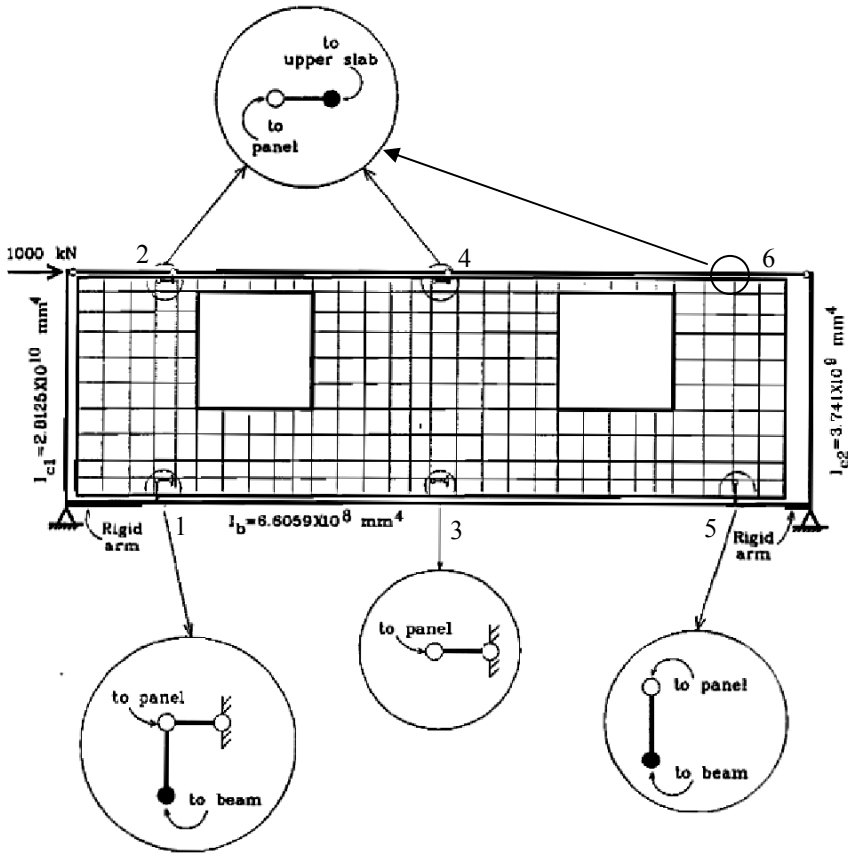

Fig. 2.5 One-bay module showing connection locations (Smith and Gaiotti, 1989)

Table 2.1 Stiffness values for the cladding connections (Smith and Gaiotti, 1989)

CONNECTION NO.	RESTRAINT DIRECTIONS	FACTORS AFFECTING FLEXIBILITY OF CONNECTIONS IN RESTRAINT DIRECTIONS	STIFFNESS VALUES (kN/mm)
1	Horizontal Vertical Out-of-plane	Plates-flex., HSS-flex., shear, tors. HSS in flex. & shear, comp. of plates (not relevant)	200 450
2	Horizontal Out-of-plane	Sum of shear flexibilities of legs (not relevant)	1167
3	Horizontal Out-of-plane	Sum of shear flexibilities of legs (not relevant)	1167
4	Horizontal Out-of-plane	Sum of shear flexibilities of legs (not relevant)	1167
5	Vertical Out-of-plane	HSS in flex. & shear, comp. of plates (not relevant)	450
6	Out-of-plane	(not relevant)	-----

Table 2.2 Description of analyses and results (Smith and Gaiotti, 1989)

ANALYSIS NO.	DESCRIPTION	TOP DISPLACEMENT (mm)	FLEXIBILITY (mm/kN)
I	Structural frame alone without panels	126.35	$126.35X10^{-3}$
II	Complete module, that is, panel connected to actual frame	3.62	$3.62X10^{-3}$
III	Complete module, but effectively without columns i.e. assigning these a very small inertia	17.08	$17.08X10^{-3}$
IV	Complete module, but with panel and conections assigned to be effectively rigid	0.52	$0.52X10^{-3}$
V	Complete module, but with the beam assigned to be effectively rigid in flexure	1.51	$1.51X10^{-3}$

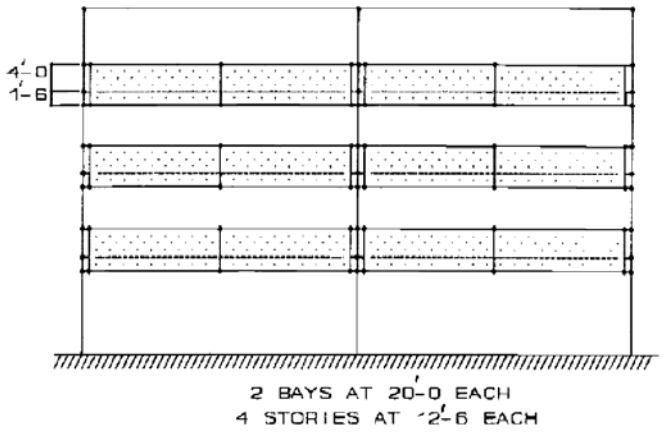

Fig. 2.6 Four-story structural model with cladding (Charney and Harris, 1989)

Table 2.3 Effect of panel thickness on lateral drift (Charney and Harris, 1989)

Panel Thickness (inches)	Deformation Source (inches)				
	Beams	Columns	Connections	Panels	Total
0.0	0.1940	0.2580	-	-	0.4520
2.0	0.0713	0.1796	0.0468	0.0272	0.3249
4.0	0.0614	0.1738	0.0575	0.0174	0.3101
6.0	0.0577	0.1716	0.0619	0.0130	0.3042
60.0	0.0503	0.1700	0.0714	0.0004	0.2921

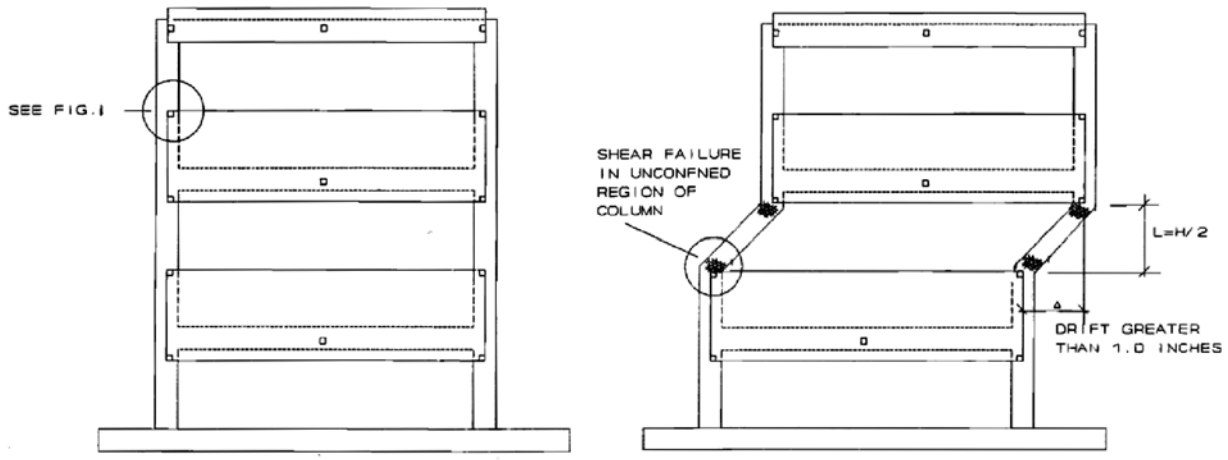

(a) (b)

Fig. 2.7 (a) Frame with cladding panels, (b) Frame failure by cladding restraint (Charney and Harris, 1989)

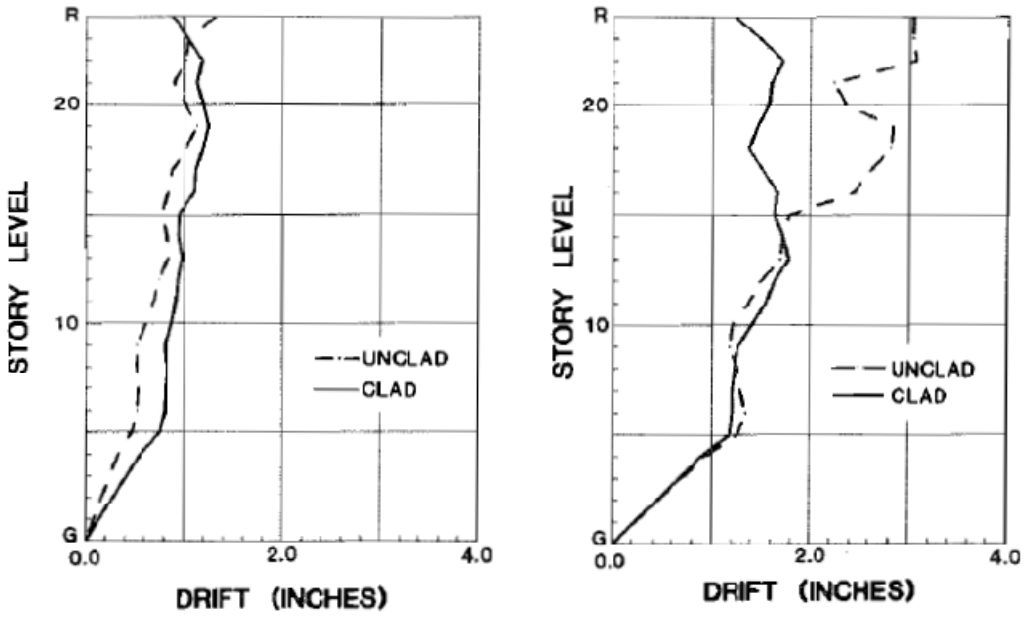

(a) (b)

Fig. 2.8 Peak interstory drift on face 2 for (a) 1940 N-S El Centro, (b) 1966 Parkfield (Goodno and Palsson, 1986)

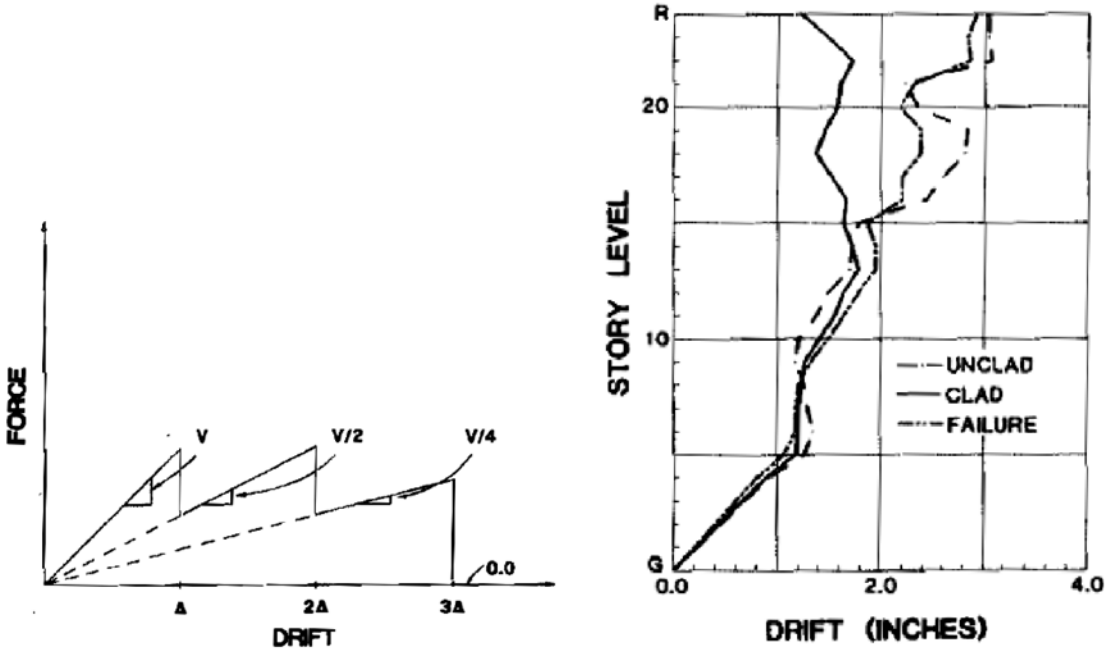

(a) (b)

Fig. 2.9 (a) Incremental failure model, (b) Peak interstory drift on face 2 for 1966 Parkfield (Goodno and Palsson, 1986)

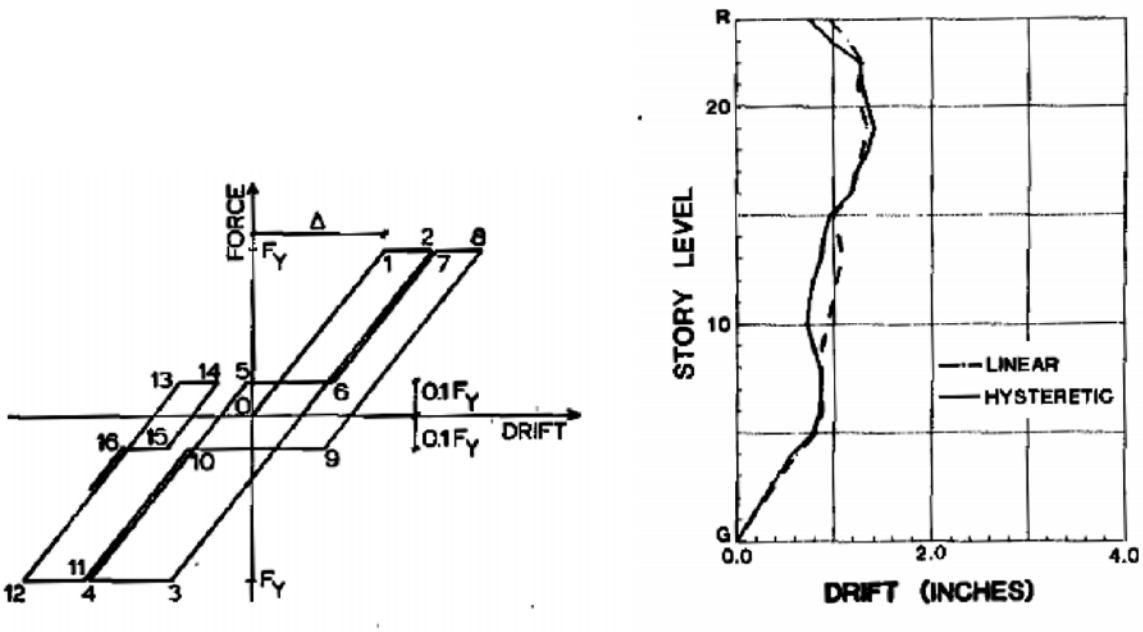

(a) (b)

Fig. 2.10 (a) Hysteretic model, (b) Peak interstory drift on face 4 for 1940 El Centro (Goodno and Palsson, 1986)

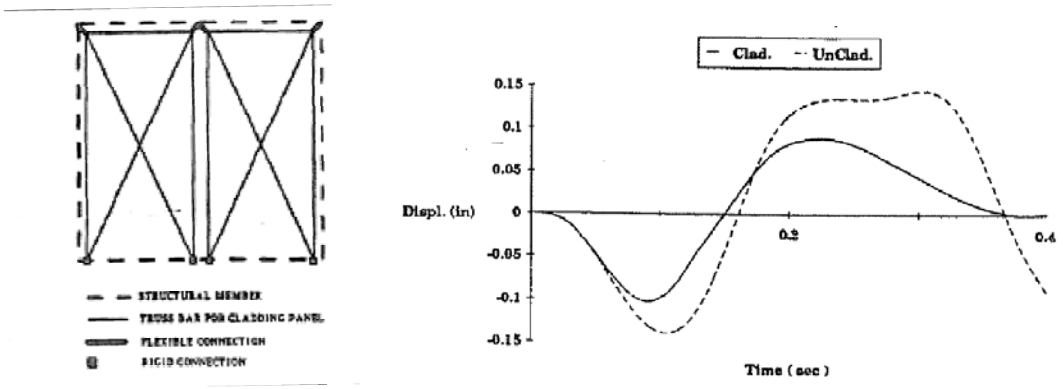

(a) (b)

Fig. 2.11 (a) Two panel model, (b) Time-history of roof drift (Wolz *et al.*, 1992)

Table 2.4 Events and significance of loading steps (Wang, 1987)

Step	Drift	Event or Significance
68	+ 1/250	First visible connection failure at short rod of a lateral connection.
159 (after the first cycle of +1/125 story drift.)	0	Many lateral sliding connections on the verge of complete fracture of short rods. Connections are loosened wherever possible, and panels chained to steel frame.
207 (ninth cycle)	-1/125	Beginning of appearance of significant cracking in concrete panels at the tube bearing connection locations.
307	+1/60	Complete compression of some joints accompanied by jump in panel stresses.
340	-1/60	Beginning of appearance of significant cracking in "L" shaped column covers.
(*	1/50	U.B.C. derived criteria for cladding design of the test specimen.)
380 (first cycle)	+1/40	Beginning of appearance of significant cracking in flat column covers.
429 (first cycle)	-1/40	Beginning of appearance of significant cracking in concrete wall panels at the angle bearing connection locations.

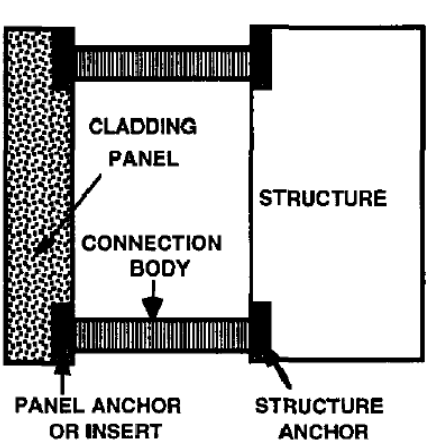

(a)

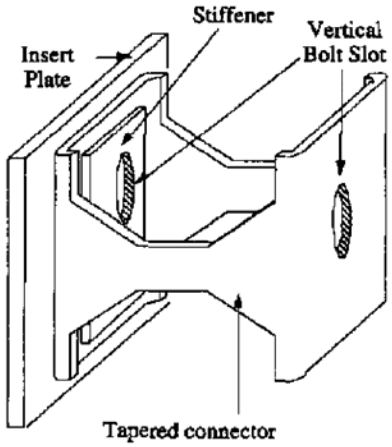

(b)

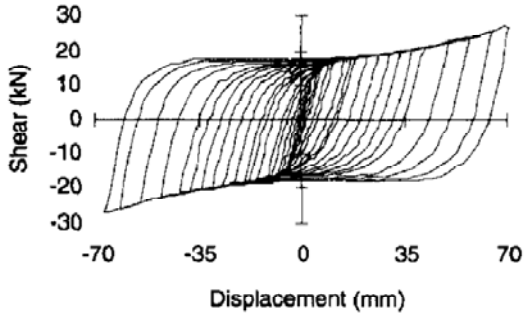

(c)

Fig. 2.12 (a) Cladding system, (b) Advanced tapered connection, (c) Advanced connector hysteresis behavior

Table 2.5 Summary of existing analytical models of precast cladding systems

Reference	Panel elements	Connection elements	Supporting framing elements	Assumptions	Software	Types of analyses
Henry and Roll (1986)	Linear plane stress finite element	Linear beam-column	Linear beam-column	Vertical dofs neglected	LSTAT & LDYN	- Linear static analysis - Modal analysis
Henry, Goodspeed, and Calvin (1986)	Rigid box frame (linear beam-column elements)	Linear beam-column	Linear beam-column	Rigid beam element can be used to represent panels	PAFEC	- Linear static analysis
Charney and Harris (1989)	Linear 4-node finite element	Linear beam-column	Linear beam-column	Connections deformed in bending about minor axis	SAP90	- Linear static analysis
Sack, Beers, and Thomas (1989)	Linear 2-D plane finite elements	Linear and nonlinear beam-column	Linear beam-column	Connectors behave as elastic-perfectly plastic	SAPFAP & SAPIV	- Linear static analysis - Nonlinear static analysis - Linear dynamic analysis
GA Tech research team (1980-1988)	Not modeled	Linear and nonlinear (term in stiffness matrix)	Linear beam-column	Cladding not physically modeled	STRUDL	- Modal analysis - Linear & nonlinear dynamic analyses
Smith and Gaiotti (1989)	Linear plane stress finite elements	Vertical and horizontal linear links	Linear beam-column	Only one-bay was modeled	Not specified	- Linear static analysis

Chapter 3: Analytical Models of Multistory Buildings with Precast Cladding

Previous research on the interaction between precast cladding panels and the supporting moment frame was presented in Chapter 2, and the analytical aspects of existing models were summarized in Table 2.4. In all of the models, linear material behavior was assumed for the elements of the moment frame, and only a few models used nonlinear material behavior for the cladding connections. In addition, only a limited number of dynamic time-history analyses have been performed.

In this section, a nonlinear analytical model is developed to capture the interaction between the cladding panels and the supporting moment frame and to determine the demands in the cladding connectors. The nine-story LA SAC building (as described in Foutch 2000) is used as the study building. The moment frame is modeled with nonlinear beam-column elements, the cladding panels are modeled as rigid-frame elements, and the cladding panel connections are modeled as nonlinear zero-length elements. The response of the study building with and without cladding panels was evaluated using modal analyses, static pushover analyses, and dynamic time-history analyses.

3.1 NINE-STORY SAC BUILDING

The seismic assessment of multistory steel moment-resisting frames by the SAC Joint Venture after the 1994 Northridge earthquake revealed that many buildings using this type of lateral force resisting system did not perform as intended. The SAC model buildings were designed according to the 1994 Uniform Building Code and represent typical 3-, 9-, and 20-story office buildings in Los Angeles, Seattle, and Boston. In this report, the 9-story SAC building for the Los Angeles site is selected as the study model. The structural framing plan and elevation are shown in Fig. 3.1 and Fig. 3.2. The nine-story building contains five bays in the east-west direction and five bays in the north-south direction. There are two, five-bay moment-resisting frames that act as the primary lateral-force resisting system in each direction (shown as thick lines in Fig. 3.2). The remaining framing (shown as thin lines in Fig. 3.2) is constructed with shear connections that are meant to resist gravity loads only; however, in reality they do provide some semi-rigid moment-rotation behavior.

The SAC nine-story building has been extensively studied in the past, and this building was selected as the study building in this research because it is well known in the structural engineering research community and has served as a benchmark building in the structural analysis of moment-resisting frames. The nine-story LA SAC model building was designed

according to the 1994 Uniform Building Code (UBC, 1994) to represent a typical office building. During the 1995 SAC Phase II and in the following years, numerous numerical studies of the SAC buildings were performed. Many of these early studies focused on the effect that different modeling assumptions had on the global and element seismic demands (Foutch, 2000; Lee and Foutch, 2000; Lee and Foutch, 2002; Krawinkler, 2000; Yun and Foutch, 2000). These researchers performed parametric studies comparing different modeling assumptions. For example, analytical results of simple models using centerline dimensions were compared to more complex models that considered P-Δ effects, panel zone deformations (Krawinkler, 2000), the contribution of gravity frames (Foutch, 2000), the strength of floor slabs (Gupta and Krawinkler, 1999), and column base fixity (Stojadinovic *et al*., 1998). In the next section, the modeling approach and assumptions are outlined for the structural models used in the research in this dissertation.

3.2 MODELING APPROACH AND ASSUMPTIONS

As discussed above, several different modeling approaches have been used for the SAC building. The comparisons of the results using these assumptions are not given here; however, the reader is referred to Foutch (2000) and Krawinkler (2000) for an introduction to the many possible modeling approaches for this building.

The modeling approach for the multistory buildings with cladding in this dissertation is discussed in the sections below. The building dimensions, beam-column member sizes, connection details, total seismic masses, and more can be found in Foutch (2000). First, the modeling approach is given for the structural framing with no cladding system attached (termed the "bare frame"). This is the building model that structural engineers and researchers use currently. Then, the design and modeling assumptions for the cladding system are discussed.

The bare frame structure used in this thesis is very similar to the bare frame structures analyzed in Foutch (2000) and Gupta and Krawinkler (1999). The building is modeled as a two-dimensional frame that represents half of the structure in the north-south direction (see Fig. 3.1 and Fig. 3.2). The frame is assigned half of the seismic mass of the structure, distributed at each floor level. The seismic masses are discussed in Section 3.2.4. Using the terminology in Gupta and Krawinkler (1999), the bare frame model used in this dissertation can be considered a blend between the M1 and M2A models. The bare frame model is constructed using centerline dimensions (the columns and beams extend from centerline to centerline), and the stiffness, strength, and shear distortions of the panel zones are neglected (M1 model characteristics). The bare-frame model is also constructed considering all dependable contributions of stiffness and strength, such as the floor slab, interior gravity framing, and shear connections (M2A model characteristics). It has been shown that by using centerline dimensions for the columns (instead of using clear span dimensions) that the contributions of the column flexural deformations to interstory drift can be easily overestimated by a factor of two or more, as the contribution of the columns to the story drift is proportional to the cube of the column length (Gupta and Krawinkler, 1999). However, in the research of this dissertation, it is more important to create a typical baseline model that is on the conservative side with respect to interstory drifts, which is what this bare-frame model accomplishes.

The model also includes the effect of all other "dependable" contributions to strength and stiffness. All gravity columns and the weak-axis columns of the SMRFs are included in the

model as a dummy frame. The effect of the floor slab of all exterior moment-frame beams is considered. The strength and stiffness of all simple shear connections are included in the model. The following sections discuss the modeling assumptions in more detail.

3.2.1 Moment-Resisting Element Behavior and Modeling

The beam-column elements of the moment-resisting frame are modeled with nonlinear force beam-column elements capable of representing distributed plasticity along their length. Five integration points are used along the length of all moment-resisting elements. At each of these points, fiber sections are used to accurately represent the distribution of stress and strain across the beam-column sections. The fiber sections of the columns model the wide-flange sections, and the fiber sections of the beams model both the wide-flange sections and composite floor deck. The effective width of the composite floor deck is calculated from the equations in Kato *et al*. (1984). The stress-strain relationship of the steel is defined using the Guiffre-Menegotto-Pinto Model with a yield stress of 50 ksi (neglecting statistical variation of Fy, giving a conservative value for the bare-frame model) and a post-yield strain hardening of 3%. The beam-to-column moment connections are reduced-beam section (RBS) connections with their hysteretic behavior calibrated from the experimental tests by Engelhardt *et al*. (2000). The modeled hysteretic force-deformation curve for a typical beam-column connection, shown in Fig. 3.7, accurately represents the isotropic and kinematic hardening/softening of the experimental force-deformation curve. The beam-column stiffness and resisting forces are transformed from local coordinates to the global coordinates using the corotational transformation, which captures secondary effects from large displacements and P-Δ effects.

3.2.2 Modeling of Interior (Simple) Frames

The effects of all gravity and orthogonal moment-resisting columns, beams forming part of the simple frames, and simple connections are modeled through an equivalent one-bay frame (with one dummy column) attached to the primary moment-resisting frame with rigid link elements. The dummy frame is shown in Fig. 3.1 as the dashed lines. At each story level, the columns of the equivalent bay have a moment of inertia equal to half the sum of moment of inertia of all gravity columns and orthogonal MRF columns, with the correct bending axis represented. A similar approach is used for the axial capacity of the equivalent columns. The bending strength at all column ends is, also, half the sum of the strength of all gravity columns and orthogonal MRF columns, calculated about the representative axes. The beams connecting the two columns of the equivalent bay are modeled as elastic elements with rotational springs at both ends. The elastic beams are given a stiffness equal to the sum of the stiffness of all the beams forming part of the interior frames at each floor level. Rotational springs are used to model the equivalent strength and stiffness of all the shear (simple) connections. Each spring represents the cumulative strength of half the number of simple connections.

3.2.3 Shear (Simple) Connections

Experimental studies have shown that the bending resistance of shear tab connections used in gravity framing is not negligible. For the analytical models in this paper, the simple shear connection model developed by Astaneh-Asl (2005) is used to represent the moment-rotation behavior of the shear connections. The definition of the moment-rotation relationship of the shear connection is given in Fig. 3.8. The experimental and modeled moment-rotation curve of the simple shear connections are shown in Fig. 3.9. The stiffness and strength of these shear connections were accounted for in the modeling of the simple frames discussed in Section 3.2.2.

3.2.4 Modeling of Cladding Systems

Finite element models of the cladding systems were added to the bare frame of the nine-story SAC building to investigate the effect of the cladding on the building response and to determine the demands in the cladding connectors. Three different types of cladding are investigated. Each type of cladding system is attached to the bare frame model described in Section 3.2. The models are shown graphically in Fig. 3.3.

(1) Cladding type 1 (C1) – consists of alternating spandrel panels and window glazing. The spandrel panels are attached to the bare frame with push-pull connections (threaded rods), vertical bearing connections, and a rigid lateral connection. The spandrel panels are 360 in. wide by 78 in. tall by 5 in. thick. The window glazing is ignored in the analytical model.

(2) Cladding type 2 (C2) – consists of full story-height panels with cutouts for windows. The panels are attached with push-pull connections (threaded rods), vertical bearing connections, and a rigid lateral connection. The panels are 360 in. wide by 156 in. tall by 5 in. thick. The window cutouts are ignored in the analytical model.

(3) Cladding type 3 (C3) – consists of spandrel panels and column covers. The spandrel panels are attached to the bare frame with push-pull connections (threaded rods), vertical bearing connections, and a rigid lateral connection. The column covers are spaced at every 180 in. horizontally along the building and are attached to the spandrel panels with horizontally slotted (bolted) connections at their tops and pinned (bolted) connections at their bottoms. The spandrel panels are 360 in. wide by 78 in. tall by 5 in. thick, and the column covers are 54 in. wide by 78 in. tall by 5 in. thick. The window glazing is ignored in the analytical model.

The detailed elevations of the three cladded models are shown in Fig. 3.4, Fig. 3.5, and Fig. 3.6, for models C1, C2, and C3, respectively. The locations of the different types of connections are shown on the left of the figures, and the analytical representations are shown on the right of the figures.

The precast cladding panels are assumed to be rigid, and they are modeled with two-dimensional frames comprised of rigid elastic beam elements. The two types of cladding panels in the SAC building are spandrel panels and column covers. The spandrel panels (shown as light gray in Fig. 3.3) are attached at their corners to the columns of the supporting frame with push-pull connections (threaded rods) and are attached to the beams of the supporting frame with vertical bearing connections and a rigid lateral connection. The push-pull connections and rigid lateral connection resist lateral deformations between the frame and the cladding panels, and the bearing connections resist the gravity loads of the panel. Since the rigid lateral connection is very stiff in the horizontal direction and the vertical bearing connections are very stiff in the vertical

direction, the horizontal displacement, vertical displacement, and rotation of the middle of the spandrel panel approximately equals the displacements and rotation of the mid-span of the floor beam. Therefore, the vertical bearing connections and rigid lateral connections are transformed into a displacement constraint in the middle of the spandrel panel that matches the spandrel panel's displacements to the floor beam displacements at mid-span.

The column cover panels in cladding type C3 are spaced at every 180 in. horizontally along the building and are attached to the spandrel panels with two horizontally slotted (bolted) connections at their tops and two pinned (bolted) connections at their bottoms. A detailed elevation of the cladding system C3 is shown in Fig. 3.6. The connection types are shown on the left and the analytical representation is shown on the right.

The detailed drawings of the push-pull connection, lateral rigid connection, vertical bearing connection, and column cover connections are shown in Fig. 3.10, Fig. 3.11, Fig. 3.12, Fig. 3.13, and Fig. 3.14. Photographs of a typical push-pull connection, rigid lateral connection, and vertical bearing connection are shown in Fig. 3.15.

3.2.5 Force-Deformation Behavior of Cladding Connections

As discussed in the previous sections and shown in Fig. 3.4, Fig. 3.5, and Fig. 3.6, the cladding panels are attached to the moment-resisting frame with various connectors. The push-pull connections and column cover connections are modeled as nonlinear zero-length spring elements in OpenSees. The connection force deformation relationships are prescribed for each connection in the horizontal shear and vertical shear directions (the rotational capacity of the connections is very small and can be neglected).

The push-pull connection assembly modeled in this dissertation was tested by McMullin *et al*. (2004). The test specimen consisted of four push-pull threaded rod connectors attached to plates on either end. The clear length of the threaded rods was approximately 8.0 inches long, and the diameter of the rods was 1.0 inch. The researchers tested the connection to determine the force-deformation curve for different directions of loading. The specimens were tested under a monotonically increasing load, and the contributions of the different components of the push-pull connections to the total force and displacement were recorded. The force-deformation envelope for the in-plane shear was found to be approximately bilinear: the total initial stiffness of the four push-pull connectors was 26.67 kip/in with a yield force of 20.0 kips and a yield deformation of 0.75 inches The post-yield stiffness was 8.0 kip/in., which continued to a deformation of approximately 2.2 inches. Fracture of the threaded rods occurred at 2.8 inches. The four threaded rods in the test acted in parallel, so force-deformation properties of one threaded rod translate to an initial stiffness of 6.67 kip/in., yield force of 5.0 kip, yield deformation of 0.75 inches, post-yield stiffness of 2.0 kip/in., deformation at maximum strength of 2.2 inches, and a fracture deformation of 2.8 inches. Using these values, the hysteretic force-deformation curve for one push-pull connector is plotted in Fig. 3.16.

The force-deformation properties of the column cover connections were obtained from tests by Crawford and Kulak (1968). The test specimens were 3/4-inch diameter ASTM 325 bolts installed in ASTM A36 steel plates that were 4 inches by 4 inches in size. The holes in the plates for the bolts were 13/16-inch diameter drilled holes. A total of six identical specimens were tested. The specimens were tested in shear at a load rate of 0.025 inches per minute. All specimens showed failure in shear at the thread run-out portion of the bolt. The load deformation

curve fitted to the results of the six tests is shown in Fig. 3.17. For low levels of deformation, the relationship is approximately linear, and as the deformation approaches the ultimate force, the connection force increases at a decreasing rate. The mathematical expression for the force-deformation curve that best fits the data is shown in Equation 3.1.

$$R = R_{ult}(1 - e^{-10\Delta})^{0.55} \quad \text{Eq. 3.1}$$

The mean maximum connection force was 74.0 kips, and the mean maximum shear deformation was 0.34 inches. The mean force-deformation curves for the column cover connections used in the analytical models are shown in Fig. 3.18. The curve for the bottom connectors and top connectors is the same except that the curve for the top connectors is shifted by a deformation of 1.5 inches. This shift accounts for the fact that the top connectors contain a 4 inch wide horizontal slot, and approximately 1.5 inches should remain on either side if the bolt is near the center of the slot. As interstory drift occurs, the bolt slides within the horizontal slot, and for large interstory drifts, the bolt impacts the end of the slot and causes deformation in the connection.

The nonlinear force-deformation curve for the column cover connections is modified for the analysis in OpenSees by using an elastic-perfectly plastic model. The initial stiffness is 575 kip/in., the yield force is 68.0 kips, and the yield deformation is 0.12 inches. The top connector is modeled using the elastic-perfectly plastic gap element in OpenSees. The initial stiffness of the gap element is 575 kip/in., the yield force is 68.0 kips, and the gap width is 1.5 in.

3.2.6 Consideration of Seismic Mass

In most structural analysis models of moment-resisting framed buildings, the mass of the building is assigned to the beam-column nodes. This representation simplifies the assignment of mass to the frame while accurately representing the distribution of mass throughout the structure. A breakdown of the SAC building weight and mass values for each floor can be found in Foutch (2000). For the bare frame model, half of the total building mass is assigned to the frame (since there are two moment-resisting frames in each direction). The mass values account for the steel framing, floor deck and roof, ceilings/flooring, mechanical/electrical, interior partitions, and exterior cladding. The mass values are assigned to the beam-column nodes according to the distribution in Table 3.2.

In the models with cladding systems (C1, C2, and C3), the mass of the building is divided between the beam-column nodes in the moment-resisting frame and the nodes of the spandrel panels and column cover panels. The masses of the spandrel panels and columns covers are resolved to the four corners of the panels, as shown in Fig. 3.4, Fig. 3.5, and Fig. 3.6. Thus, the mass assigned to the beam-column nodes of the moment-resisting frame consists of all contributions to the mass except for the mass of the cladding panels. The distribution of mass between the moment-resisting frame and the cladding system is shown in Table 3.3 for Model C1, in Table 3.4 for Model C2, and in Table 3.5 for Model C3. This approach assures that all of the models contain exactly the same total seismic mass.

3.3 WINDOW GLAZING SYSTEM

The window glazing system was not explicitly represented in the analytical models described in Section 3.2. The contribution of the glazing system to the lateral strength and stiffness of the building is minimal due to the lack of strength of the glass panes. However, the damage to the glazing system is considered in the repair cost analyses in Chapter 7. A detailed elevation of the precast cladding system with glazing is shown in Fig. 3.19 (shown for cladding type C3). In type C3, there are two window panes per opening between the column covers.

The glazing system used in this research is a relatively simple system. The system is described here for the cladding type C3, which is the most common type of cladding system (the other cladding types use a similar glazing system). The window panes are of dimensions 5.0 feet wide and 6.0 feet tall. The glass types used depend on their location in the building: 25 mm (1 in.) annealed insulating glass units (IGUs) are typically used where safety is not a concern, and heat-strengthened IGUs are used when the panes are located within 18 inches of the ground or within 4 feet of a doorway. The IGU panes consist of two 1/4-inch glass panes separated by 1/2-inch of air space. Older buildings typically have 1/4-inch thick annealed monolithic glass units. In this SAC study building, both the 25 mm (1 in.) annealed and heat-strengthened IGUs are selected as the glass units.

According to Behr and Worrell (1998), the most common framing system used to surround the glass panes is a dry-glazed, narrow mullion system. Accordingly, the framing system selected for the SAC building is the Kawneer 1600^{TM} wall system. Typical cross-sections of this system are shown in Fig. 3.20. The glass panes are placed in the framing system (also termed “glazing pocket”), and 3/8 inches of glass bite is provided around all edges of the glass. Glass bite is the amount the glass pane extends into the glazing pocket to ensure air and water tightness. This amount of glass bite leaves approximately 1/2-inch of clearance between the glass edges and the top, bottom, and right sides of the glazing pocket. There is 1/8-inch of clearance on the left side of the glass edge. The lower edge of the glass pane is supported by two aluminum setting blocks that are capped with hard rubber pads. The glass is dry-glazed, meaning that it is held in the glazing pocket by interior and exterior Santoprene gaskets. The gaskets act as rubber wedges that hold the glass pane in the glazing pocket.

3.4 QUANTITY TAKE-OFF OF CLADDING SYSTEMS

The cladding types described in Section 3.2.4 and shown in Fig. 3.3 have different amounts of panels, windows, and cladding components. To aid in their comparisons, the quantity take-off of the cladding components are given in Table 3.6. These quantities will be used to determine the repair quantities for the repair cost analyses in Chapter 7.

Cladding type C1 consists of alternating spandrel panels and window panes. The spandrel panels make up approximately 48% of the total exterior surface area of the building, and the window system makes up the remaining 52%. Approximately 16,650 linear feet of caulking is needed to seal the joints between the adjacent spandrel panels and between the panels and the window system. Approximately 23,760 linear feet of rubber gasket is needed to glaze the window panes to the window framing.

Cladding type C2 consists of full story-height spandrel panels with cut-outs for windows. The surface area of the spandrel panels makes up approximately 66% of the total exterior surface

area of the building, and the window system makes up approximately 30%. Approximately 21,060 linear feet of caulking is needed to seal the joints between the adjacent spandrel panels and between the panels and the window system. Approximately 15,840 linear feet of rubber gasket is needed to glaze the window panes to the window framing.

Cladding type C3 consists of spandrel panels that cover the floor beams, column cover panels that span between adjacent floors, and windows between the column cover panels. The surface areas of the spandrel panels and column cover panels make up approximately 48% and 14% of the total exterior surface area of the building, respectively. The window system makes up approximately 30% of the total exterior surface area of the building. Approximately 16,650 linear feet of caulking is needed to seal the joints between the adjacent spandrel panels and between the panels and the window system. Approximately 15,840 linear feet of rubber gaskets are needed to glaze the window panes to the window framing.

The seismic performance and damages states of the window panes, caulking, and rubber gaskets are discussed in detail in Chapter 7.

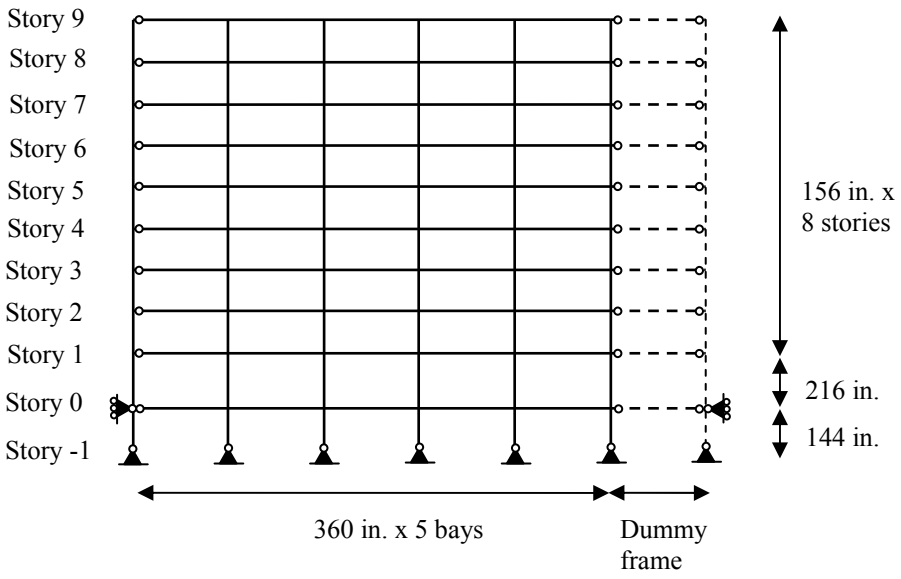

Fig. 3.1 Exterior elevation of Bare Frame Model

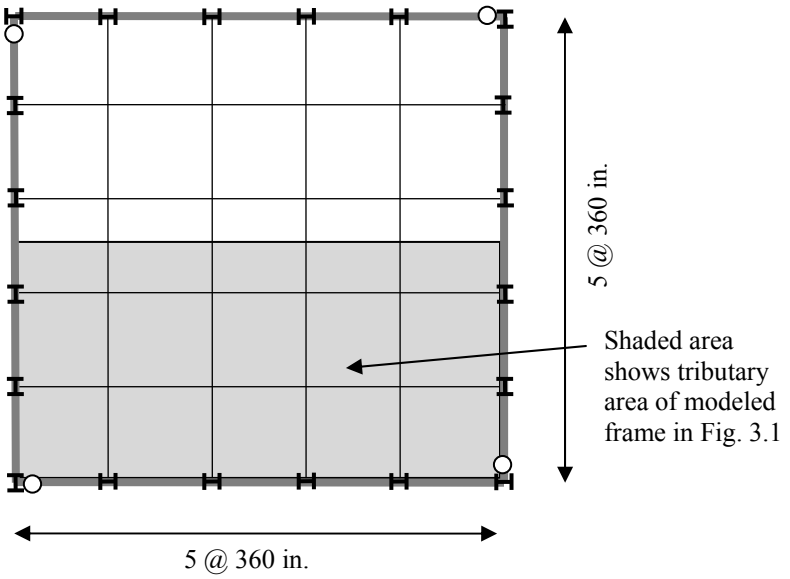

Fig. 3.2 Plan view of Bare Frame Model (thick lines show moment framing; thin lines show gravity framing)

Table 3.1 Sections for beam and column elements

	NS Moment-Resisting Frame			*NS Gravity Frames*		
STORY/	COLUMNS		GIRDERS	COLUMNS		BEAMS
FLOOR	Exterior	Interior		Below penthouse	Others	
-1/0	W14×370	W14×500	W36×150	W14×211	W14×193	W18×35
0/1	W14×370	W14×500	W36×150	W14×211	W14×193	W16×26
1/2	W14×370	W14×500	W36×150	W14×211	W14×193	W16×26
2/3	W14×370	W14×455	W33×141	W14×159	W14×145	W16×26
3/4	W14×370	W14×455	W33×141	W14×159	W14×145	W16×26
4/5	W14×283	W14×370	W33×141	W14×120	W14×109	W16×26
5/6	W14×283	W14×370	W33×130	W14×120	W14×109	W16×26
6/7	W14×257	W14×283	W27×102	W14×90	W14×82	W16×26
7/8	W14×257	W14×283	W27×94	W14×90	W14×82	W16×26
8/9	W14×233	W14×257	W24×62	W14×61	W14×48	W14×22

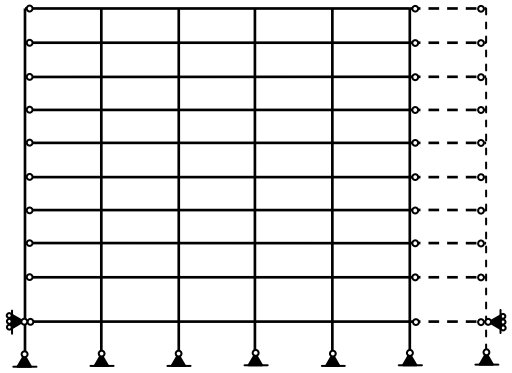

Bare frame
No cladding

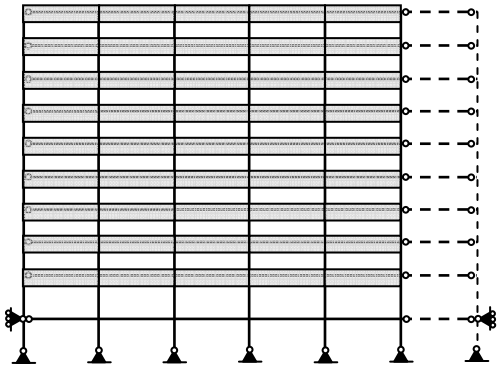

Cladding type 1
Spandrel panels

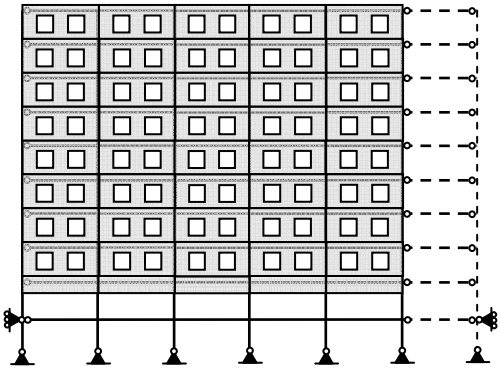

Cladding type 2
Full panels with window cutouts

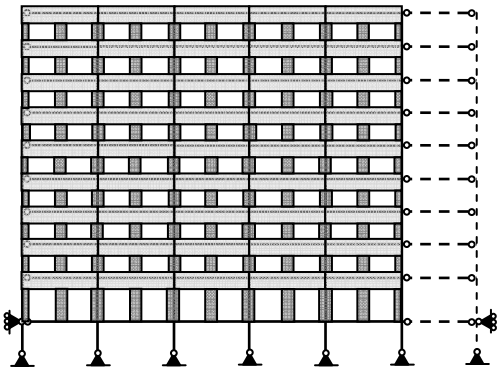

Cladding type 3
Spandrel panels and column covers

Fig. 3.3 Exterior framing and cladding of SAC Building (north-south) direction

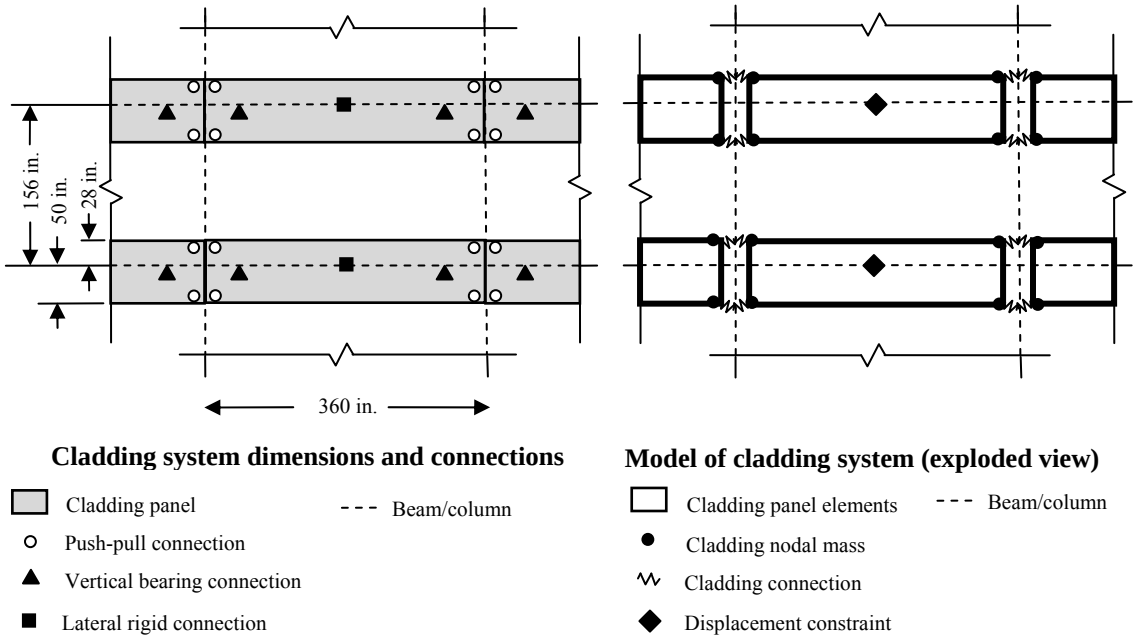

Fig. 3.4 Detailed elevation of Model C1: (left) view showing connection types, (right) model view

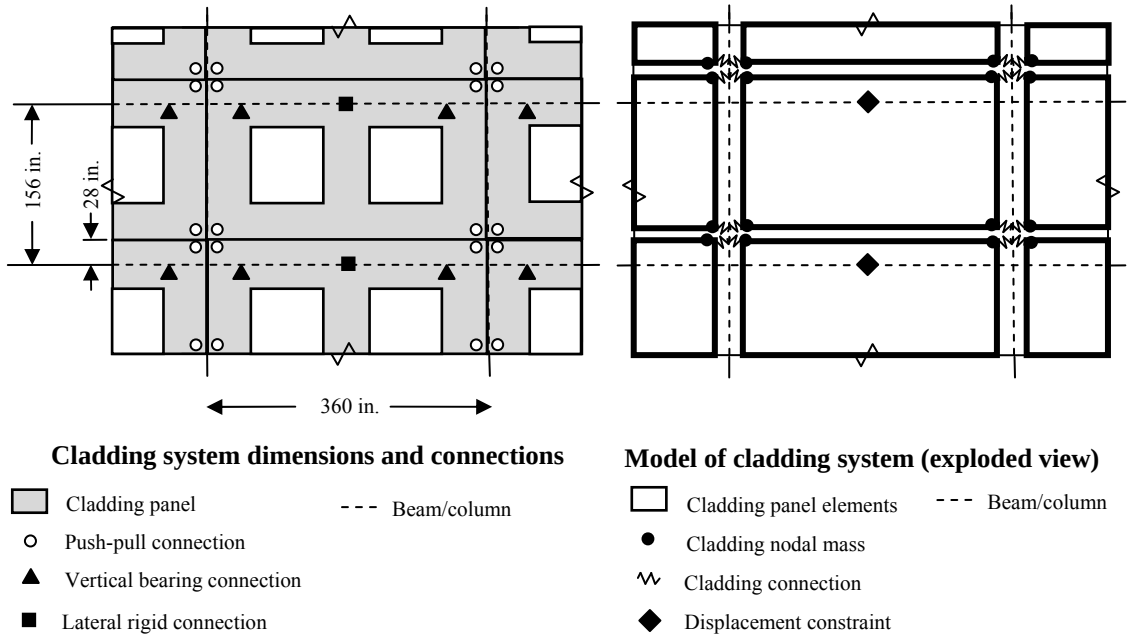

Fig. 3.5 Detailed elevation of Model C2: (left) view showing connection types, (right) model view

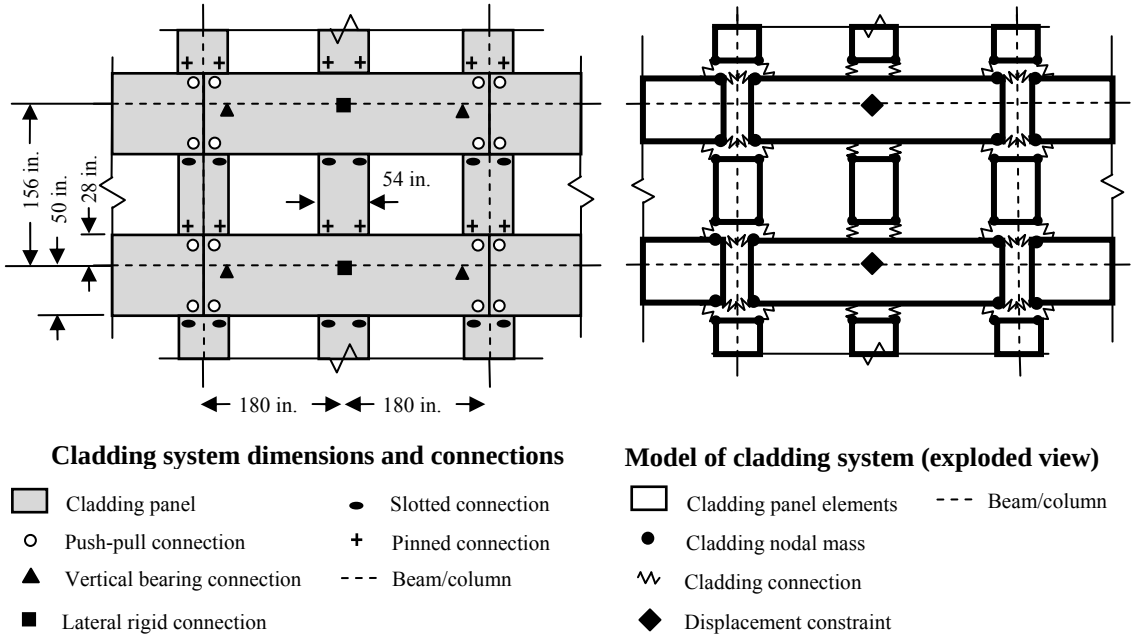

Fig. 3.6 Detailed elevation of Model C3: (left) view showing connection types, (right) model view

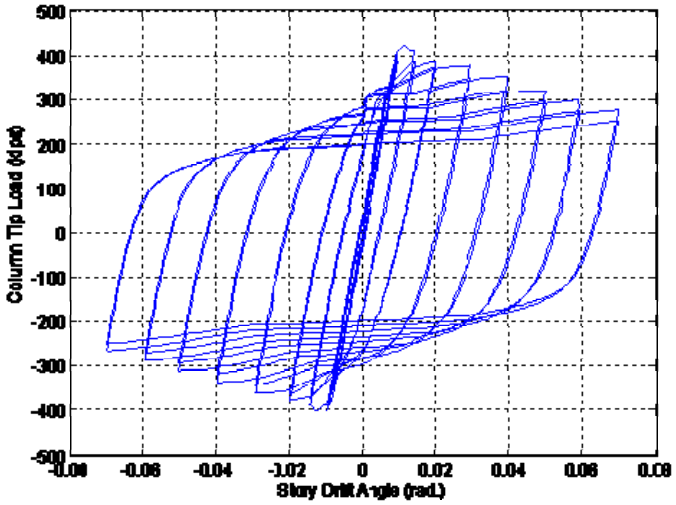

Fig. 3.7 Modeled force-deformation hysteretic curve for the beam-column assembly [based on test results from Engelhardt *et al.* (2000)]

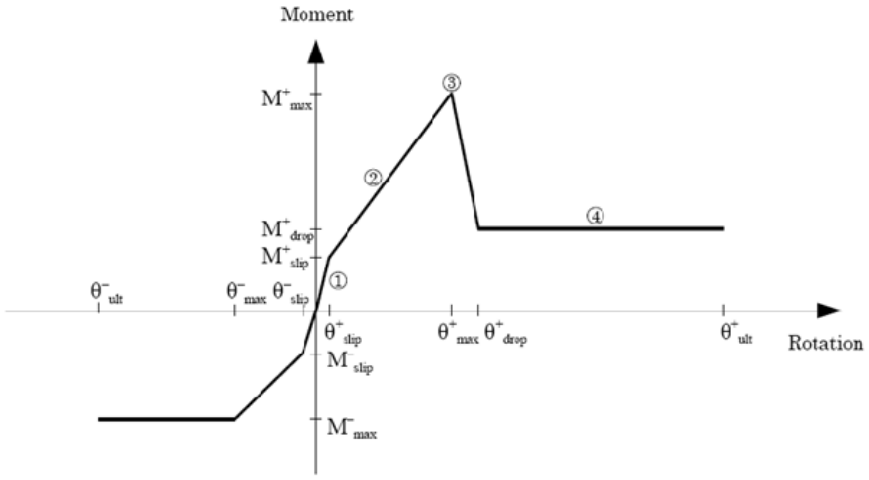

$$M^{+}_{slip} = 0.25\ M^{+}_{max} \qquad \theta^{+}_{slip} = 0.0042 \text{ radians}$$
$$M^{+}_{max} = 38\%\ M_p \qquad \theta^{+}_{max} = 0.03 \text{ radians}$$
$$M^{+}_{drop} = 0.55\ M^{+}_{max} \qquad \theta^{+}_{drop} = 0.04 \text{ radians}$$

$$M^{-}_{slip} = 0.50\ M^{-}_{max} \qquad \theta^{-}_{slip} = 0.0042 \text{ radians}$$
$$M^{-}_{max} = 11\%\ M_p \qquad \theta^{-}_{max} = 0.02 \text{ radians}$$

Fig. 3.8 Moment-rotation relationship for shear connectors [based on test results from Astaneh-Asl (2000)]

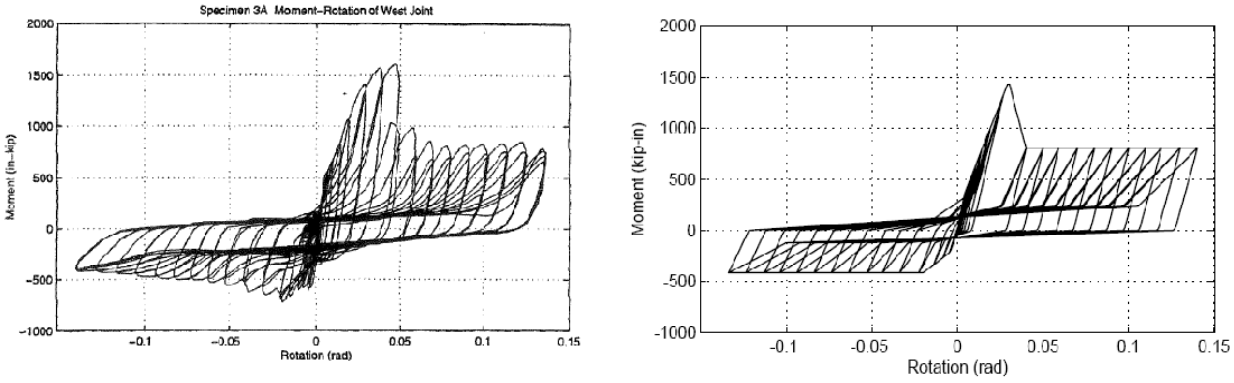

Fig. 3.9 Comparison of measured (left) from Liu and Astaneh-Asl (2000) and modeled (right) moment-rotation behavior of shear connection

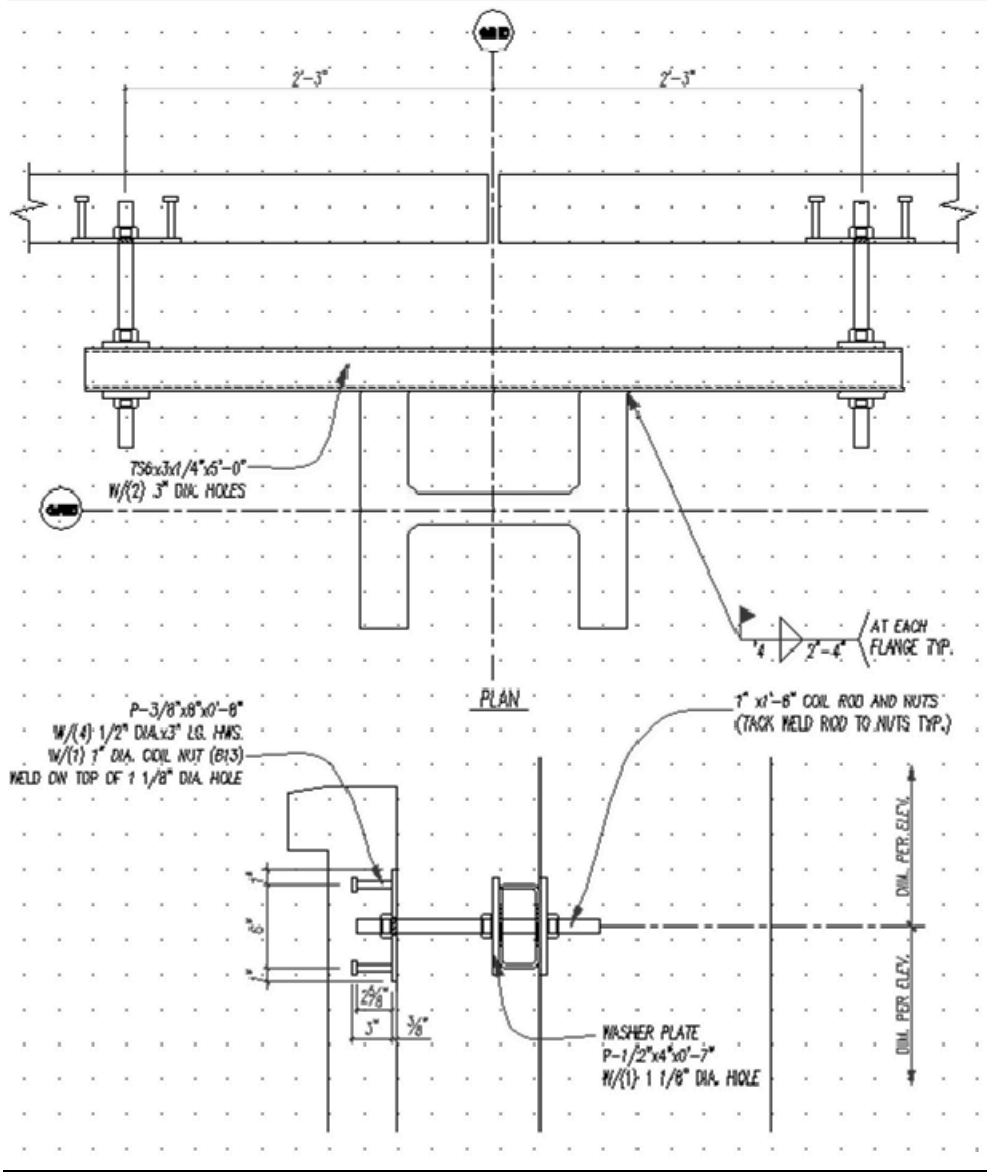

Fig. 3.10 Plan (above) and section (below) of threaded rod push-pull connection

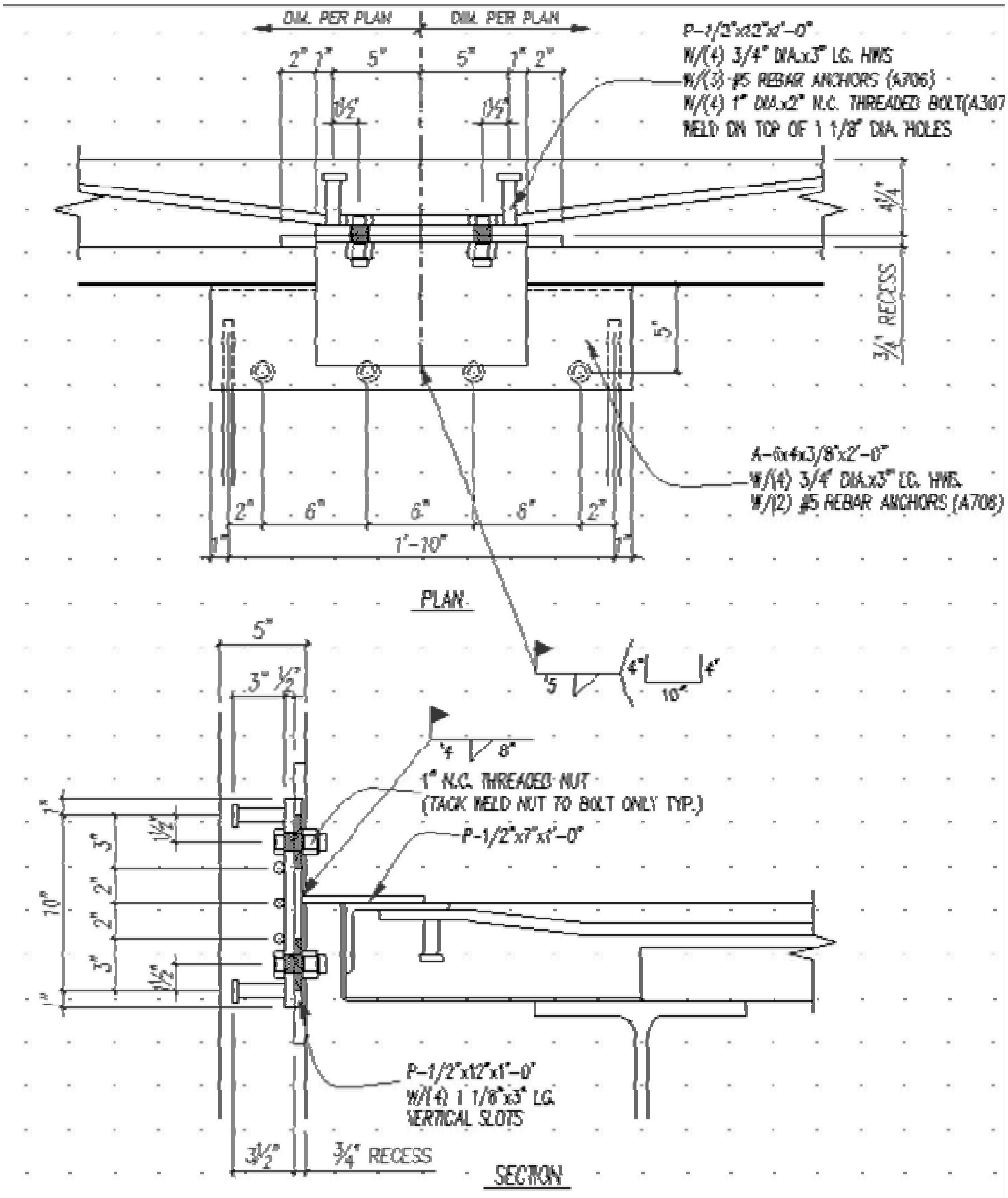

Fig. 3.11 Plan (above) and section (below) of rigid lateral connection

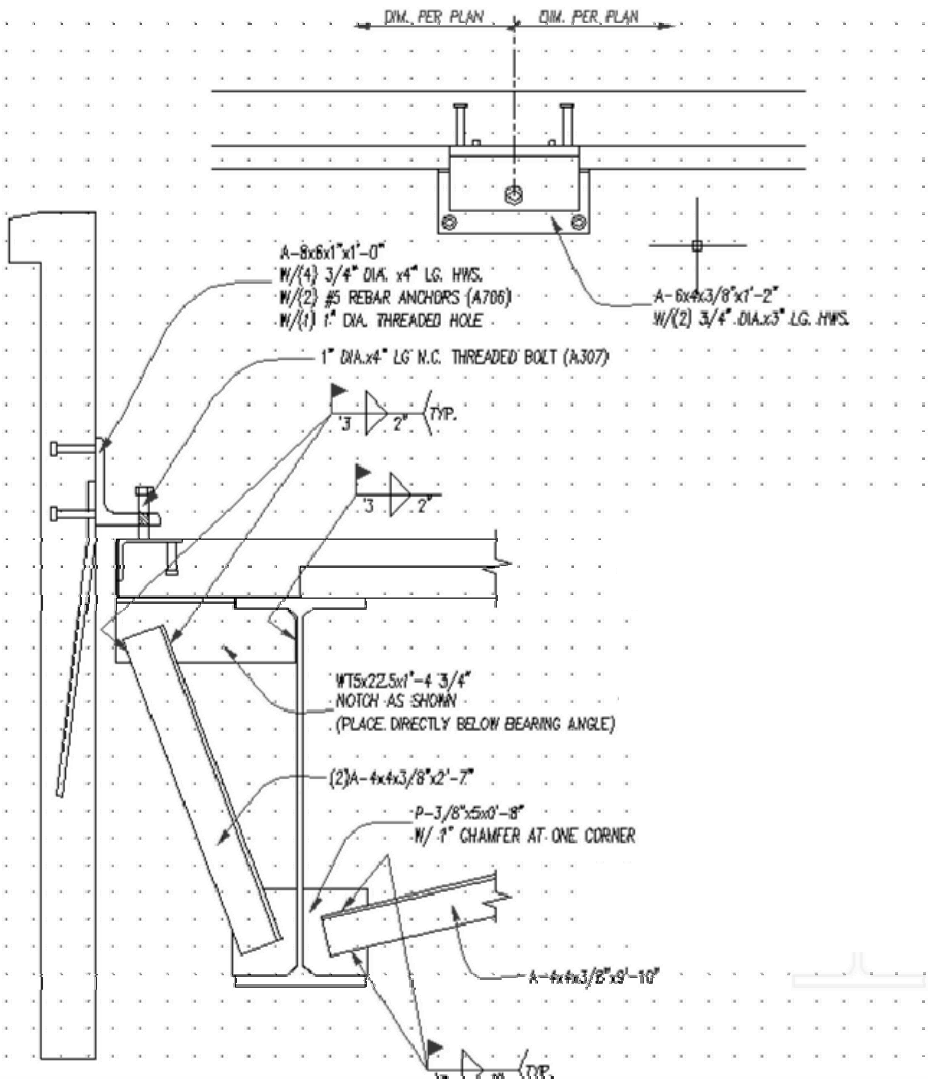

Fig. 3.12 Plan (above) and section (below) of vertical bearing connection

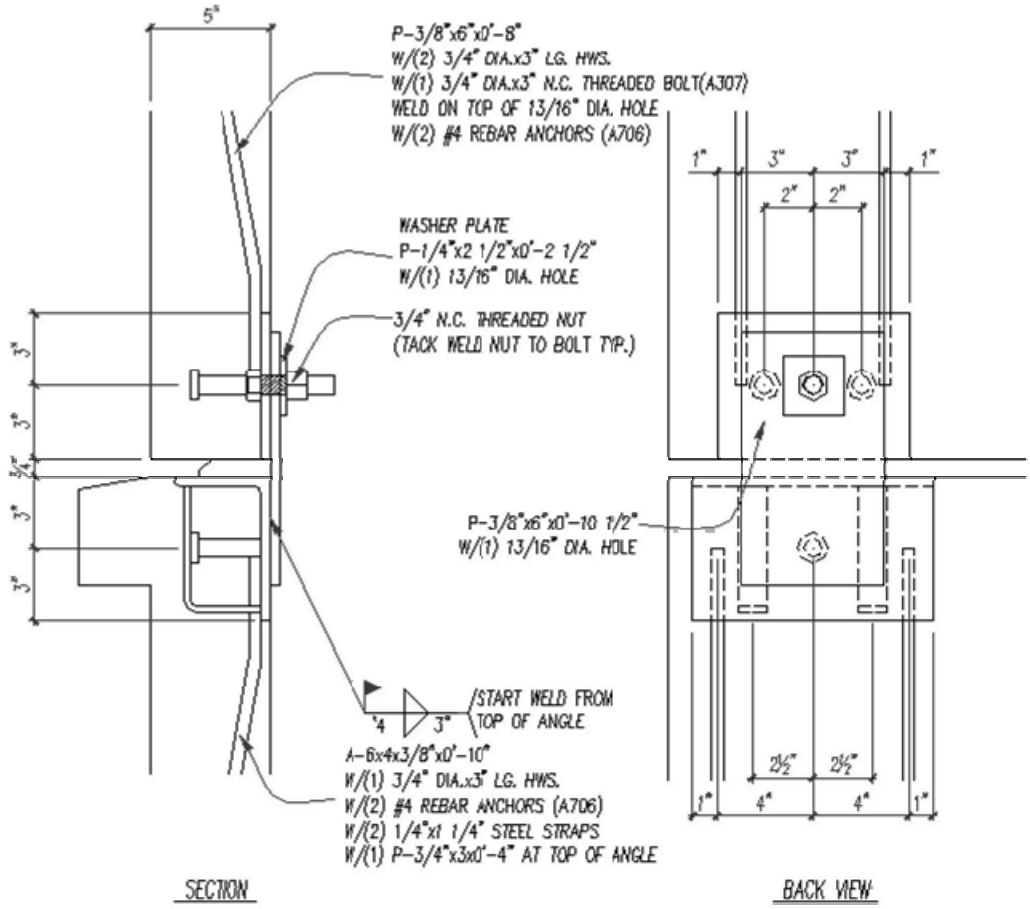

Fig. 3.13 Section (left) and back view (right) of the bottom column cover connection

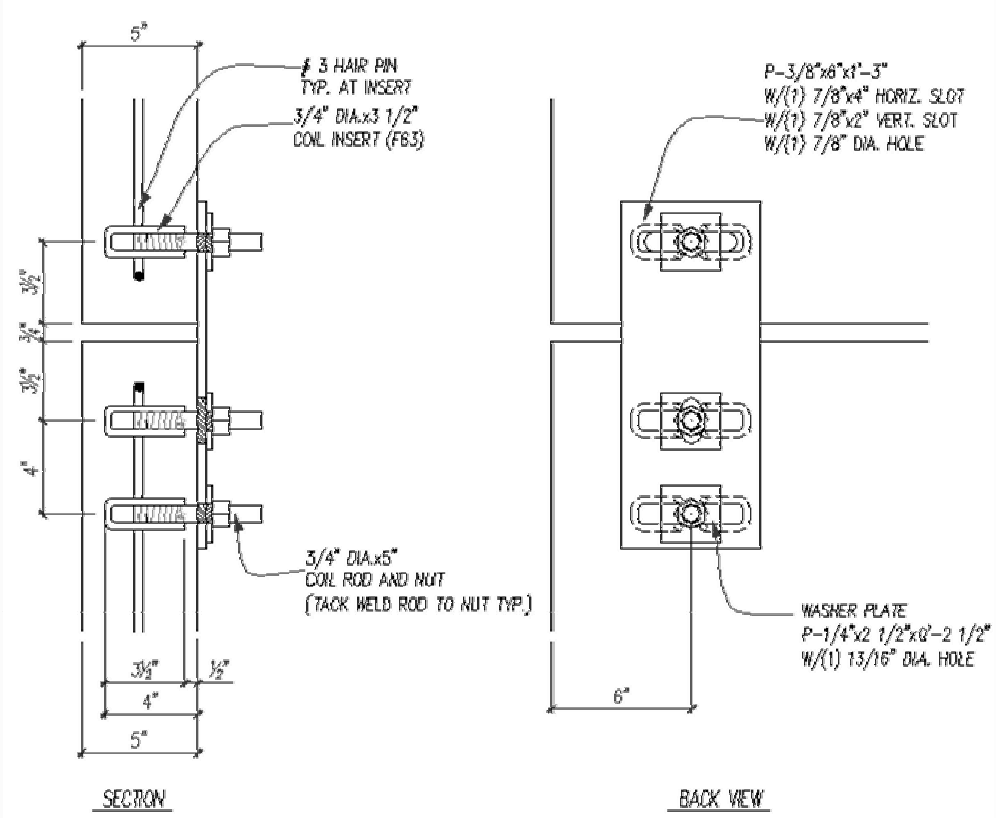

Fig. 3.14 Section (left) and back view (right) of the top column cover connection

Push-pull connection

Vertical bearing connection

Rigid lateral connection

Fig. 3.15 Photographs of push-pull, vertical bearing, and rigid lateral connections during construction of the San Jose State University Library (Photos: McMullin (2006))

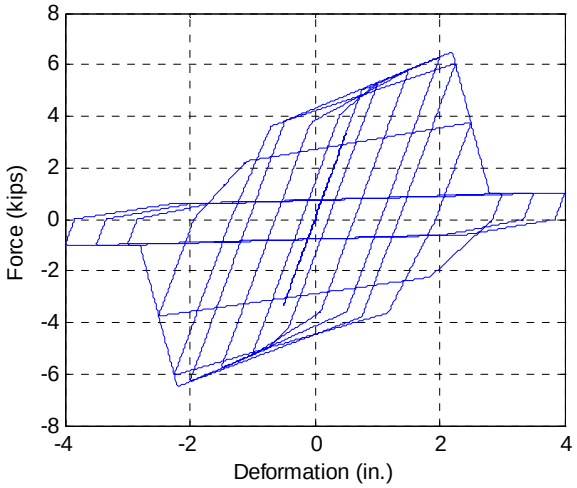

Fig. 3.16 Hysteretic force-deformation curve for the push-pull connection assembly

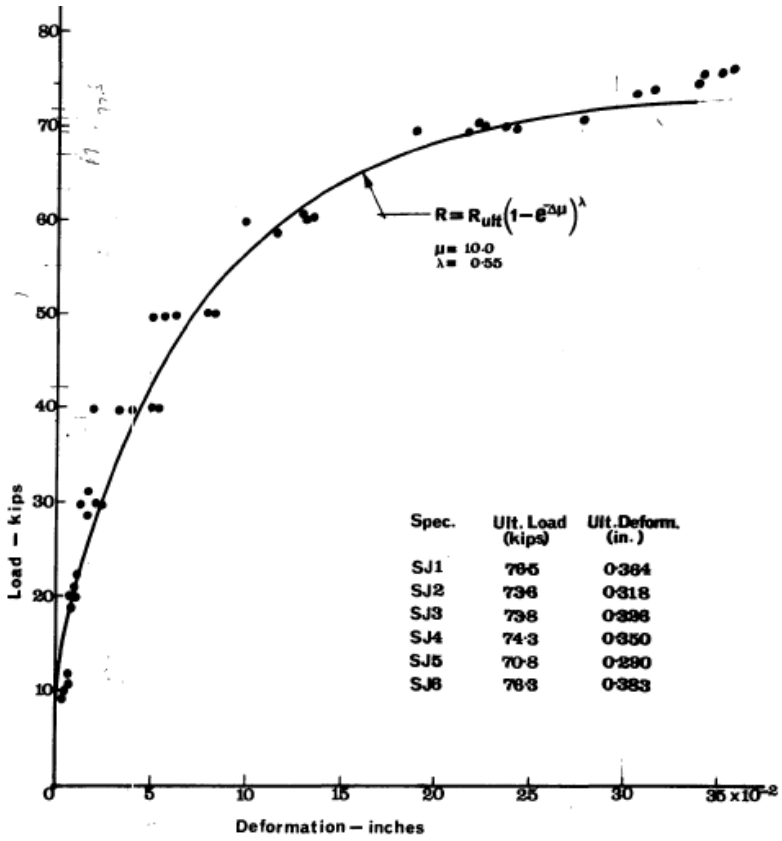

Fig. 3.17 Force-deformation curve for column cover connections determined by Crawford and Kulak (1968)

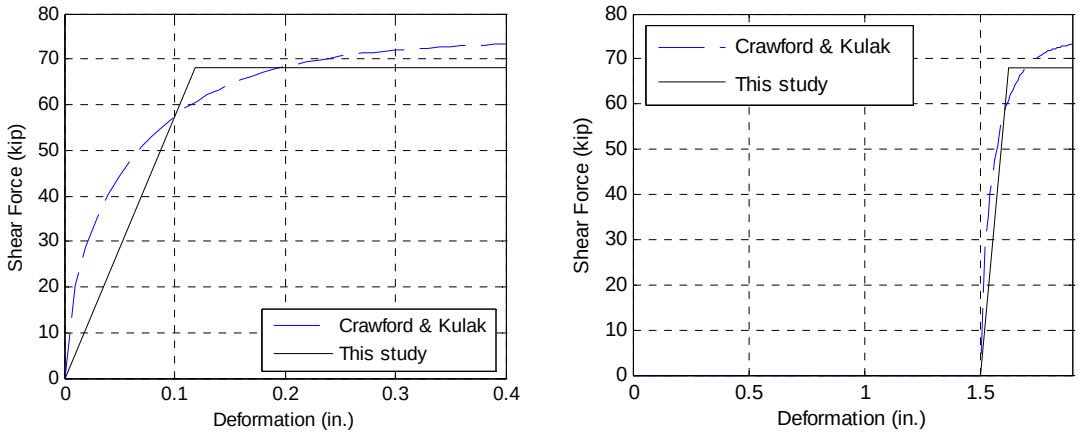

Fig. 3.18 Force-deformation curve for the bottom column cover connection (left) and top column cover connection (right)

Table 3.2 Mass values for bare frame model

Story	Mass value at each beam-column node in story *i* (kip*sec^2/in.)
1	0.479
2-8	0.471
9	0.508

Table 3.3 Mass values for Model C1

Story	Mass value at each beam-column node in story *i* (kip*sec^2/in.)	Mass value at each corner node of spandrel panel in story *i* (kip*sec^2/in.)
1	0.454	0.0076
2-8	0.446	0.0076
9	0.482	0.0076

Table 3.4 Mass values for Model C2

Story	Mass value at each beam-column node in story *i* (kip*sec^2/in.)	Mass value at each corner node of spandrel panel in story *i* (kip*sec^2/in.)
1	0.446	0.010
2-8	0.437	0.010
9	0.474	0.010

Table 3.5 Mass values for Model C3

Story	Mass value at each beam-column node in story *i* (kip*sec^2/in.)	Mass value at each corner node of spandrel panel in story *i* (kip*sec^2/in.)	Mass value at each corner node of column cover panel in story *i* (kip*sec^2/in.)
1	0.447	0.0076	0.0011
2-8	0.438	0.0076	0.0011
9	0.475	0.0076	0.0011

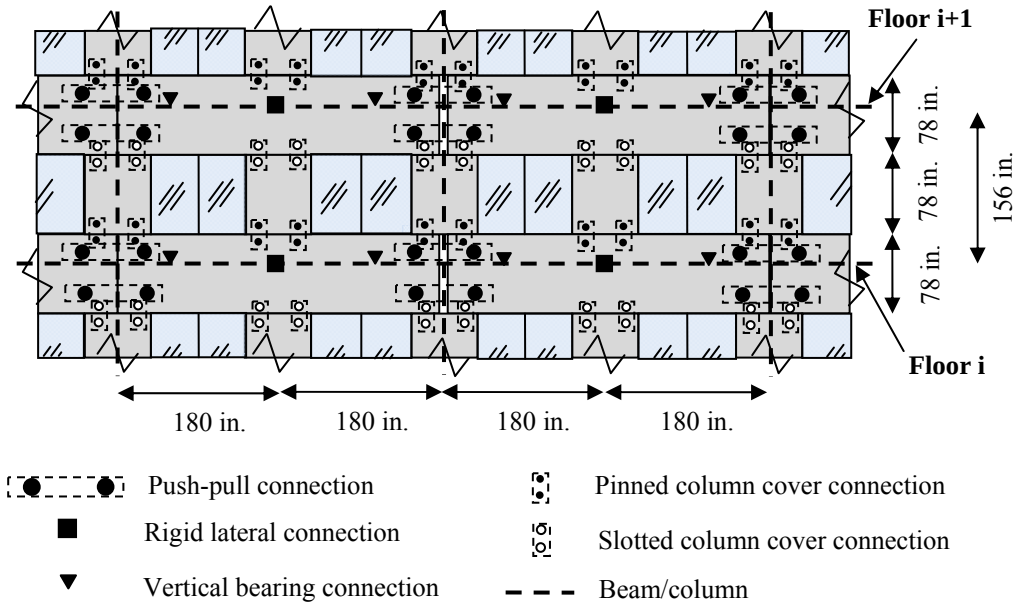

Fig. 3.19 Detailed elevation of cladding system C3 and window panes

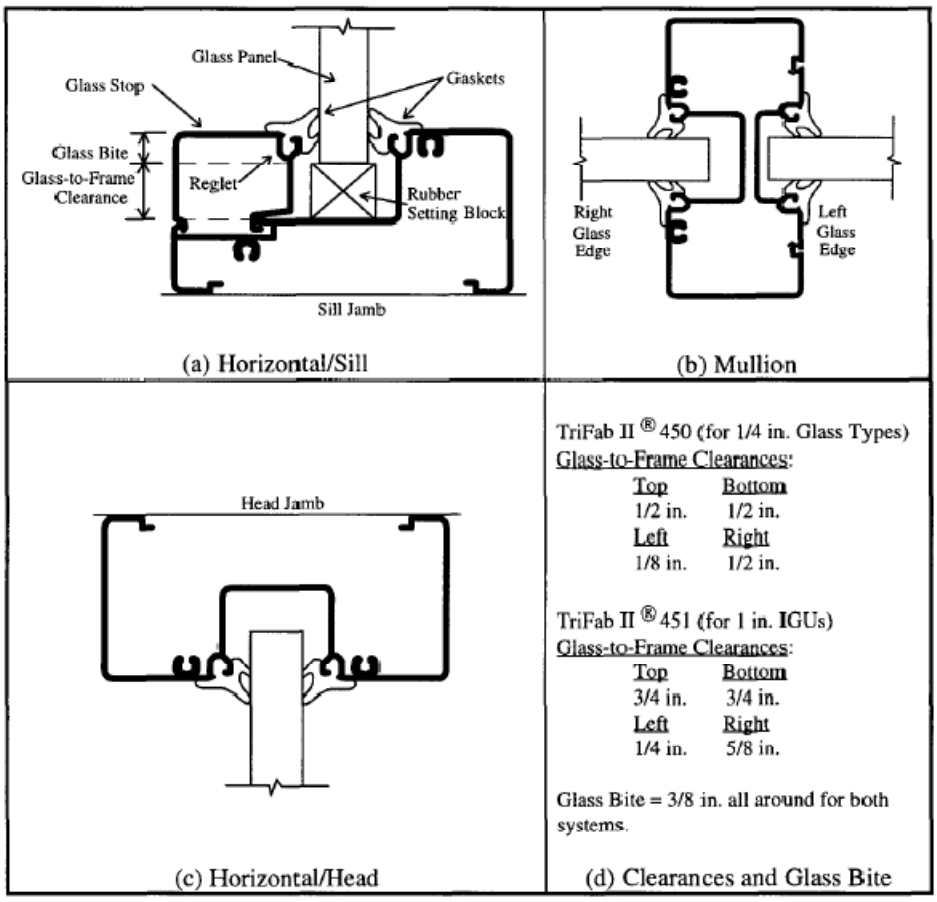

Fig. 3.20 Details of the window glazing system

Table 3.6 Quantity take-off of cladding systems

Component	Cladding Type		
	C1	C2	C3
Spandrel panels	180 panels each 30’ wide by 6.5’ high = 35,100 sf (48% of total exterior surface area)	180 panels each 30’ wide by 13’ high with window cutouts = 70,200 sf (66% of total exterior surface area)	180 panels each 30’ wide by 6.5’ high = 35,100 sf (48% of total exterior surface area)
Column cover panels	none	none	324 panels each 54” wide by 78” high + 72 panels each 27” wide by 78” high = 10,530 sf (14% of total exterior surface area)
Caulking	1,850 lf per story = 16,650 lf total	2,340 lf per story = 21,060 lf total	1,850 lf per story = 16,650 lf total
Window panes	1,080 panes each 5’ wide by 6’ high (52% of total exterior surface area)	720 panes each 5’ wide by 6’ high (30% of total exterior surface area)	720 panes each 5’ wide by 6’ high (30% of total exterior surface area)
Gaskets for window system	2,640 lf per story = 23,760 lf total	1,760 lf per story = 15,840 lf total	Total length = 15,840 lf
Push-pull connections	40 conn. per story = 360 conn. total	40 conn. per story = 360 conn. total	40 conn. per story = 360 conn. total
Column cover connections	none	none	176 conn. per story = 1,584 conn. total

Chapter 4: Seismic Response Analysis of a Multistory Building with Cladding

In this chapter, the performance of the models described in Chapter 3 is investigated with modal analyses, nonlinear pushover analyses, and nonlinear dynamic time-history analyses. The overall behavior of the models with cladding (C1, C2, and C3) is compared to the bare frame model (BF), and the behavior of the cladding connections is compared across the models with cladding.

4.1 MODAL ANALYSES

An eigenvalue (modal) analysis was carried out to investigate the effect of the cladding panels and connections on the modal periods and mode shapes of the building. The total building mass is the same for all models; however, the distribution of the mass is different between the models. The details of the assignment of nodal masses were discussed in Chapter 3.

An analysis of a building's vibration periods provides information on how the building might respond to lateral excitation. Depending on the predominant frequency of the ground motion, a building with a shorter (or longer) fundamental period might be subjected to higher (or lower) intensity shaking. The first three modal periods are given in Table 4.1 and in Fig. 4.1 for each model. The fundamental period varied between 2.05 and 2.13 seconds. There is only 4% difference between the fundamental period of the bare frame and cladding type C2. In addition to the current models C1, C2, and C3, a new model (C3+caulk, shown in Fig. 4.2) was analyzed to determine the influence of the caulking between the column covers and the spandrel panel on the fundamental period. Experimental tests by Mark Hildebrand at Willis Construction (2009) on the caulking used in cladding revealed that a bead of caulking has approximately 35 pounds per linear inch of strength and a failure deformation of 1.5 inches. Thus, the stiffness of the 54-inch length of caulking used in the column cover to spandrel panel joint is 35 lb/in*54 in/1.5 in. = 1,260 lb/in. However, even considering this additional stiffness, the fundamental period of cladding type C3 decreased by only 2%, which is well within the model error bounds. The bare frame had the longest fundamental period of 2.13 sec., while cladding type C2 has the shortest period of 2.05 sec. (4% decrease), due to the fact that this cladding system spans the entire height of the story and therefore is more effective at stiffening the building. Goel and Chopra (1997) compiled the measured fundamental vibration periods in multistory steel moment-resisting buildings. For the height of the nine-story SAC building, their equations give an upper bound of 2.26 sec. and a lower bound of 1.41 sec. The fundamental periods of all modes are located within the upper 85% of this range, providing good agreement with the measured periods. The

differences in the modal periods for higher mode vibrations are much less significant than in the fundamental mode. In the previous analytical studies summarized in Chapter 2, we saw models of cladding systems that decrease the fundamental period of a bare frame structure by 18-48%; however, in this study using newer and more realistic modeling approaches, the cladding system does not significantly affect the vibration properties of the building (at most a 4% difference). This result agrees better with the measured data that a cladding system affects the fundamental period of a multistory building by only a small amount (Meyyappa *et al*., 1981).

The effective modal mass percentages, a measure of how much of the total mass is activated in each vibration mode, are provided in Table 4.2 and Fig. 4.3 for the first three modes. A mode with a high effective modal mass percentage indicates that this mode dominates the lateral response of the building for an arbitrary ground motion. However, there may be certain ground motions (near fault motions), building sites (directivity effects, soft soil), or structural properties (tall buildings) that activate a second or third mode just as much or possibly more than the fundamental mode. In all of the analytical models in this study, the first three modes contribute to approximately 97-99% of the total lateral response, indicating that these three modes capture essentially all of the lateral dynamic response of the building. The first mode contributes over 80% to the total response, which is typical of moment-resisting frame buildings with an approximately uniform distribution of structural properties and mass.

An analysis of a building's mode shapes gives insight into the deformed shape of the building during an earthquake. Depending on the properties of the ground motion, one or more of the modes is activated, and the deformed shape can be a superposition of the mode shapes. The first three mode shapes are shown in Fig. 4.4. The first mode shape of all models is approximately linear, and the modal ordinates are almost identical (the model with cladding type C2 has slightly higher modal ordinates in the middle stories). The second and third mode shapes of the models are virtually identical, indicating that the cladding does not have much of an effect on the free vibration displacements caused by higher modes.

4.2 STATIC NONLINEAR PUSHOVER ANALYSES

Static nonlinear pushover analyses of the models were performed to investigate the lateral base shear and roof displacement relationship of the building. The typical pushover curve for buildings consists of an initial linear branch in which the structural members deform in their elastic range, followed by a yield zone where the beam-column members start developing plastic hinges. As lateral deformation continues, more plastic deformation occurs, and the post-yield strength of the building softens.

For the static pushover analyses in this study, the applied reference forces vary linearly over the height of the building to match the fundamental mode shape. The reference forces are applied to the beam-column nodes of the moment-resisting frame, and in the models with cladding, the reference forces are divided between the moment-resisting frame and the cladding panels according to their relative tributary weights. The pushover analyses were solved using displacement control: the horizontal displacement at the roof level was monitored, and the reference forces were scaled uniformly to achieve displacement increments of 0.3 inches at the roof. The pushover analyses were continued until a roof drift ratio of 0.10 radians (146.4 in.) was achieved. The 2-norm of the displacement increment was used to measure the convergence at each time step. The Newton-Raphson solution algorithm (with tangent stiffness or initial

stiffness), Broyden algorithm, and Newton-Raphson with Line Search algorithm were used in a conditional loop to achieve convergence throughout the analyses.

4.2.1 Global Behavior

The base-shear versus roof drift capacity (pushover) curve is shown in Fig. 4.5. The base shear is normalized with respect to the building weight (10,422 kips), and the roof drift is normalized with respect to the overall building height (1,464 inches above ground level). The curves reveal that the bare frame and models with cladding have approximately the same initial stiffness. The pushover curves for the bare frame model (BF), cladding type C1, and cladding type C2 have approximately the same post-yield response as well. The pushover curves for these three models have a negative slope after yielding, which is attributed to P-Δ effects. The cladding systems of models C1 and C2 consist of spandrel panels attached to the columns of the moment frame, and from the global pushover results, these models do not seem to provide any significant addition of lateral strength to the frame. Model C3, consisting of spandrel panels and column cover panels, has a different post-yield response than the other models. Model C3 has a yield point of 24% of the building weight, which is 25% higher than the yield point of 18% of the building weight for the other models. This increase shows that cladding type C3 participates in the building response in an appreciable manner, attracting more pushover force due to building shortening so that it takes more control-point load to yield the steel frame. The post-yield portion of the curve for model C3 is jagged, which is due to the failure of the column cover connectors as the building displaces laterally. The failure of the column cover connections begins just after 0.01 rad. roof drift, resulting in a decrease in the lateral strength of the frame. From 0.02 to 0.03 rad. roof drift, more of the connections fail, and the base shear strength remains relatively constant at 21.5% of the building weight. Then, at approximately 0.03 rad. roof drift, the base shear capacity starts to increase and more of the column cover connections fail. This post-yield increase in base shear is due to vertical confinement of the cladding system from the effects of building shortening during the pushover analysis. As the structure is displaced laterally, the interstory height decreases and the column covers are pinched between the spandrel panels. The roof displaces 2.3 in. downward at 0.05 rad. roof drift, as shown in Fig. 4.6. In moderate to large magnitude events, the building is expected to respond in the 2-4% roof drift range. In this range, there is only 9% difference between the strength of Model C3 and Models BF, C1, and C2.

The deflected shapes of the building at selected roof drift ratios are shown in Fig. 4.7. The values of roof drift ratio on the horizontal axis correspond only to the drifts at the roof, and the line represents the deflected shape of the building profile (i.e. the drift ratios for the other stories cannot be read off the horizontal axis). At a roof drift level of 0.007 rad., which corresponds to the Immediate Occupancy level in FEMA 356 (FEMA, 2000), all models follow approximately the same linear deformed shape. At a roof drift level of 0.025 rad., which corresponds to the Life Safety level in FEMA 356, stories 3-5 displace more than the other stories, creating the upward curving shape. The bare frame model, Model C1, and Model C2 have approximately the same deflected shape, while model C3 undergoes larger displacements in the middle stories. At a roof drift of 0.05 rad., which corresponds to the Collapse Prevention level in FEMA 356, even more displacement occurs in the middle stories, with model BF having slightly lower displacements than the models with cladding.

4.2.2 Element Demands

As the building undergoes large lateral displacements, plastic hinges develop in the beam-column members, typically at the member ends. In this section, the plastic hinge rotations are compared between the bare frame model and models with cladding to determine the effect that the cladding has on the distribution of plastic hinge demand in the moment-resisting beams and columns. The plastic hinge rotation is calculated as the curvature at the end of the beam-column divided by the yield curvature. The plastic hinge rotations in the elements of the models are shown as bubble plots in Fig. 4.8-Fig. 4.10. The rotation demands are compared to the acceptance criteria for reduced beam sections in FEMA 356, Table 5-6 (FEMA, 2000), repeated for convenience below in Equations 4.1-4.3:

Immediate Occupancy: $\theta_{max} = 0.0125 - 0.0001d$ Eq. 4.1

Life Safety: $\theta_{max} = 0.0380 - 0.0002d$ Eq. 4.2

Collapse Prevention: $\theta_{max} = 0.0500 - 0.0003d$ Eq. 4.3

The variable d is the depth of the beam-column element. For the nine-story SAC building, the above acceptance criteria translate to approximately 0.01 rad., 0.03 rad., and 0.04 rad. for the Immediate Occupancy (IO), Life Safety (LS), and Collapse Prevention (CP) performance levels, respectively. Fig. 4.8, Fig. 4.9, and Fig. 4.10 show the bubble plots for all models at 0.007 rad., 0.025 rad., and 0.05 rad. roof drift, respectively. The sizes of the bubbles represent the magnitude of the plastic hinge rotation demand, and the colors of the bubbles correspond to satisfying a particular performance level. The maximum plastic hinge rotations in each story are shown on the right hand side of the figures along the height of the building. At 0.007 rad. roof drift (Fig. 4.8), there is little plastic hinge deformation in any of the models, and all rotations are less than the Immediate Occupancy acceptance criteria. At 0.025 rad. roof drift (Fig. 4.9), models BF, C1, and C2 have approximately the same plastic hinge demands, and Life Safety is satisfied at all hinge locations. In model C3, there are increased rotational demands in the lower stories, and at floors two and three, there are hinges that exceed the life safety criteria. The plastic hinge rotations in model C3 at stories two and three are 25% larger than those in the other models. At 0.05 rad. roof drift (Fig. 4.10), significant plastic hinging occurs in all models, especially in the lower stories. The plastic hinge demands are similar between the bare frame model and model C1, while model C2 has higher demands at the lower stories. The plastic hinge rotations in the beams in model C3 are slightly less than the rotations in the other models and more distributed along the building height; however, in model C3, some plastic hinging develops in some of the columns.

The pushover analyses have revealed that the element demands (plastic hinge rotations) are very similar between the four models. However, as the building undergoes more significant drift, the plastic hinges increase in the lower stories and are 25% larger in model C3 at 2.5% roof drift. Under significant drift, the plastic hinges start to redistribute in model C3 and column hinging may develop.

4.2.3 Behavior of Cladding Connectors

The deformations and forces in the push-pull and column cover connections were also recorded during the pushover analysis. As the interstory drift increases during the pushover analysis, the deformations in the connectors increase as the spandrel panels and column cover panels displace in-plane relative to the structural frame. The total deformation in the connectors is taken equal to the vector sum of horizontal and vertical deformations. The vector sum of the deformations in the push-pull connectors are shown in Fig. 4.11, Fig. 4.12, and Fig. 4.13 for roof drifts of 0.007 rad., 0.025 rad., and 0.05 rad., respectively. The bubble plots show the magnitude of the deformations in the push-pull connections, and at the right side of the figures, the maximum connector deformations in each story are shown along the building height. The colors in the bubbles represent satisfaction of certain performance levels of the push-pull connections. The performance levels are assigned using the push-pull force-deformation curve defined in Chapter 3. The Immediate Occupancy (IO) performance level is satisfied until a deformation of 0.5 inches (two-thirds of the yield deformation), the Life Safety (LS) performance level is satisfied until a deformation of 1.25 inches (one and two-third times the yield deformation), and the Collapse Prevention (CP) performance level is satisfied until a deformation of 2.2 inches (deformation at maximum strength). The performance states are shown on the force-deformation curve of the push-pull connectors in Fig. 3.16.

At 0.007 rad. roof drift, model C3 has the lowest push-pull deformations, followed closely by model C1. The deformations in model C2 are largest because the spandrel panels span the entire story height and must accommodate the entire interstory drift. The spandrel panels in models C1 and C3 are of the same design; however, the deformations in model C3 are slightly less than in model C1 because the column covers in model C3 absorb some of the deformations. In models C1 and C3, some of the push-pull connections are in the Life Safety performance level, and in model C2, some of the connections in the lower stories are in the Collapse Prevention level. These connections are at risk for failure at a very low roof drift.

At 0.025 rad. roof drift, model C1 has the lowest push-pull deformations, followed by model C3 and then model C2. Model C3 has higher deformations in the lower stories compared to model C1. The push-pull deformations in model C2 are approximately twice as large as the deformations in model C1. The connectors in model C1 are in the Collapse Prevention level in the lower stories and in the Life Safety level for the upper stories. In model C2, most of the deformation in the push-pull connectors exceed the Collapse Prevention performance level and are far beyond the fracture deformation. In model C3, some of the connector deformations exceed the Collapse Prevention level deformation in the lower stories, while the deformations in the upper stories are in the Life Safety and Immediate Occupancy performance level.

At 0.05 rad. roof drift, most of the push-pull connectors exceed the Collapse Prevention performance level and have fractured. The cladding system at this point is not as much of a concern because for this level of roof drift, the moment-resisting frame is at risk of collapse as well.

Cladding type C3 consists of column cover panels that span between the spandrel panels. The vector sum of the horizontal and vertical shear deformations in the column cover connections were recorded during the pushover analysis. The bubble plots of shear deformation demands are shown in Fig. 4.15, Fig. 4.16, and Fig. 4.17 for the bottom connectors (pinned) and the top connectors (slotted). In the bubble plots, the sizes of the bubbles represent the magnitude of the shear deformation, and the color of the bubbles corresponds to satisfying a particular

performance level. The performance levels are assigned using the column cover connector force-deformation curves defined in Chapter 3. The Immediate Occupancy (IO) performance level is satisfied until a shear deformation of 0.06 inches (half the yield deformation), the Life Safety (LS) performance level is satisfied until a shear deformation of 0.12 inches (the yield deformation), and the Collapse Prevention (CP) performance level is satisfied until a shear deformation of 0.25 inches (twice the yield deformation). Since there is a 1.5 inch gap on either side of the bolt in the top connectors, deformations in the connectors do not occur until after the interstory drift exceeds 1.5 inches.

At 0.007 rad. roof drift, all top and bottom column cover connectors satisfy the Immediate Occupancy performance level, except for a few connectors in the first story that satisfy the Life Safety criteria. At 0.025 rad. roof drift, about half of the column cover connectors in the building have exceeded the Collapse Prevention level in the top and bottom connectors. The connectors in the top stories satisfy the Immediate Occupancy and Life Safety performance levels. The column cover connections appear to deform very quickly as interstory drift increases slowly. The damaged column connections are concentrated in the lower stories (since the interstory drift is concentrated in these stories). At 0.05 rad. roof drift, almost all of the column cover connectors at the top of the panels (slotted connections) have exceeded the Collapse Prevention criteria. From this analysis, we can see that even in low to moderate drifts, the push-pull and column covers can become significantly damaged.

4.3 DYNAMIC TIME-HISTORY ANALYSES

Dynamic time-history analyses were performed to further investigate the seismic behavior of both the structural frame and the cladding connectors. A nonlinear model and dynamic time-history analyses are assumed to minimize epistemic uncertainty in the results and provide the best estimate of the response. The earthquake ground motions were applied uniformly at the base of the model. The Newton-Raphson solution algorithm (with tangent stiffness or initial stiffness), Broyden algorithm, and Newton-Raphson with Line Search algorithm were used in a conditional loop to achieve convergence throughout the analyses. The Newmark integrator (γ=0.5, β=0.25) was used to increment the next time step. Rayleigh damping of 2% was added to the first three modes of all models.

There are several different procedures to address ground motion scaling in time-history analyses. The first procedure, termed the “cloud” or direct method (Shome and Cornell, 1999), uses a wide selection of many ground motions that are representative of the site seismicity. The cloud method uses no prior scaling of the ground motions. Some common derivatives of the cloud method involves grouping the ground motions into distinct magnitude and distance bins to disaggregate the source of the seismic hazard, scaling the cloud of records to a function of the median intensity for each bin, or scaling all of the ground motions by a common factor (i.e. 1.5 or 2). The second procedure, known as the incremental dynamic analysis (IDA) procedure, involves the stepwise increase of the intensity of a few select ground motions (Vamvatsikos and Cornell, 2002). The maximum values of the engineering demand parameters are plotted against the corresponding intensity measure to produce a dynamic pushover curve. To achieve comparison with the cloud method, several motions are required and several scaling steps must be used. The third procedure, termed the “stripe” method, involves scaling all of the ground motions to the same intensity at a select few intensity levels or “stripes.” For each selected

intensity level, all ground motions are scaled first, structural analysis is performed to compute the engineering demand parameters, and then the results are plotted to give a "stripe" of data. Stripe analysis is a special case of IDA.

In this study, the cloud method with ground motion binning and scaling is used to perform the time-history analyses. A total of seven bins of 20 records each were used, totaling 140 ground motions. Each ground motion record has one horizontal and one vertical acceleration component. The first two bins are identical to a subset of those selected by Medina and Krawinkler (2003). The ground motions in these bins were recorded on free field sites that can be classified as site class D according to the NEHRP seismic provisions. These two bins, termed LMSR and LMLR correspond to magnitude distance bins: large magnitude + small distance (LMSR), and large magnitude + large distance (LMLR). The third and fourth bins, I880-N and I880-P were created from the ground motions selected for the I-880 PEER testbed study (Kunnath, 2006). The site for these ground motions is located near the Hayward fault; therefore, the ground motions are anticipated to exhibit distinct directivity effects. The I880-N bin contains all of the original fault normal motions, and the I880-P bin contains all of the original fault parallel motions. The final three bins of ground motions consist of the original SAC ground motions, developed for the 50% in 50 years, 10% in 50 years, and 2% in 50 years probabilities of exceedance. These ground motions were selected for a building site in Los Angeles in Seismic Zone 4 with stiff soil. A detailed discussion of the three SAC bins can be found in Somerville *et al*. (1997). The earthquake magnitude and distance from rupture to building site is plotted (M-R plot) in Fig. 4.18 for each ground motion. For each bin, all ground motions were scaled by a common factor to ensure a range of response in the elastic and inelastic ranges. The scaling factors for each bin are given in Table 4.3.

4.3.1 Global Behavior

The global behavior of steel-moment resisting frames due to earthquake excitation is typically described in terms of interstory drift ratios, residual (permanent) drifts, and floor accelerations. These engineering demand parameters (EDPs) were recorded during the time-history analyses of the analytical models.

The interstory drift ratio is an important EDP because it helps to describe global damage to drift sensitive components of the building such as structural framing, interior partitions, exterior cladding, and window glazing. The interstory drift ratios in story 9 (top story) are plotted in Fig. 4.19, Fig. 4.20, and Fig. 4.21 for selected ground motions in the LA50, LA10, and LA2 bins, respectively. The maximum interstory drift ratios for each plot are marked at their corresponding times in the figures. As shown in Fig. 4.19 for the LA50 bin, the maximum interstory drifts are very similar between the bare frame model and models with cladding. For the selected motions, the overall shapes of the response history of interstory drift are also very similar, with little to no residual interstory drift. From these selected motions, it seems that the addition of any cladding to the bare frame model has little to no influence on the maximum interstory drift.

The response history of interstory drift in story 9 is plotted in Fig. 4.20 for selected motions in the LA10 bin. For the LA05 and LA17 ground motions, the cladding does not have a significant effect on the maximum interstory drift or shape of the response history. However, for the LA13 motion, model C3 causes a 27% decrease in the maximum interstory drift of the bare

frame model, and for the LA16 motion, model C3 causes a 48% decrease in the maximum interstory drift of the bare frame model. The other models with cladding (C1 and C2) cause a smaller, but still significant, reduction.

The response history of interstory drift in story 9 is plotted in Fig. 4.21 for selected motions in the LA2 bin. The plots show that the bare frame model, model C1, and model C2 have similar shapes of the response history of drift, and their maximum drift values are approximately similar. However, the shape of the response history of drift in model C3 is significantly different than in the other models. For the selected ground motions, the time at which the maximum interstory drift occurs in model C3 is different than in the other models, and the residual interstory drift is much less in model C3 than in the other models. For these four ground motions, the maximum interstory drift ratio in story 9 of model C3 is up to 57% smaller than in the other models.

From the results above, it appears that the consideration of cladding reduces the maximum interstory drift of the bare frame, especially for large intensity earthquakes. However, to confirm these results, trends must be determined considering all ground motions. The effects of a particular earthquake on a building are usually expressed in terms of maximum values of engineering demand parameters (i.e. drift, floor acceleration, etc.). For some structural systems, such as braced frames, the number of cycles of certain amplitude is also used to quantify damage due to low cycle fatigue of the braces. In this study, only the trends for the maximum values of the engineering demand parameters are discussed, which is typical for multistory steel moment-resisting frames.

The most common method of computing expected values of EDPs is to compute the median value of the maximum EDP for different ground motion bins (possibly scaled to a specific spectral acceleration). Fig. 4.22 shows the median maximum interstory drift ratio for each ground motion bin along the height of the building. The maximum drift ratios occur in the upper stories, except for the LA2 bin, in which larger interstory drifts occur in the lower stories (most likely due to near field effects). For bins LMLR, I880-P, and LA50, the interstory drifts in the models with cladding are very similar to the interstory drifts in the bare frame model. For the other bins, the cladding causes a more significant decrease in the median interstory drifts. For example, in the LA10 and LA2 bins, model C3 has median interstory drifts that are up to 33% lower than in the bare frame model. The insights gained from comparing median values of the EDPs in separate bins are valuable; however, the comparisons are made piecewise between ground motion bins, and it is difficult to determine what level of earthquake intensity measure (IM) has caused a certain magnitude of EDP.

A more complete way to determine the expected value of maximum EPDs is to plot the data points as a "cloud" in the EDP-IM space. Trends can be observed over a range of seismic intensities with this approach. To facilitate later repair cost analyses using this data, the EDP data are assumed to have a lognormal distribution when conditioned on IM, the conditional mean of EDP given IM is linear in log space, and the conditional dispersion of EDP given IM is constant (Mackie *et al*., 2008a). This relationship between EDP and IM is termed a "demand model." The demand model is represented by Equation 4.4 in log space and Equation 4.5 in linear space. The two unknown coefficients in the demand model and the unknown dispersion $\sigma_{EDP|IM}$ can be computed using least-squares regression. In linear EDP-IM space, the demand model coefficients become $a = exp(A)$ and $b = B$. The variable $\widehat{EDP}$ is the median, or mean of the natural log of the data points, of the engineering demand parameter.

$$\ln\left(\widehat{EDP}\right) = A + B\ln(IM) \quad \text{Eq. 4.4}$$

$$\widehat{EDP} = a(IM)^b \quad \text{Eq. 4.5}$$

The relationship between EDP and IM will be studied for several EDPs relevant to the study building. First, the global EDPs (interstory drift ratios, residual interstory drift ratios, and floor accelerations) are studied to determine the effect that the cladding systems have on the global response of the bare structural frame. As an initial example, the maximum interstory drifts in story 9 of the bare frame model (BF) are plotted against their corresponding spectral acceleration at the fundamental mode of the building in Fig. 4.23. In the plot on the left side, a linear-linear scale is used for the EDP-IM space. The data points have a high concentration for EDPs less than 0.02 rad. and spectral accelerations less than 0.5g. The dispersion in the data increases for larger EDP values. In the plot on the right side, a natural log-log scale is used for the EDP-IM space, showing a clear linear trend in the data. The maximum interstory drift in story 9 vs. spectral acceleration at the fundamental mode is plotted for all four models in Fig. 4.24, and as discussed above, a least-squares regression is used to describe the mean maximum interstory drift and corresponding dispersion. The trend lines for the mean interstory drift ratios in story 9 are shown in Fig. 4.25 along with the coefficients of the demand model. The dispersion σ shown in the Figures corresponds to $\sigma_{EDP/IM}$. This conditional dispersion is calculated using all of the data points and is assumed to be constant (homoskedastic) over the range of IM considered. Dispersion values of 0.35 or less represent a good fit and efficient choice of IM to describe the demand model.

The demand model of maximum interstory drift vs. first mode spectral acceleration is shown in Fig. 4.26 for all stories. In the first and second stories, the conditional means of the maximum interstory drift ratios are very similar between the four models. In stories 3-7, the maximum interstory drifts of models BF, C1, and C2 are still very similar, with their trend lines of mean drifts and dispersions being almost equal. As one progresses up the height of the building, the trend line of maximum interstory drift for model C3 starts to diverge from the other models: the mean of the maximum interstory drifts in model C3 are less than those in the bare frame model, especially for large spectral accelerations. At the same time, the dispersion in the interstory drift data for model C3 are much less than the dispersion in the other models.

One advantage of the cloud method of analyzing the time-history results is that spectral accelerations corresponding to different probabilities of exceedance for a certain site can be used with the plots to read off the corresponding EDPs. The building is assigned to be on the UC Berkeley campus, and the expected spectral accelerations at this site were determined from the probabilistic seismic hazard analysis of the campus (URS, 2007). The design probabilistic average horizontal spectral accelerations are 0.11g, 0.34g, and 0.65g corresponding to events with a 50% probability of exceedance in 50 years (72 year return period), 10% probability of exceedance in 50 years (475 year return period), and 2% probability of exceedance in 50 years (2475 year return period), respectively. The mean maximum interstory drift ratios for the four models are shown in Table 4.4 for these three probabilities of exceedance. For the 50% PE in 50 year event, the maximum drift ratios are greatest in the top story for all models. Model BF has the highest interstory drifts, with models C1 and C2 having similar drifts in stories 1-6 (within approximately 10% of the maximum drifts of the bare frame model). Model C3 has the lowest interstory drifts, especially in the upper stories where the mean maximum drifts in model C3 are 18-22% lower than those in the bare frame model. For the 10% PE in 50 year event, the mean

maximum interstory drifts in the bare frame model are largest in the upper stories of the building, with the largest value of 0.021 rad. occurring in story 8. Model C1 has mean maximum interstory drifts that are the most similar to the bare frame model, with drifts that are within 10% of the drifts in the bare frame model. Model C2 has mean maximum interstory drifts that are up to 20% less than the drifts in the bare frame model (in the upper stories), while model C3 has maximum interstory drifts that are up to 27% less than the drifts in the bare frame model. For the 2% PE in 50 year event, the mean maximum interstory drifts in the bare frame model are largest in the middle stories of the building, with the largest value of 0.033 rad. occurring in story 4. Again, model C1 has mean maximum interstory drifts that are most similar to the bare frame model (drifts are 10% less than the bare frame drifts), and model C2 has maximum interstory drifts that are up to 20% less than the drifts in the bare frame. The mean maximum interstory drifts in model C3 are up to 33% lower than those in the bare frame model.

Another important engineering demand parameter for multistory steel moment-resisting frame buildings is the residual interstory drift ratio, which is the interstory drift ratio that remains after the ground shaking has stopped. The residual drift is due to nonlinear deformation that does not re-center itself at the end of free vibration after the earthquake. Residual interstory drift is an important EDP because it helps to describe global damage to operating components of the buildings such as elevators, doors and egress paths, and the seams between adjacent components (window panes, cladding, etc.). In addition, excessive residual interstory drift may lead to partial or complete collapse of the building. The mean residual interstory drifts for all models are plotted in Fig. 4.27 up the height of the building. The trends in the plots of residual interstory drift are similar to the trends in the plots of maximum interstory drift: as the spectral acceleration increases, model C3 has lower residual interstory drifts than the other models. Similar to the case of maximum interstory drift ratios, the mean values of the residual interstory drifts are calculated using the linear demand model for the three selected probabilities of exceedance. The mean values of residual interstory drift are shown in Table 4.5. For the 50% and 10% PE in 50 year events, the residual interstory drifts in all models and stories are negligible with mean values less than 0.002 rad. For the 2% PE in 50 year event, the mean residual interstory drift ratios are less than 0.005 rad., which is much less than the 0.01 rad. residual drift ratio limit for the Life Safety performance criteria in FEMA 356. The mean residual drifts for the frames with cladding are less than those in the bare frame model, and the residual drifts in model C3 are up to 53% less than the residual drifts in the bare frame model. The cladding systems and their connections seem to act like springs to help bring the structure back to its undeformed shape.

The last global engineering demand parameter considered in this study is the maximum floor acceleration. Floor accelerations are used to predict the damage to acceleration sensitive components in the building, such as ceiling systems, chimneys, and mechanical and electrical equipment. The median values of the maximum floor accelerations are shown in Fig. 4.28 for each ground motion bin. The floor acceleration is the total acceleration, or the sum of the ground motion acceleration and the structural acceleration. For all bins, the floor accelerations of models BF, C1, and C2 are very similar. The difference in floor acceleration between the bare frame model and the models with cladding is minimal for the LMLR and LA50 bins, which contain ground motions of lower intensity. For the other bins, model C3 has significantly higher median values of maximum floor accelerations, which are attributed to the racking motion of the column cover panels. The linear demand model is used to determine the mean values of maximum floor acceleration. In Fig. 4.29 the linear trends are shown for each model and story, and in Table 4.6, the mean values are shown for the three probabilities of exceedance. The mean maximum floor

accelerations in models C1 and C2 are only 10% less than the floor accelerations in the bare frame model for all three levels of intensity. For model C3, the mean values of the maximum floor accelerations are up to 35%, 63%, and 97% greater than the floor accelerations in the bare frame model for the 50%-, 10%-, and 2%-in-50 year probabilities of exceedance, respectively. The largest mean values of the maximum floor accelerations occur in the upper stories.

4.3.2 Element Demands

In this section, the effect that the cladding systems have on the structural element demands is investigated by comparing the maximum plastic hinge rotations between the different models. The maximum plastic hinge rotations are a commonly used engineering demand parameter to determine the amount of damage sustained to the beam-column connections in the moment-resisting frame. The cladding panels are connected to the structural framing, which may cause a redistribution of forces and deformations in the elements.

In Fig. 4.30, the maximum values of the plastic hinge rotations in the beam elements in each floor are plotted as the data points in the log-log EDP-IM space. The trend lines represent the demand model for the mean value of the maximum plastic hinge rotations. The plots for each story show that the differences in the maximum values seem to be small. Similar to the case of interstory drift, residual drift, and floor acceleration, the dispersion in the data points increases as one moves up the height of the building. In addition, the data points for each story form a distinct "S" shape, indicating that for low levels of spectral acceleration, the maximum plastic hinge rotation increases slowly. Then, the plastic hinge fully forms across the section, and the plastic hinge rotation increases rapidly for little change in spectral acceleration. This behavior is followed by another hardening zone as the steel material continues to yield. The mean values of the maximum plastic hinge rotations using the linear demand model are shown in Table 4.7 for the three probabilities of exceedance. For the 50% and 10% PE in 50 year events, the maximum plastic hinge rotations are very small, with values less than 0.008 rad. For the 2% PE in 50 year event, the plastic hinge rotations in all models are less than 0.025 rad., which is less than the Life Safety plastic hinge criterion of approximately 0.03 rad. set by FEMA 356. The mean values of maximum plastic hinge rotations in model C2 and C3 are the smallest of the four models, with values up to 33% less than the plastic hinge rotations in the bare frame model.

4.3.3 Behavior of Cladding Connectors

The response histories of the push-pull and column cover connectors were also recorded during the time-history analyses to gain insight into how much the cladding connectors deform during earthquake excitation. The push-pull connectors deform when the spandrel panel moves relative to the structural frame during interstory drift. The mechanics of the connector deformations are discussed in detail in Chapter 5.

The total deformation in the push-pull connectors is taken as the vector sum of the horizontal and vertical components of the shear deformation in the connector. The response history of the vector sum deformation in the center spandrel panel in story 9 is plotted in Fig. 4.31 for four selected ground motions in the LA50 bin. For each ground motion, the deformation in the connector in model C2 is the largest among the three models because the spandrel panels

in model C2 span from one story to the next, and the push-pull connectors in this model must accommodate the entire interstory drift. The spandrel panel configuration is the same in models C1 and C3, and from the plots, the vector sum deformations of the push-pull connectors in models C1 and C3 appear to be very similar. The push-pull deformations in models C1 and C3 are approximately 50-60% of the push-pull deformations in model C2. In Fig. 4.32, the vector sum deformation is plotted for a spandrel panel in story 9 for four selected ground motions in the LA10 bin. The push-pull deformations in model C1 are again approximately 50-60% of the deformations in model C2. However, in this case, the push-pull deformations in model C3 are slightly less than the push-pull deformations in model C1. In Fig. 4.33, the vector sum deformation is plotted for a spandrel panel in story 9 for four selected ground motions in the LA2 bin. In this case, the push-pull deformations in model C1 are approximately 40% of the deformations in model C2, and the push-pull deformations in model C3 are approximately 50% of the deformations in model C1. For ground motions LA37 and LA39, there is residual deformation in the push-pull connectors at the end of the ground motion: the residual deformation is largest for model C2 and smallest for model C3.

The median values of the maximum push-pull deformations up the height of the building are plotted in Fig. 4.34 for each ground motion bin. For all bins, the largest median values of maximum push-pull deformations occur in model C2, and the smallest deformations occur in model C3. The median maximum deformations in model C1 are approximately 10-50% greater than those in model C3.

The demand model defined in Equation 4.4 is used to determine the mean relationship between the maximum push-pull deformation and spectral acceleration. The plots of maximum push-pull deformation and spectral acceleration at the fundamental mode are shown in Fig. 4.35 for each story. In story 1, the maximum deformations are approximately equal between the three models, since the geometry of the spandrel panel in the first story is the same for all models. For stories 2-6, the maximum push-pull deformations in models C1 and C3 are very similar, and in stories 7-9, the maximum deformations are smaller in model C3 than in model C1. This behavior is largely due to the fact that model C3 undergoes smaller interstory drifts than model C1. As discussed previously, the maximum deformations in model C2 are much larger than the maximum deformations in models C1 and C3.

The mean values of the maximum push-pull deformations for three probabilities of exceedance are shown in Table 4.8 up the height of the building. For the 50% PE in 50 year event, the mean values are less than 0.9 inches in models C1 and C3 and less than 1.90 inches in model C2. Similar to the case of interstory drift, the maximum mean values of the push-pull deformations occur in the upper stories of the building, since these elements are drift-sensitive. The mean values of the maximum push-pull deformations in model C2 are up to 130% larger than the mean values in model C1, and the mean values in model C3 are up to 32% smaller than the mean values in model C1. For the 10% PE in 50 year event, the mean values of the maximum push-pull deformations are less than 1.3 in., 2.8 in., and 1.0 in. in models C1, C2, and C3, respectively. The mean values in model C2 are up to 150% larger than the mean values in model C1, and the mean values in model C3 are up to 37% smaller than the mean values in model C1. For the 2% PE in 50 year event, the mean values of the maximum push-pull deformations are less than 2.0 in., 4.7 in., and 1.6 in. in models C1, C2, and C3, respectively. The mean values in model C2 are up to 170% larger than the mean values in model C1, and the mean values in model C3 are up to 42% smaller than the mean values in model C1.

The performance criteria for the push-pull connectors described in Section 4.2.3 is repeated below for convenience:

- Immediate Occupancy (IO): 0.5 inches (two-thirds of the yield deformation)
- Life Safety (LS) performance: 1.25 inches (one and two-third times the yield deformation)
- Collapse Prevention (CP): 2.2 inches (deformation at maximum strength)

For the 50% PE in 50 year event, the LS performance criterion is satisfied in models C1 and C3, and the CP performance criterion is satisfied in model C2 in stories 3-9. For the 10% PE in 50 year event, the LS performance criterion is satisfied in models C1 and C3 (except for story 7 in model C1), while the CP performance criterion is exceeded in model C2 in stories 3-9. For the 2% PE in 50 year event, the CP performance criterion is satisfied in models C1 and C3, while the CP performance criterion is exceeded in model C2.

The column cover panels are connected to the adjacent spandrel panels with a single bolted connection at each of the four corners of the column cover panel. The deformation in the column cover connections occur during interstory drift as the spandrel panels move relative to one another. As interstory drift occurs, the bolts in the connections at the top of the column covers slide within the slotted hole, and for large interstory drifts, the bolt impacts the end of the slotted hole which deforms the bolt. Vertical deformation develops in the connectors as the column cover rotates due to interstory drift. The mechanics of the column cover connector deformation is discussed in detail in Chapter 5. The total deformation in a connector is equal to the vector sum of the horizontal and vertical deformations. The values of the vector sum deformations of the four connectors are approximately equal, as shown in Chapter 5.

The response history of the horizontal force in the slotted connection at the top of a column cover panel at the center of the building in story 9 is shown in Fig. 4.36 for one ground motion in each of the LA50, LA10, and LA2 bins. For the LA55 ground motion in the LA50 bin, the horizontal force spikes very few times as the bolt impacts the end of the slotted hole during the large amplitude portions of shaking. The amplitudes of force are less than 30 kips. For the LA13 ground motion in the LA10 bin, the bolt impacts the end of the slot many more times because of the higher intensity of ground shaking. The amplitudes of horizontal force in this case are up to 50 kips. For the LA31 ground motion in the LA2 bin, the bolt impacts the end of the slot many times with amplitudes up to 70 kips. The force-deformation relationship for the column cover connectors is elastic perfectly-plastic, and thus, it would be difficult to use the force in the connector as the EDP for the connector performance state. Therefore, a better choice of EDP is the connector deformation. The response-history of the vector sum deformation in a column cover connector in story 9 is shown in Fig. 4.37 for the LA55, LA13, and LA31 ground motions. For the LA55 ground motion, the connector maximum deformations are less than 0.1 inches, which is slightly less than the yield value for the connector. For the LA13 ground motion, the maximum vector sum deformation in story 9 is slightly less than 0.3 inches, which is close to the connector fracture deformation. There is also a residual deformation of 0.08 inches in the connector because the column cover does not return to its initial position after the earthquake. For the LA31 ground motion, the maximum vector sum deformation is approximately 0.47 inches, which exceeds the fracture deformation of 0.34 inches.

The median values of the maximum vector sum deformation in the column cover connectors are plotted in Fig. 4.38 up the height of the building. There is a high risk of failure of

the column cover connectors for the LA10 and LA2 bins, since the median values in these bins exceed the fracture deformations.

The demand model defined in Equation 4.4 is used to determine the trends in the mean values of maximum column cover deformations up the height of the building. In Fig. 4.39, the maximum column cover deformations are plotted against the spectral acceleration at the fundamental period of the building. The mean value conditioned on the spectral acceleration is plotted as a line in the log-log EDP-IM space. The data shows that in log-log space there is significant dispersion in the maximum values of deformation for very low spectral accelerations and very little dispersion for higher levels of spectral acceleration. The mean values of maximum column cover deformation are calculated using the demand model in Equation 4.4 for the three probabilities of exceedance, as shown in Table 4.9. The performance criteria for the column cover connectors described in Section 4.2.3 is repeated below for convenience:

- Immediate Occupancy (IO): 0.06 inches (half of the yield deformation)
- Life Safety (LS) performance: 0.12 inches (the yield deformation)
- Collapse Prevention (CP): 0.25 inches (twice the yield deformation)

For the 50% PE in 50 year event, the LS performance criterion is satisfied in all stories, for the 10% PE in 50 year event, the CP performance criterion is satisfied in all stories, and for the 2% PE in 50 year event, the CP performance criterion is exceeded in all stories.

The results of the time-history show that the interstory drifts in the moment-frame cause significant deformations in the push-pull connectors and the column cover connectors. These connections are the most critical because the stiffness and strength of the other connections (vertical bearing connections and rigid lateral connections) are large enough that they do not deform or become significantly damaged.

Table 4.1 Modal periods of bare frame and models with cladding

Model	Period (sec.)		
	Mode 1	Mode 2	Mode 3
BF	2.13	0.80	0.46
C1	2.11	0.79	0.45
C2	2.05	0.76	0.44
C3	2.09	0.77	0.44
C3 with caulk	2.05	0.76	0.43

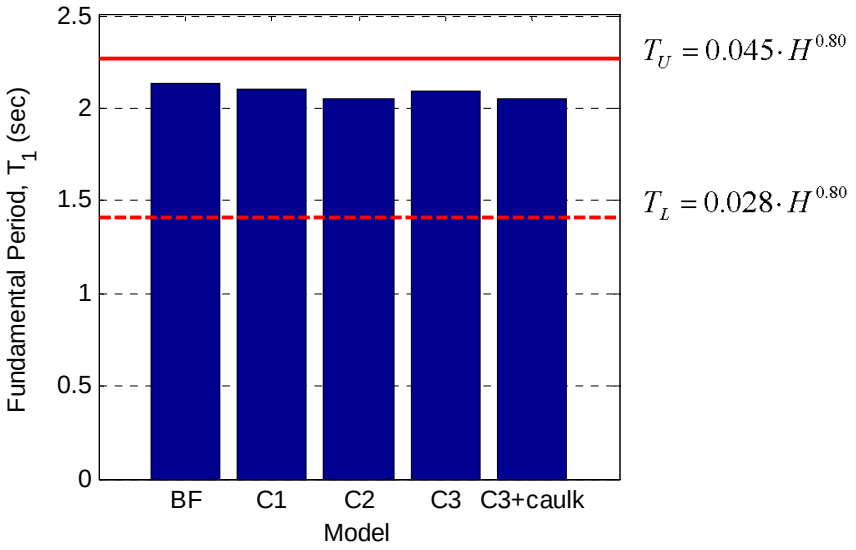

Fig. 4.1 Comparison of first mode period for different cladding systems to the measured upper and lower bounds by Goel and Chopra (1997)

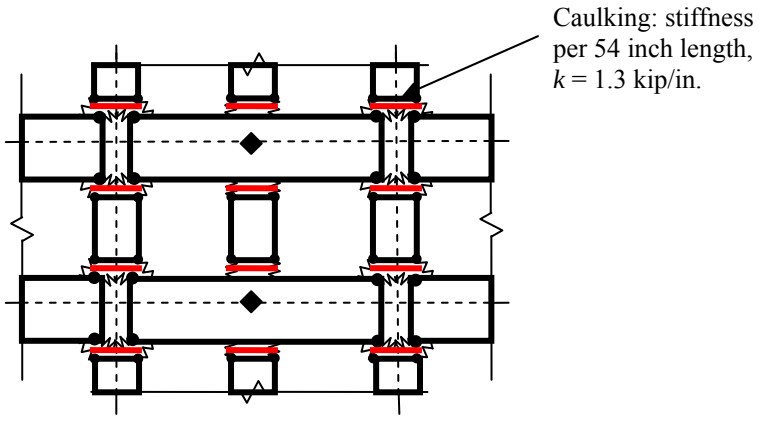

Fig. 4.2 Cladding system type C3 shown with caulking between the column covers and spandrel panels

Table 4.2 Effective modal mass percentages

Model	Effective Modal Mass Percentage (%)		
	Mode 1	Mode 2	Mode 3
BF	81.3	12.0	4.4
C1	81.8	11.9	4.3
C2	82.7	11.5	4.0
C3	81.6	11.9	4.3

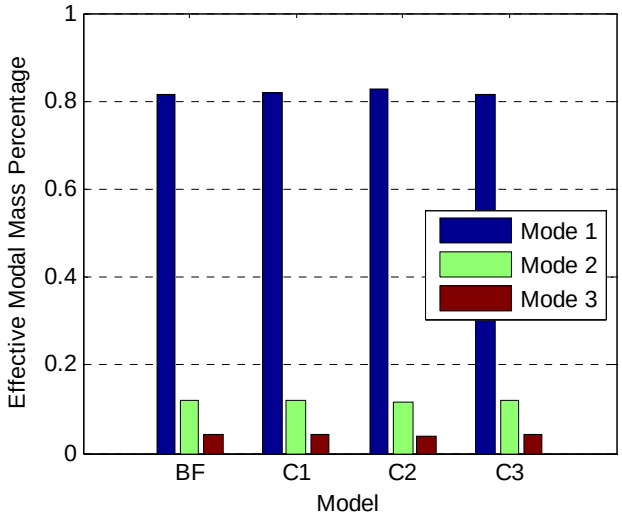

Fig. 4.3 Comparison of effective modal mass percentages for the first three modes

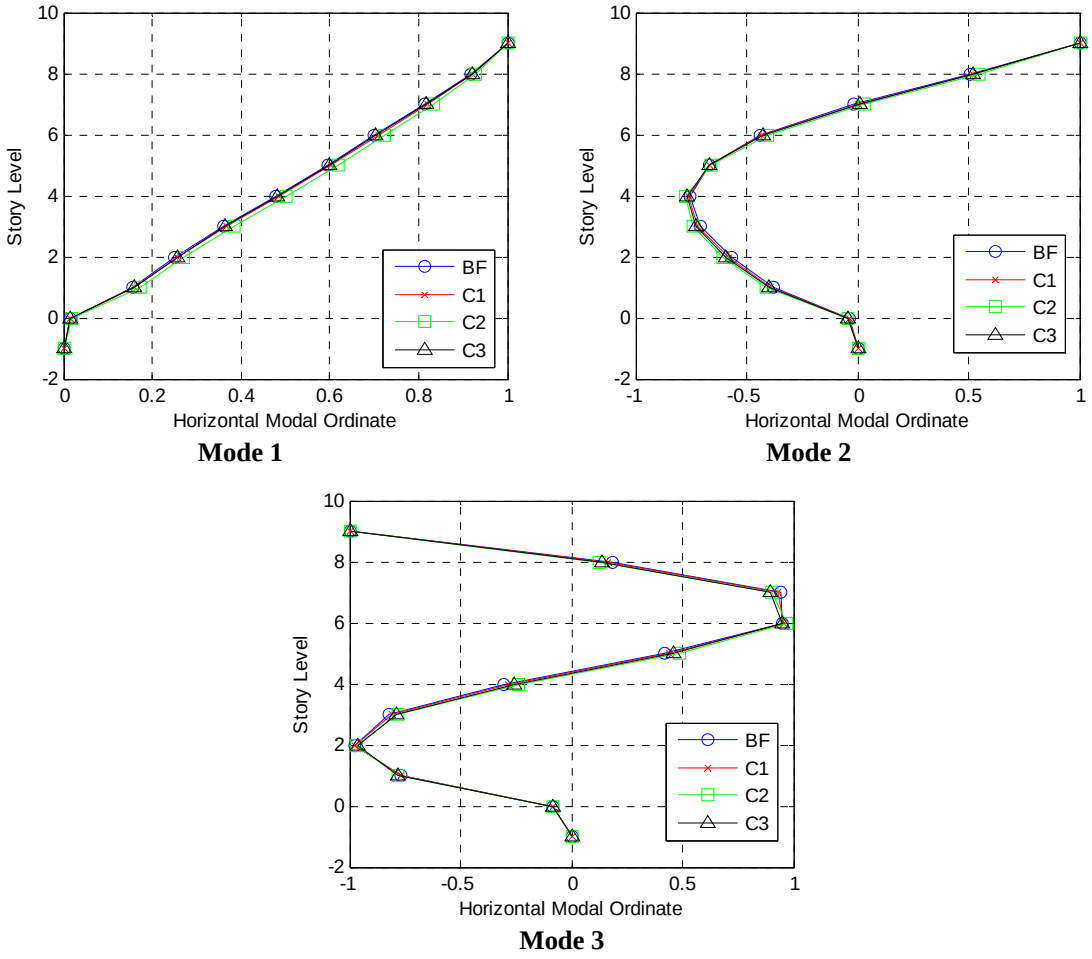

Fig. 4.4 Comparison of mode shapes for the first three modes

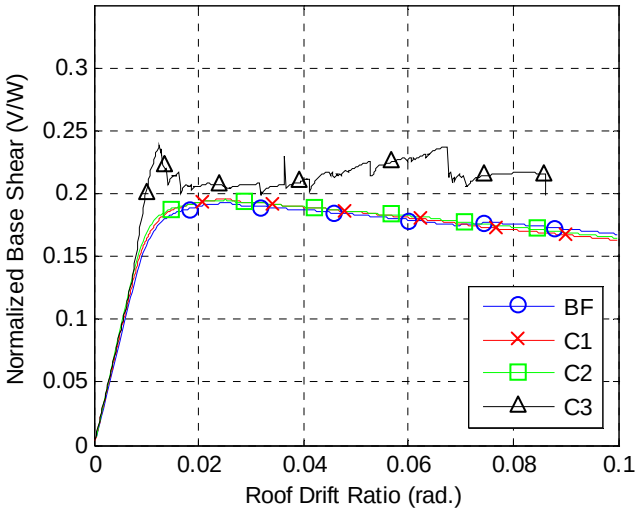

Fig. 4.5 Comparison of static pushover curve for different cladding systems

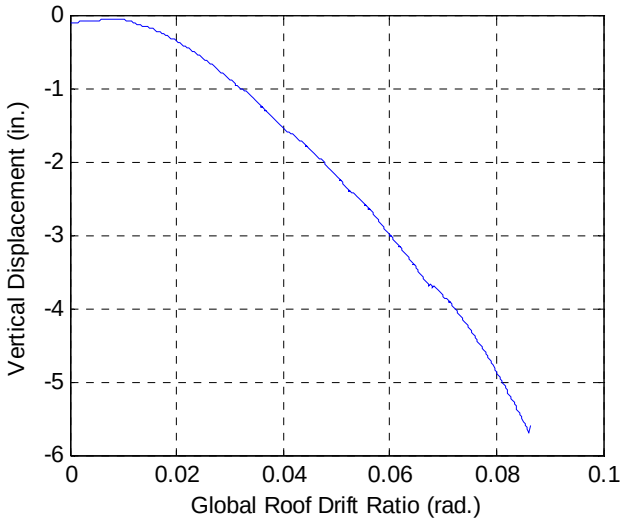

Fig. 4.6 Building shortening of Model C3 during pushover analysis

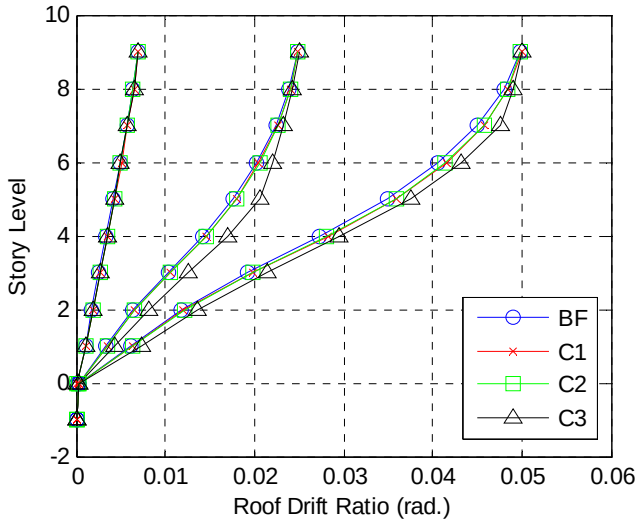

Fig. 4.7 Deflected shape during pushover analysis at roof drift ratios of 0.7%, 2.5%, and 5%

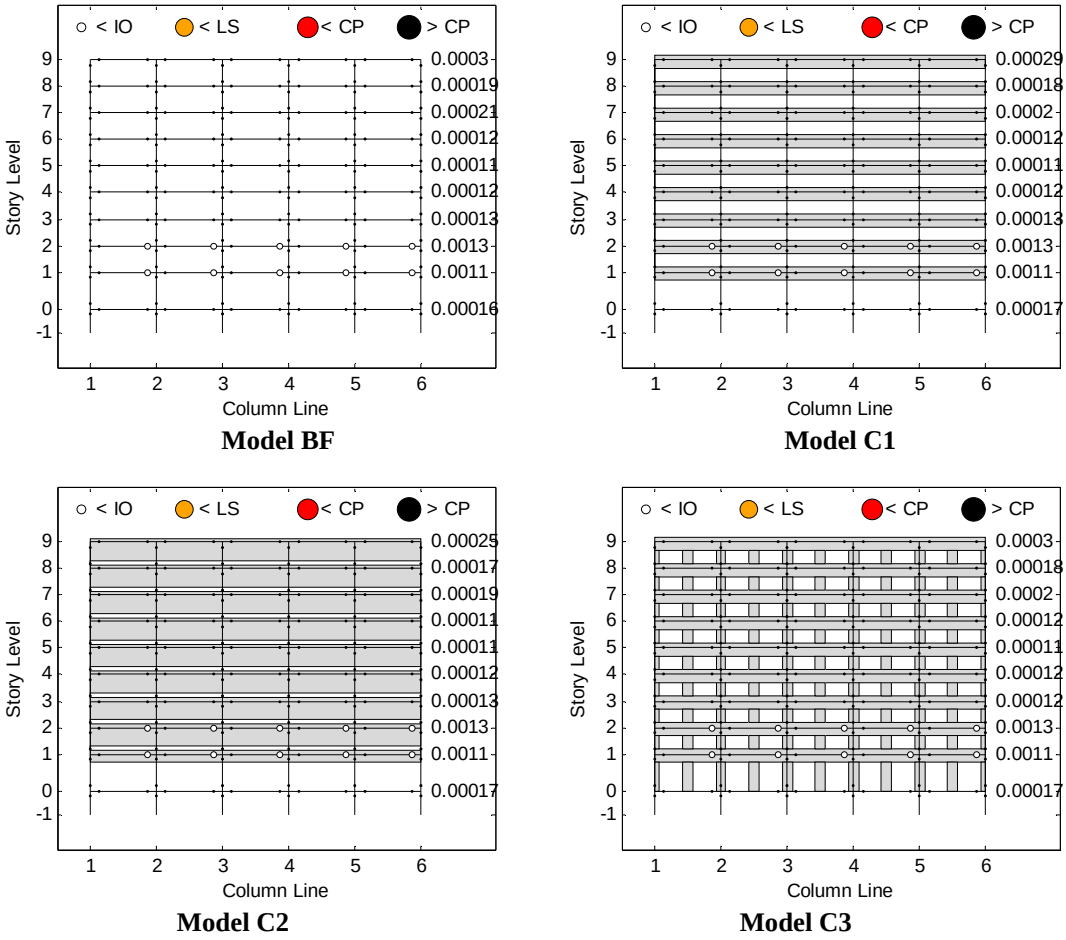

Fig. 4.8 Beam/column plastic hinge demands at 0.7% roof drift

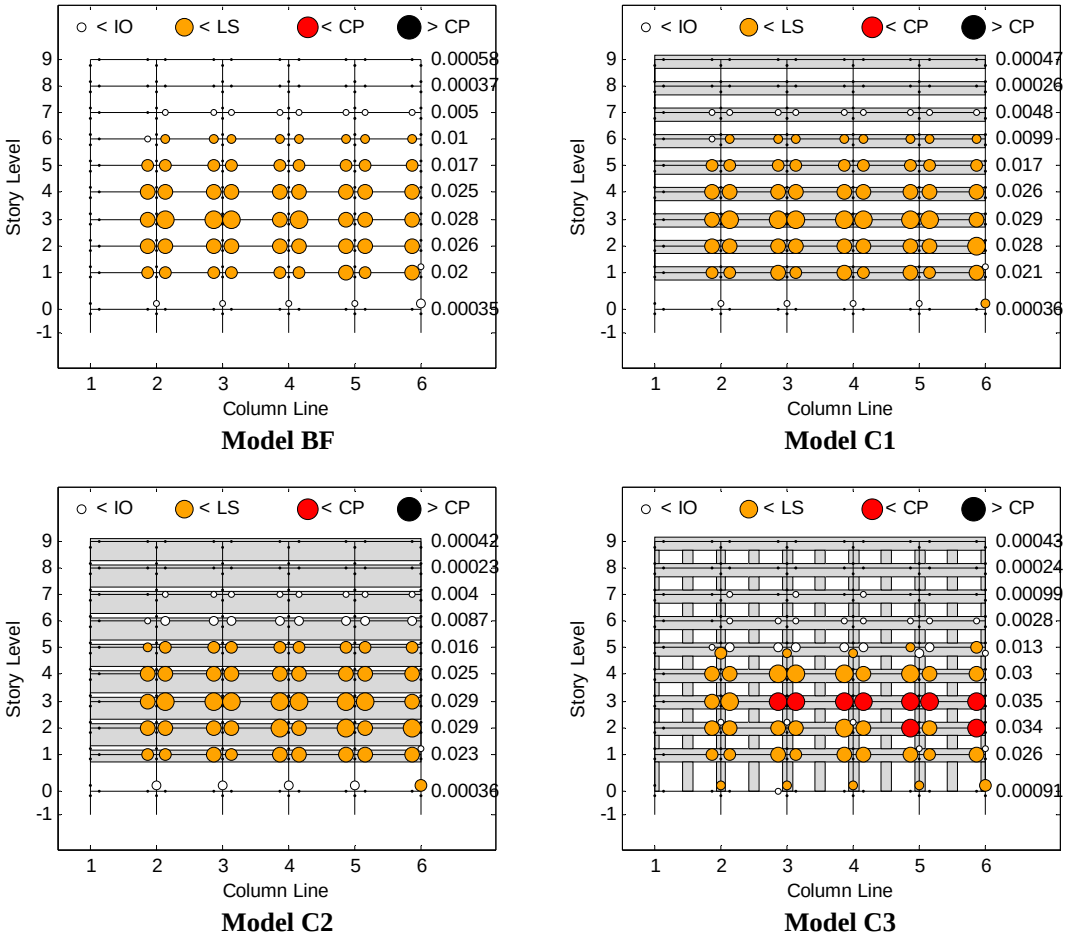

Fig. 4.9 Beam/column plastic hinge demands at 2.5% roof drift

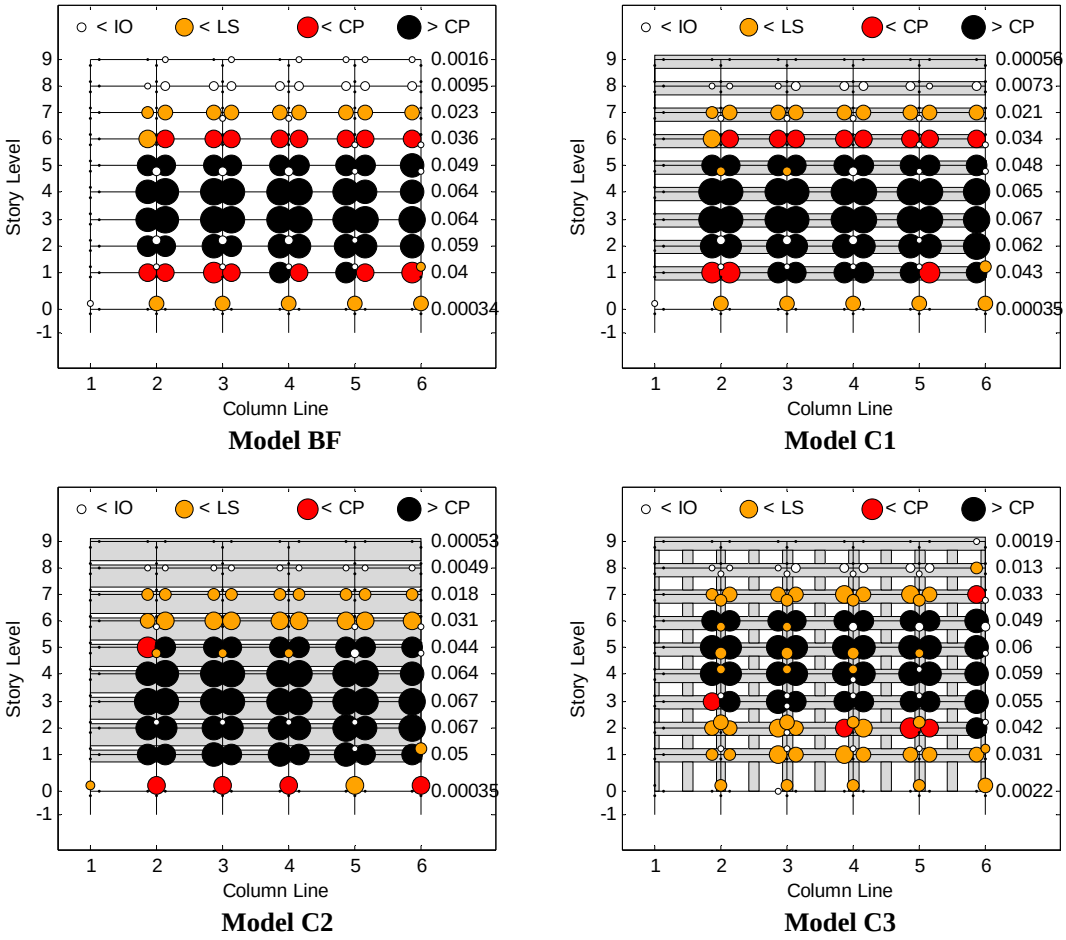

Fig. 4.10 Beam/column plastic hinge demands at 5% roof drift

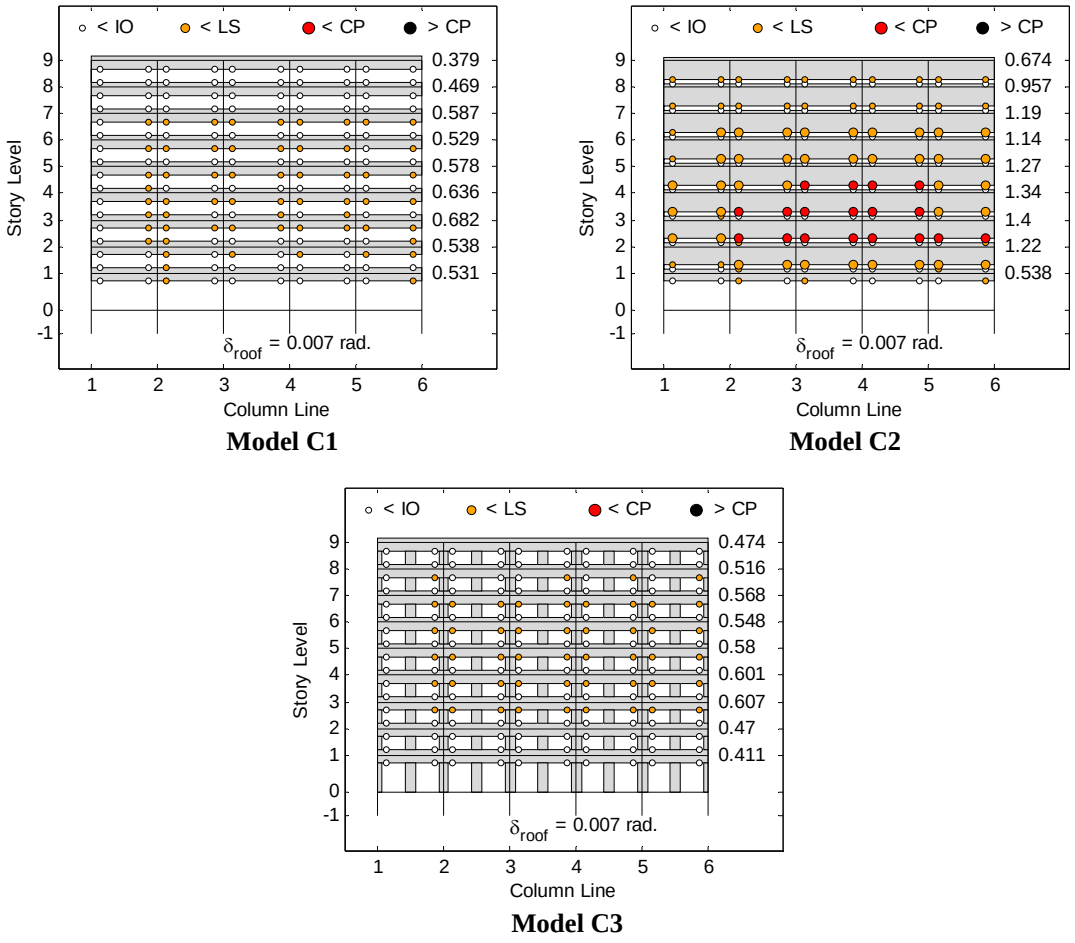

Fig. 4.11 Push-pull connector deformations at 0.7% roof drift

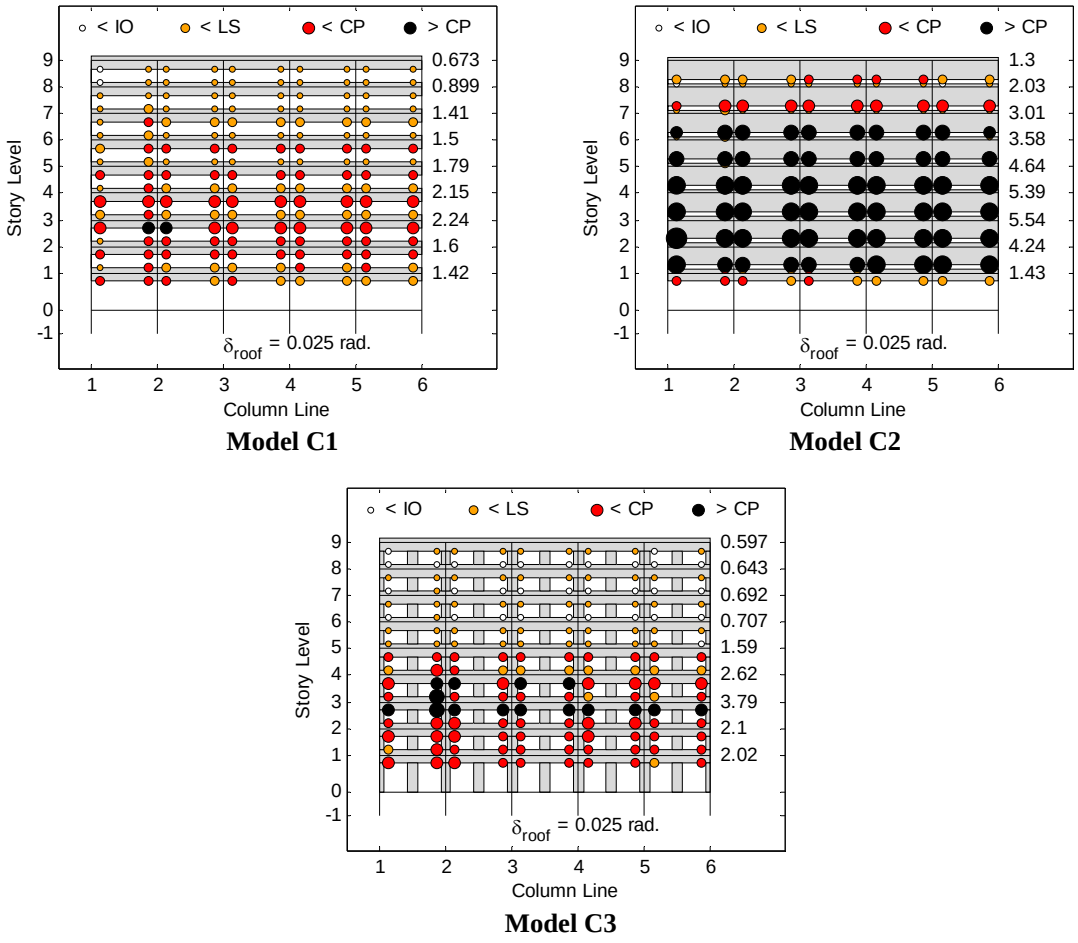

Fig. 4.12 Push-pull connector deformations at 2.5% roof drift

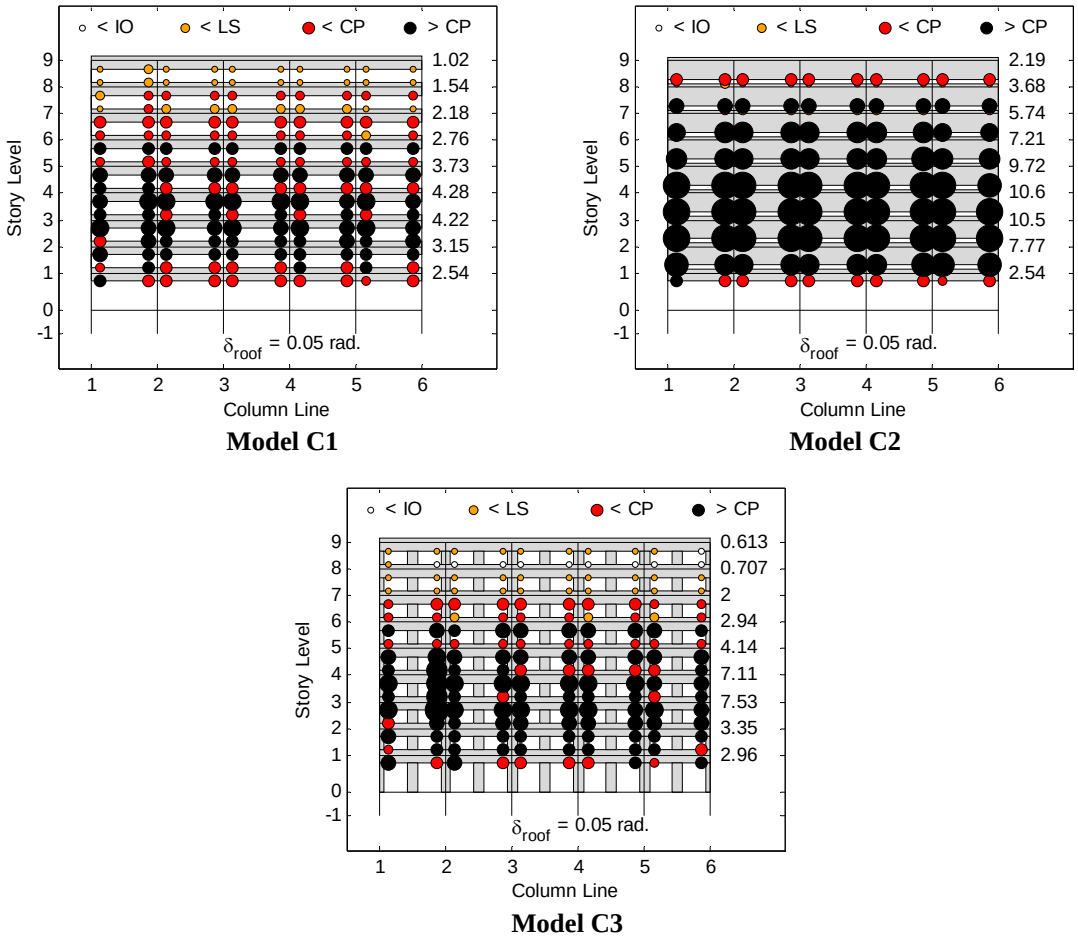

Fig. 4.13 Push-pull connector deformations at 5% roof drift

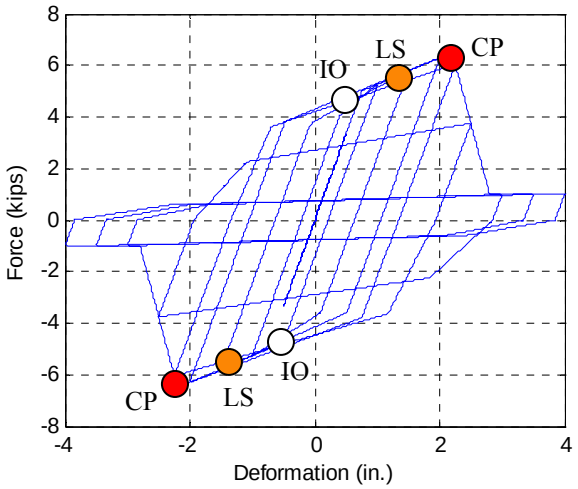

Fig. 4.14 Performance states of the push-pull connectors on the force-deformation curve

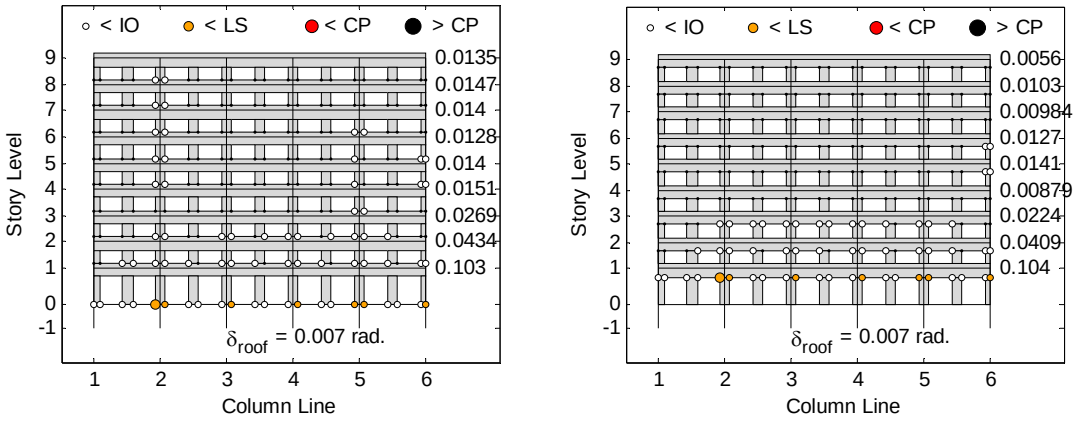

Bottom connectors **Top connectors**

Fig. 4.15 Column cover connector deformations at 0.7% roof drift

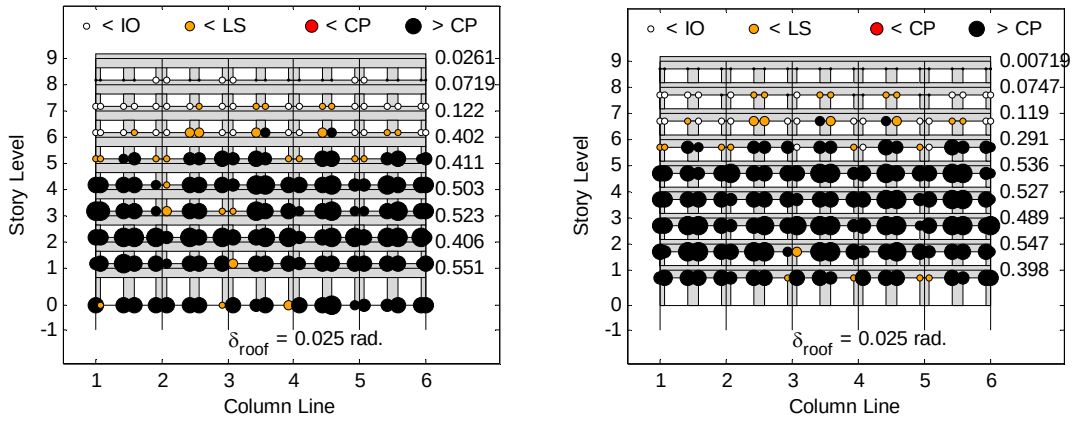

Bottom connectors **Top connectors**

Fig. 4.16 Column cover connector deformations at 2.5% roof drift

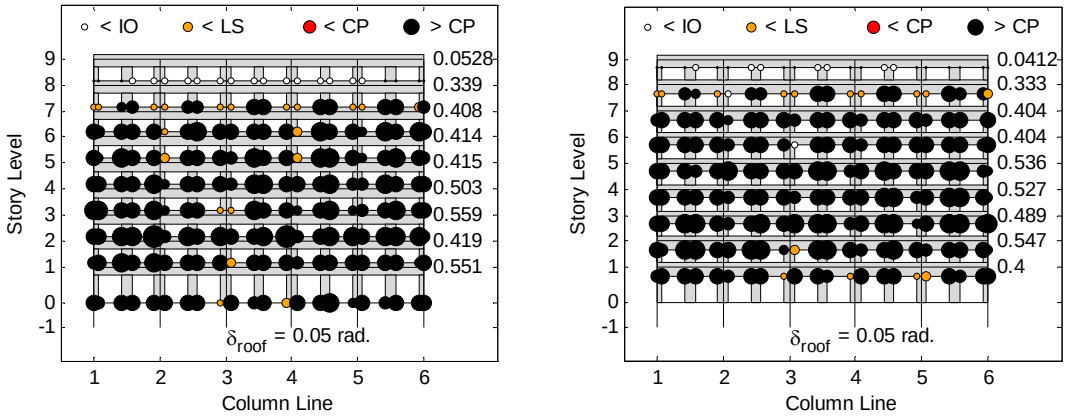

Fig. 4.17 Column cover connector deformations at 5% roof drift

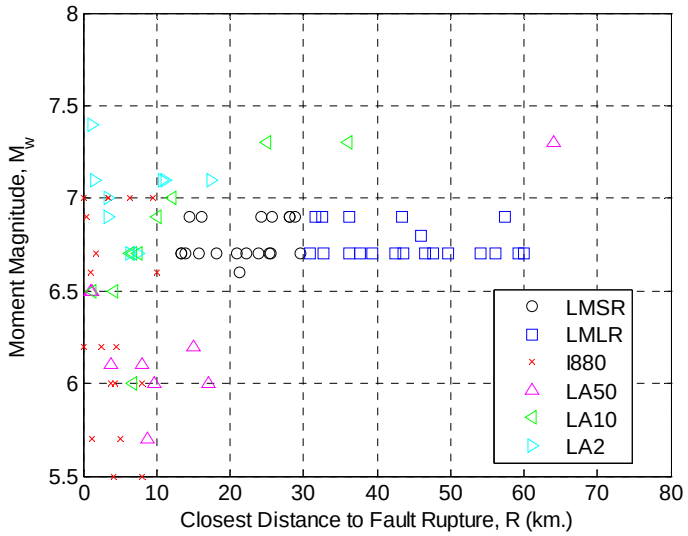

Fig. 4.18 Magnitude-distance bins for the selected suites of ground motions

Table 4.3 Scaling factors for ground motion bins

Bin	Scale Factor
LMSR	2.0
LMLR	2.0
I880-N	1.5
I880-P	1.5
SAC 50% PE in 50 yrs	1.0
SAC 10% PE in 50 yrs	1.0
SAC 2% PE in 50 yrs	1.0

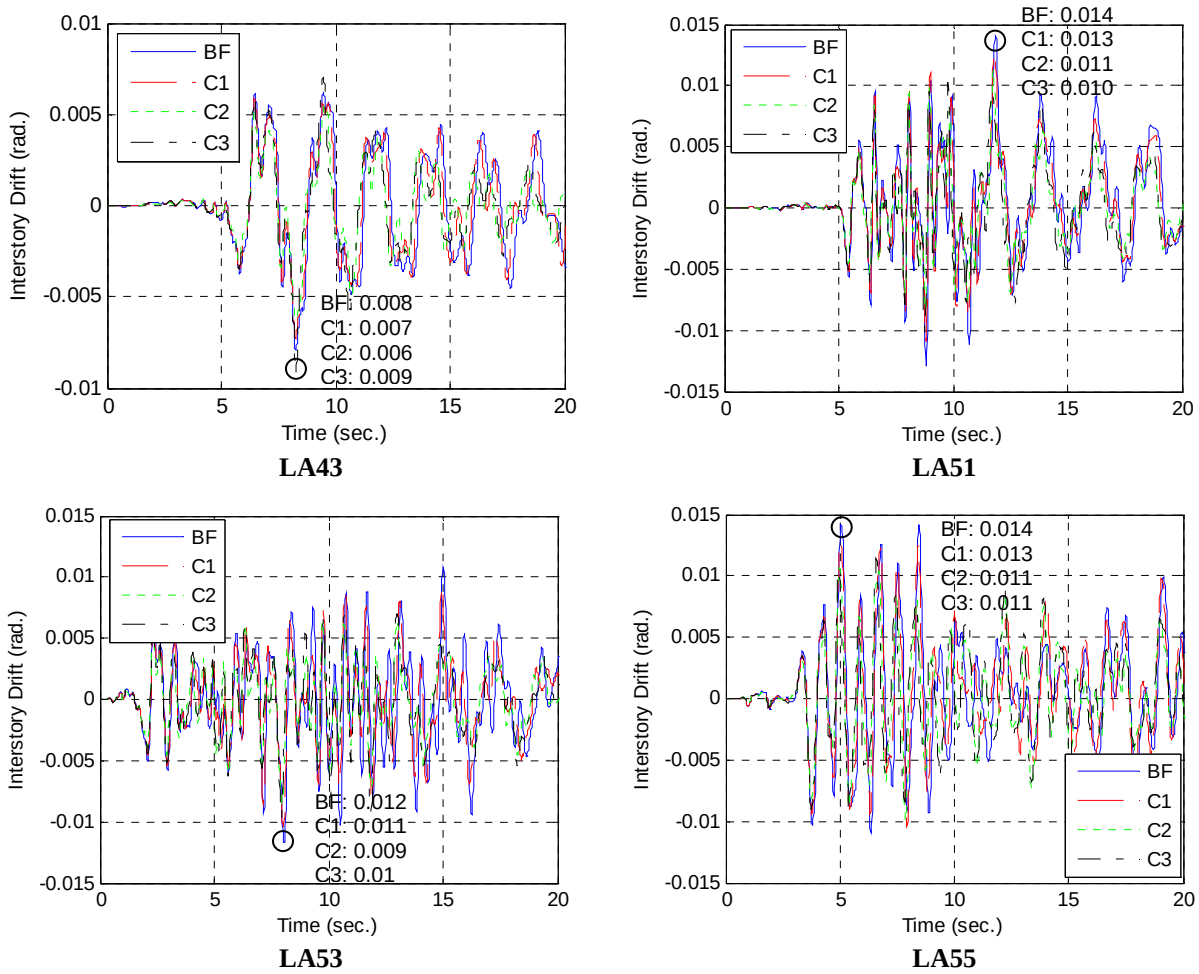

LA43 **LA51**

LA53 **LA55**

Fig. 4.19 Comparison of interstory drift ratios at story 9 for select ground motions in the LA50 bin

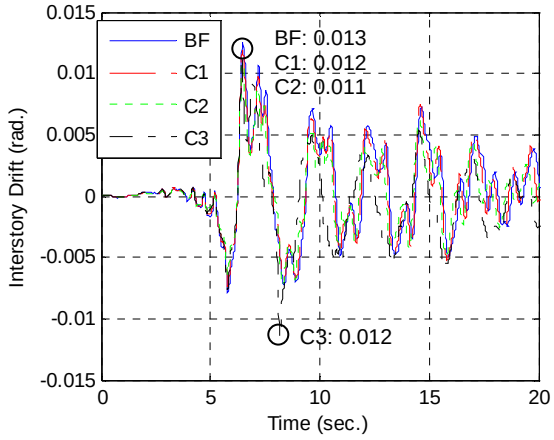

LA05

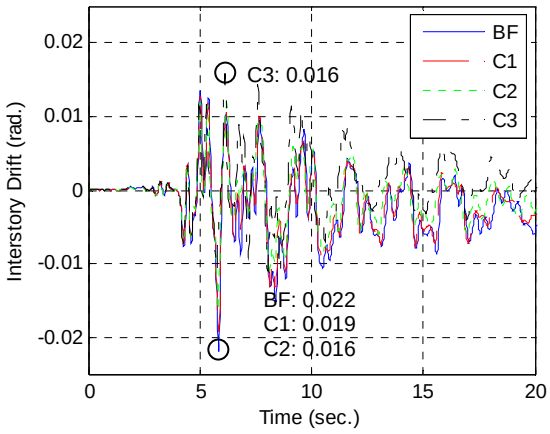

LA13

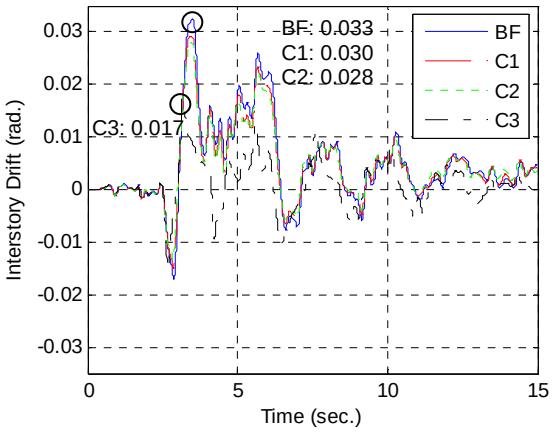

LA16

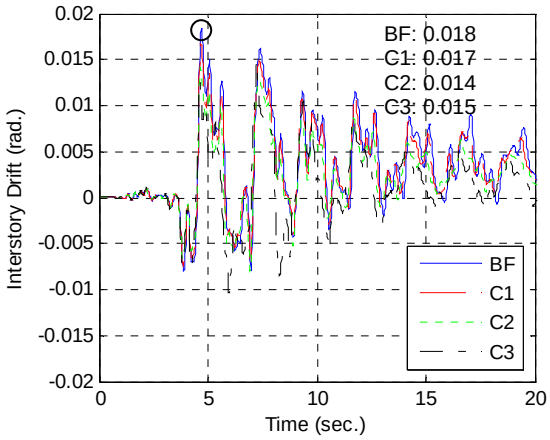

LA17

Fig. 4.20 Comparison of interstory drift ratios at story 9 for select ground motions in the LA10 bin

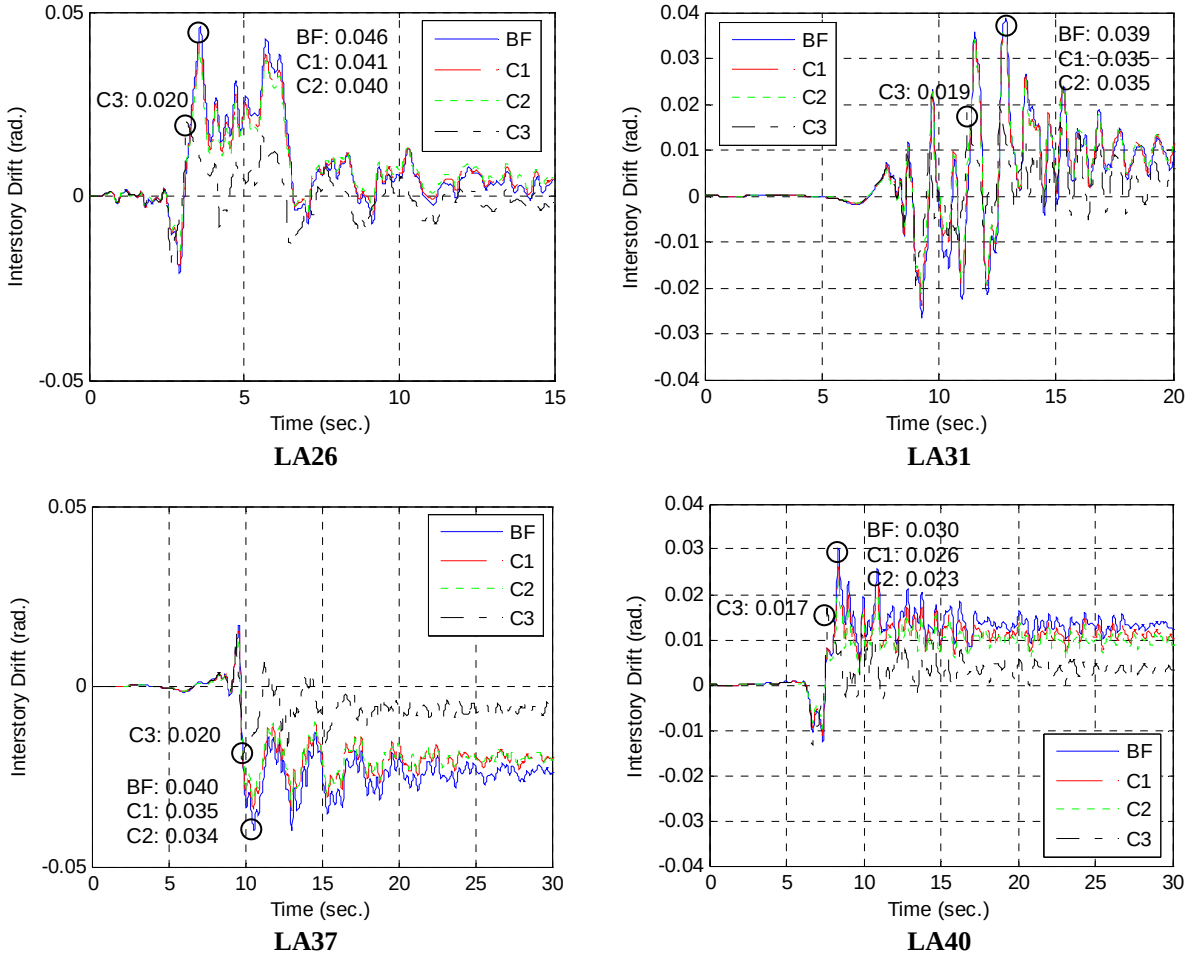

Fig. 4.21 Comparison of interstory drift ratios at story 9 for select ground motions in the LA2 bin

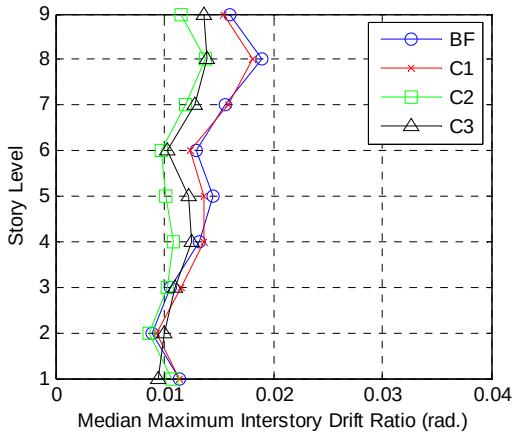

LMSR

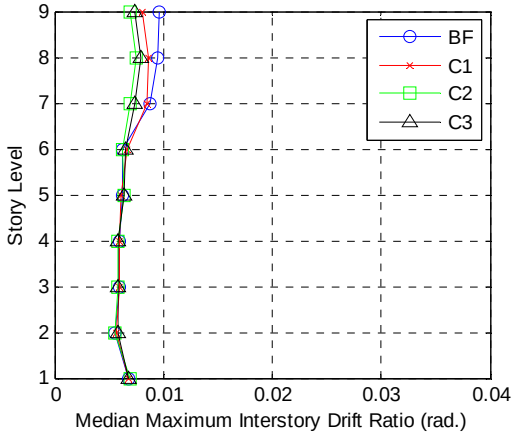

LMLR

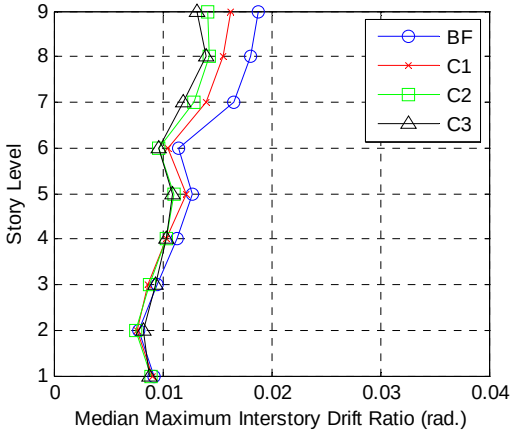

I880-N

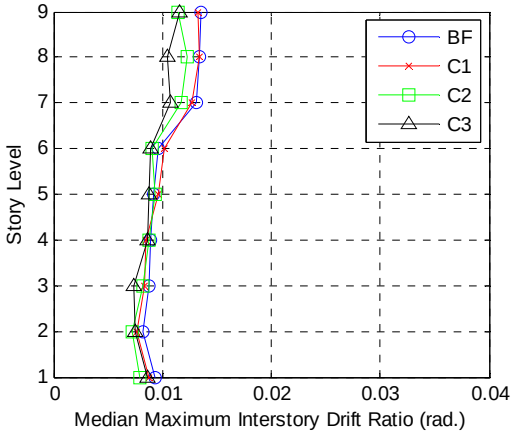

I880-P

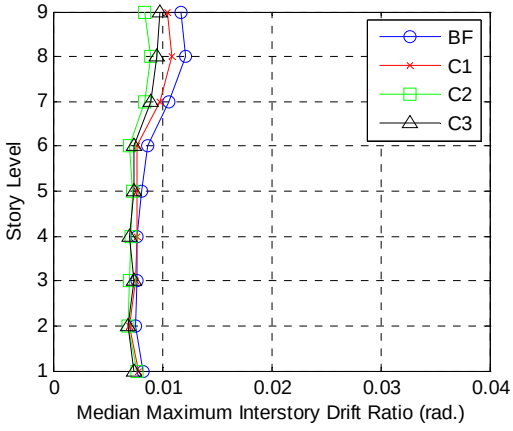

LA50

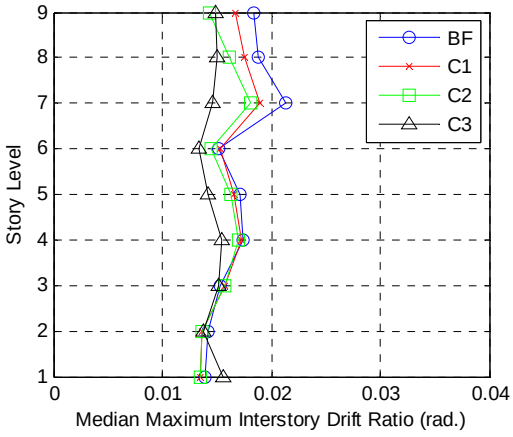

LA10

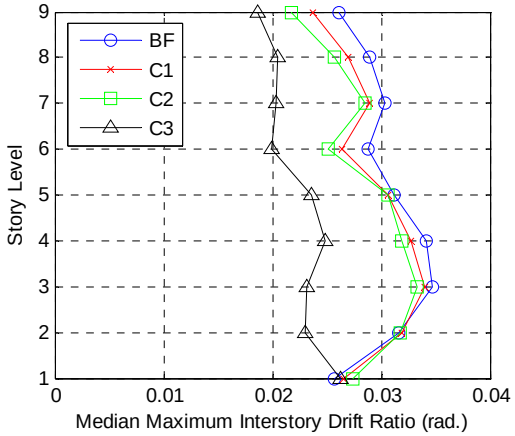

Fig. 4.22 Comparison of median peak interstory drift profiles for different earthquake bins

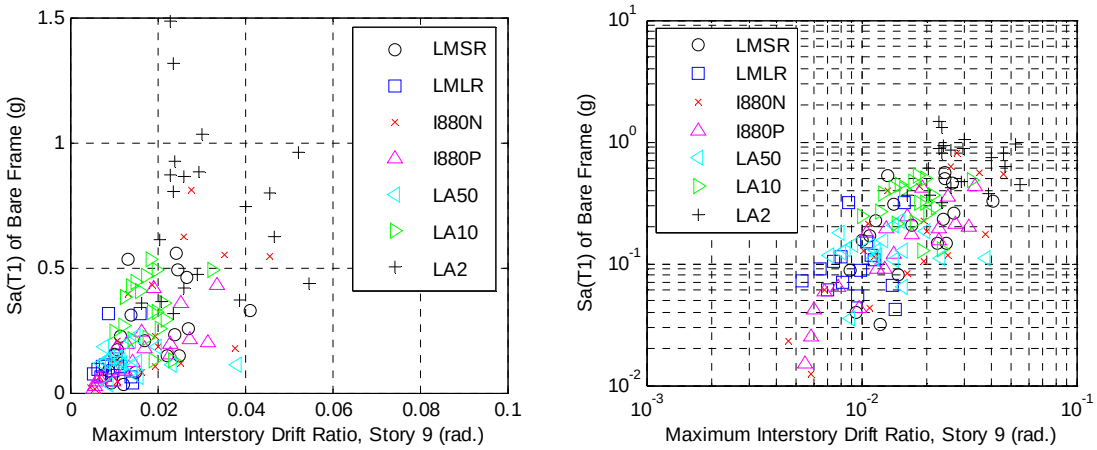

Fig. 4.23 Maximum interstory drift ratios for the bare frame (BF) model (left: linear scale, right: logarithmic scale)

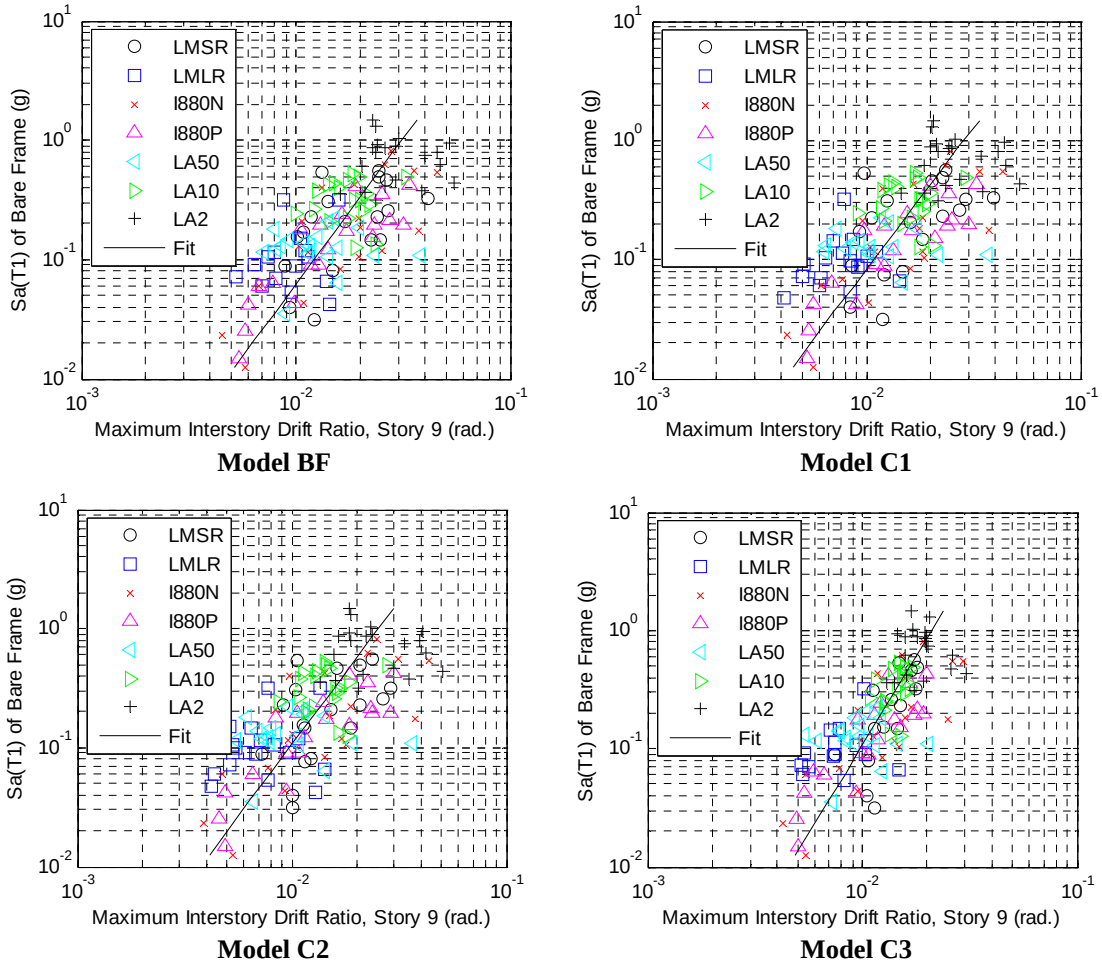

Fig. 4.24 Maximum interstory drift ratios in story 9 for different models

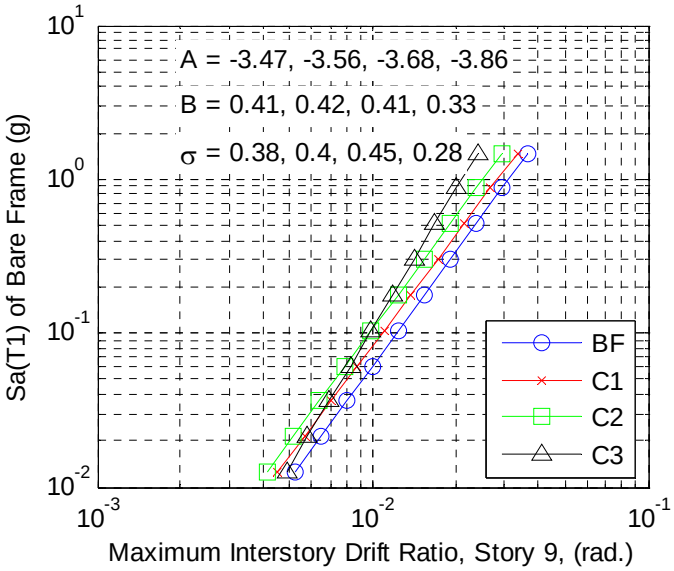

Fig. 4.25 Comparison of linear regression fit of maximum interstory drift ratio in story 9

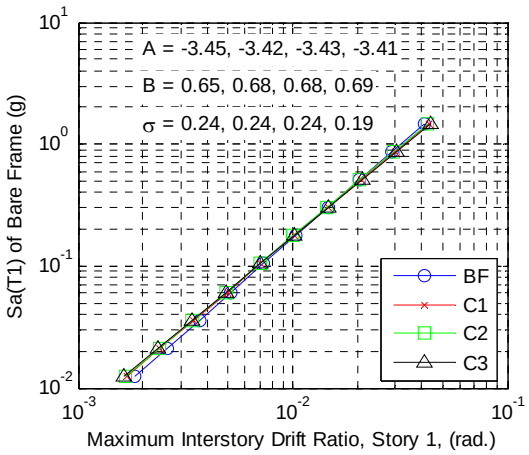
A = -3.45, -3.42, -3.43, -3.41
B = 0.65, 0.68, 0.68, 0.69
σ = 0.24, 0.24, 0.24, 0.19
BF
C1
C2
C3
Sa(T1) of Bare Frame (g)
Maximum Interstory Drift Ratio, Story 1, (rad.)

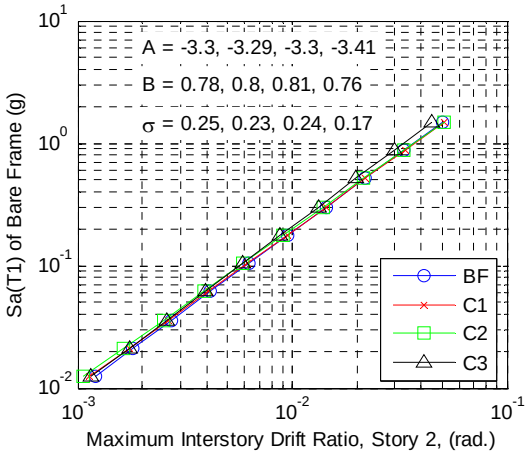
A = -3.3, -3.29, -3.3, -3.41
B = 0.78, 0.8, 0.81, 0.76
σ = 0.25, 0.23, 0.24, 0.17
BF
C1
C2
C3
Sa(T1) of Bare Frame (g)
Maximum Interstory Drift Ratio, Story 2, (rad.)

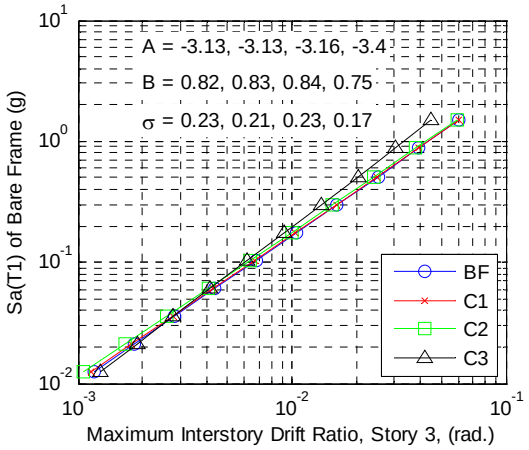
A = -3.13, -3.13, -3.16, -3.4
B = 0.82, 0.83, 0.84, 0.75
σ = 0.23, 0.21, 0.23, 0.17
BF
C1
C2
C3
Sa(T1) of Bare Frame (g)
Maximum Interstory Drift Ratio, Story 3, (rad.)

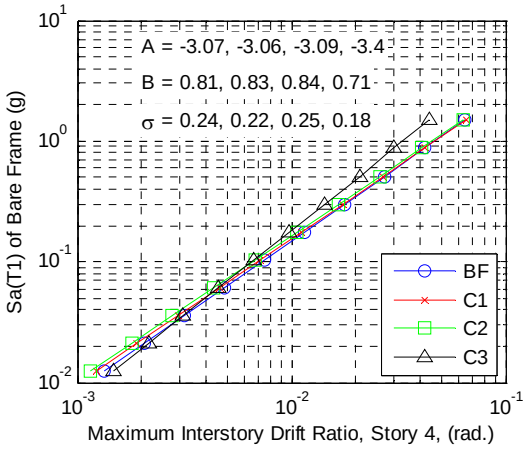
A = -3.07, -3.06, -3.09, -3.4
B = 0.81, 0.83, 0.84, 0.71
σ = 0.24, 0.22, 0.25, 0.18
BF
C1
C2
C3
Sa(T1) of Bare Frame (g)
Maximum Interstory Drift Ratio, Story 4, (rad.)

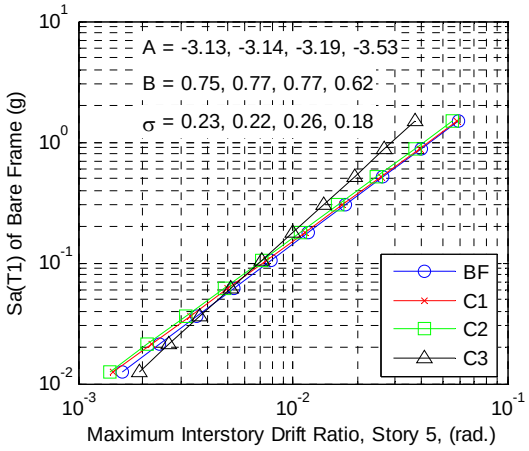
A = -3.13, -3.14, -3.19, -3.53
B = 0.75, 0.77, 0.77, 0.62
σ = 0.23, 0.22, 0.26, 0.18
BF
C1
C2
C3
Sa(T1) of Bare Frame (g)
Maximum Interstory Drift Ratio, Story 5, (rad.)

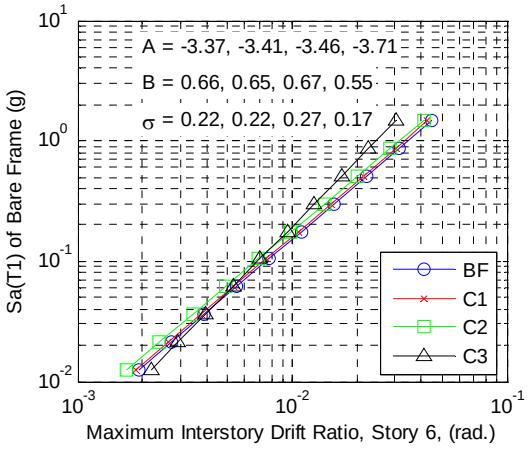
A = -3.37, -3.41, -3.46, -3.71
B = 0.66, 0.65, 0.67, 0.55
σ = 0.22, 0.22, 0.27, 0.17
BF
C1
C2
C3
Sa(T1) of Bare Frame (g)
Maximum Interstory Drift Ratio, Story 6, (rad.)

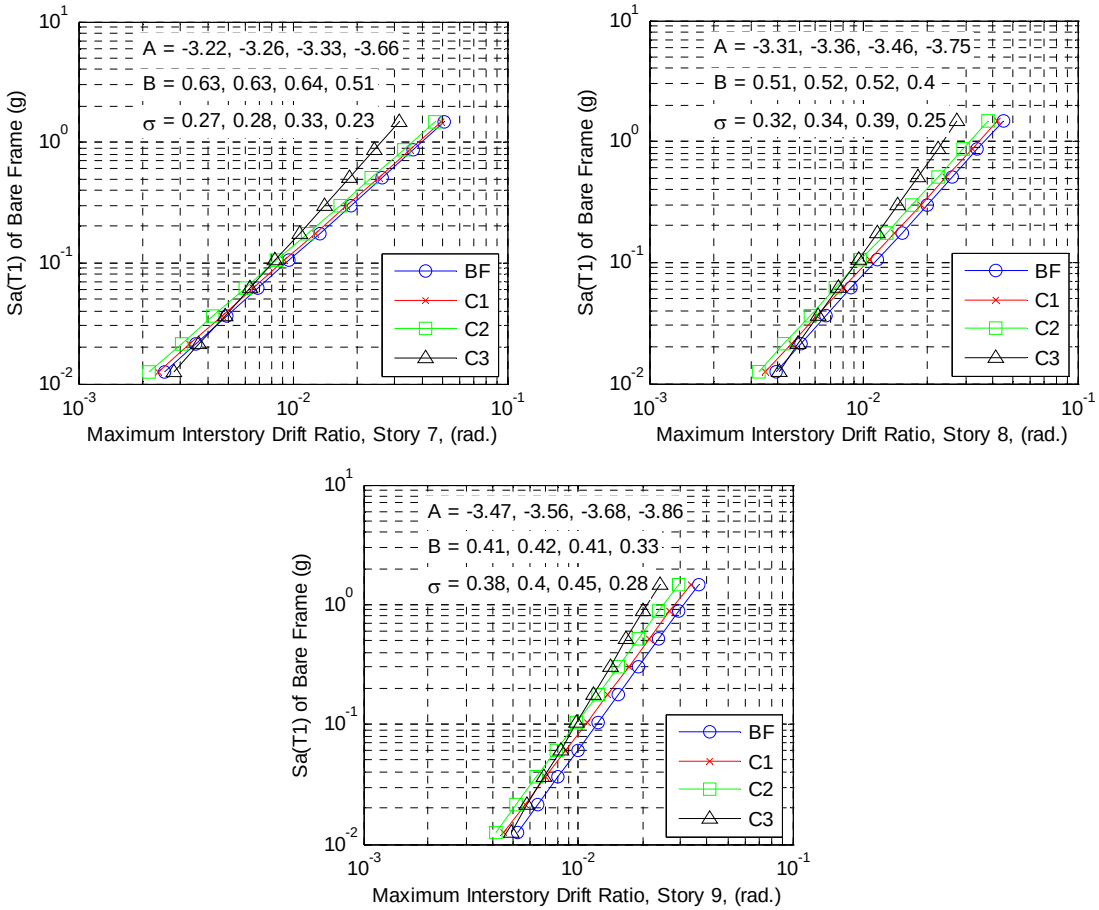

Fig. 4.26 Comparison of maximum interstory drifts for different story levels

Table 4.4 Mean maximum drift ratios for three probabilities of exceedance

Story	Model	Hazard Level					
		50% PE in 50 yrs $Sa(T_1) = 0.11g$		10% PE in 50 yrs $Sa(T_1) = 0.34g$		2% PE in 50 yrs $Sa(T_1) = 0.65g$	
		Maximum Drift Ratio (rad.)	% Difference from Model BF	Maximum Drift Ratio (rad.)	% Difference from Model BF	Maximum Drift Ratio (rad.)	% Difference from Model BF
1	BF	0.0093	-	0.0152	-	0.0240	-
	C1	0.0091	-2.2	0.0152	0.0	0.0245	2.1
	C2	0.0090	-3.2	0.0150	-1.3	0.0241	0.4
	C3	0.0090	-3.2	0.0152	0.0	0.0247	2.9
2	BF	0.0084	-	0.0151	-	0.0263	-
	C1	0.0083	-1.2	0.0151	0.0	0.0266	1.1
	C2	0.0079	-6.0	0.0147	-2.6	0.0260	-1.1
	C3	0.0078	-7.1	0.0138	-8.6	0.0238	-9.5
3	BF	0.0092	-	0.0171	-	0.0306	-
	C1	0.0090	-2.2	0.0169	-1.2	0.0305	-0.3
	C2	0.0086	-6.5	0.0163	-4.7	0.0296	-3.3
	C3	0.0081	-12.0	0.0143	-16.4	0.0243	-20.6
4	BF	0.0100	-	0.0185	-	0.0329	-
	C1	0.0097	-3.0	0.0182	-1.6	0.0328	-0.3
	C2	0.0092	-8.0	0.0174	-5.9	0.0316	-4.0
	C3	0.0086	-14.0	0.0148	-20.0	0.0245	-25.5
5	BF	0.0105	-	0.0185	-	0.0316	-
	C1	0.0100	-4.8	0.0179	-3.2	0.0310	-1.9
	C2	0.0095	-9.5	0.0171	-7.6	0.0295	-6.6
	C3	0.0090	-14.3	0.0144	-22.2	0.0224	-29.1
6	BF	0.0100	-	0.0164	-	0.0260	-
	C1	0.0095	-5.0	0.0157	-4.3	0.0249	-4.2
	C2	0.0089	-11.0	0.0147	-10.4	0.0235	-9.6
	C3	0.0086	-14.0	0.0131	-20.1	0.0193	-25.8
7	BF	0.0121	-	0.0195	-	0.0304	-
	C1	0.0115	-5.0	0.0186	-4.6	0.0292	-3.9
	C2	0.0106	-12.4	0.0172	-11.8	0.0271	-10.9
	C3	0.0099	-18.2	0.0145	-25.6	0.0207	-31.9
8	BF	0.0139	-	0.0205	-	0.0294	-
	C1	0.0128	-7.9	0.0191	-6.8	0.0276	-6.1
	C2	0.0118	-15.1	0.0174	-15.1	0.0251	-14.6
	C3	0.0109	-21.6	0.0148	-27.8	0.0197	-33.0
9	BF	0.0143	-	0.0195	-	0.0261	-
	C1	0.0128	-10.5	0.0176	-9.7	0.0237	-9.2
	C2	0.0115	-19.6	0.0157	-19.5	0.0211	-19.2
	C3	0.0112	-21.7	0.0144	-26.2	0.0182	-30.3

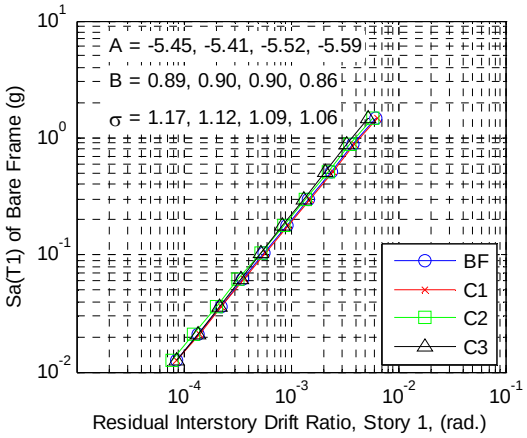
A = -5.45, -5.41, -5.52, -5.59
B = 0.89, 0.90, 0.90, 0.86
σ = 1.17, 1.12, 1.09, 1.06
BF
C1
C2
C3
Sa(T1) of Bare Frame (g)
Residual Interstory Drift Ratio, Story 1, (rad.)

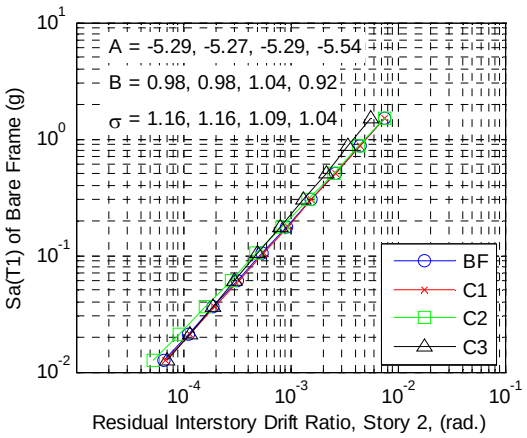
A = -5.29, -5.27, -5.29, -5.54
B = 0.98, 0.98, 1.04, 0.92
σ = 1.16, 1.16, 1.09, 1.04
BF
C1
C2
C3
Sa(T1) of Bare Frame (g)
Residual Interstory Drift Ratio, Story 2, (rad.)

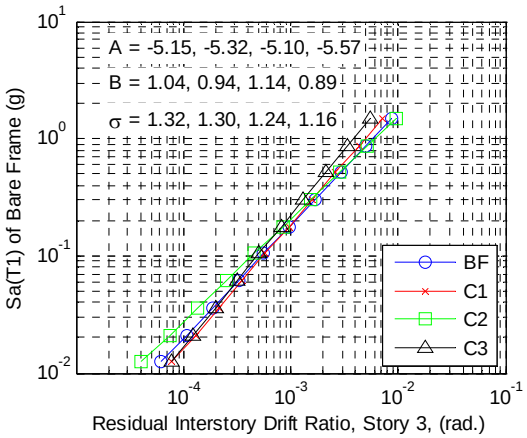
A = -5.15, -5.32, -5.10, -5.57
B = 1.04, 0.94, 1.14, 0.89
σ = 1.32, 1.30, 1.24, 1.16
BF
C1
C2
C3
Sa(T1) of Bare Frame (g)
Residual Interstory Drift Ratio, Story 3, (rad.)

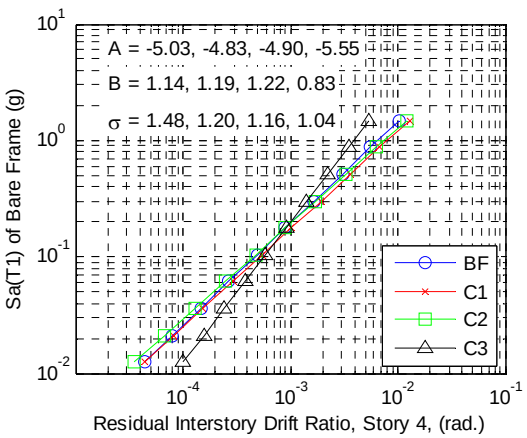
A = -5.03, -4.83, -4.90, -5.55
B = 1.14, 1.19, 1.22, 0.83
σ = 1.48, 1.20, 1.16, 1.04
BF
C1
C2
C3
Sa(T1) of Bare Frame (g)
Residual Interstory Drift Ratio, Story 4, (rad.)

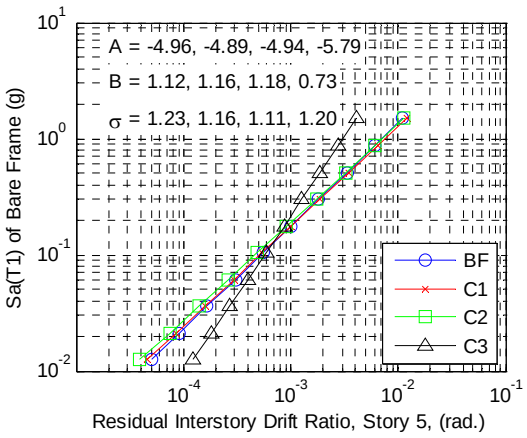
A = -4.96, -4.89, -4.94, -5.79
B = 1.12, 1.16, 1.18, 0.73
σ = 1.23, 1.16, 1.11, 1.20
BF
C1
C2
C3
Sa(T1) of Bare Frame (g)
Residual Interstory Drift Ratio, Story 5, (rad.)

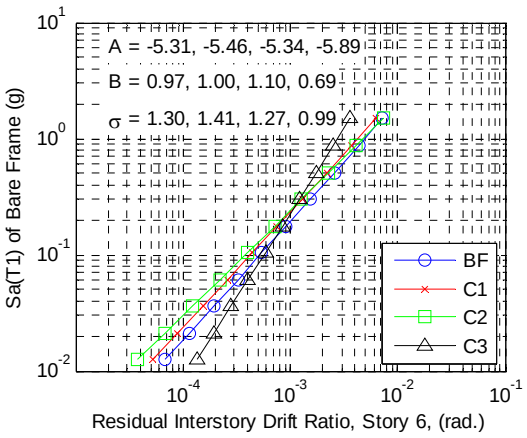
A = -5.31, -5.46, -5.34, -5.89
B = 0.97, 1.00, 1.10, 0.69
σ = 1.30, 1.41, 1.27, 0.99
BF
C1
C2
C3
Sa(T1) of Bare Frame (g)
Residual Interstory Drift Ratio, Story 6, (rad.)

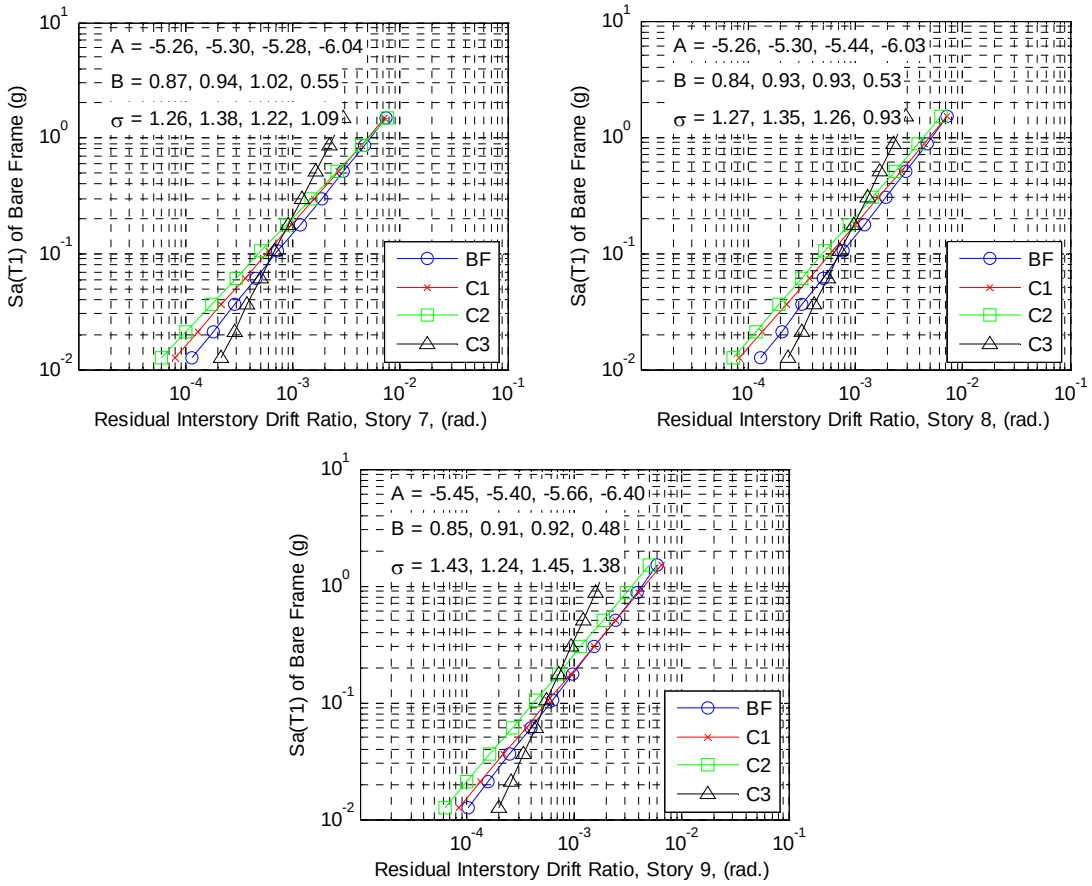

Fig. 4.27 Comparison of linear regression fit of maximum residual interstory drift ratio

Table 4.5 Mean residual drift ratios for three probabilities of exceedance

Story	Model	Hazard Level					
		50% PE in 50 yrs $Sa(T_1) = 0.11g$		10% PE in 50 yrs $Sa(T_1) = 0.34g$		2% PE in 50 yrs $Sa(T_1) = 0.65g$	
		Residual Drift Ratio (rad.)	% Difference from Model BF	Residual Drift Ratio (rad.)	% Difference from Model BF	Residual Drift Ratio (rad.)	% Difference from Model BF
1	BF	0.0008	-	0.0016	-	0.0029	-
	C1	0.0008	0.0	0.0016	0.0	0.0030	3.4
	C2	0.0007	-12.5	0.0014	-12.5	0.0027	-6.9
	C3	0.0007	-12.5	0.0014	-12.5	0.0026	-10.3
2	BF	0.0008	-	0.0016	-	0.0033	-
	C1	0.0008	0.0	0.0017	6.2	0.0034	3.0
	C2	0.0007	-12.5	0.0017	6.2	0.0032	-3.0
	C3	0.0007	-12.5	0.0014	-12.5	0.0027	-18.2
3	BF	0.0008	-	0.0018	-	0.0037	-
	C1	0.0008	0.0	0.0017	-5.6	0.0033	-10.8
	C2	0.0007	-12.5	0.0017	-5.6	0.0037	0.0
	C3	0.0007	-12.5	0.0014	-22.2	0.0026	-29.7
4	BF	0.0007	-	0.0018	-	0.0040	-
	C1	0.0008	14.3	0.0021	16.7	0.0048	20.0
	C2	0.0007	0.0	0.0019	5.6	0.0044	10.0
	C3	0.0008	14.3	0.0015	-16.7	0.0027	-32.5
5	BF	0.0008	-	0.0019	-	0.0043	-
	C1	0.0008	0.0	0.0020	5.3	0.0046	7.0
	C2	0.0008	0.0	0.0018	-5.3	0.0043	0.0
	C3	0.0008	0.0	0.0013	-31.6	0.0022	-48.8
6	BF	0.0008	-	0.0016	-	0.0032	-
	C1	0.0006	-25.0	0.0014	-12.5	0.0028	-12.5
	C2	0.0006	-25.0	0.0014	-12.5	0.0030	-6.3
	C3	0.0007	-12.5	0.0013	-18.8	0.0020	-37.5
7	BF	0.0010	-	0.0019	-	0.0036	-
	C1	0.0008	-20.0	0.0017	-10.5	0.0033	-8.3
	C2	0.0007	-30.0	0.0016	-15.8	0.0033	-8.3
	C3	0.0008	-20.0	0.0013	-31.6	0.0019	-47.2
8	BF	0.0011	-	0.0020	-	0.0036	-
	C1	0.0009	-18.2	0.0017	-15.0	0.0033	-8.3
	C2	0.0007	-36.4	0.0015	-25.0	0.0029	-19.4
	C3	0.0009	-18.2	0.0013	-35.0	0.0019	-47.2
9	BF	0.0009	-	0.0016	-	0.0030	-
	C1	0.0008	-11.1	0.0016	0.0	0.0030	0.0
	C2	0.0006	-33.3	0.0012	-25.0	0.0023	-23.3
	C3	0.0007	-22.2	0.0010	-37.5	0.0014	-53.3

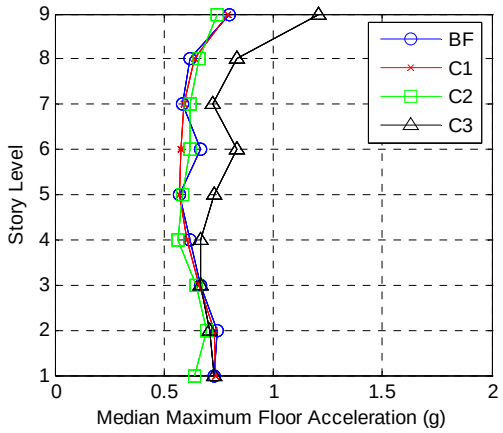

LMSR

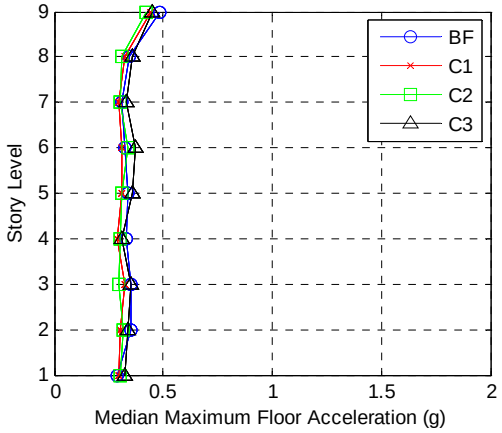

LMLR

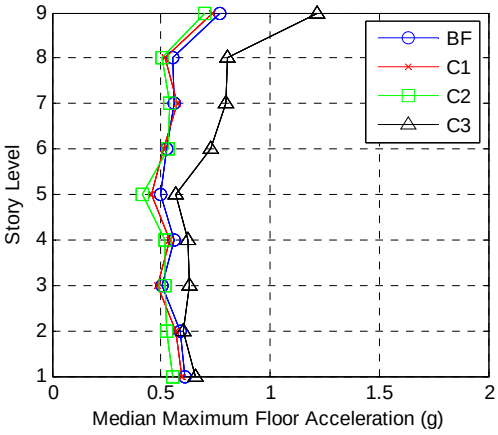

I880-N

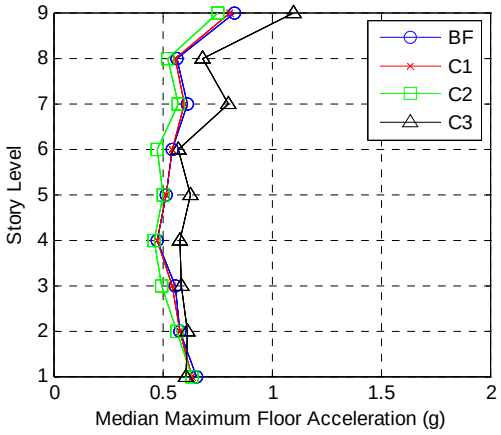

I880-P

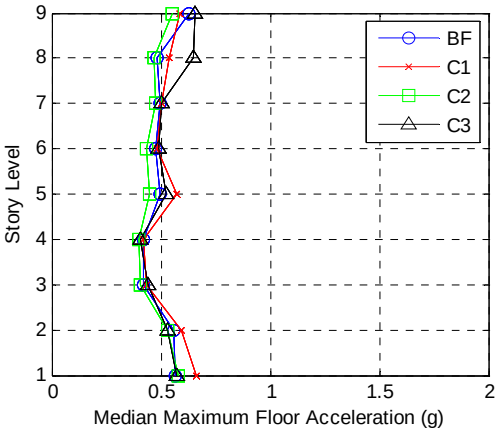

LA50

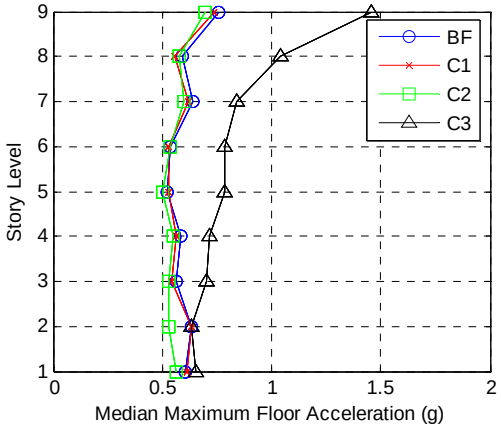

LA10

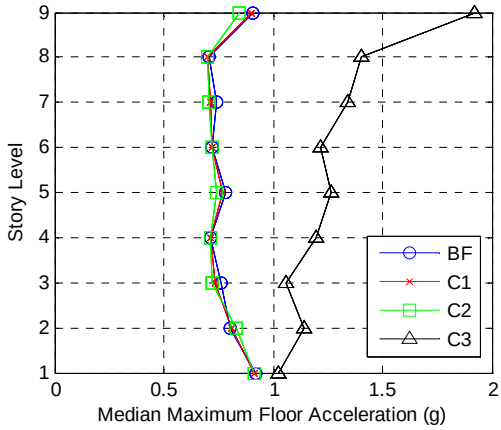

LA2

Fig. 4.28 Comparison of median peak floor acceleration profiles for different earthquake bins

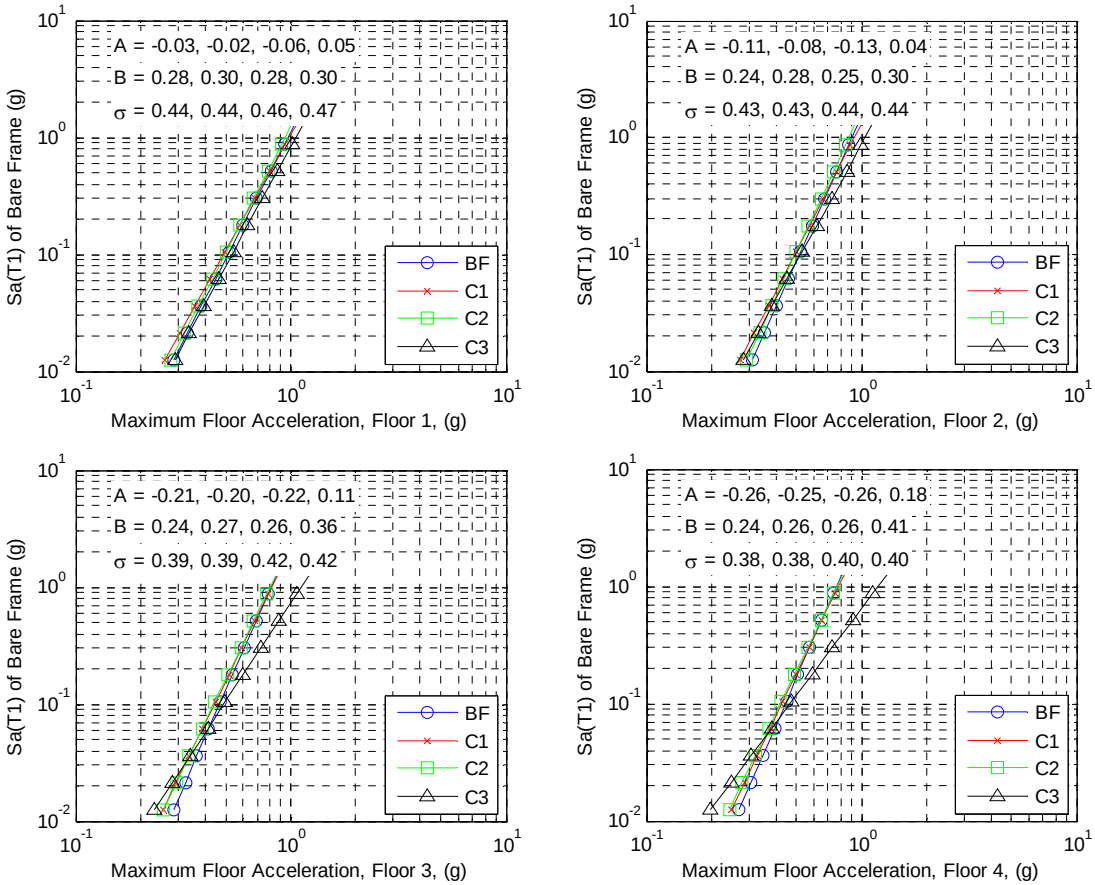

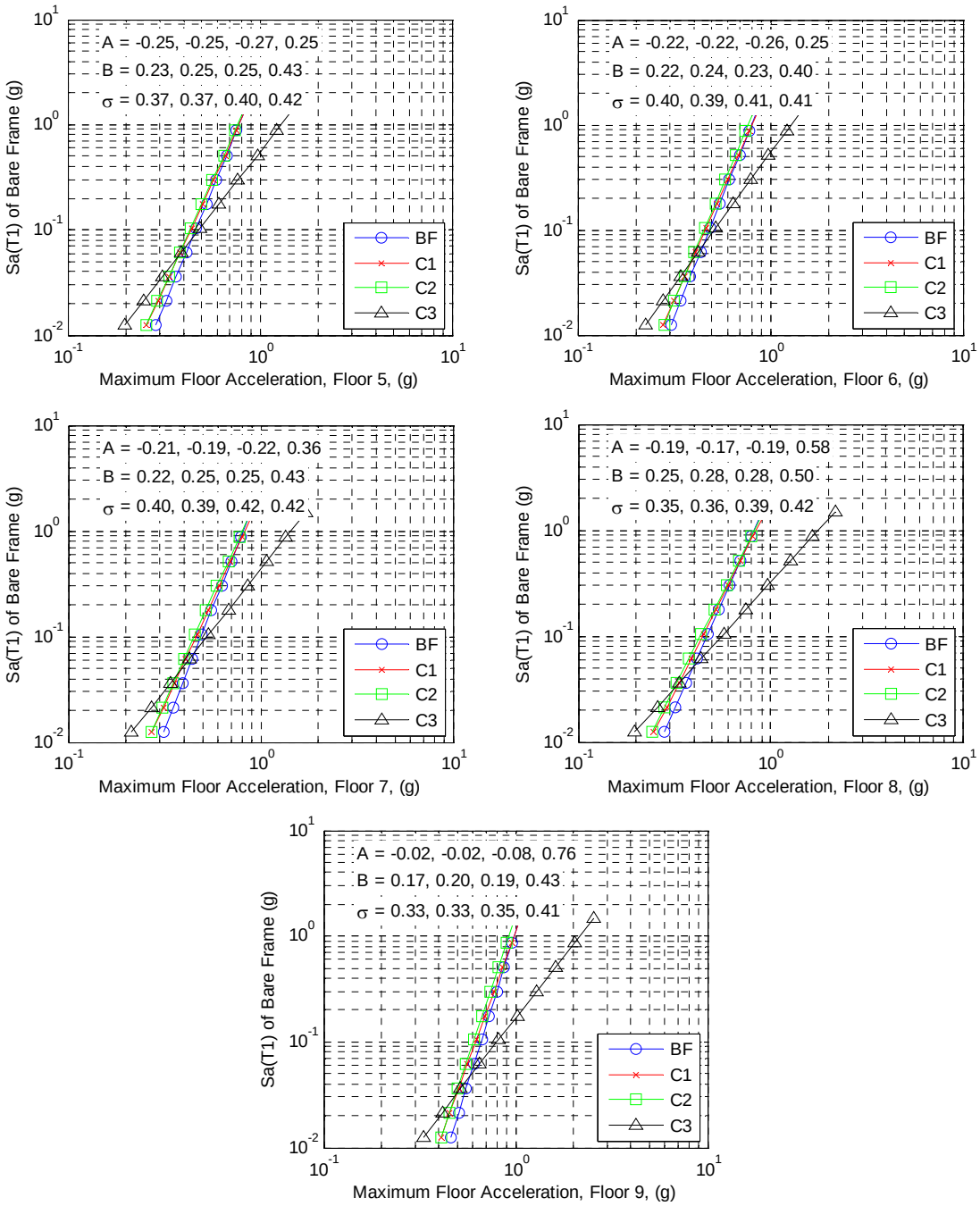

Fig. 4.29 Comparison of maximum floor acceleration for different story levels

Table 4.6 Mean maximum floor accelerations for three probabilities of exceedance

Floor	Model	Hazard Level					
		50% PE in 50 yrs $Sa(T_1) = 0.11g$		10% PE in 50 yrs $Sa(T_1) = 0.34g$		2% PE in 50 yrs $Sa(T_1) = 0.65g$	
		Maximum Floor Acceleration (g)	% Difference from Model BF	Maximum Floor Acceleration (g)	% Difference from Model BF	Maximum Floor Acceleration (g)	% Difference from Model BF
1	BF	0.57	-	0.71	-	0.86	-
	C1	0.55	-3.5	0.70	-1.4	0.86	0.0
	C2	0.55	-3.5	0.68	-4.2	0.83	-3.5
	C3	0.60	5.3	0.75	5.6	0.93	8.1
2	BF	0.57	-	0.68	-	0.81	-
	C1	0.55	-3.5	0.68	0.0	0.82	1.2
	C2	0.55	-3.5	0.66	-2.9	0.79	-2.5
	C3	0.59	3.5	0.74	8.8	0.91	12.3
3	BF	0.51	-	0.62	-	0.73	-
	C1	0.49	-3.9	0.60	-3.2	0.73	0.0
	C2	0.49	-3.9	0.60	-3.2	0.72	-1.4
	C3	0.57	11.8	0.74	19.4	0.95	30.1
4	BF	0.49	-	0.59	-	0.69	-
	C1	0.48	-2.0	0.58	-1.7	0.70	1.4
	C2	0.47	-4.1	0.57	-3.4	0.69	0.0
	C3	0.55	12.2	0.75	27.1	1.00	44.9
5	BF	0.51	-	0.60	-	0.71	-
	C1	0.48	-5.9	0.59	-1.7	0.70	-1.4
	C2	0.48	-5.9	0.58	-3.3	0.69	-2.8
	C3	0.57	11.8	0.79	31.7	1.07	50.7
6	BF	0.53	-	0.62	-	0.73	-
	C1	0.51	-3.8	0.61	-1.6	0.72	-1.4
	C2	0.50	-5.7	0.59	-4.8	0.70	-4.1
	C3	0.60	13.2	0.82	32.3	1.08	47.9
7	BF	0.54	-	0.63	-	0.74	-
	C1	0.51	-5.6	0.62	-1.6	0.74	0.0
	C2	0.50	-7.4	0.60	-4.8	0.72	-2.7
	C3	0.63	16.7	0.88	39.7	1.19	60.8
8	BF	0.52	-	0.62	-	0.74	-
	C1	0.50	-3.8	0.62	0.0	0.75	1.4
	C2	0.49	-5.8	0.60	-3.2	0.73	-1.4
	C3	0.69	32.7	1.00	61.3	1.43	93.2
9	BF	0.71	-	0.81	-	0.91	-
	C1	0.67	-5.6	0.78	-3.7	0.90	-1.1
	C2	0.65	-8.5	0.75	-7.4	0.85	-6.6
	C3	0.96	35.2	1.32	63.0	1.79	96.7

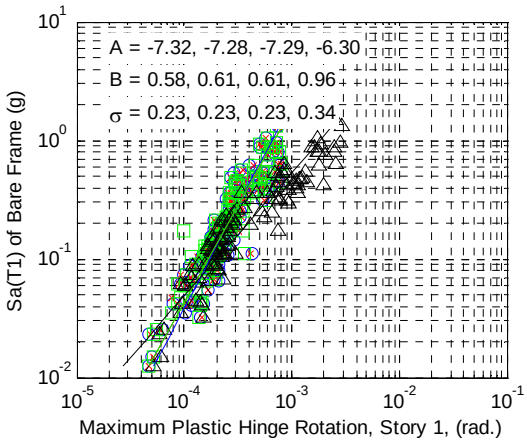
A = -7.32, -7.28, -7.29, -6.30
B = 0.58, 0.61, 0.61, 0.96
σ = 0.23, 0.23, 0.23, 0.34
Sa(T1) of Bare Frame (g)
Maximum Plastic Hinge Rotation, Story 1, (rad.)

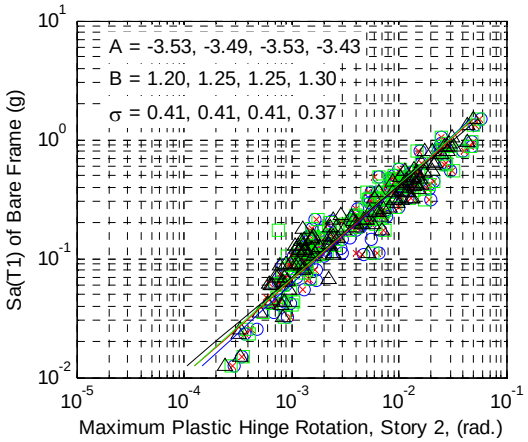
A = -3.53, -3.49, -3.53, -3.43
B = 1.20, 1.25, 1.25, 1.30
σ = 0.41, 0.41, 0.41, 0.37
Sa(T1) of Bare Frame (g)
Maximum Plastic Hinge Rotation, Story 2, (rad.)

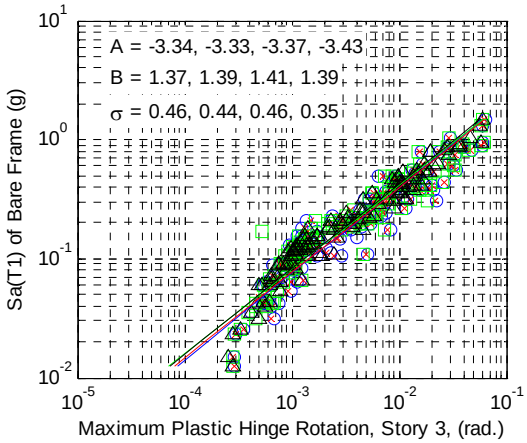
A = -3.34, -3.33, -3.37, -3.43
B = 1.37, 1.39, 1.41, 1.39
σ = 0.46, 0.44, 0.46, 0.35
Sa(T1) of Bare Frame (g)
Maximum Plastic Hinge Rotation, Story 3, (rad.)

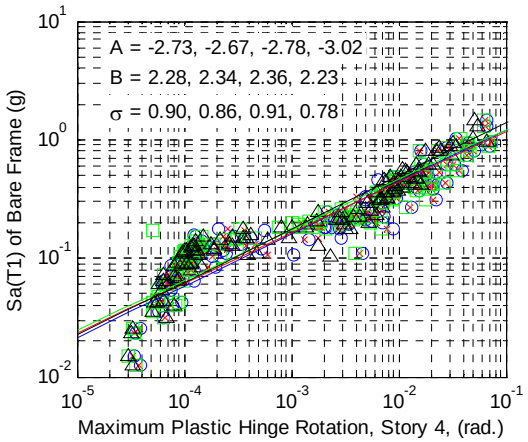
A = -2.73, -2.67, -2.78, -3.02
B = 2.28, 2.34, 2.36, 2.23
σ = 0.90, 0.86, 0.91, 0.78
Sa(T1) of Bare Frame (g)
Maximum Plastic Hinge Rotation, Story 4, (rad.)

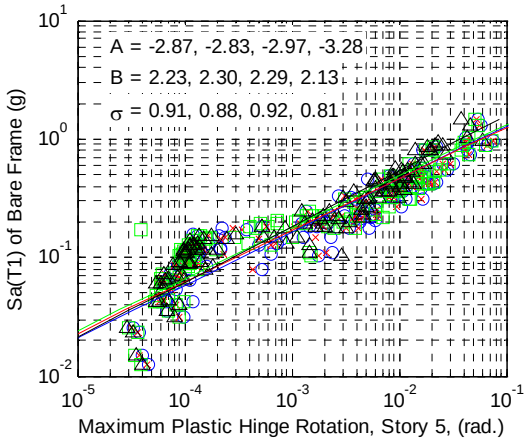
A = -2.87, -2.83, -2.97, -3.28
B = 2.23, 2.30, 2.29, 2.13
σ = 0.91, 0.88, 0.92, 0.81
Sa(T1) of Bare Frame (g)
Maximum Plastic Hinge Rotation, Story 5, (rad.)

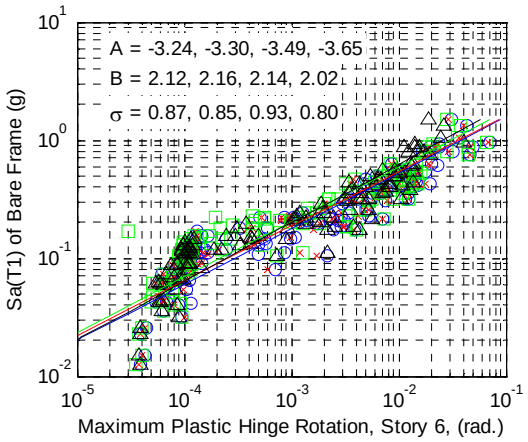
A = -3.24, -3.30, -3.49, -3.65
B = 2.12, 2.16, 2.14, 2.02
σ = 0.87, 0.85, 0.93, 0.80
Sa(T1) of Bare Frame (g)
Maximum Plastic Hinge Rotation, Story 6, (rad.)

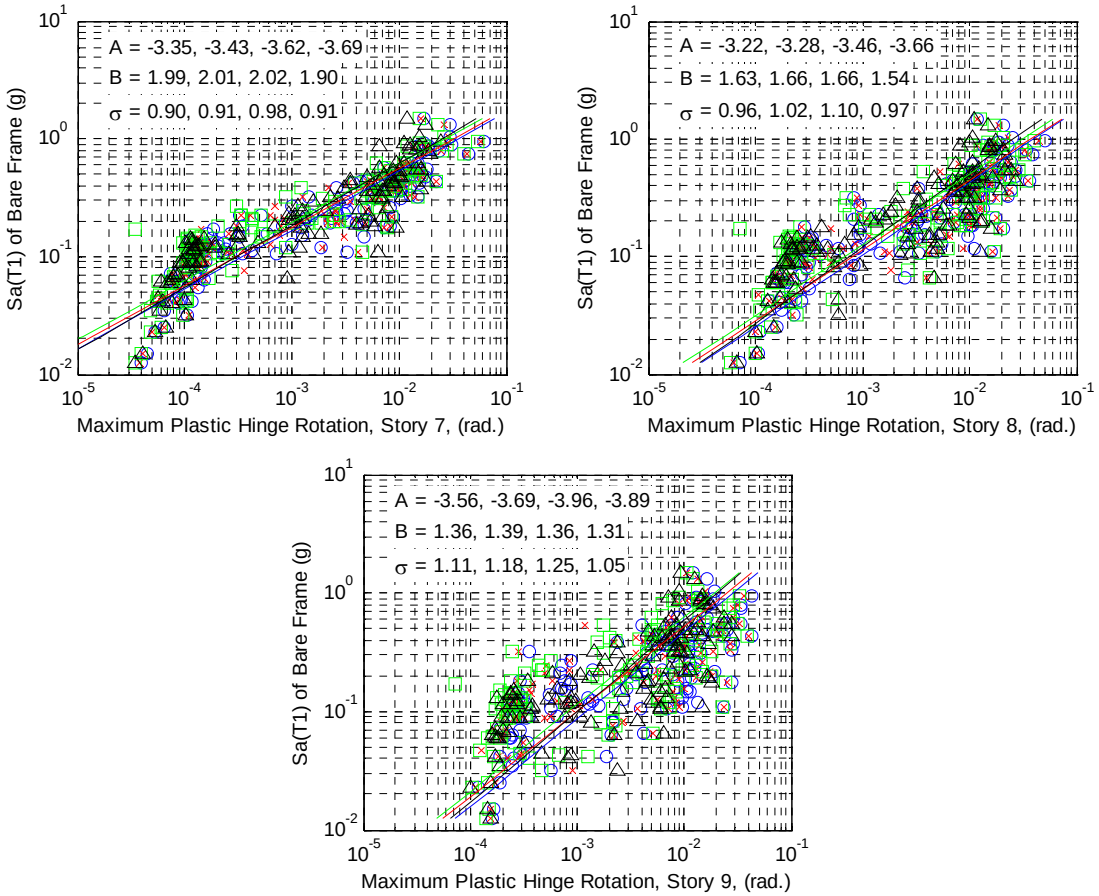

Fig. 4.30 Comparison of maximum plastic hinge rotations for different story levels

Table 4.7 Mean maximum plastic hinge rotations for three probabilities of exceedance

Floor	Model	Hazard Level		
		50% PE in 50 yrs $Sa(T_1) = 0.11g$	10% PE in 50 yrs $Sa(T_1) = 0.34g$	2% PE in 50 yrs $Sa(T_1) = 0.65g$
		Maximum Plastic Hinge Rotation (rad.)	Maximum Plastic Hinge Rotation (rad.)	Maximum Plastic Hinge Rotation (rad.)
1	BF	0.0002	0.0003	0.0005
	C1	0.0002	0.0003	0.0005
	C2	0.0002	0.0003	0.0005
	C3	0.0003	0.0006	0.0012
2	BF	0.0030	0.0074	0.0174
	C1	0.0029	0.0073	0.0178 (+2.3%)
	C2	0.0028	0.0071	0.0172 (-1.1%)
	C3	0.0027	0.0073	0.0185 (+6.3%)
3	BF	0.0026	0.0074	0.0195
	C1	0.0026	0.0073	0.0197 (+1.0%)
	C2	0.0024	0.0069	0.0187 (-4.1%)
	C3	0.0023	0.0067	0.0178 (-8.7%)
4	BF	0.0009	0.0048	0.0244
	C1	0.0008	0.0048	0.0251 (+2.9%)
	C2	0.0007	0.0042	0.0224 (-8.2%)
	C3	0.0007	0.0038	0.0186 (-23.8%)
5	BF	0.0008	0.0045	0.0217
	C1	0.0008	0.0043	0.0219 (+1.0%)
	C2	0.0007	0.0037	0.0190 (-12.4%)
	C3	0.0007	0.0033	0.0150 (-30.9%)
6	BF	0.0007	0.0035	0.0157
	C1	0.0006	0.0032	0.0146 (-7.0%)
	C2	0.0005	0.0026	0.0121 (-22.9%)
	C3	0.0006	0.0026	0.0109 (-30.6%)
7	BF	0.0008	0.0036	0.0149
	C1	0.0007	0.0033	0.0136 (-8.7%)
	C2	0.0006	0.0027	0.0112 (-24.8%)
	C3	0.0007	0.0029	0.0110 (-26.2%)
8	BF	0.0018	0.0062	0.0197
	C1	0.0016	0.0057	0.0184 (-6.6%)
	C2	0.0013	0.0047	0.0153 (-22.3%)
	C3	0.0014	0.0045	0.0133 (-32.5%)
9	BF	0.0021	0.0060	0.0159
	C1	0.0018	0.0051	0.0136 (-14.5%)
	C2	0.0014	0.0040	0.0106 (-33.3%)
	C3	0.0017	0.0046	0.0116 (-27.0%)

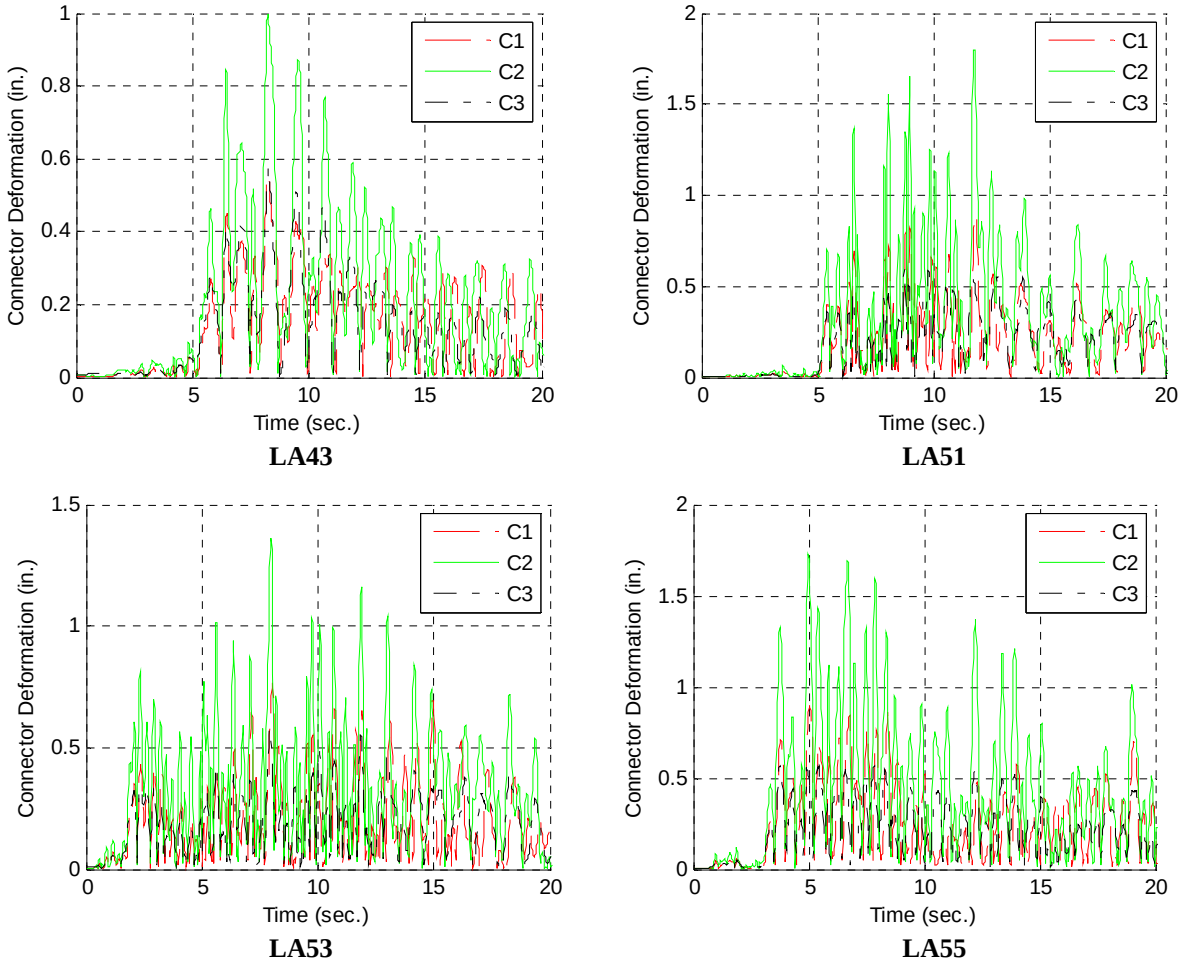

Fig. 4.31 Comparison of vector sum push-pull deformations at story 9 for select ground motions in the LA50 bin

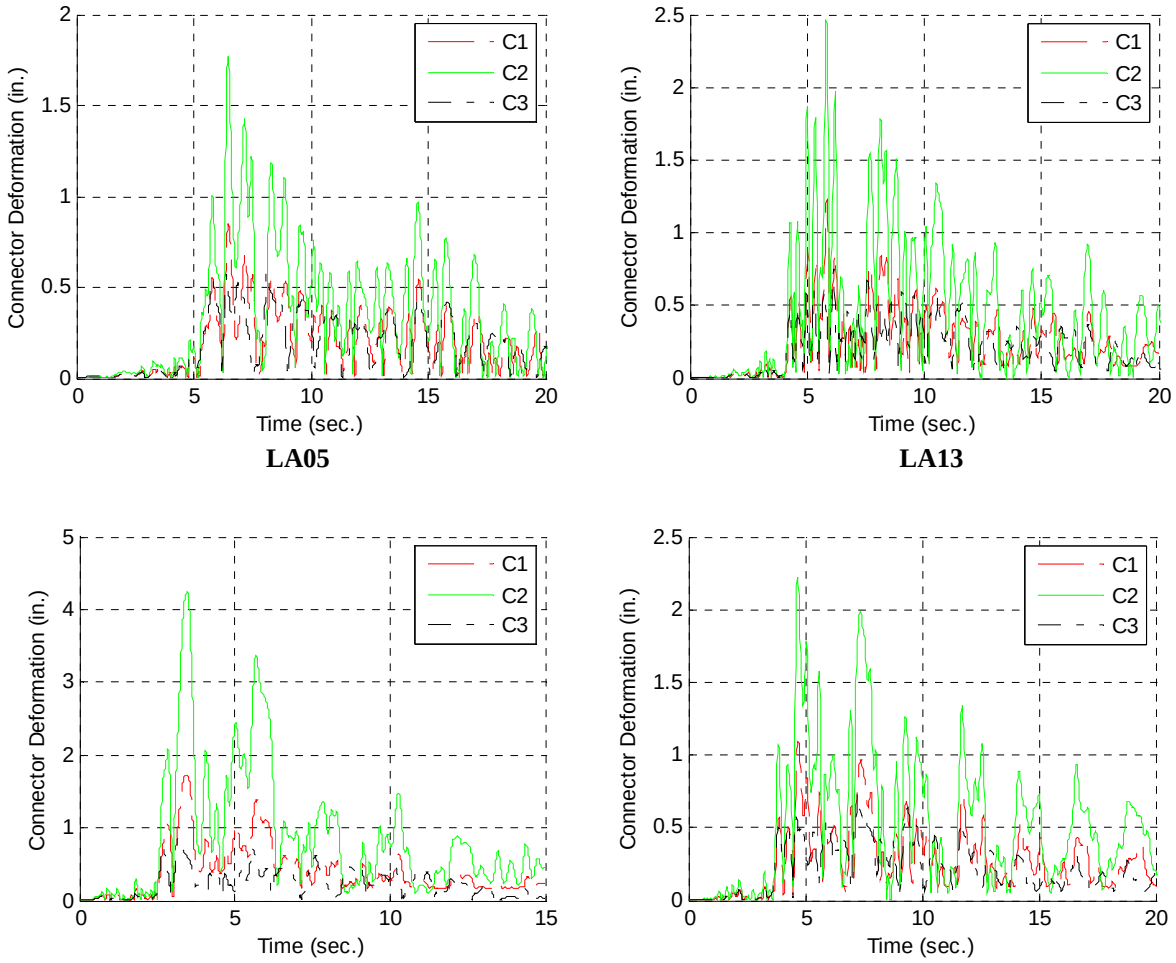

Fig. 4.32 Comparison of vector sum push-pull deformations at story 9 for select ground motions in the LA10 bin

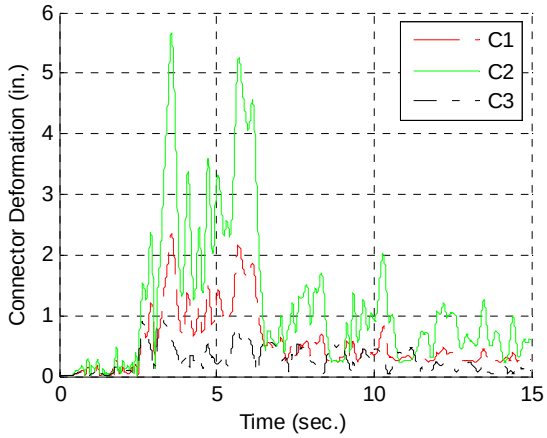

LA26

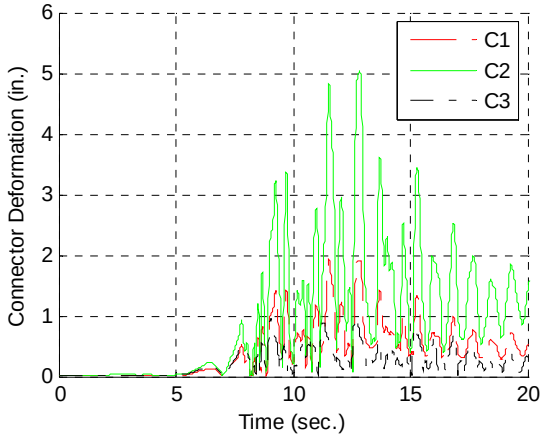

LA31

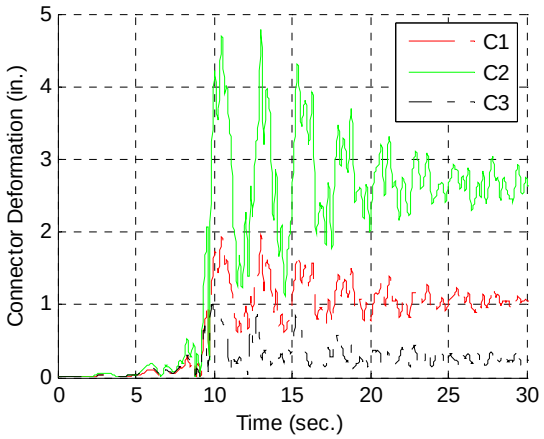

LA37

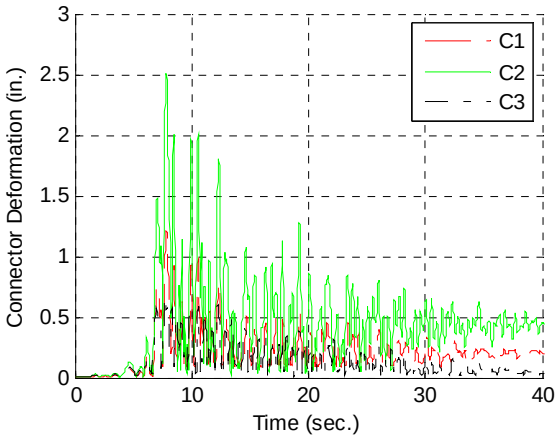

LA39

Fig. 4.33 Comparison of vector sum push-pull deformations at story 9 for select ground motions in the LA2 bin

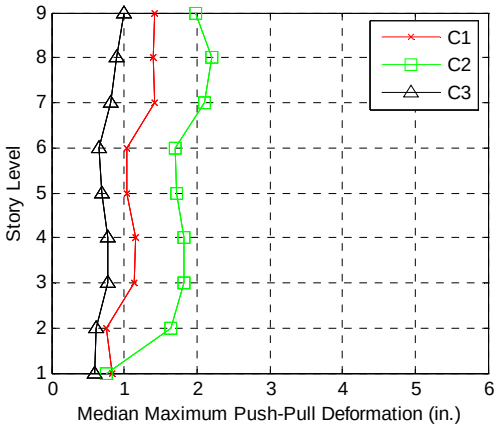

LMSR

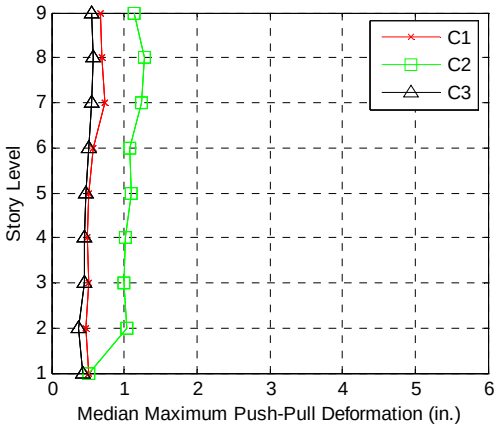

LMLR

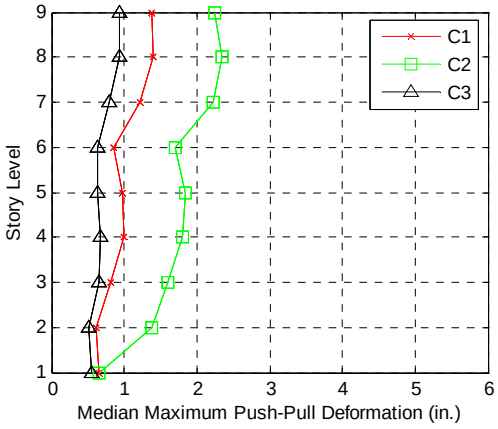

I880-N

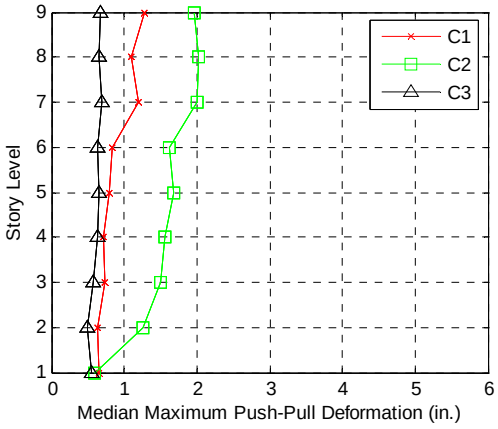

I880-P

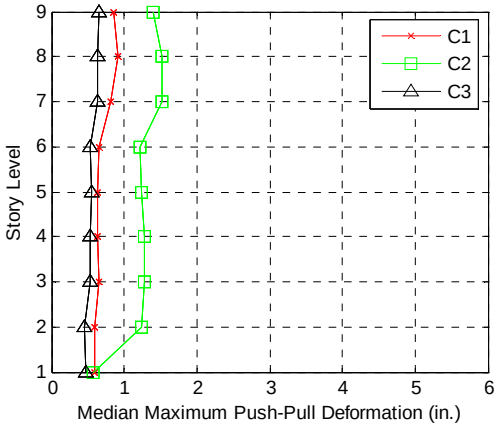

LA50

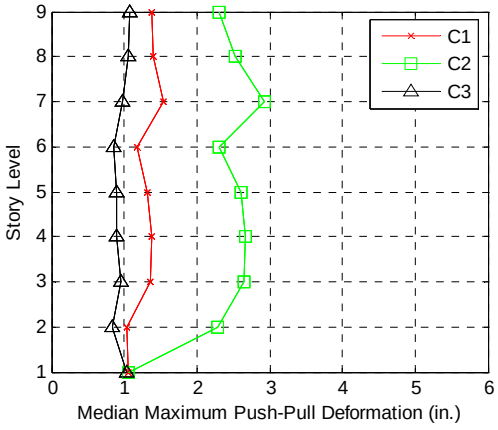

LA10

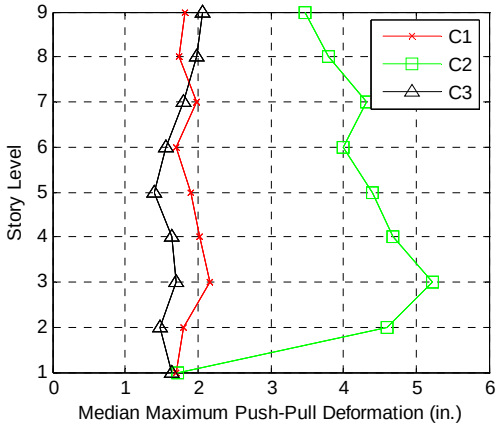

LA2

Fig. 4.34 Comparison of median peak push-pull deformation profiles for different earthquake bins

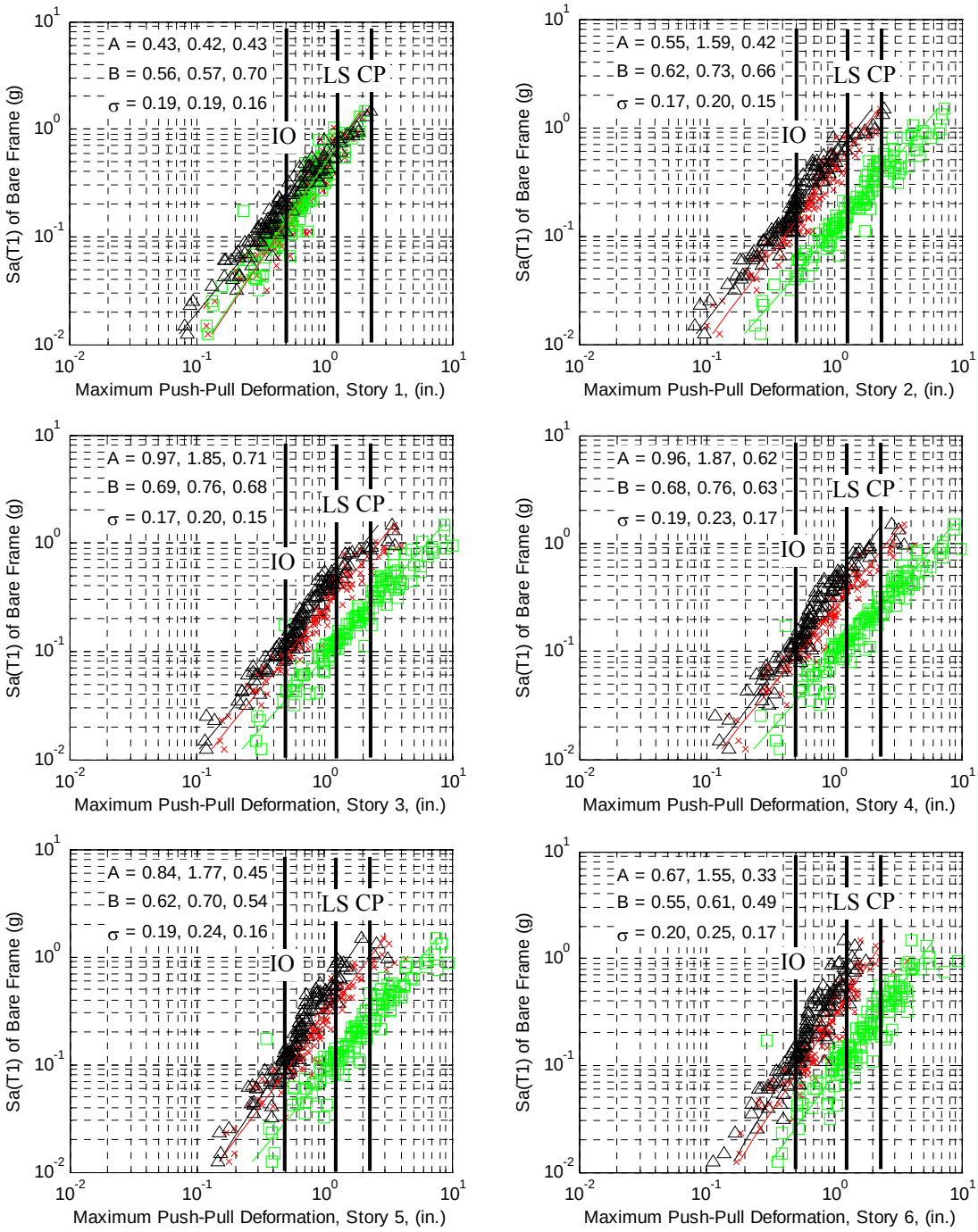
A = 0.43, 0.42, 0.43
B = 0.56, 0.57, 0.70
σ = 0.19, 0.19, 0.16
IO
LS CP
Sa(T1) of Bare Frame (g)
Maximum Push-Pull Deformation, Story 1, (in.)
A = 0.55, 1.59, 0.42
B = 0.62, 0.73, 0.66
σ = 0.17, 0.20, 0.15
IO
LS CP
Sa(T1) of Bare Frame (g)
Maximum Push-Pull Deformation, Story 2, (in.)
A = 0.97, 1.85, 0.71
B = 0.69, 0.76, 0.68
σ = 0.17, 0.20, 0.15
IO
LS CP
Sa(T1) of Bare Frame (g)
Maximum Push-Pull Deformation, Story 3, (in.)
A = 0.96, 1.87, 0.62
B = 0.68, 0.76, 0.63
σ = 0.19, 0.23, 0.17
IO
LS CP
Sa(T1) of Bare Frame (g)
Maximum Push-Pull Deformation, Story 4, (in.)
A = 0.84, 1.77, 0.45
B = 0.62, 0.70, 0.54
σ = 0.19, 0.24, 0.16
IO
LS CP
Sa(T1) of Bare Frame (g)
Maximum Push-Pull Deformation, Story 5, (in.)
A = 0.67, 1.55, 0.33
B = 0.55, 0.61, 0.49
σ = 0.20, 0.25, 0.17
IO
LS CP
Sa(T1) of Bare Frame (g)
Maximum Push-Pull Deformation, Story 6, (in.)

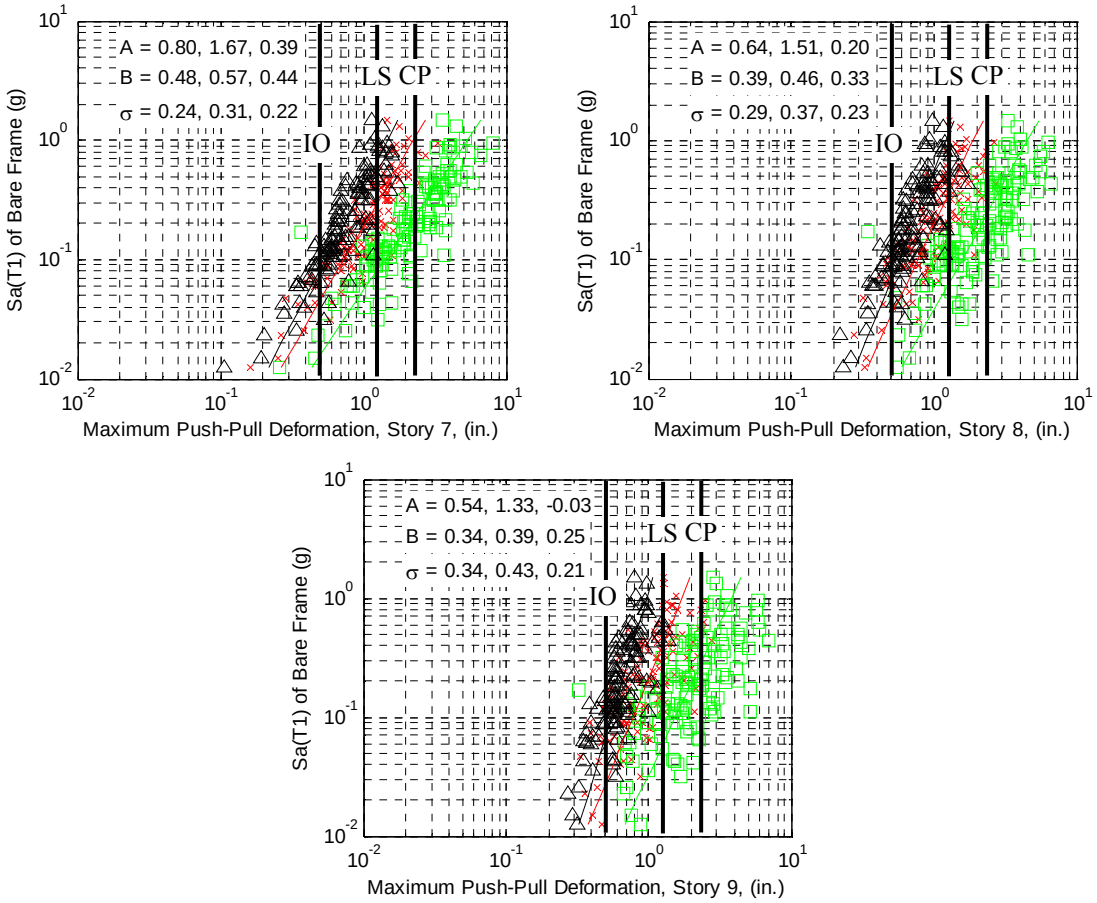

Fig. 4.35 Comparison of maximum push-pull deformation for different story levels (red X = model C2, green squares = model C3, black triangles = model C3)

Table 4.8 Mean maximum push-pull deformations for three probabilities of exceedance

Story	Model	Hazard Level		
		50% PE in 50 yrs $Sa(T_1) = 0.11g$	10% PE in 50 yrs $Sa(T_1) = 0.34g$	2% PE in 50 yrs $Sa(T_1) = 0.65g$
		Maximum Push-Pull Deformation (in.)	Maximum Push-Pull Deformation (in.)	Maximum Push-Pull Deformation (in.)
1	C1	0.53	0.81	1.21
	C2	0.52 (-1.9%)	0.80 (-1.2%)	1.19 (-1.7%)
	C3	0.41 (-22.6%)	0.70 (-13.5%)	1.14 (-5.8%)
2	C1	0.53	0.85	1.32
	C2	1.22 (+130%)	2.13 (+150%)	3.57 (+170%)
	C3	0.43 (-18.9%)	0.71 (-16.5%)	1.14 (-13.6%)
3	C1	0.72	1.20	1.96
	C2	1.49 (+106%)	2.66 (+121.7%)	4.56 (+132%)
	C3	0.57 (-20.8%)	0.95 (-20.8%)	1.53 (-22.0%)
4	C1	0.72	1.20	1.94
	C2	1.54 (+114%)	2.73 (+128%)	4.66 (+140%)
	C3	0.57 (-20.8%)	0.92 (-23.3%)	1.43 (-26.3%)
5	C1	0.71	1.13	1.77
	C2	1.56 (+120%)	2.65 (+134%)	4.34 (+145%)
	C3	0.57 (-19.7%	0.85 (-24.8%)	1.25 (-29.4%)
6	C1	0.70	1.05	1.55
	C2	1.47 (+110%)	2.34 (+122%)	3.62 (+133%)
	C3	0.55 (-21.4%)	0.80 (-23.8%)	1.13 (-27.1%)
7	C1	0.89	1.29	1.81
	C2	1.79 (+101%)	2.77 (+114%)	4.15 (+129%)
	C3	0.65 (-27.0%)	0.90 (-30.2%)	1.23 (-32.0%)
8	C1	0.90	1.21	1.60
	C2	1.89 (+110%)	2.68 (+121%)	3.72 (+133%)
	C3	0.65 (-27.8%)	0.84 (-30.5%)	1.06 (-33.8%)
9	C1	0.90	1.16	1.49
	C2	1.81 (+101%)	2.43 (+109%)	3.21 (+115%)
	C3	0.61 (-32.2%)	0.73 (-37.0%)	0.87 (-41.6%)

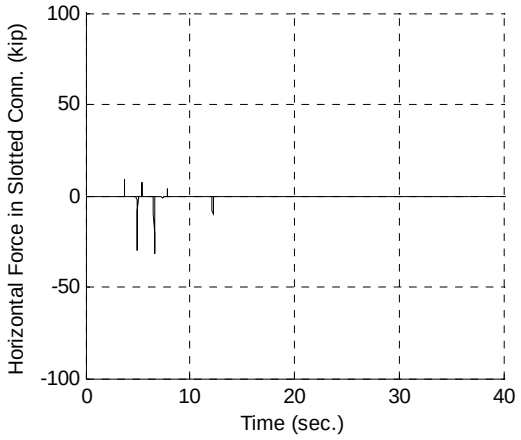

LA55 from LA50 bin

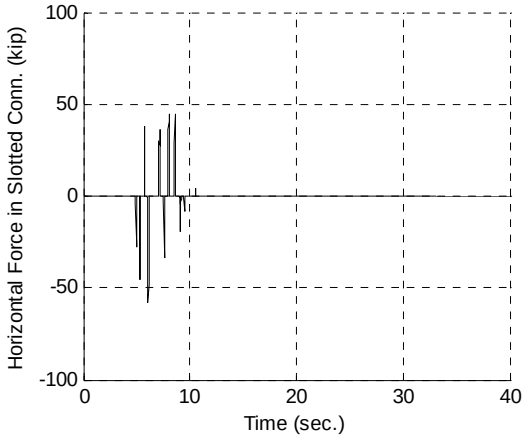

LA13 from LA10 bin

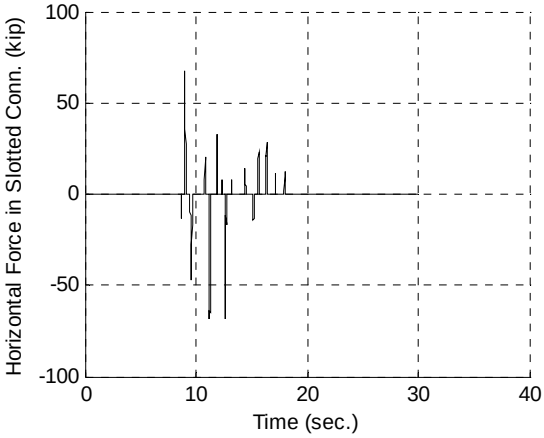

LA31 from LA2 bin

Fig. 4.36 Horizontal force in slotted connection in story 9 for three intensity levels

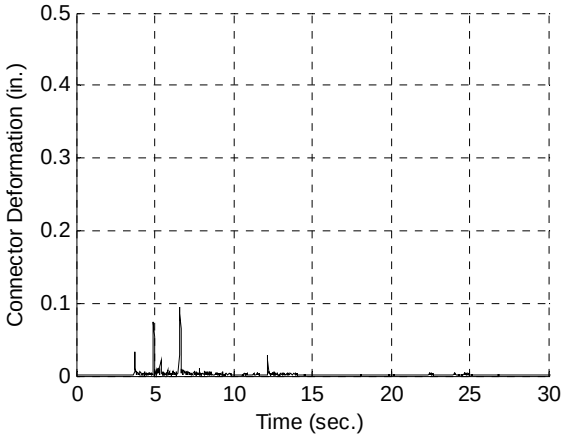

LA55 from LA50 bin

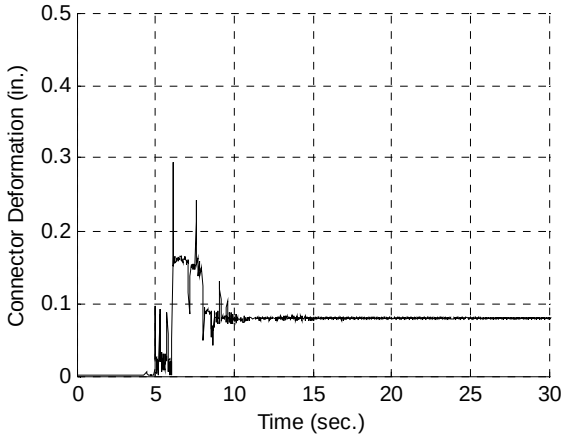

LA13 from LA10 bin

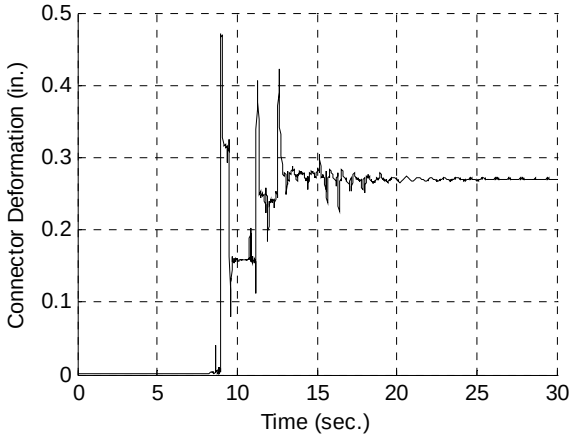

LA31 from LA2 bin

Fig. 4.37 Vector sum deformation in column cover connection at story 9 for three intensity levels

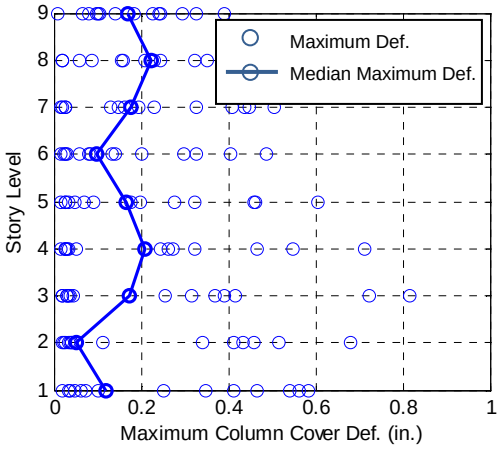

LMSR

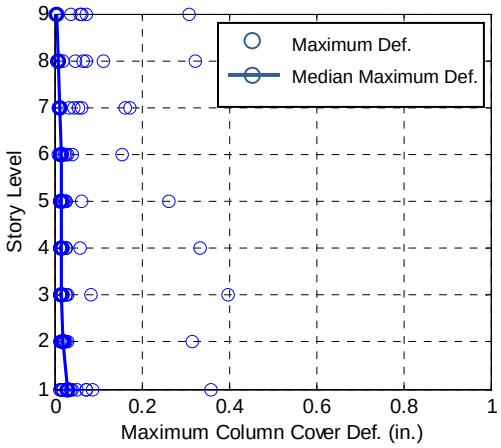

LMLR

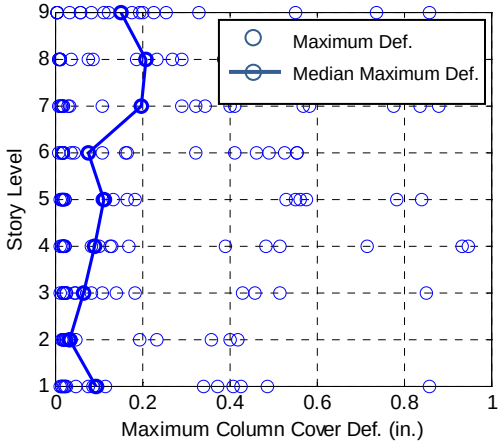

I880-N

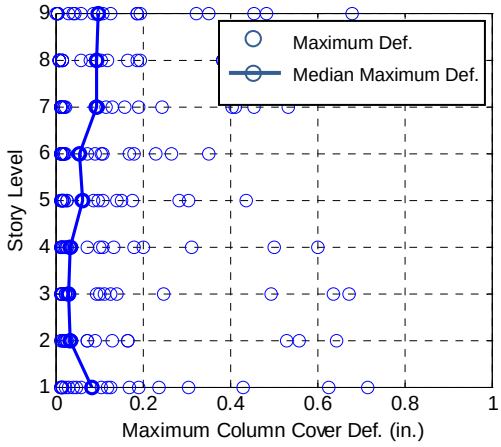

I880-P

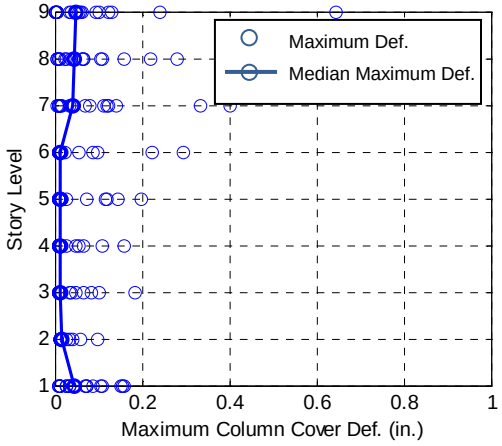

LA50

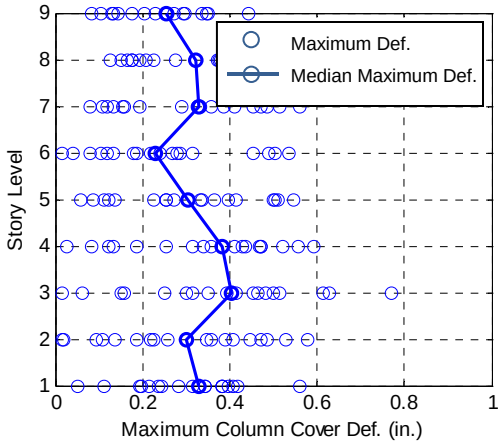

LA10

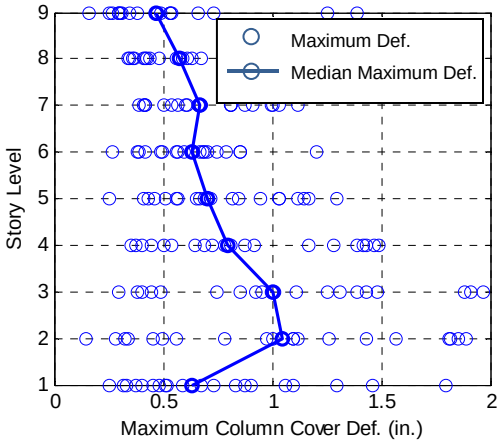

Fig. 4.38 Comparison of median peak column-cover connector deformation profiles for different earthquake bins

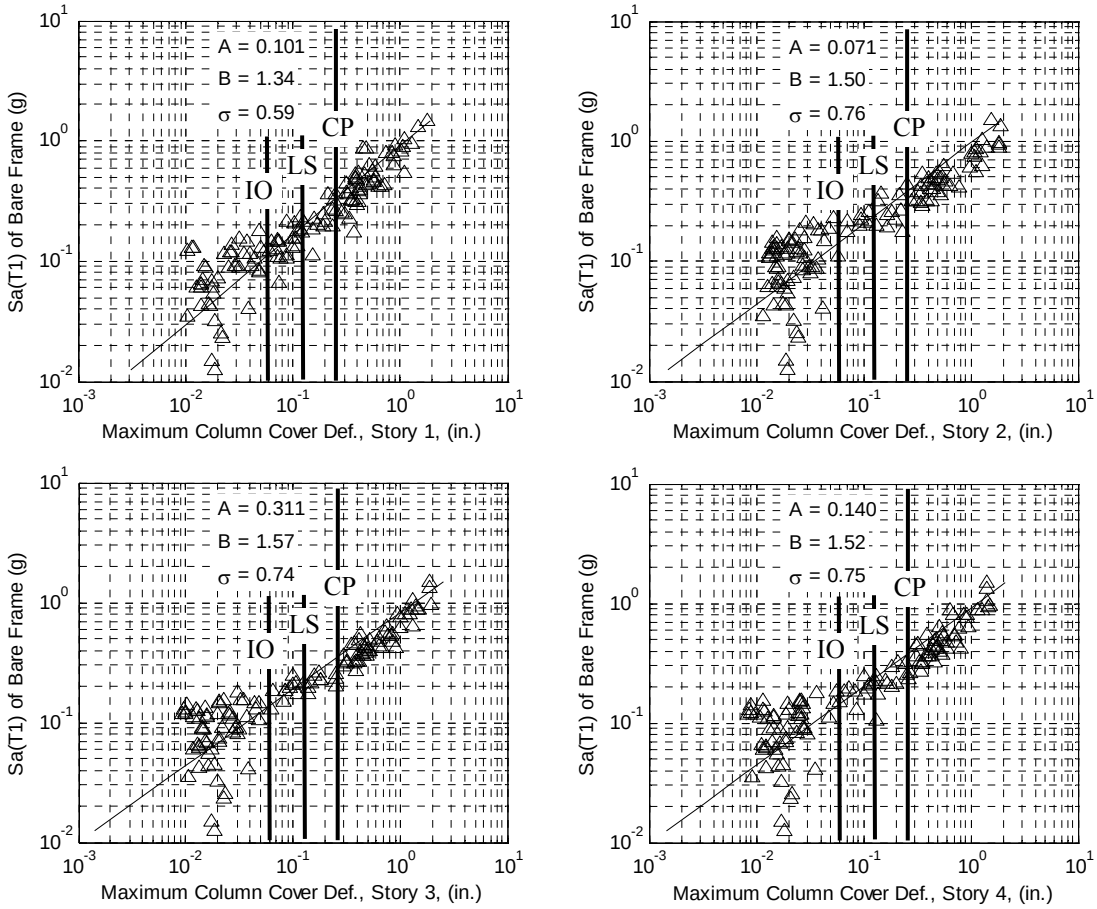

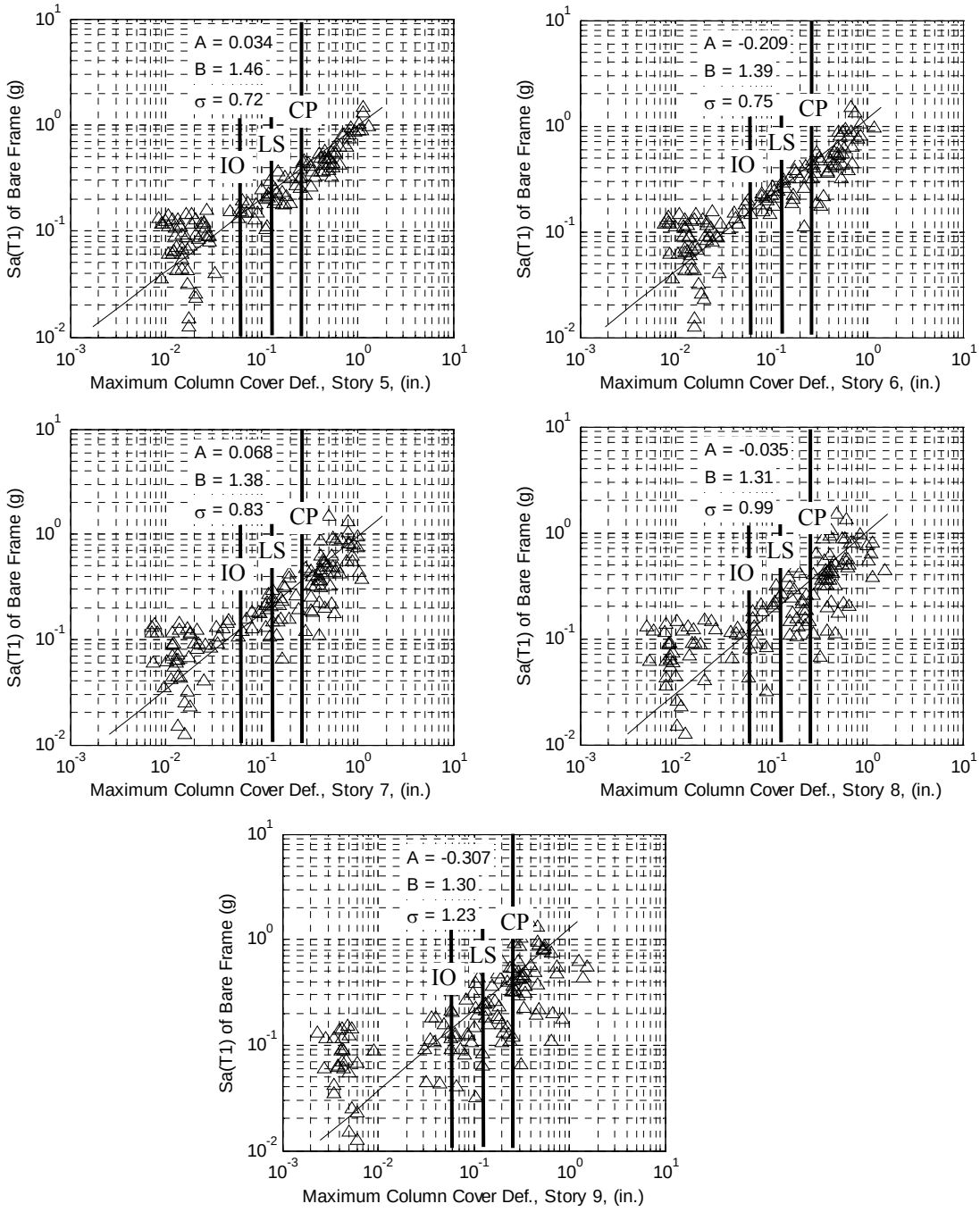

Fig. 4.39 Maximum deformation in the column cover connectors

Table 4.9 Mean maximum column cover deformations for three probabilities of exceedance

Story	Model	Hazard Level		
		50% PE in 50 yrs $Sa(T_1) = 0.11g$	10% PE in 50 yrs $Sa(T_1) = 0.34g$	2% PE in 50 yrs $Sa(T_1) = 0.65g$
		Maximum Column Cover Deformation (in.)	Maximum Column Cover Deformation (in.)	Maximum Column Cover Deformation (in.)
1	C3	0.087	0.241	0.621
2	C3	0.063	0.195	0.564
3	C3	0.070	0.229	0.695
4	C3	0.065	0.204	0.598
5	C3	0.065	0.197	0.553
6	C3	0.058	0.166	0.446
7	C3	0.078	0.222	0.591
8	C3	0.081	0.218	0.550
9	C3	0.063	0.167	0.420

Chapter 5: Analytical Expressions to Estimate Seismic Demands in Cladding System Components

In Chapter 3, analytical models of buildings with cladding systems were developed using OpenSees. Nonlinear elements were used to define the hysteretic force-deformation behavior of the push-pull connections and column cover connections. These models were analyzed to quantify the seismic demands in the push-pull and column cover connections, which are summarized in Chapter 4.

Creating an explicit model of a building with a cladding system is time consuming, and the additional number of elements and degrees of freedom in the model is large enough to prohibitively slow down the time-history analyses. For example, the bare frame (BF) model in Chapter 3 contains 157 nodes and 199 elements, while the cladding type C3 model contains 1,349 nodes and 2,221 elements. In practice, structural engineers probably would not take the extra effort to model the cladding system.

In this chapter, analytical expressions are derived that estimate the seismic demands in the push-pull and column cover connections based on the deformations of the bare frame. These equations use the time-history results from the bare frame model to estimate the connection demands in the models with cladding. Comparisons with the demands from the time-history analyses show that the analytical equations provide good estimations of the demands.

A method is presented that uses the response quantities from the pushover analysis of the bare frame (BF) model in the analytical equations to develop design equations for the maximum deformations in the cladding connections. The goal of presenting these equations is to allow a practicing engineer to estimate seismic demands on cladding connections and components without creating a complicated model and performing extensive analyses. These equations apply for regular structures (setbacks and discontinuities in plan and elevation were not considered in this research) with dominant first-mode response and fundamental vibration periods between 1 and 2.5 sec. The equations are applicable for buildings that are 3 to 20 stories in height.

5.1 DEFORMATIONS IN CLADDING SYSTEM

The restraints provided by the various cladding connections force the cladding system to deform in a particular manner. The force-deformation properties of each connection were described in Chapter 3. The rigid lateral connection is very stiff in the horizontal and vertical directions, and the vertical bearing connection is very stiff in the vertical direction. Since the rigid lateral connection and vertical bearing connections all attach the spandrel panel to the floor

beam, their combined action forces the spandrel panel to move laterally with the same displacement (translation and rotation) as the center of the floor beam.

A detailed elevation of cladding type C3 is shown in Fig. 5.1. As interstory drift develops, the cladding system deforms as shown in Fig. 5.2. The locations of the various connectors are shown in Fig. 5.3. The spandrel panels translate and rotate, deforming the push-pull connections. The column cover panels translate and rotate from the movement of the spandrel panels. The next two sections describe the mechanics of how the push-pull connectors and column cover connectors deform.

5.1.1 Push-Pull Connections

The deformations in the push-pull connections develop from two consequences of the interstory drift: the curvature of the columns and the curvature of the floor beam. The column undergoes double curvature, which creates a horizontal displacement incompatibility between the shape of the displaced column and the rigid vertical side of the spandrel panels, as shown in Fig. 5.4. The difference between these two shapes (the curved column and the straight edge of the cladding panel), shown as δx in Fig. 5.4, can be approximated by using the beam-column node rotation angle ϕ_i (shown as the dashed line in Fig. 5.4).

The other source of deformation is the curvature of the floor beam. During lateral frame deformation that causes interstory drift, the floor beam undergoes elastic double curvature (since the plastic hinges are located at the beam ends), and the spandrel panel follows the rotation of the center node of the floor beam, θ_i. This spandrel panel rotation creates horizontal and vertical deformations in the push-pull connections.

The horizontal deformation $\delta_{x,b}$ and the vertical deformation $\delta_{y,b}$ of the push-pull connection at the bottom of the spandrel panel, given in Equations 5.1 and Equation 5.2, are a function of the spandrel panel dimension y_b (defined in Fig. 5.1), the length of the spandrel panel L, the beam-column node rotation ϕ_i, and the beam center node rotation θ_i at floor i. The horizontal and vertical deformations are combined in Equation 5.3 as a total deformation $\delta_{total,b}$ using their vector sum.

$$\delta_{x,b} = y_b(\phi_i + \theta_i) \quad \text{Eq. 5.1}$$

$$\delta_{y,b} = \frac{L}{2}\theta_i \quad \text{Eq. 5.2}$$

$$\delta_{total,b} = \sqrt{{\delta_{x,b}}^2 + {\delta_{y,b}}^2} \quad \text{Eq. 5.3}$$

In a similar way, the deformations in the push-pull connectors at the top of the spandrel panels are found using Equations 5.4, 5.5, and 5.6. At the top connectors, the dimension y_t is used instead of the dimension y_b.

$$\delta_{x,t} = y_t(\phi_i + \theta_i) \quad \text{Eq. 5.4}$$

$$\delta_{y,t} = \frac{L}{2}\theta_i \quad \text{Eq. 5.5}$$

$$\delta_{total,t} = \sqrt{{\delta_{x,t}}^2 + {\delta_{y,t}}^2} \quad \text{Eq. 5.6}$$

In all of the equations above, the nodal rotations ϕ_i and θ_i are to be input as absolute (positive) quantities. The derivation of the equations for the push-pull deformations is purely geometric and does not involve the properties of the connectors themselves. This derivation assumes that the spandrel panels behave as rigid blocks (i.e. do not deform) and that all deformation occurs in the connectors.

5.1.2 Column Cover Connections

The column cover connections are pinned and slotted bolt connections that attach the column cover to the spandrel panel. The connection, described in Chapter 3 and shown in Figures 3.13 and 3.14, consists of a bolt at each corner of the column cover panel: the two bolts at the bottom of the panel are attached in a standard-sized hole, and the two bolts at the top of the panel are attached in a horizontally slotted hole. This connection allows the column cover panel to be properly aligned and permits movement of the bolt within the slotted hole during earthquakes. When the interstory drift exceeds the available gap on either side of the bolt, the column cover connections become loaded and deform in shear, assuming there is no appreciable friction and the bolt is straight and not over-tightened or stuck.

As described in Chapter 3, the force-deformation curve of the bolts is nonlinear. However, to obtain analytical expressions to estimate the column cover deformations, a linear structural analysis will be performed. The deformed shape of the column cover panel is shown in Fig. 5.2. There are two sources of the deformations to the column cover panels: interstory drift and rotations of the adjacent spandrel panels. The deformations are determined from structural analysis as a support movement problem, as shown in Fig. 5.5. As the spandrel panels (the supports) move, the column cover displaces and rotates causing shear deformations in the connections. As the structural frame deforms under horizontal seismic load, the story height decreases by a small amount due to second order geometry effects, which creates additional deformations in the column cover connectors. The story shortening Δv is related to the interstory drift Δh by Equation 5.7:

$$\Delta v = \frac{\Delta h^2}{2H} \quad \text{Eq. 5.7}$$

The variables Δh and H are the interstory drift and story height, respectively. The horizontal and vertical deformation components are solved for each of the four connectors, and the total deformation in each connector is the vector sum of the two components. Each step of the derivation of the equations is presented in Appendix A; the horizontal and vertical deformations in each of the four connectors in story *i* are shown in Equation 5.8.

$$(\delta_{x1}, \delta_{y1}, \delta_{x2}, \delta_{y2}, \delta_{x3}, \delta_{y3}, \delta_{x4}, \delta_{y4}) = \qquad \text{Eq. 5.8}$$

$$\begin{pmatrix}
\frac{X^2}{4(X^2+Y^2)}\left[2(y_t\theta_{i-1} + y_b\theta_i + \Delta_{h,i} - g) + Y(\theta_{i-1} + \theta_i)\right] \\
\frac{1}{4H(X^2+Y^2)}\left[X^3H(\theta_{i-1} - \theta_i) - {\Delta_{h,i}}^2(X^2 + Y^2) + 2XY^2H\theta_{i-1} + 2XYH(y_t\theta_{i-1} + y_b\theta_i) + 2XYH(\Delta_{h,i} - g)\right] \\
\frac{-X^2}{4(X^2+Y^2)}\left[2(y_t\theta_{i-1} + y_b\theta_i + \Delta_{h,i} - g) + Y(\theta_{i-1} + \theta_i)\right] \\
\frac{-1}{4H(X^2+Y^2)}\left[X^3H(\theta_{i-1} - \theta_i) + {\Delta_{h,i}}^2(X^2 + Y^2) + 2XY^2H\theta_{i-1} + 2XYH(y_t\theta_{i-1} + y_b\theta_i) + 2XYH(\Delta_{h,i} - g)\right] \\
\frac{-X^2}{4(X^2+Y^2)}\left[2(y_t\theta_{i-1} + y_b\theta_i + \Delta_{h,i} - g) + Y(\theta_{i-1} + \theta_i)\right] \\
\frac{1}{4H(X^2+Y^2)}\left[X^3H(\theta_{i-1} - \theta_i) - {\Delta_{h,i}}^2(X^2 + Y^2) - 2XY^2H\theta_i - 2XYH(y_t\theta_{i-1} + y_b\theta_i) - 2XYH(\Delta_{h,i} - g)\right] \\
\frac{X^2}{4(X^2+Y^2)}\left[2(y_t\theta_{i-1} + y_b\theta_i + \Delta_{h,i} - g) + Y(\theta_{i-1} + \theta_i)\right] \\
\frac{-1}{4H(X^2+Y^2)}\left[X^3H(\theta_{i-1} - \theta_i) + {\Delta_{h,i}}^2(X^2 + Y^2) - 2XY^2H\theta_i - 2XYH(y_t\theta_{i-1} + y_b\theta_i) - 2XYH(\Delta_{h,i} - g)\right]
\end{pmatrix}$$

The values θ_i and θ_{i-1} are the rotations of the center of the beam above and below the column cover. The value $\Delta_{h,i}$ is the interstory drift in story i, and the value g is the gap on either side of the bolt in the slotted hole (usually assumed as the slot width minus the bolt diameter divided by two). The variables X and Y are the dimensions of the column cover panel, and H is the story height, shown in Fig. 5.1. The variables y_t and y_b are the relevant dimensions of the spandrel panel. In Equation 5.8, the interstory drift $\Delta_{h,i}$ and the nodal rotations θ_i and θ_{i-1} are to be input as absolute (positive) quantities. The total deformation $\delta_{total,j}$ of connector j (j = 1, 2, 3, 4) is computed in Equation 5.9 using the horizontal (x) and vertical (y) components in Equation 5.8:

$$\delta_{total,j} = \sqrt{{\delta_{x,j}}^2 + {\delta_{y,j}}^2} \qquad \text{Eq. 5.9}$$

Equation 5.8 is valid for the case when the absolute value of the interstory drift is equal to or larger than the gap width, g, in the slotted connection (see Fig. 5.5). For the case when the absolute value of the interstory drift is less than the gap width, the column cover connections do not deform horizontally from interstory drift; however, they still deform due to the spandrel panel rotations and story shortening. The column cover connection deformations are given in Equation 5.10 for the case when $\Delta_{h,i} < g$.

$(\delta_{x1}, \delta_{y1}, \delta_{x2}, \delta_{y2}, \delta_{x3}, \delta_{y3}, \delta_{x4}, \delta_{y4}) =$

$$\begin{pmatrix} \frac{X^2}{4(X^2+Y^2)}[2(y_t\theta_{i-1}+y_b\theta_i)+Y(\theta_{i-1}+\theta_i)] \\ \frac{1}{4H(X^2+Y^2)}\left[X^3H(\theta_{i-1}-\theta_i)-\Delta_{h,i}{}^2(X^2+Y^2)+2XY^2H\theta_{i-1}+2XYH(y_t\theta_{i-1}+y_b\theta_i)\right] \\ \frac{-X^2}{4(X^2+Y^2)}[2(y_t\theta_{i-1}+y_b\theta_i)+Y(\theta_{i-1}+\theta_i)] \\ \frac{-1}{4H(X^2+Y^2)}\left[X^3H(\theta_{i-1}-\theta_i)+\Delta_{h,i}{}^2(X^2+Y^2)+2XY^2H\theta_{i-1}+2XYH(y_t\theta_{i-1}+y_b\theta_i)\right] \\ \frac{-X^2}{4(X^2+Y^2)}[2(y_t\theta_{i-1}+y_b\theta_i)+Y(\theta_{i-1}+\theta_i)] \\ \frac{1}{4H(X^2+Y^2)}\left[X^3H(\theta_{i-1}-\theta_i)-\Delta_{h,i}{}^2(X^2+Y^2)-2XY^2H\theta_i-2XYH(y_t\theta_{i-1}+y_b\theta_i)\right] \\ \frac{X^2}{4(X^2+Y^2)}[2(y_t\theta_{i-1}+y_b\theta_i)+Y(\theta_{i-1}+\theta_i)] \\ \frac{-1}{4H(X^2+Y^2)}\left[X^3H(\theta_{i-1}-\theta_i)+\Delta_{h,i}{}^2(X^2+Y^2)-2XY^2H\theta_i-2XYH(y_t\theta_{i-1}+y_b\theta_i)\right] \end{pmatrix} \quad \text{Eq. 5.10}$$

In the structural analysis used to derive the equations for column cover connector deformations, it was assumed that all connectors have equal linear shear stiffness *k*. This assumption is used only to enable a closed form solution for the connector deformations. The consequences of this assumption will be investigated in Section 5.2.

5.1.3 Window Glazing System

The design of the window glazing system was described in Chapter 3. The window panes become damaged from interstory drift that causes the window framing to contact the window panes. The deformation of the window glazing system occurs as follows: the window frame deflects as a frame until the frame bears upon the glass at the loaded corner and in the region of the diagonally opposite corner. At this point, the glass rotates within the window frame, thereby permitting considerable additional interstory drift. When the glass is seated in the two diagonally opposite corners, only a very small interstory drift increment may occur before cracking of the glass, which is due to the shortening of the diagonal as a result of the buckling of the glass.

The definitions of the dimensions of a single window pane and frame are given in Fig. 5.6. The window pane, of dimensions b_p and h_p, is dry-glazed into a window frame with horizontal clearances of c_1 on both sides and vertical clearances of c_2 on top and bottom. The drift at which the window frame begins to pinch the glass pane, the clear drift Δ_{clear}, is computed from a geometric relationship. The relationship is based on the principle that a rectangular window frame anchored to adjacent stories becomes a parallelogram as a result of interstory drift, and that glass-to-frame contact occurs when the length of the shorter diagonal of the parallelogram is equal to the diagonal of the panel itself. This relationship was first mentioned in Bouwkamp and Meehan (1960), and the current design codes (ASCE 7, FEMA 356, etc.) reference this publication when computing Δ_{clear}.

The exact equation for the clear drift is given in Equation 5.11.

$$\Delta_{clear} = 2c_1 + b_p - \sqrt{b_p{}^2 - 4c_2h_p - 4c_2{}^2} \quad \text{Eq. 5.11}$$

An approximation to the above equation, which is stated in the design codes, is given in Equation 5.12.

$$\Delta_{clear} = 2c_1\left(1 + \frac{h_p}{b_p}\frac{c_2}{c_1}\right) \quad \text{Eq. 5.12}$$

The exact equation (Equation 5.11) and approximate equation (Equation 5.12) are plotted in Fig. 5.7 for values of c_1 = 0.5 in., c_2 = 0.5 in., and b_p = 60 in. The clear drift determined from Equation 5.12 agrees very well with the clear drift determined from Equation 5.11 for a wide range of glass pane heights h_p.

The clear drifts calculated form Equation 5.12 are plotted in Fig. 5.8 for various values of horizontal clearance, c_1, vertical clearance, c_2, and glass pane aspect ratios, h_p/b_p. These plots can be used as design aids to determine the correct combination of c_1, c_2, and h_p/b_p. For example, assume we know from response spectrum or time-history analyses that a maximum interstory drift of 3.2 inches must be accommodated by the window glazing system and that there is an architectural requirement that the window panes have an aspect ratio of h_p/b_p = 1.5. Then, from Fig. 5.8, we can determine that a glazing system with the following combinations of c_1 and c_2 prevent the glass pane from contacting the window frame: c_1 = 0.25 in. and c_2 = 1.0 in.; c_1 = 0.5 in. and c_2 = 0.75 in. or 1.0 in.; c_1 = 0.75 in. and c_2 = 0.75 in. or 1.0 in.; and c_1 = 1.0 in. and c_2 = 0.5 in., 0.75 in., or 1.0 in.

5.2 COMPARISON OF CONNECTOR DEFORMATIONS FROM ANALYTIC EXPRESSIONS AND TIME-HISTORY RESULTS

The analytical equations derived in Section 5.1.1 and 5.1.2 estimate the deformations in the push-pull and column cover connections using response quantities (interstory drift and nodal rotations) of the structural (bare) frame. In this section, these equations will be used to compute the maximum values of deformation in the push-pull and column cover connections using the structural response quantities (interstory drifts and nodal rotations) of the bare frame model (BF). These equations also help to validate the maximum deformations computed from the time-history results.

5.2.1 Push-Pull Connections

The deformations in the push-pull connectors were recorded during the time-history analyses described in Chapter 4. The total deformation in a connector was computed as the vector sum of the horizontal and vertical components of deformation. The deformations in the push-pull connectors are drift-sensitive: the larger the interstory drift, the larger the deformations in the push-pull connections. As discussed in Section 5.1.1, the amount of rotation of the beam-column node ϕ_i (which is directly correlated to the interstory drift) and rotation of the center node of the beam θ_i determine the amount of deformation in the push-pull connection. Moreover, the absolute values of the maximum deformation in the push-pull connectors $\delta_{total,b}$ and $\delta_{total,t}$ for a ground motion was found to occur at the same time in the ground motion record as the maximum rotation of the beam-column node ϕ_i. Thus, the maximum values of the push-pull

deformations $\delta_{total,b,max}$ and $\delta_{total,t,max}$ can be computed from the maximum rotation of the beam-column nodes ϕ_i and the corresponding rotation of the center node in the beams, θ_i. This procedure is outlined in the equations below.

Bottom connectors:	Top connectors:	
$\delta_{x,b,max} = y_b(\phi_{i,max} + \theta_{i,max})$	$\delta_{x,t,max} = y_t(\phi_{i,max} + \theta_{i,max})$	Eq. 5.13
$\delta_{y,b,max} = \frac{L}{2}\theta_{i,max}$	$\delta_{y,t,max} = \frac{L}{2}\theta_{i,max}$	Eq. 5.14
$\delta_{total,b,max} = \sqrt{\delta_{x,b,max}{}^2 + \delta_{y,b,max}{}^2}$	$\delta_{total,t,max} = \sqrt{\delta_{x,t,max}{}^2 + \delta_{y,t,max}{}^2}$	Eq. 5.15

The variables y_b and y_t are the vertical dimensions of the spandrel panel, shown in Fig. 5.1. The variable L is the length of the spandrel panel. The values of nodal rotations in story i, $\phi_{i,max}$ and $\theta_{i,max}$, used in above equations are taken from the results of the time-history results of the bare frame model (BF). The absolute (positive) values of the nodal rotations $\phi_{i,max}$ and $\theta_{i,max}$ are to be used in the equations. These equations allow the engineer to obtain estimates of the maximum demands in the push-pull connections using just a bare frame model (without explicitly modeling the cladding system).

The maximum push-pull connector demands are calculated using these analytical equations for the ground motions in the LA50, LA10, and LA2 bins (20 ground motions in each bin). Then, the median and standard deviations of the maximum values of deformation are computed using Equations 5.16 and 5.17, respectively. Matlab pseudo-code is used to denote the sample median as $\tilde{\delta} = \text{median}(*)$ and the sample standard deviation as $\sigma = \text{std}(*)$. The vector $\Delta_{total,b,max}$ (bottom push-pull connectors) and $\Delta_{total,t,max}$ (top push-pull connectors) are vectors holding the maximum deformation values for all 20 ground motions in a particular bin (i.e. $\Delta_{total,b,max} = [\delta_{total,b,max,1}, \delta_{total,b,max,2}, \ldots, \delta_{total,b,max,20}]$).

Bottom connectors:	Top connectors:	
$\tilde{\delta}_{total,b,max} = \text{median}(\Delta_{total,b,max})$	$\tilde{\delta}_{total,t,max} = \text{median}(\Delta_{total,t,max})$	Eq. 5.16
$\sigma_{total,b,max} = \text{std}(\Delta_{total,b,max})$	$\sigma_{total,t,max} = \text{std}(\Delta_{total,t,max})$	Eq. 5.17

The median and standard deviation values of the maximum push-pull deformations are computed for selected locations that are representative of typical demands up the height of the building. In this case, a center spandrel panel is chosen up the height of the building. The reader is referred to Fig. 5.9 for the locations of the selected spandrel panels and Fig. 5.3 for the location of the top and bottom push-pull connections.

The maximum values of the push-pull deformations from the time-history analyses of the ground motions in the LA50, LA10, and LA2 bins are shown in Fig. 5.10, Fig. 5.11, and Fig. 5.12, respectively, as the blue circles. The values for the bottom push-pull connectors are shown on the left side of the figures, and the values for the top connectors are shown on the right side. The median values of the maximum push-pull deformations from the time-history analyses are

plotted as the thick solid blue line, and the median plus one standard deviation (84th-percentile) values are plotted as the thin solid blue line. As a comparison, the median values of the maximum deformations computed from Equation 5.16 are shown as the thick dashed black line with triangle markers, and the median plus one standard deviation (84th-percentile) values are plotted as the thin dashed black line with triangle markers. As can be seen in the figures, the median values of maximum push-pull deformations are estimated fairly well with the analytical equations. The median plus one standard deviation values computed from Equations 5.16 and 5.17 are larger than the values from the time-history analyses in the upper stories. The median and median plus one standard deviation values and the error percentages are also given in Table 5.1 (for the bottom push-pull connectors) and Table 5.2 (for the top push-pull connectors) for the LA50, LA10, and LA2 ground motion bins. The error in the median and median plus one standard deviation is computed as the percentage difference between the values from the time-history analyses and the analytical equations. Positive errors indicate that the equations overestimate the results of the time-history analyses, and negative errors indicate that the equations underestimate the results.

From Table 5.1, the median values of the maximum deformations in the bottom connectors (calculated with Equation 5.16) are within 9% of the "exact" median values using the time-history results for the LA50 bin. The median plus one standard deviation values (84th-percentile) are within 10% for stories 1-7, while stories 8-9 have much higher errors, due to significant deviations in the beam-column node rotations from the time-history analyses.

For the LA10 bin, the median values calculated from Equation 5.16 are within 8% of the "exact" median values in stories 1-6, while the errors are 15-25% for stories 7-9. The 84th-percentile values using the analytical equations follow a similar trend as in the LA50 bin: the error percentages are low (within 10%) for the lower stories and much higher (up to 38%) for the upper stories.

For the LA2 bin, the error percentages for the median values calculated with Equation 5.16 are up to 27%, and the errors in the calculated median plus one standard deviation values are up to 52%. The errors in the lower stories are larger in the LA2 bin than the errors in the LA50 and LA10 bins, which is due to more significant nonlinearity in the lower stories for the LA2 bin motions.

Similar comparisons can be made for the top push-pull connectors using Table 5.2. The main result is that by using the response values of the bare frame model in the analytical expressions of Equation 5.16 and 5.17, fairly good estimates are made of the median value of the maximum deformation in the bottom and top push-pull connections for the 50%-in-50 year and 10%-in-50 year probability of exceedance levels. The estimated 84th-percentile values of the maximum deformations at these two levels could serve as conservative design values.

5.2.2 Column Cover Connections

The deformations in the column cover connectors were recorded during the time-history analyses described in Chapter 4. The total deformation in a connector was computed as the vector sum of the horizontal and vertical components of deformation. Similar to the push-pull connectors, the deformations in the column cover connectors are drift-sensitive: the larger the interstory drift, the larger deformations in the connectors. As discussed in Section 5.1.2, the amount of interstory drift $\Delta_{h,i}$ and rotations of the center node of the beam above (θ_i) and below

(θ_{i-1}) the column cover determine the amount of deformation in the column cover connections. Moreover, the absolute values of the maximum deformation in the column cover connectors, $\delta_{total,j}$, for a ground motion was found to occur at the same time as the maximum interstory drift. Thus, the maximum values of the connector deformations $\delta_{total,max}$ can be computed from the maximum interstory drift at story i, $\Delta_{h,i,max}$, and the corresponding rotations of the center node in the beam above ($\theta_{i,maz}$) and below ($\theta_{i-i,max}$) the column cover. The four connectors in Fig. 5.5 have slightly different total deformations, as shown by Equation 5.8. Connectors 2 and 3 have larger vector sum deformations than connectors 1 and 4, so the equations for connectors 2 and 3 are used in this method to produce a conservative estimate. This procedure is outlined in the equations below.

Column cover connectors:

$$\delta_{x,max} = \frac{-X^2}{4(X^2+Y^2)}\left[2(y_t\theta_{i-1,max} + y_b\theta_{i,max} + \Delta_{h,i,max} - g) + Y(\theta_{i-1,max} + \theta_{i,max})\right] \quad \text{Eq. 5.18}$$

$$\delta_{y,max} = \frac{-1}{4H(X^2+Y^2)}\left[X^3H(\theta_{i-1,max} - \theta_{i,max}) + \Delta_{h,i,max}{}^2(X^2+Y^2) + 2XY^2H\theta_{i-1,max} + 2XYH(y_t\theta_{i-1,max} + y_b\theta_{i,max}) + 2XYH(\Delta_{h,i,max} - g)\right] \quad \text{Eq. 5.19}$$

$$\delta_{total,max} = \sqrt{\delta_{x,max}{}^2 + \delta_{y,max}{}^2} \quad \text{Eq. 5.20}$$

The values of interstory drift and nodal rotations in story i, $\Delta_{h,i,max}$, $\theta_{i,max}$, and $\theta_{i-i,max}$ used in above equations are taken from the results of the time-history results of the bare frame model (BF). The absolute (positive) values of the interstory drift $\Delta_{h,i,maz}$ and the nodal rotations $\theta_{i,max}$ and $\theta_{i-1,max}$ are to be used in the equations. These equations allow the engineer to obtain estimates of the maximum demands in the column cover connections using just a bare frame model (without explicitly modeling the cladding system).

The maximum column cover connector demands are calculated using Equation 5.20 for the ground motions in the LA50, LA10, and LA2 bins (20 ground motions in each bin). Then, the median and standard deviations of the maximum values of deformation are computed using Equations 5.21 and 5.22, respectively. Matlab pseudo-code is used to denote the sample median as $\tilde{\delta} = \text{median}(*)$ and the sample standard deviation as $\sigma = \text{std}(*)$. The vector $\Delta_{total,max}$ holds the maximum deformation values for all 20 ground motions in a particular bin (i.e. $\Delta_{total,max} = [\delta_{total,max,1}, \delta_{total,max,2}, \ldots, \delta_{total,max,20}]$).

For each column cover connector:

$$\tilde{\delta}_{total,max} = \text{median}(\Delta_{total,max}) \quad \text{Eq. 5.21}$$

$$\sigma_{total,max} = \text{std}(\Delta_{total,max}) \quad \text{Eq. 5.22}$$

The median and standard deviation values of the maximum column cover deformations are computed for selected locations that are representative of typical demands up the height of the building. In this case, the center column cover panel is chosen up the height of the building.

The reader is referred to Fig. 5.13 for the locations of the selected column cover panels and Fig. 5.3 for the location of the column cover connections.

The maximum values of the column cover deformations from the time-history analyses of the ground motions in the LA50, LA10, and LA2 bins are shown in Fig. 5.14, Fig. 5.15, and Fig. 5.16, respectively, as the blue circles. The median values of the maximum deformations from the time-history analyses are plotted as the thick solid blue line, and the median plus one standard deviation (84^{th}-percentile) values are plotted as the thin solid blue line. As a comparison, the median values of the maximum deformations computed from Equation 5.21 are shown as the thick dashed black line with triangle markers, and the median plus one standard deviation (84^{th}-percentile) values are plotted as the thin dashed black line with triangle markers. As can be seen in the figures, the median values of maximum column cover deformations are estimated fairly well with the analytical equations. The median plus one standard deviation values computed from Equations 5.21 and 5.22 are larger than the values from the time-history analyses. The median and median plus one standard deviation values and the error percentages are also given in Table 5.3 for the LA50, LA10, and LA2 ground motion bins. The error in the median and median plus one standard deviation is computed as the percentage difference between the values from the time-history analyses and the analytical equations. Positive errors indicate that the equations overestimate the results of the time-history analyses, and negative errors indicate that the equations underestimate the results.

From Table 5.3, the median values of the maximum deformations in the column cover connectors (calculated with Equation 5.21) are very small for the LA50 bin. The median values from the time-history analyses are up to 0.016 inches, which represents only 13% of the yield value). For the LA50 bin, the majority of the ground motions are not large enough to cause the bolt in the upper slotted connections to impact the end of the slotted hole. For this bin, the median values of maximum deformation computed with Equation 5.21 are up to 224% larger than the median maximum values from the time-history analyses. The analytical equations may not address all of the factors that determine the amount of deformation for smaller earthquakes. However, the deformations computed by the analytical equations are still so small that they do not cause concern for the safety of the connectors. The median plus one standard deviation values (84^{th}-percentile) calculated with the equations are slightly more accurate, with the maximum error percentage of 127% compared to the time-history results.

For the LA10 bin, the median values of maximum deformation are at or exceeding the fracture deformation of 0.34 inches. The median values calculated from Equation 5.21 are within 23% of the "exact" median values from the time-history analyses. The 84^{th}-percentile values using the analytical equations are much more accurate than in the LA50 bin: the error percentages are within 28% of the values from the time-history analyses. At each story, the 84^{th}-percentile values computed with the equation are larger than the values from the time-history results.

For the LA2 bin, the error percentages for the median value calculated with Equation 5.21 are within 12%, while the errors in the calculated median plus one standard deviation values are up to 53%. The median values of maximum deformation from the time-history analyses are up to three times the fracture deformation of the connector; the column cover panels have a high chance of failure in the large intensity earthquakes.

5.3 USING THE PUSHOVER ANALYSIS RESULTS TO COMPUTE THE CONNECTOR DEFORMATIONS

In this section, the response quantities from the nonlinear static pushover analysis of the bare-frame model (BF) are used to compute deformations in the push-pull and column cover connectors. This approach of computing the connector deformations is a further simplification of the method described in Section 5.2 which uses the results of the time-history analyses.

The target response quantities (interstory drifts and nodal rotations) of the bare-frame are computed using the nonlinear static procedure from Chapter 3 of FEMA 356 (FEMA, 2000) at selected seismic intensity levels. These response quantities are used in the analytical equations to determine the expected push-pull and column cover connector deformations. These deformations are compared to the mean values of the maximum push-pull and column cover deformations determined from the time-history analyses in Chapter 4.

5.3.1 Target Bare-Frame Response Quantities at Selected Intensity Levels

The push-pull and column cover connector deformations are to be computed from the target response quantities of the bare-frame model (BF) at selected seismic intensity levels. The target response quantities are determined from the nonlinear static procedure (pushover analysis) from Chapter 3 of FEMA 356 (FEMA, 2000).

The nonlinear pushover curve of the bare-frame model (determined in Chapter 4) is shown in Fig. 5.17. In accordance with the procedure outlined in FEMA 356, a bilinear curve is fitted to the pushover curve to determine the effective yield strength V_y, effective lateral stiffness K_e, and effective fundamental period T_e. The effective modal period T_e is calculated using Equation 5.23.

$$T_e = T_i\sqrt{\frac{K_i}{K_e}} \qquad \text{Eq. 5.23}$$

The value T_i is the initial fundamental period of the bare-frame model determined from the modal analysis. The variable K_i is the initial lateral stiffness of the building determined from the pushover curve, and the variable K_e is the effective lateral stiffness of the building determined from Fig. 5.17. Using the effective fundamental period, the target roof displacement is determined using Equation 5.24.

$$\delta_t = C_0C_1C_2C_3S_a\frac{{T_e}^2}{4\pi^2}g \qquad \text{Eq. 5.24}$$

The value S_a is the spectral acceleration at the effective fundamental period T_e of the bare-frame for the selected seismic intensity level (i.e. 10% probability of exceedance in 50 years, as determined from the USGS). The value g is equal to the acceleration due to gravity (i.e. 386.4 in/sec^2). The variables C_0, C_1, C_2, and C_3 are the modification factors given in section 3.3.3.3.2 of FEMA 356. The C_0 factor relates the spectral displacement of an equivalent SDOF system to the roof displacement of the building MDOF system (commonly called the first mode

participation factor). From the modal analysis, the first mode participation factor (C_0) of the bare-frame model is equal to 1.38. The C_1 factor relates expected maximum inelastic displacements to displacements calculated for linear elastic response. Since the first mode period of the structure (T_1 = 2.13 sec.) is in the constant velocity region of a pseudo-spectral acceleration diagram, the C_1 factor is equal to 1.0. The C_2 factor represents the effect of a pinched hysteretic shape, stiffness degradation, and strength deterioration on the maximum displacement response. For the steel moment-frame used in this research, the C_2 factor is equal to 1.0. The C_3 factor represents increased displacements due to dynamic P-Δ effects. For buildings with positive post-yield stiffness, C_3 is set equal to 1.0. For buildings with negative post-yield stiffness, the value of C_3 is calculated using Equation 5.25.

$$C_3 = 1.0 + \frac{|\alpha|(R-1)^{1.5}}{T_e} \qquad \text{Eq. 5.25}$$

The value of α is the ratio of the post-yield stiffness to the effective elastic stiffness of the bilinear pushover curve shown in Fig. 5.17. The value R is the ratio of the elastic strength demand to the calculated yield strength coefficient; R is determined using Equation 5.26.

$$R = \frac{S_a}{V_y/W} C_m \qquad (R \geq 1) \qquad \text{Eq. 5.26}$$

The variable S_a is the spectral acceleration at the effective fundamental period of the bare-frame for the selected seismic intensity level (i.e. 10% probability of exceedance in 50 years, as determined from the USGS). The variable V_y is the effective yield strength determined from the blinear pushover curve in Fig. 5.17. The variable W is the seismic weight of the building. The variable C_m is the effective mass factor, which is determined from Table 3-1 in FEMA 356. For the nine-story SAC building, the value of C_m is equal to 1.0 since it is a steel moment-frame building with its fundamental period in the constant velocity region.

The values of the above variables and coefficients are calculated for the nine-story building. Using the procedure outlined in FEMA 356 and Fig. 5.17, the initial lateral stiffness is 119 kip/in, and the effective lateral stiffness is 117 kip/in. The fundamental period determined from an eigenvalue analysis is 2.13 sec. Thus, the effective fundamental period, calculated using Equation 5.23, is equal to 2.14 sec. The site location chosen for the nine-story SAC building in this research is on the UC Berkeley campus in Berkeley, California. The values of the spectral acceleration S_a at the effective fundamental period of the bare-frame for the 50%-, 20%-, 10%-, and 2%-in-50 year probability of exceedance levels are 0.11g, 0.22g, 0.34g, and 0.65g, respectively (determined in Chapter 4). The value of the coefficients are C_0 = 1.38, C_1 = 1.0, and C_2 = 1.0. The seismic weight W of the nine-story SAC building is 10,422 kips, and the effective yield strength of the building is 1,980 kips. The value of C_m is 1.0. Thus, the value of R is 1.0, 1.2, 1.8, and 3.4 for the 50%-, 20%-, 10%-, and 2%-in-50 year probability of exceedance levels, respectively. The value for α for use in Equation 5.25 is equal to 0.025. Therefore, the value of C_3 is 1.00, 1.00, 1.00, and 1.04 for the 50%-, 20%-, 10%-, and 2%-in-50 year probability of exceedance levels. Using these values, the target roof displacements are calculated for each seismic intensity level using Equation 5.24. The target roof displacements are 6.74 in., 13.48 in., 20.84 in., and 41.42 in. for the 50%-, 20%-, 10%-, and 2%-in-50 year probability of exceedance levels, respectively.

Now that the target roof displacement has been determined for the selected seismic intensity levels, the corresponding interstory drifts Δh_i, the beam-column node rotations ϕ_i, and the beam center node rotations θ_i at story i of the bare-frame can be determined based on the deflected shape of the structure at this target displacement. The interstory drifts and node rotations for the bare-frame structure are shown in Fig. 5.18 and Fig. 5.19 for the four seismic intensities. These response quantities are then used in the analytical equations to compute the deformations in the push-pull connectors and column cover connectors.

5.3.2 Push-Pull Connections

As shown in Section 5.1.1, the deformations in the push-pull connectors are computed from the rotations of the beam-column nodes and the rotations of the beam center node of the bare-frame model. To avoid confusion with Section 5.2, the beam-column node rotations and the beam center node rotations at story i of the bare-frame, determined from the pushover analysis at the target displacement (for a certain seismic intensity), are denoted as $\phi_{i,PO}$ and $\theta_{i,PO}$, respectively. Using these rotations (which are both taken as positive rotations), the deformations corresponding to the target roof displacement are computed with the procedure outlined below.

Bottom connectors:	Top connectors:	
$\delta_{x,b,PO} = y_b(\phi_{i,PO} + \theta_{i,PO})$	$\delta_{x,t,PO} = y_t(\phi_{i,PO} + \theta_{i,PO})$	Eq. 5.27
$\delta_{y,b,PO} = \frac{L}{2}\theta_{i,PO}$	$\delta_{y,t,PO} = \frac{L}{2}\theta_{i,PO}$	Eq. 5.28
$\delta_{target,b} = \sqrt{{\delta_{x,b,PO}}^2 + {\delta_{y,b,PO}}^2}$	$\delta_{target,t} = \sqrt{{\delta_{x,t,PO}}^2 + {\delta_{y,t,PO}}^2}$	Eq. 5.29

The total deformations in the bottom and top connectors, $\delta_{target,b}$ and $\delta_{target,t}$, respectively, are the vector sum of their horizontal and vertical components. These total deformations in each story correspond to the target roof displacement for the selected seismic intensity.

The mean and standard deviation of the maximum deformations in the bottom push-pull connectors, determined from the time-history analyses, were given in Figure 4.35 and Table 4.8 of Chapter 4. These mean and mean plus one standard deviation (time-history) values of the maximum push-pull deformations are shown in Fig. 5.20 and Fig. 5.21 for the 50%, 20%, 10%, and 2%-in-50 year probability of exceedance levels. As a comparison, the total deformations in the bottom connectors at the target roof displacement, $\delta_{target,b}$, computed with Equation 5.29 is also shown in Fig. 5.20 and Fig. 5.21 for the 50%, 20% 10%, and 2%-in-50 year probability of exceedance levels. To compute the design values of the total deformation in the bottom push-pull connectors, a factor is multiplied by the deformations at the target roof displacement, $\delta_{target,b}$, to increase $\delta_{target,b}$ to the mean plus one standard deviation values from the time-history analyses. For simplicity, this multiplying factor, F_{pp}, is assumed to be constant up the height of the building. The design values of the deformations in the push-pull connectors are summarized in Equation 5.30.

Bottom connectors: Top connectors:

$$\delta_{design,b} = F_{pp}\delta_{target,b} \qquad \delta_{design,t} = F_{pp}\delta_{target,t} \qquad \text{Eq. 5.30}$$

The multiplying factors are found by scaling the deformations at the target roof displacement to as close to the mean plus one standard deviation values from the time-history analyses as possible (in a least squares sense). In this research, the multiplying factor, F_{pp}, used to compute the design deformations, $\delta_{design,b}$, are approximately 1.7, 1.4, 1.3, and 1.2 for the 50%-, 20%-, 10%-, and 2%-in-50 year probability of exceedance levels, respectively. The multiplying factors for the top push-pull connectors are taken equal to the multiplying factors in the bottom connectors.

The design values of the push-pull connectors, computed as the product of the target deformation and the multiplying factor, are shown in Fig. 5.20 and Fig. 5.21 for the 50%-, 20%-, 10%-, and 2%-in-50 year probability of exceedance levels. The design values provide a conservative estimate of the maximum total deformation for the selected seismic intensities. For high seismic intensities (2% PE in 50 years), the method outlined in this section is not applicable because at this level, the bare-frame exhibits highly nonlinear behavior and is at risk of collapse. As shown in Fig. 5.21b, the profile of the design deformations is significantly different from the mean plus one standard deviation deformations from the time-history results. The variation of F_{pp} with the seismic intensity (spectral acceleration at the fundamental period) is shown in Fig. 5.22. The factor decreases with increasing seismic intensity level. The dotted line in the curve represents the relationship for high seismic intensities; the method discussed in this section is not applicable for these seismic levels. A measure of the reliability index corresponding to the design deformations is computed as the average number of standard deviations that the design deformations are from the mean deformations computed from the time-history analyses. The reliability indexes are 2.7, 2.3, 2.3, and 2.7 for the 50%-, 20%-, 10%-, and 2%-in-50 year probability of exceedance levels.

5.3.3 Column Cover Connections

As shown in Section 5.1.2, the deformations in the column cover connectors are computed from the interstory drifts and the rotations of the beam center nodes of the bare-frame model. To avoid confusion with Section 5.2, the interstory drifts and beam-column node rotations at story i of the bare-frame, determined from the pushover analysis at the target displacement (for a certain seismic intensity), are denoted as $\Delta h_{i,PO}$ and $\theta_{i,PO}$, respectively. Using these drifts and rotations (which are both taken as positive values), the deformations corresponding to the target roof displacement are computed with the equations below. The four connectors in Fig. 5.5 have slightly different total deformations, as shown by Equation 5.8. However, connectors 2 and 3 have larger vector sum deformations than connectors 1 and 4, so their equations are used in this method.

Column cover connectors:

$$\delta_{x,PO} = \frac{-X^2}{4(X^2+Y^2)}\left[2(y_t\theta_{i-1,PO} + y_b\theta_{i,PO} + \Delta_{h,i,PO} - g) + Y(\theta_{i-1,PO} + \theta_{i,PO})\right] \qquad \text{Eq. 5.31}$$

$$\delta_{y,PO} = \frac{-1}{4H(X^2+Y^2)}\left[X^3H\left(\theta_{i-1,PO} - \theta_{i,PO}\right) + {\Delta_{h,i,PO}}^2(X^2+Y^2) + 2XY^2H\theta_{i-1,PO} + 2XYH(y_t\theta_{i-1,PO} + y_b\theta_{i,PO}) + 2XYH(\Delta_{h,i,PO} - g)\right] \quad \text{Eq. 5.32}$$

$$\delta_{target} = \sqrt{{\delta_{x,PO}}^2 + {\delta_{y,PO}}^2} \quad \text{Eq. 5.33}$$

The total deformation in the column cover connectors, δ_{target}, is the vector sum of their horizontal and vertical components. These total deformations in each story correspond to the target roof displacement for the selected seismic intensity.

The mean and standard deviation of the maximum deformations in the column cover connectors, determined from the time-history analyses, were given in Figure 4.39 and Table 4.9 of Chapter 4. These mean and mean plus one standard deviation (time-history) values of the maximum column cover connector deformations are shown Fig. 5.23 and Fig. 5.24 for the 50%, 20%, 10%, and 2%-in-50 year probability of exceedance levels. As a comparison, the target deformations in the column cover connectors, δ_{target}, computed with Equation 5.33 is also shown in Fig. 5.23 and Fig. 5.24 for the 50%, 20% 10%, and 2%-in-50 year probability of exceedance levels. To compute the design values of the total deformation in the column cover connectors, a factor is multiplied by the deformations at the target roof displacement, δ_{target}, to increase δ_{target} to the mean plus one standard deviation values from the time-history analyses. For simplicity, this multiplying factor, F_{cc}, is assumed to be constant up the height of the building. The design value of the deformations in the column cover connectors is summarized in Equation 5.34.

$$\delta_{design} = F_{cc}\delta_{target} \quad \text{Eq. 5.34}$$

The multiplying factors are found by scaling the deformations at the target roof displacement to as close to the mean plus one standard deviation values from the time-history analyses as possible (in a least squares sense). In this research, the multiplying factor, F_{cc}, used to compute the design deformations, δ_{design}, are approximately 2.0, 2.5, 2.7, and 2.9 for the 50%-, 20%-, 10%-, and 2%-in-50 year probability of exceedance levels, respectively.

The design values of the column cover connectors, computed as the product of the target deformation and the multiplying factor, are shown in Fig. 5.23 and Fig. 5.24 for the 50%-, 20%-, 10%-, and 2%-in-50 year probability of exceedance levels. The design values provide a conservative estimate of the maximum total deformation for the selected seismic intensities. For high seismic intensities (2% PE in 50 years), the method outlined in this section is not applicable because at this level, the bare-frame exhibits highly nonlinear behavior and is at risk of collapse. As shown in Fig. 5.24b, the profile of the design deformations is significantly different from the mean plus one standard deviation deformations from the time-history results. The variation of F_{cc} with the seismic intensity (spectral acceleration at the fundamental period) is shown in Fig. 5.25. The factor increases with increasing seismic intensity level. The dotted line in the curve represents the relationship for high seismic intensities; the method discussed in this section is not applicable for these seismic levels. A measure of the reliability index corresponding to the design deformations is computed as the average number of standard deviations that the design deformations are from the mean deformations computed from the time-history analyses. The reliability indexes are 1.3, 1.3, 1.1, and 1.0 for the 50%-, 20%-, 10%-, and 2%-in-50 year probability of exceedance levels.

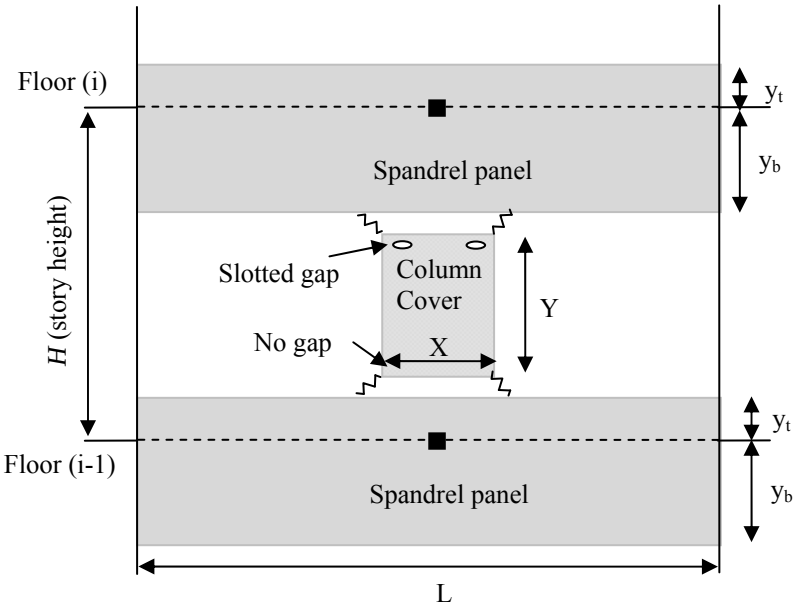

Fig. 5.1 Cladding system showing spandrel panels and column cover

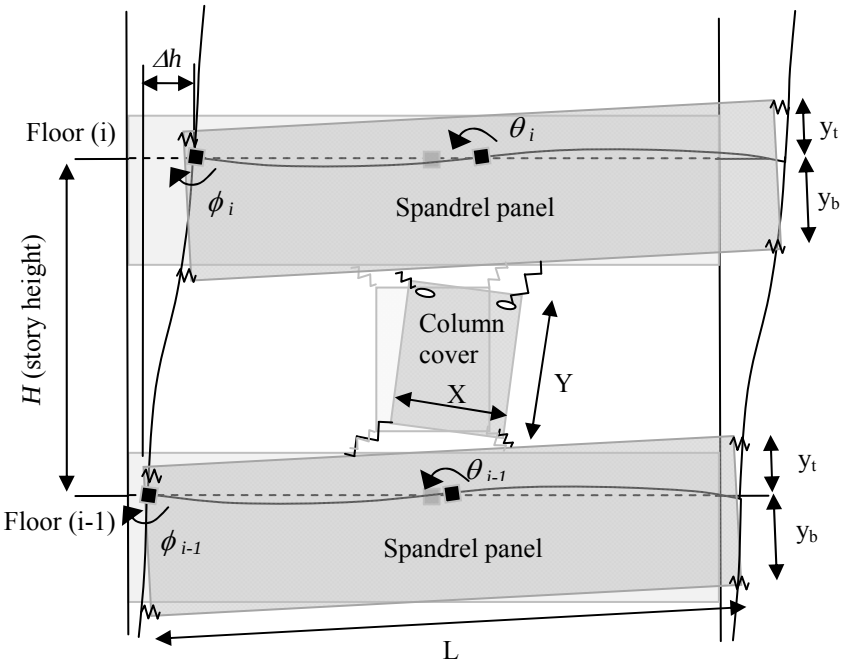

Fig. 5.2 Deformed cladding system

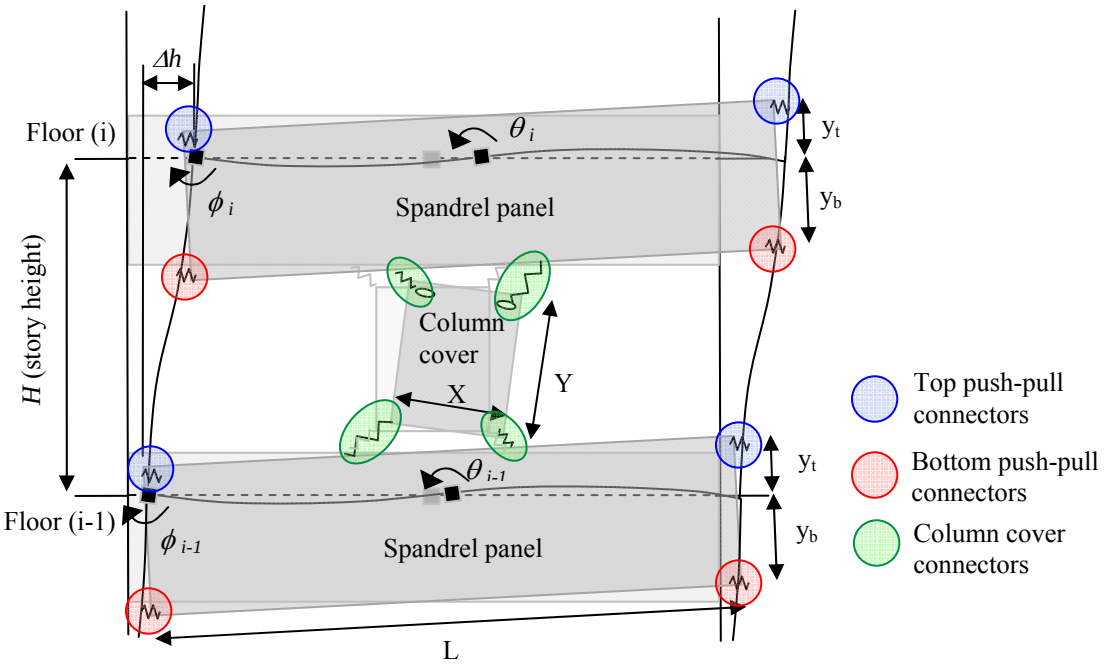

Fig. 5.3 Deformed cladding system showing location of top push-pull connectors, bottom push-pull connectors, and column cover connectors

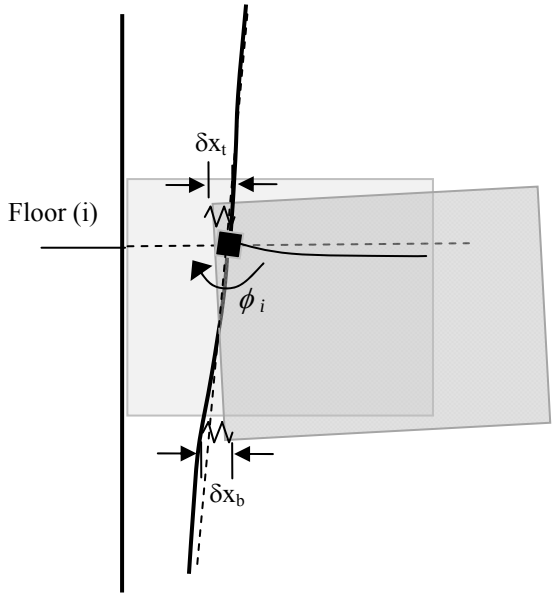

Fig. 5.4 Close-up view of one side of spandrel panel showing deformation of push-pull connectors

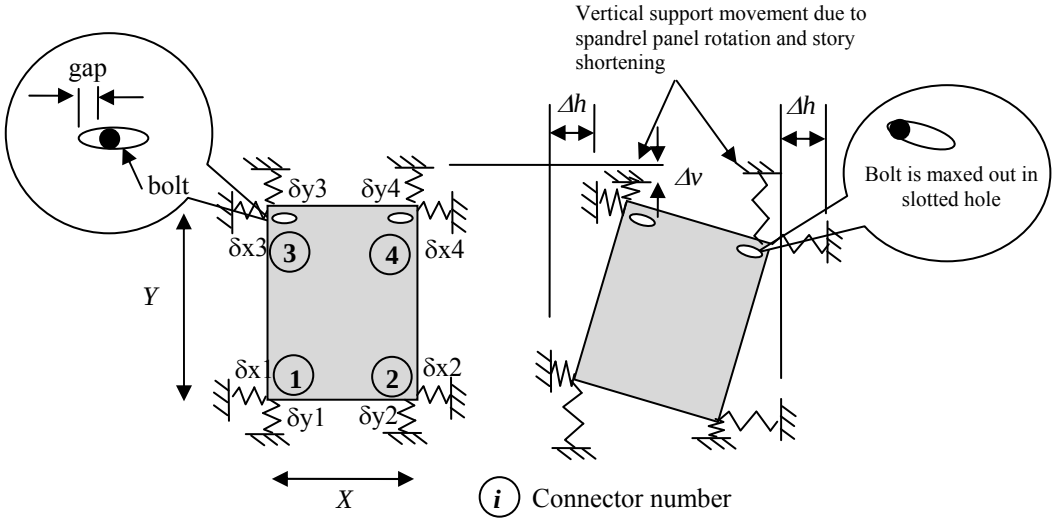

Fig. 5.5 Deformation of connections can be analyzed as a support movement problem

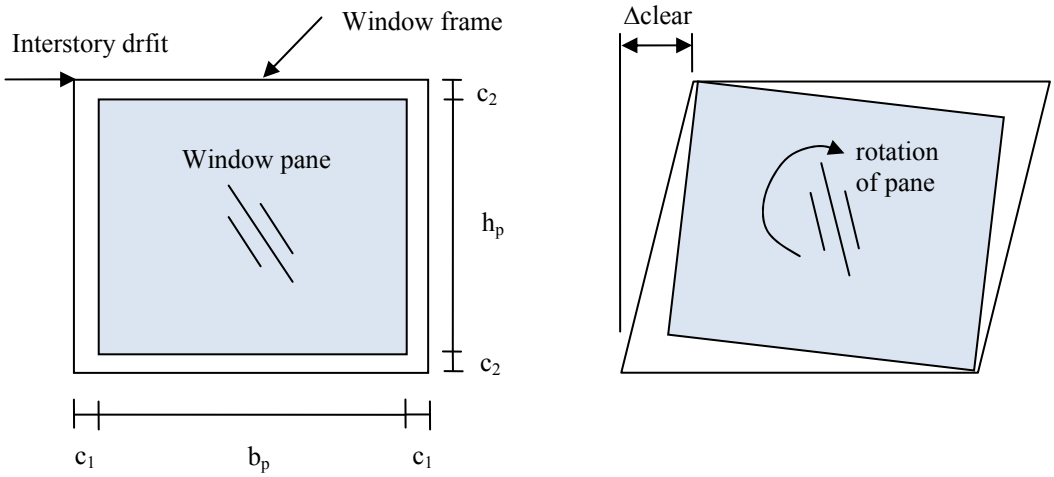

(a) Undeformed configuration

(b) Deformed configuration: glass pane coming into contact with window framing at displacement Δclear.

Fig. 5.6 Damage to the glass pane starts to occur at the clear drift, Δ_{clear}, the drift at which the frame impacts the glass

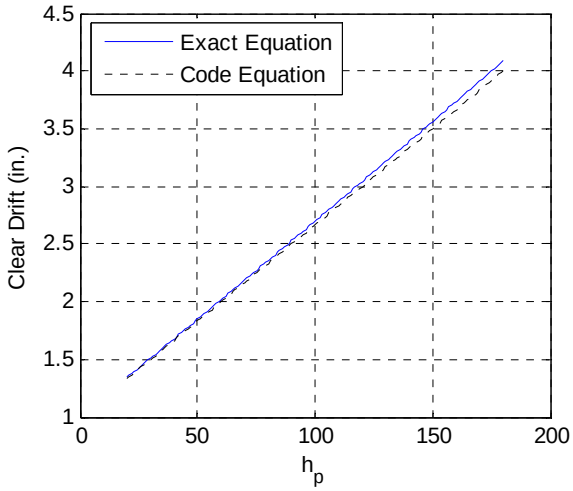

Fig. 5.7 The code equation for clear drift is a very good approximation to the exact equation

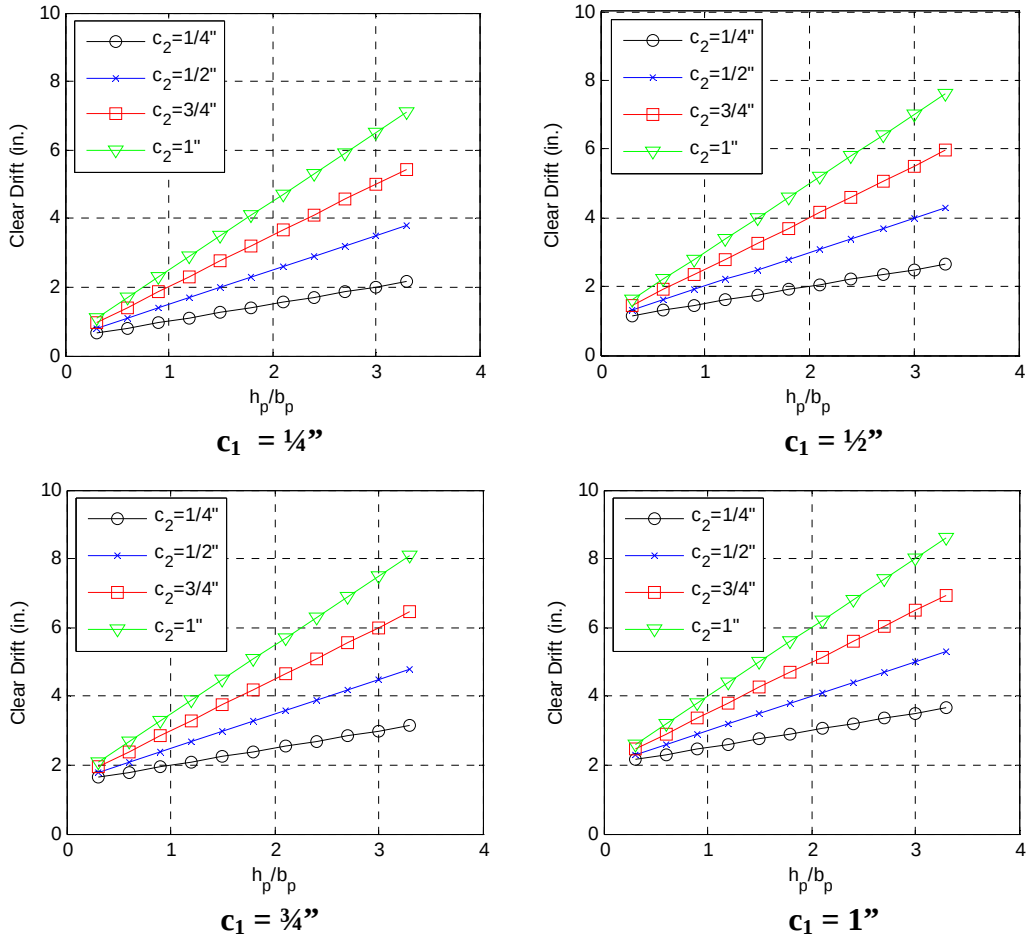

Fig. 5.8 The code equation for clear drift is plotted for various edge clearances and pane aspect ratios

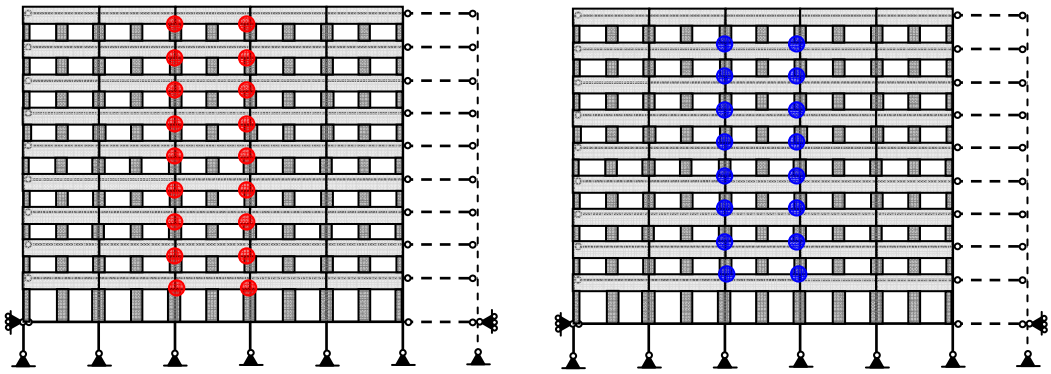

Bottom push-pull connectors in center spandrel panel

Top push-pull connectors in center spandrel panel

Fig. 5.9 Location of representative push-pull connectors for comparison study

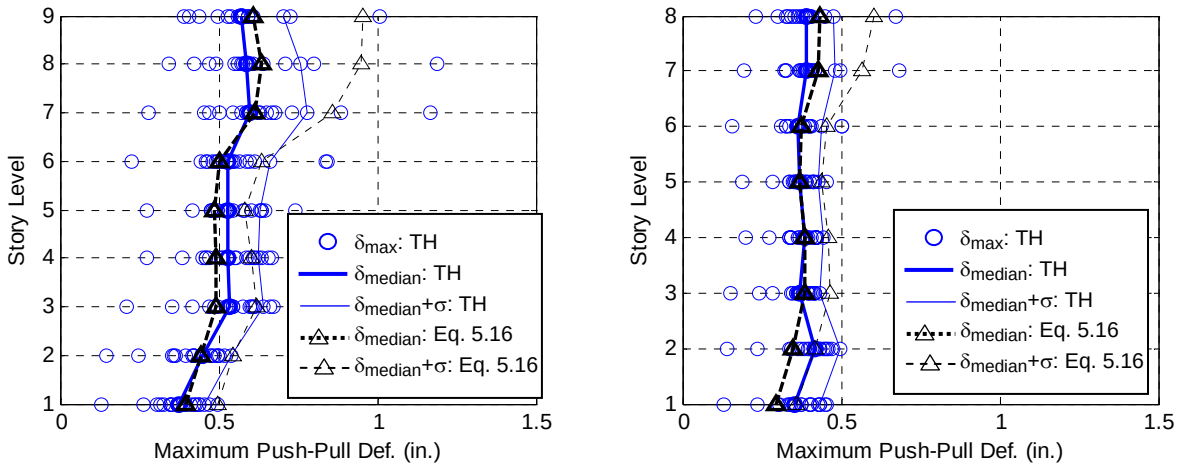

(a) connectors at bottom of panel

(b) connectors at top of panel

Fig. 5.10 LA50: Comparison of median values of peak push-push deformations from time history results and analytical equations for (a) connectors at bottom of panel and (b) connectors at top of panel in LA50 bin

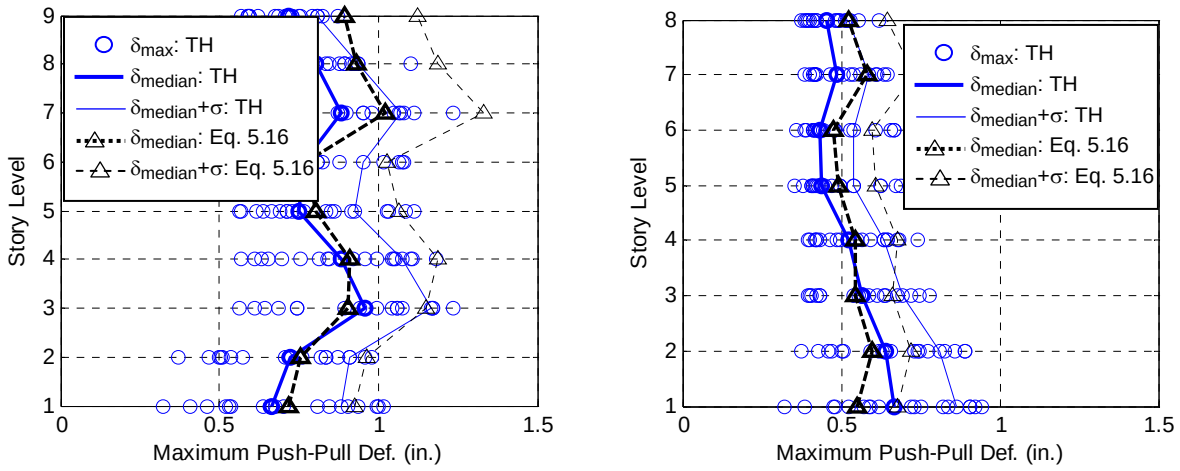

(a) connectors at bottom of panel (b) connectors at top of panel

Fig. 5.11 LA10: Comparison of median values of peak push-push deformations from time history results and analytical equations for (a) connectors at bottom of panel and (b) connectors at top of panel for LA10 bin

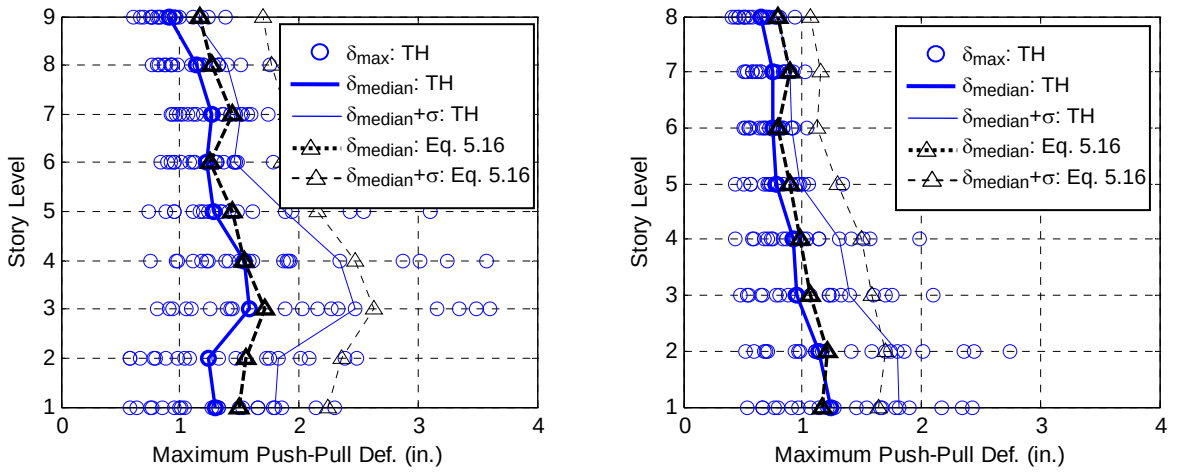

(a) connectors at bottom of panel (b) connectors at top of panel

Fig. 5.12 LA2: Comparison of median values of peak push-push deformations from time history results and analytical equations for (a) connectors at bottom of panel and (b) connectors at top of panel for LA2 bin

Table 5.1 Bottom push-pull connectors: comparison of median values of peak deformation from time history results and analytical equations

Story	Ground Motion Bin	Median Peak Deformation			Median + σ Peak Deformation		
		Time History (in.)	Equation 5.16 (in.)	Percent Error (%)	Time History (in.)	Equation 5.16 (in.)	Percent Error (%)
1	LA50	0.37	0.39	5.5	0.46	0.50	8.7
	LA10	0.67	0.72	8.0	0.88	0.92	4.8
	LA2	1.30	1.50	15.6	1.80	2.24	24.5
2	LA50	0.45	0.44	-1.3	0.54	0.54	0.0
	LA10	0.72	0.76	4.7	0.91	0.96	5.6
	LA2	1.24	1.56	25.4	1.83	2.35	28.5
3	LA50	0.53	0.49	-7.5	0.64	0.62	-4.0
	LA10	0.96	0.90	-5.8	1.17	1.15	-1.3
	LA2	1.58	1.71	8.3	2.48	2.63	6.0
4	LA50	0.53	0.49	-7.5	0.63	0.61	-3.6
	LA10	0.88	0.91	2.8	1.08	1.19	10.2
	LA2	1.54	1.54	0.0	2.35	2.47	5.4
5	LA50	0.53	0.49	-7.5	0.63	0.58	-8.0
	LA10	0.75	0.81	7.7	0.93	1.06	15.0
	LA2	1.29	1.44	11.7	1.89	2.16	14.4
6	LA50	0.53	0.50	-4.7	0.66	0.63	-4.0
	LA10	0.77	0.77	0.0	0.95	1.03	7.7
	LA2	1.22	1.26	3.0	1.46	1.86	27.1
7	LA50	0.60	0.61	2.8	0.78	0.86	10.3
	LA10	0.89	1.02	15.8	1.07	1.33	24.5
	LA2	1.26	1.45	14.3	1.51	1.91	26.2
8	LA50	0.59	0.64	8.3	0.76	0.95	24.6
	LA10	0.81	0.93	15.5	0.93	1.19	27.2
	LA2	1.14	1.27	12.2	1.39	1.77	26.7
9	LA50	0.57	0.61	6.1	0.70	0.96	36.1
	LA10	0.72	0.89	24.9	0.81	1.12	38.9
	LA2	0.92	1.17	27.4	1.11	1.69	52.6

Table 5.2 Top push-pull connectors: comparison of median values of peak deformation from time history results and analytical equations

Story	Ground Motion Bin	Median Peak Deformation			Median + σ Peak Deformation		
		Time History (in.)	Equation 5.16 (in.)	Percent Error (%)	Time History (in.)	Equation 5.16 (in.)	Percent Error (%)
1	LA50	0.35	0.29	-16.5	0.43	0.36	-17.1
	LA10	0.67	0.55	-17.5	0.86	0.68	-21.7
	LA2	1.24	1.17	-5.9	1.82	1.64	-9.9
2	LA50	0.42	0.35	-16.5	0.50	0.42	-16.2
	LA10	0.64	0.60	-7.0	0.81	0.72	-11.1
	LA2	1.14	1.21	6.3	1.80	1.70	-5.6
3	LA50	0.37	0.39	4.9	0.44	0.47	7.1
	LA10	0.57	0.54	-4.3	0.69	0.66	-4.3
	LA2	0.95	1.07	12.9	1.40	1.58	13.1
4	LA50	0.39	0.39	0.0	0.44	0.46	3.5
	LA10	0.52	0.55	4.4	0.64	0.68	6.7
	LA2	0.92	0.98	6.3	1.31	1.50	14.7
5	LA50	0.37	0.37	0.0	0.43	0.44	2.5
	LA10	0.44	0.49	11.8	0.54	0.61	13.0
	LA2	0.78	0.89	14.9	0.98	1.29	31.5
6	LA50	0.37	0.38	3.1	0.44	0.46	4.3
	LA10	0.44	0.48	9.8	0.54	0.60	11.6
	LA2	0.76	0.80	5.2	0.91	1.13	24.7
7	LA50	0.39	0.43	10.1	0.48	0.57	17.8
	LA10	0.49	0.58	19.6	0.59	0.73	24.0
	LA2	0.75	0.90	18.8	0.90	1.16	27.9
8	LA50	0.39	0.43	11.2	0.47	0.60	27.4
	LA10	0.45	0.52	15.6	0.52	0.65	23.4
	LA2	0.65	0.80	23.1	0.79	1.07	35.2

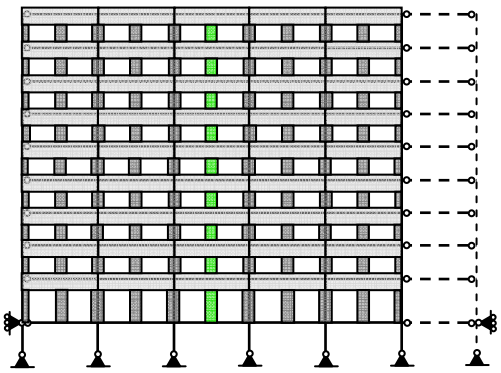

Column cover connectors in center column cover panel

Fig. 5.13 Location of representative column cover connectors for comparison study

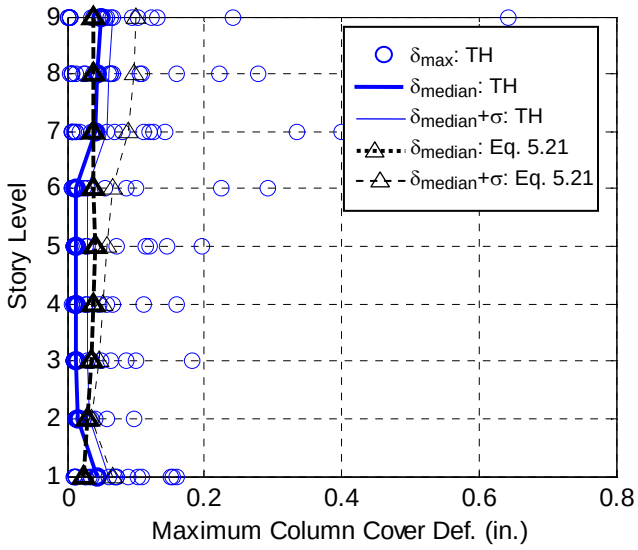

Fig. 5.14 LA50: Comparison of median values of peak column cover deformations from time history results and analytical equations for LA50 bin

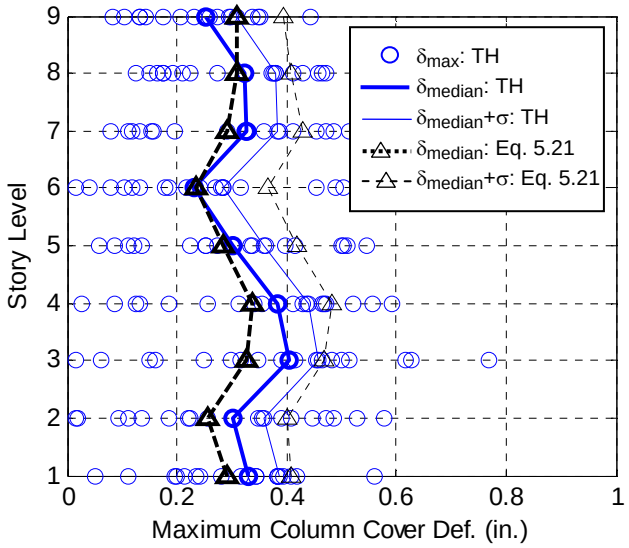

Fig. 5.15 LA10: Comparison of median values of peak column cover deformations from time history results and analytical equations for LA10 bin

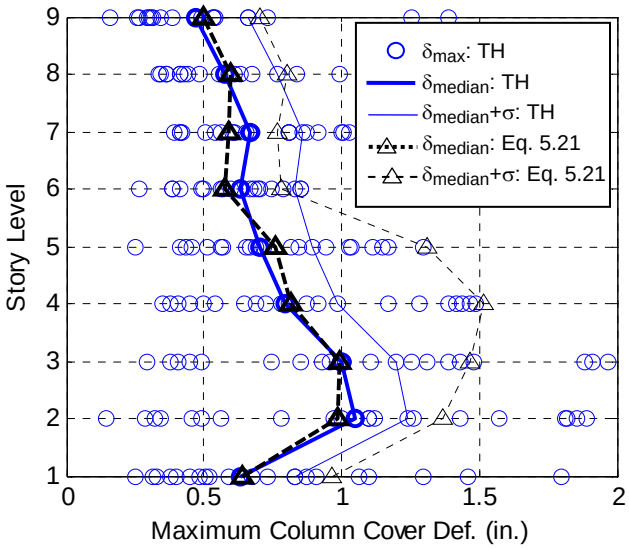

Fig. 5.16 LA2: Comparison of median values of peak column cover deformations from time history results and analytical equations for LA2 bin

Table 5.3 Comparison of median values of peak deformation in column cover connectors from time history results and analytical equations

Story	Ground Motion Bin	Median Peak Deformation			Median + σ Peak Deformation		
		Time History (in.)	Equation 5.21 (in.)	Percent Error (%)	Time History (in.)	Equation 5.21 (in.)	Percent Error (%)
1	LA50	0.045	0.024	-46.7	0.062	0.066	6.7
	LA10	0.33	0.29	-11.7	0.39	0.41	5.7
	LA2	0.64	0.64	0.0	0.83	0.97	16.8
2	LA50	0.016	0.030	91.8	0.032	0.037	12.7
	LA10	0.30	0.26	-14.9	0.36	0.40	12.5
	LA2	1.05	0.98	-6.2	1.24	1.37	10.1
3	LA50	0.013	0.036	175.4	0.030	0.047	55.9
	LA10	0.40	0.33	-18.7	0.46	0.47	2.1
	LA2	1.00	1.00	0.0	1.20	1.46	22.5
4	LA50	0.012	0.038	223.9	0.029	0.052	82.3
	LA10	0.38	0.34	-12.0	0.44	0.48	10.0
	LA2	0.80	0.82	2.6	0.99	1.52	53.4
5	LA50	0.013	0.040	219.2	0.029	0.058	98.4
	LA10	0.30	0.28	-6.1	0.36	0.42	17.4
	LA2	0.70	0.76	8.1	0.90	1.31	46.3
6	LA50	0.012	0.037	201.3	0.029	0.066	127.4
	LA10	0.23	0.24	2.7	0.29	0.36	27.9
	LA2	0.63	0.58	-9.2	0.83	0.78	-5.3
7	LA50	0.040	0.039	-3.5	0.057	0.090	56.8
	LA10	0.33	0.29	-11.1	0.38	0.43	11.6
	LA2	0.67	0.59	-11.5	0.86	0.77	-10.6
8	LA50	0.044	0.038	-12.1	0.061	0.099	62.8
	LA10	0.32	0.31	-5.0	0.38	0.41	7.8
	LA2	0.57	0.60	4.1	0.76	0.80	4.9
9	LA50	0.050	0.039	-21.6	0.066	0.100	51.2
	LA10	0.25	0.31	22.8	0.31	0.39	27.6
	LA2	0.47	0.50	6.7	0.66	0.70	5.9

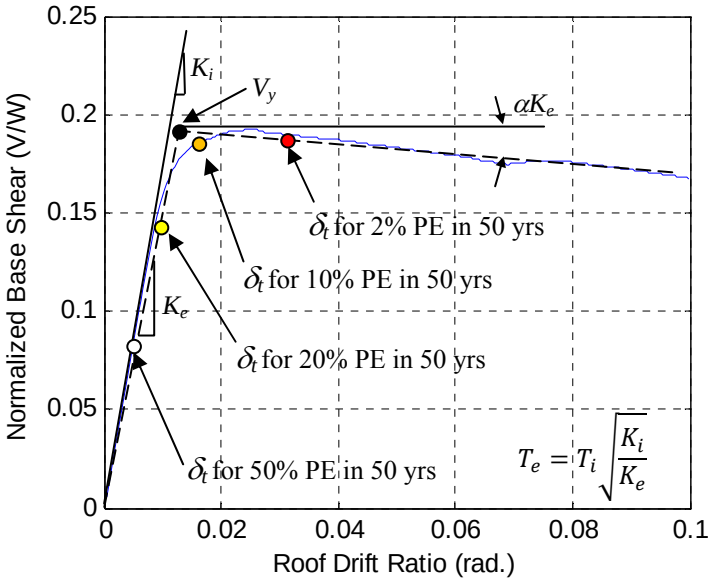

Fig. 5.17 Idealized pushover curve to determine effective yield strength V_y, effective lateral stiffness K_e, and effective fundamental period T_e, and target roof displacement δ_t at selected seismic intensities

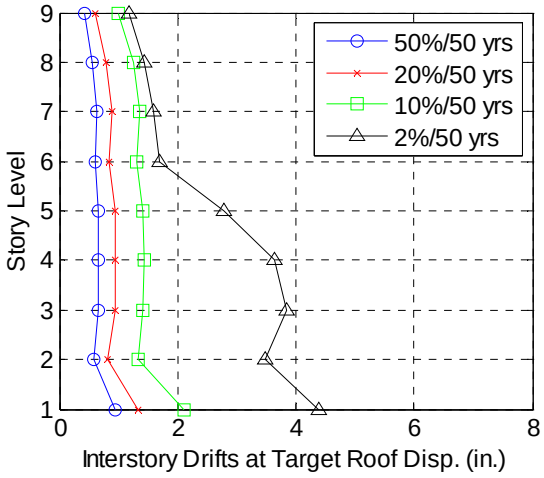

Fig. 5.18 Interstory drifts in the bare-frame model at the target roof displacement for three selected seismic intensities

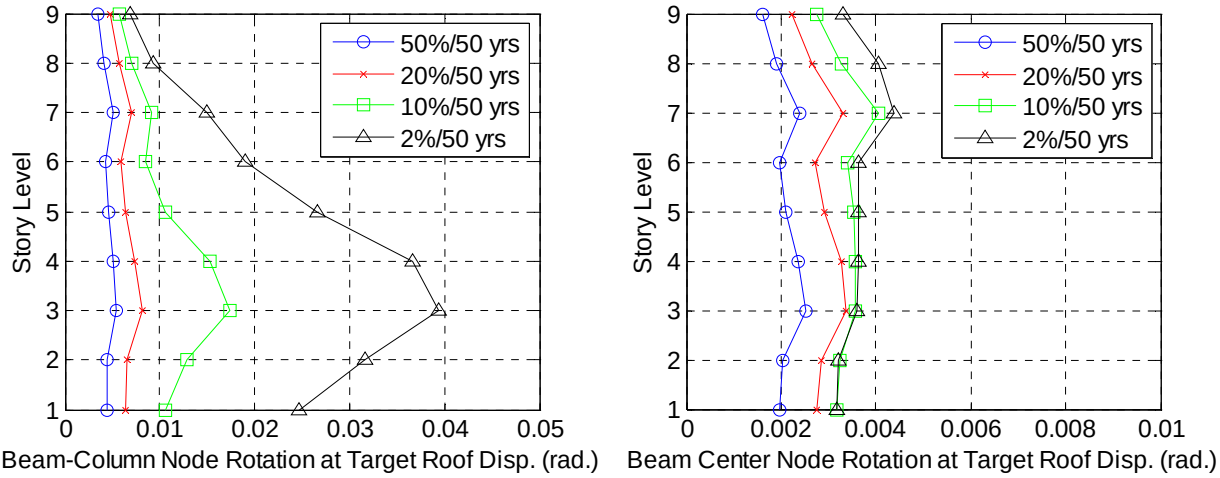

Fig. 5.19 Beam-column node rotations (left) and beam center node rotations (left) in the bare frame model at the target roof displacement for three selected seismic intensities

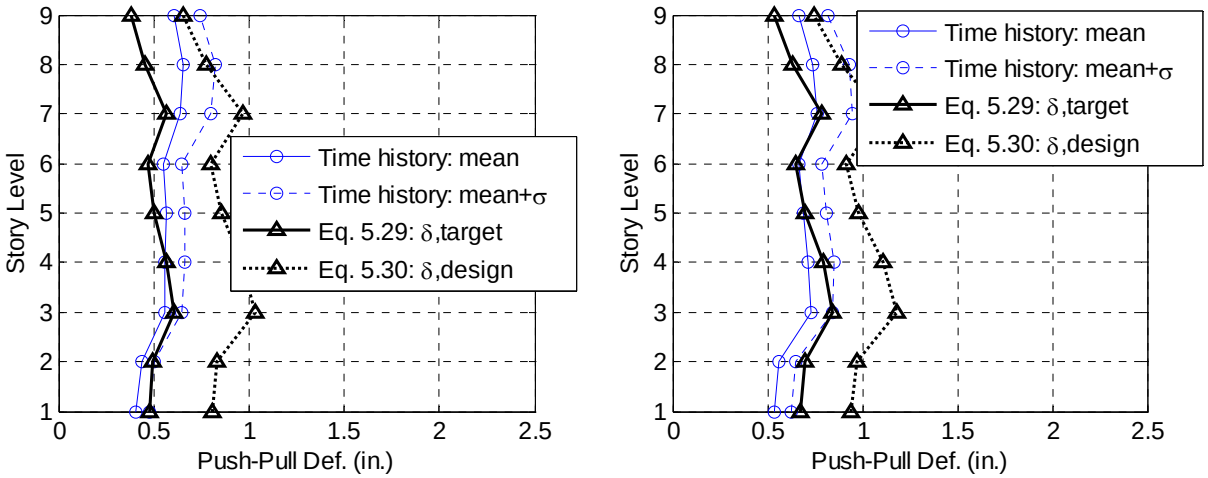

(a) 50% PE in 50 years **(b) 20% PE in 50 years**

Fig. 5.20 Plot showing the target and design deformation in the bottom push-pull connectors compared to the mean and mean plus one standard deviation deformations computed from the time-history analyses for the 50% and 20% PE in 50 years

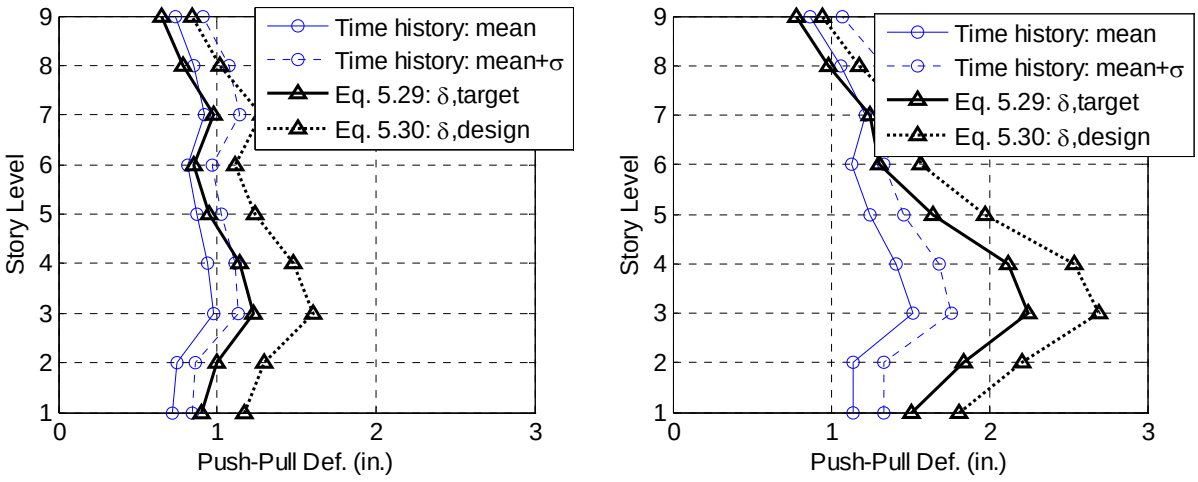

(a) 10% PE in 50 years **(b) 2% PE in 50 years**

Fig. 5.21 Plot showing the target and design deformation in the bottom push-pull connectors compared to the mean and mean plus one standard deviation deformations computed from the time-history analyses for the 10% and 2% PE in 50 years

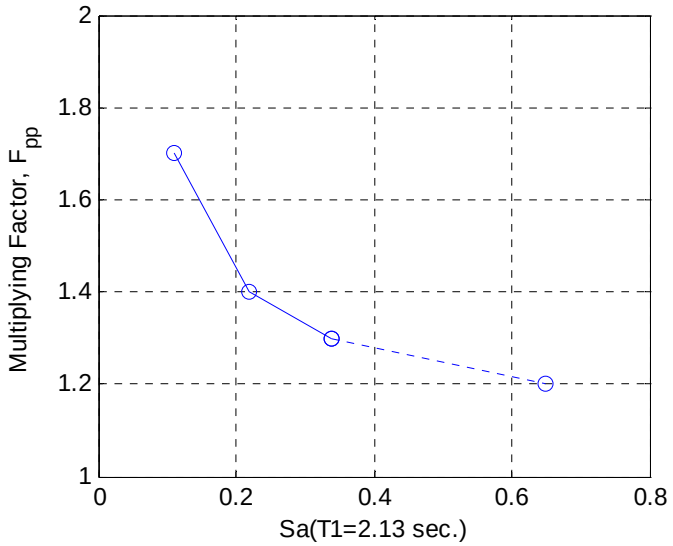

Fig. 5.22 Variation of scale factor, F_{pp}, with seismic intensity level

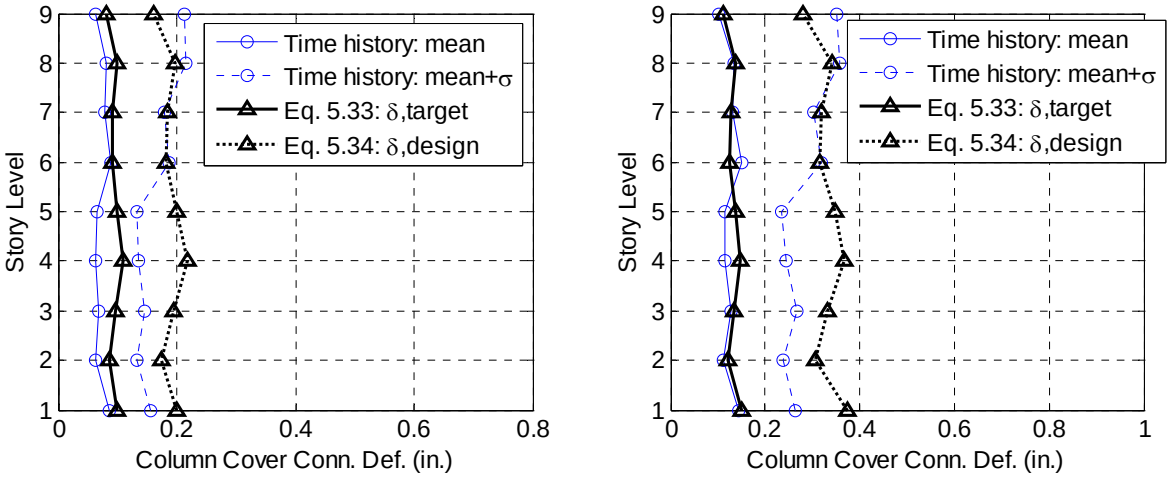

(a) 50% PE in 50 years **(b) 20% PE in 50 years**

Fig. 5.23 Plot showing the target and design deformation in the column cover connectors compared to the mean and mean plus one standard deviation deformations computed from the time-history analyses for the 50% and 20% PE in 50 years

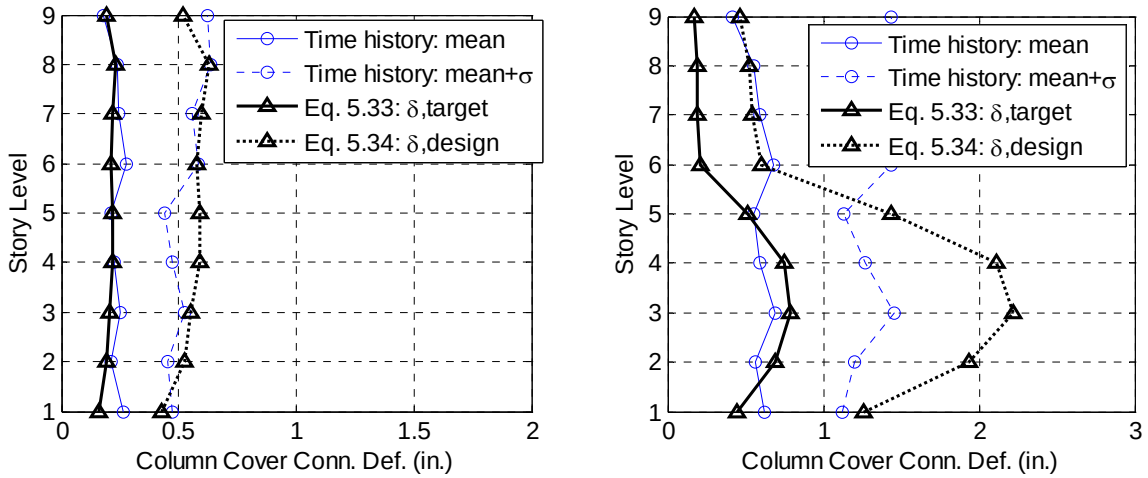

Fig. 5.24 Plot showing the target and design deformation in the column cover connectors compared to the mean and mean plus one standard deviation deformations computed from the time-history analyses for the 10% and 2% PE in 50 years

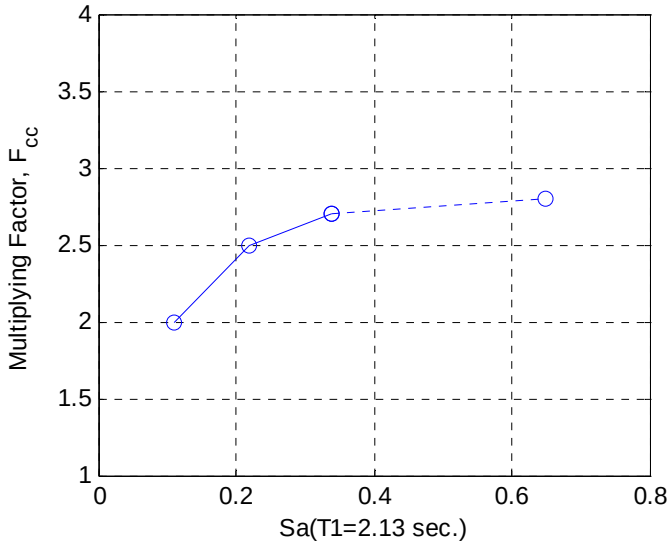

Fig. 5.25 Variation of scale factor, F_{cc}, with seismic intensity level

Chapter 6: Probabilistic Evaluation of Column Cover Connections

In this chapter, the structural reliability of the column cover panels in model C3 is investigated. The analytical results summarized in Chapter 4 revealed that the column cover connections had very high demands and were especially susceptible to failure. The analytical expressions for the column cover demands are used along with time history results of the finite element model C3 to calculate the structural reliability of the column cover connections.

The limit-state functions of the column covers are formulated using the analytical expressions for their deformations that were developed in Chapter 5. The random variables include the maximum interstory drift in each story and corresponding node rotations, the gap width in the slotted connections, and the failure deformation of the connections. The complete cladding system is analyzed story by story to determine the probability of failure of different numbers of panels per story.

The column cover connections were found to be very unreliable. Using FORM, the probabilities of failing one panel per story are as high as 44%, 70%, and 100% for the low, moderate, and high hazard level, respectively. A sensitivity analysis was performed to determine the effect of the distribution parameters and limit state parameters on the connection reliabilities. The conditional probabilities of failing one panel in a story given that a panel in another story has failed are discussed to demonstrate their usefulness in determining the state of the cladding system after an earthquake has occurred. Considering a 50 year lifetime of the building, the total story system failure probabilities were as high as 48.4%.

6.1 TIME-HISTORY ANALYSES OF MODEL C3

For the probabilistic evaluation, a site is chosen for the building and representative ground motions are selected for time-history analyses. The UC Berkeley campus is selected as the building site, and the UC Berkeley campus seismic guidelines are used to select the ground motions. The elevation of model C3 from Chapter 3 is shown in Fig. 6.1, and a detailed view of the cladding system is shown in Fig. 6.2.

6.1.1 Selected Ground Motions

The building site is located on the UC Berkeley campus in Berkeley, California. The intensity measure selected to evaluate the seismic hazard is the spectral acceleration at the first

mode period of the building. The expected spectral accelerations at this site are obtained from the probabilistic hazard curves for spectral acceleration from the UC Berkeley campus guidelines. Three hazard levels were selected that correspond to 50% probability of exceeding the spectral acceleration at the site in 50 years, 10% probability of exceedance in 50 years, and 2% probability of exceedance in 50 years. These levels are representative of low, moderate, and high levels of seismic intensity, respectively. The spectral accelerations were adjusted using FEMA 450 to account for the correct soil conditions and damping. The corrected expected spectral accelerations at the first mode period of the structure (T_1 = 2.13 sec.) are 0.11g for the low hazard level, 0.34g for the moderate hazard level, and 0.65g for the high hazard level.

Seven ground motions were selected from the University of California, Berkeley Seismic Guidelines (Somerville, 2001) to represent each hazard level. The ground motions were scaled so that their spectral acceleration at the first mode period of the structure matched the corrected expected spectral acceleration at the first mode period of the structure. The scale factors ranged between 0.3 and 3.0. The response spectra for all ground motions are shown in Fig. 6.3. These ground motions are different from the ground motions used in Chapter 4. Here, a reduced number of motions is used to represent the seismic hazard at the site to facilitate the structural reliability calculations.

6.1.2 Dynamic Time-History Analyses

Dynamic time-history analyses of the model were performed for the three hazard seismic hazard levels to determine the maximum interstory drift demand in each story. The analyses were performed with the Newmark integration scheme and 2% Rayleigh damping for all hazard levels. The interstory drifts were recorded for each time-history analysis; the maximum absolute values of the interstory drifts are shown in Table 6.1, and the maximum absolute values of the interstory drift ratios (interstory drift divided by story height) are shown in Fig. 6.4.

The maximum interstory drift ratio profiles reveal that for the low hazard level, the maximum drifts occur in the upper stories, with the mean drifts less than 0.02 rad. For the moderate hazard level, the maximum interstory drifts are distributed more evenly along the height of the building, with the mean interstory drifts less than 0.024 rad. For the high hazard level, the maximum interstory drifts are concentrated in the lower five stories, with mean values less than 0.035 rad. Many of the large intensity ground motions include near fault effects, and the characteristics of these motions cause increased demand in the lower stories of the building. The magnitudes of these drifts are similar to the results from analyses of the nine-story SAC building in previous studies (Gupta and Krawinkler, 1999).

6.2 RELIABILITY ANALYSIS OF COLUMN COVER CONNECTIONS

The equations for the approximate deformations in the column covers that were derived in Chapter 5 are used with the time-history results in Section 6.1 to determine the structural reliability of the connectors.

6.2.1 Formulation of Limit State Functions for Column Cover Connections

The analytical equations to estimate the deformation in each of the column cover connectors were derived in Chapter 5. The structural response inputs to these equations are the interstory drifts computed in Section 6.1.2 and their corresponding nodal rotations. The column cover panels in the cladding system are located between adjacent floors of the structure and between the spandrel panels. The spandrel panels are connected to the structural framing, and the column covers are connected to the spandrel panels. The spandrel panels are connected to the exterior floor beam with two vertical bearing connections (rigid in vertical direction) and one rigid lateral connection (rigid in horizontal connection) at midspan. These connections restrain the spandrel panel to move horizontally, vertically, and rotationally, the same amount as the midspan of the floor beam. Therefore, we can treat the behavior of the column cover as a semi-restrained confined block problem. A schematic of the deformation of a column cover is shown in Fig. 6.5, and the illustration of the support movement problem is shown in Fig. 6.6. The column cover is connected to the spandrel panels with one bolted connection at each corner. The bolted pinned connections at the bottom corners of the column cover each consist of one bolt connecting steel embeds in the bottom of the column cover and top of the spandrel panel. The slotted bolted connections at the top corners of the column cover each consist of one bolt in a 4-inch horizontally slotted hole connecting steel embeds in the top of the column cover and bottom of the spandrel panel. All bolts are 3/4-inch diameter ASTM 325 bolts acting in shear.

The equations for the column cover connector deformations are repeated below for convenience. The horizontal and vertical deformations in each connector are shown in Equation 6.1, and the total deformation δ_{total} is shown in Equation 6.2.

$$(\delta_{x1}, \delta_{y1}, \delta_{x2}, \delta_{y2}, \delta_{x3}, \delta_{y3}, \delta_{x4}, \delta_{y4}) = \quad \text{Eq. 6.1}$$

$$\begin{pmatrix}
\frac{X^2}{4(X^2+Y^2)}\left[2(y_t\theta_{i-1}+y_b\theta_i+\Delta_{h,i}-g)+Y(\theta_{i-1}+\theta_i)\right] \\
\frac{1}{4H(X^2+Y^2)}\left[X^3H(\theta_{i-1}-\theta_i)-{\Delta_{h,i}}^2(X^2+Y^2)+2XY^2H\theta_{i-1}+2XYH(y_t\theta_{i-1}+y_b\theta_i)+2XYH(\Delta_{h,i}-g)\right] \\
\frac{-X^2}{4(X^2+Y^2)}\left[2(y_t\theta_{i-1}+y_b\theta_i+\Delta_{h,i}-g)+Y(\theta_{i-1}+\theta_i)\right] \\
\frac{-1}{4H(X^2+Y^2)}\left[X^3H(\theta_{i-1}-\theta_i)+{\Delta_{h,i}}^2(X^2+Y^2)+2XY^2H\theta_{i-1}+2XYH(y_t\theta_{i-1}+y_b\theta_i)+2XYH(\Delta_{h,i}-g)\right] \\
\frac{-X^2}{4(X^2+Y^2)}\left[2(y_t\theta_{i-1}+y_b\theta_i+\Delta_{h,i}-g)+Y(\theta_{i-1}+\theta_i)\right] \\
\frac{1}{4H(X^2+Y^2)}\left[X^3H(\theta_{i-1}-\theta_i)-{\Delta_{h,i}}^2(X^2+Y^2)-2XY^2H\theta_i-2XYH(y_t\theta_{i-1}+y_b\theta_i)-2XYH(\Delta_{h,i}-g)\right] \\
\frac{X^2}{4(X^2+Y^2)}\left[2(y_t\theta_{i-1}+y_b\theta_i+\Delta_{h,i}-g)+Y(\theta_{i-1}+\theta_i)\right] \\
\frac{-1}{4H(X^2+Y^2)}\left[X^3H(\theta_{i-1}-\theta_i)+{\Delta_{h,i}}^2(X^2+Y^2)-2XY^2H\theta_i-2XYH(y_t\theta_{i-1}+y_b\theta_i)-2XYH(\Delta_{h,i}-g)\right]
\end{pmatrix}$$

$$\delta_{total,j} = \sqrt{{\delta_{x,j}}^2 + {\delta_{y,j}}^2} \quad \text{Eq. 6.2}$$

The variables X and Y are the column cover dimensions, y_b and y_t are the spandrel panel dimensions, H is the story height, g is the gap width in the slotted connection, the variables θ_i and θ_{i-1} are the beam center node rotations above and below the column cover, and the variable Δh_i is the interstory drift in story i.

For example, given column cover dimensions X = 54 in., Y = 78 in., spandrel panel dimensions y_b = 50 in. and y_t = 28 in., story height H = 156 in., gap length g = 1.5 in., beam center node rotations above and below $\theta_i = \theta_{i-1}$ = 0.0027 rad., and interstory drift Δh = 2.0 in., the total deformation in the connectors is δ_{total} = (0.260, 0.268, 0.268, 0.260) in. Assuming the interstory drift occurs to the right, the maximum deformations occur in connections 2 and 3 (the direction of the lateral drift does not matter since the cladding panels are symmetric).

Using the results above, the limit state functions of the column cover connections can now be formed. However, first a modification of Equation 6.2 must be made to account for the fact that if the interstory drift Δh is less than the gap width g, then the connections do not show significant deformations (i.e. the bolt in the slotted connection simply moves within the slot). This behavior can be described with the unit Heaviside step function, i.e.:

$$\delta = H(\Delta h - g)\delta_{total}$$

where

Eq. 6.3

$$H(\Delta h - g) = 1 \quad \text{if } \Delta h - g \geq 0$$
$$H(\Delta h - g) = 0 \quad \text{otherwise}$$

However, Equation 6.3 is a non-differentiable piecewise function, which violates the requirements of the limit state function for the reliability analysis. Alternatively, we can approximate the function $H(\Delta h\text{-}g)$ with the smooth logistic function

$$H(\Delta h - g) \approx \frac{1}{1+e^{-2k(\Delta h - g)}} \qquad \text{Eq. 6.4}$$

where a larger k results in a sharper transition at $\Delta h\text{-}g$.

The capacity of each connection is defined by its failure deformation δ_f. There are four limit state functions for each column cover (one for each connector):

$$g_i(\underline{x}) = \delta_f - H(\Delta h - g)(\delta_{total})_i \quad i = 1, 2, 3, 4 \qquad \text{Eq. 6.5}$$

There are ten panels in each story and nine stories in the building; therefore, there are 360 limit state functions defining the reliability of the system of the column cover panels.

6.2.2 Identification of Random Variables

The failure shear deformation δ_f is taken to be constant for all four connectors in one panel in order to reduce the number of random variables in the limit state functions. Likewise, the gap width g is equal for both top connectors in one panel. In each story, there are ten failure deformations (one for each panel), ten gap widths (one for each panel), and one interstory drift. Thus, there are a total of 9 maximum interstory drifts and corresponding beam center node rotations, 90 failure deformations, and 90 gap widths that define the random variables for the cladding system.

The maximum interstory drifts were determined in the nonlinear dynamic analyses in Section 6.1. The mean and standard deviations are shown in Table 6.1 for each hazard level. A Gumbel distribution (Type I largest value) is assumed for the maximum interstory drifts and corresponding beam center node rotations. The Gumbel distribution can be justified as the appropriate distribution for extreme response values obtained from a complete time-history record.

The distribution parameters of the connector failure deformation are determined from the results of the experimental tests in Crawford and Kulak (1968). In the tests, six connector bolts identical to the types used in the column cover connection were tested under shear deformation. The specimens were 3/4-inch diameter A325 bolts connecting ASTM A36 steel plates. The shear force and shear deformation were measured until failure of the specimens. More information about the specimens and test procedure can be found in their report. The mean value of the failure shear deformation is 0.34 inches, and the standard deviation is 0.03 inches. Based on the results of a distribution test, the Lognormal distribution is used to describe the failure deformation of the connectors. The failure deformations are assumed to be statistically independent from panel to panel and floor to floor. The slotted holes at the top connections of the column covers are each 4 inches wide. Therefore, with a 3/4-inch diameter bolt, the total available space for the bolt to move is 3.25 inches (see Fig. 6.7).

Typically, the cladding erector or contractor will try to install the column cover so that the center of the bolt aligns with the center of the slotted hole. However, this rarely happens, since tolerances are not perfect, and cladding panels often need to be shimmed to fit into the structure. The Beta distribution is assumed for the gap width, since we know that the gap width on either side of the bolt must lie somewhere between 0 and 3.25 inches. The mean value is taken as the case that the bolt is in the center of the hole, μ_g = 1.63 inches. The coefficient of variation is taken as 20%; therefore, the standard deviation is 0.33 inches. These assumptions ignore the prior history of the gap width during the initial portions of the ground motion. The initial P-wave of the ground motion is likely to cause the bolt to move back and forth within the slotted hole, and the larger S-wave will cause deformation of the bolt as it impacts the sides of the hole. In addition, we have ignored the fact that the maximum drift could occur in either direction (left or right), so that if the maximum interstory drift causes the bolt to move to the side with a smaller gap width, the probability of failure would be higher. The gap widths are assumed to be statistically independent from panel to panel and floor to floor.

A summary of the distribution parameters of the random variables for the low (50% probability of exceedance in 50 yr) hazard level are given in Table 6.2. The distribution parameters of the random variables x_{10}-x_{189} are the same for the moderate and high hazard; only random variables x_1-x_9 change, for which the distribution parameters are given in Table 6.1.

The correlation in the interstory drifts between floors is based on the seven ground motions for each hazard level. The correlation coefficients are presented in Table 6.3. The Nataf correlation distribution is assumed for the interstory drifts, since it is applicable for a wide range of correlation coefficients.

For the low hazard level, the interstory drifts between the floors are highly positively correlated. The structure is expected to remain elastic during the low hazard level events, with the drift demand following the shape of the fundamental mode of vibration (linear along height). Thus, a comparatively large drift in the first story means that there is a very high chance that the drifts in the other stories are also large. This behavior can be seen in the maximum drift profiles in Fig. 6.4a. For the moderate hazard level, some nonlinearity is expected to occur in the

structure, and therefore, the drifts between the stories do not correlate as highly as for the low hazard level. For example, as shown in Fig. 6.4b, the profiles of maximum drift intersect one another, meaning that a large drift in the first story does not necessarily translate to a large drift in the upper stories. For the high hazard level, a large amount of nonlinearity is expected to occur. As shown in Fig. 6.4c, the largest drift demand occurs in the lower stories, and the drift becomes "pinched" at story 6. This behavior can also be seen in the correlation matrix.

Since the structural framing enforces compatibility of the interstory drifts between floors, the question of whether the correlation matrix is positive definite arises. The Cholesky decomposition of the correlation matrix must be calculated in the reliability analysis, and thus, the correlation matrix must be positive definite to proceed. Two properties of positive definite matrices are that both the eigenvalues and determinant are greater than zero.

To see how the determinant of the correlation matrix changes with the number of stories considered, we first compute the determinant of the correlation matrix considering just the first and second stories. Then, we proceed to add the next story and compute the determinant of the correlation matrix considering the first three stories, and so on. The plot of the determinant versus the number of stories considered is shown in Fig. 6.8 for each hazard level. Since the determinant of the correlation matrix decreases rapidly as additional stories are added, there is a clear indication of linear dependency in the correlation matrix. When more than the first six stories are considered, the determinant of the correlation matrix becomes numerically zero. Thus, we can say that it if we know the interstory drifts of the first six stories, we can deduce the interstory drifts of the remaining stories.

Instead of deriving or inferring the relationship of interstory drift between the stories, we will use the interstory drifts of all stories and modify the correlation matrix slightly to make it positive definite (so that its determinant is not numerically zero and all eigenvalues are positive). We can make a small ridge adjustment to the correlation matrix by adding a small quantity (on the order of 1%) to the diagonal elements of the correlation matrix. This addition has the effect of attenuating the estimated relations between the variables. A large enough addition is sure to result in a positive definite matrix, but the price of this adjustment is bias in the parameter estimates, standard errors, and fit indices (Wothke, 1993).

The column cover dimensions (width X and height Y), the story height H, and the transition parameter k for the step function approximation are selected as deterministic parameters in the limit state functions. The values of the parameters are shown in Table 6.4.

6.3 COMPONENT RELIABILITY ANALYSIS

The component reliabilities of each connection are computed using the first-order reliability method (FORM) and the impoved HL-RF algorithm in CalREL. The failure deformation δ_f is taken to be constant for each connector in one panel, and the gap width g is taken to be equal in the top two connectors. In addition, the maximum interstory drift Δh is constant for all panels in one story. Therefore, the relative distribution of the deformations in the connectors is known from Equation 6.1. First, we notice that the deformations in connectors 2 and 3 are equal, and the deformations in 1 and 4 are equal. So, for a given interstory drift, gap width, and failure deformation, the total deformations in connectors 2 and 3 are larger than the total deformations in connectors 1 and 4. This is due to the fact that the column cover is pinched vertically on corners 2 and 3 when there is interstory drift.

The component reliabilities for each floor are shown in Table 6.5 for the low hazard level, Table 6.6 for the moderate hazard level, and Table 6.7 for the high hazard level. For the low hazard level, the component probabilities of failure are less than 2.2% for the lower six stories, while the component probabilities of failure of stories 7-9 are 13-44%. The values of the gap width at the design point (point of failure) are less than the mean value, and the values of the failure deformation at the design point are very close to the mean value.

For the moderate hazard level, the component probabilities of failure are less than 29% for the lower six stories, while the component probabilities of failure of stories 7-9 are 58-70%. The values of the gap width at the design point are less than the mean value for the lower six stories, and the values of the failure deformation at the design point are very close to the mean value.

For the high hazard level, the component probabilities of failure are almost 100% for the lower five stories, while the component probabilities of failure of stories 6-9 are 57-70%. The values of the gap width at the design point are larger than the mean values, and the values of the failure deformation at the design point are very close to the mean value.

The component probabilities of failure corresponding to connectors 2 and 3 presented in Table 6.5, Table 6.6, and Table 6.7 are plotted below in Fig. 6.9. In one column cover panel, since there is one random variable to define the gap width and one random variable to define the failure deformation, we can conclude that the deformation in connectors 2 and 3 are always greater than the deformation in connectors 1 and 4. Therefore, in the rest of this chapter, we will only need to consider the limit state functions that correspond to connectors 2 and 3.

The component probabilities of failure of connectors 2 and 3 are highest at the top three stories for the low and moderate hazard levels and highest at the bottom five stories for the high hazard level. The probabilities of failure for all events are very large and indicate that the typical design used for column cover connections is inadequate. For the high hazard level, there is almost a 100% certainty that connectors 2 and 3 will fail in stories 1-5. Thus, the initially supplied gap width of approximately 1.6 inches in the slotted connections is not adequate to provide a sufficiently reliable cladding design.

6.3.1 Design Point

In structural reliability theory, the vector of values of the random variables at the point of failure is called the design point. The values of the maximum interstory drift at the design point from the FORM analysis are summarized in Fig. 6.10, Fig. 6.11, and Fig. 6.12 for the low, moderate, and high hazard levels. For each hazard level, the design point maximum interstory drifts for connectors 2 and 3 in each story are compared to the mean value of interstory drift from Section 6.1.2. For the low hazard level, the design point interstory drifts are greater than the mean drifts at all stories. The design point interstory drifts are furthest from the mean in story 1 and closest to the mean in story 9.

For the moderate hazard level, the design point interstory drifts are larger than the mean drifts at story 1 and smaller than the mean drifts at story 9. At the intermediate stories, the design point interstory drifts straddle the mean drift value.

For the high hazard level, the design point interstory drifts in the limit state functions for connectors 2 and 3 are larger than the mean drifts for almost all stories. For connectors 2 and 3 in

story 4, the design point interstory drift is larger than the mean drift at story 7, and for connectors 2 and 3 in story 5, the design point interstory drift is larger than the mean drift at stories 7-9.

In general, random variables that have a lower value than the mean at the design point at failure contribute to the capacity of the connection, while random variable that have a higher value than the mean at the design point at failure are demand (load) variables. However, in this case, the random variables corresponding to the loads (maximum interstory drift) are highly correlated, and therefore, the classification of the random variables as "capacity" or "demand" cannot be determined through a comparison of the design point with respect to its mean vector.

6.3.2 Importance Vectors

Importance vectors are calculated to ascertain whether the random variables contribute to the capacity or demand of the connection. In addition, the relative importance of the random variables with respect to the connector reliability can be determined. The importance vector γ, calculated from Equation 6.6, corresponds to the importance of the random variables in the original x-space.

$$\gamma = \frac{\alpha J_{u,x} \hat{D}}{\| \alpha J_{u,x} \hat{D} \|} \qquad \text{Eq. 6.6}$$

where, $J_{u,x}$ is the Jacobian of the transformation at the design point between the standard normal space and the original space, α is the unit vector in the standard normal space pointing towards the design point, and $\hat{D}$ is the diagonal matrix of standard deviations of the random variables. The importance vector γ is shown in Table 6.8 for connectors 2 and 3 in each story level for the low hazard level.

If the value of γ for a random variable is negative, then the variable is classified as a capacity variable, and if the value of γ is positive, then the variable is classified as a demand variable. As expected, for each story, the gap width and failure deformation are classified as capacity variables, and the maximum interstory drift is classified as a demand variable. The magnitude of the absolute value of γ determines the order of importance of the random variables. For each story, the interstory drift has the largest impact on the reliability of the connectors, followed by the gap width and then the failure deformation.

The importance vector δ determines the effect of statistically equivalent variations in the mean values, assuming fixed standard deviations of the random variables, on the reliability index β: $\delta = \nabla_{\mu} \beta \cdot \underline{D} = \{ \partial \beta_i / \partial \mu_i \cdot \sigma_i \}$. A positive δ corresponds to an increase in the reliability index, indicating that the random variable can be classified as a capacity variable. Conversely, a negative δ corresponds to a demand variable, reducing the reliability index or equivalently increasing the failure probability. A ranking of the elements of δ can be considered as the ranking of the importance of the means of the random variables. For example, the mean value of the maximum interstory drift has a larger effect on the connector reliability than the mean value of the failure deformation, while holding the standard deviations of both variables fixed. The importance vector δ is shown in Table 6.8 for connectors 2 and 3 in each story level for the low hazard level.

The importance vector η determines the effect of statistically equivalent variations in the standard deviations of the random variables, assuming fixed means, on the reliability index β: $\eta = \nabla_\sigma \beta \cdot \underline{D} = \{\partial \beta_i / \partial \sigma_i \cdot \sigma_i\}$. A ranking of the elements of η can be considered as the ranking of the importance of the standard deviations of the random variables. For example, the standard deviation of the maximum interstory drift has a larger effect on the connector reliability than the standard deviation of the failure deformation, while holding the means of both variables fixed. The importance vector η is shown in Table 6.8 for connectors 2 and 3 in each story level for the low hazard level.

The importance vectors for the moderate and high hazards levels are not presented here; the importance vectors for the higher hazard levels result in the same variable classifications and relative importance as for the low hazard level.

6.3.3 Sensitivity Analysis

A sensitivity analysis was performed to determine how changes in the distribution parameters of the random variables and changes in the values of the limit-state parameters affect the probability of failure of connectors 2 and 3 (failure of one panel). The sensitivities of the distribution parameters of the random variables are shown in Table 6.9 for the low hazard level.

We could modify the structural properties of the building to change the maximum horizontal drift demand; however, in this study we will assume the structural properties are given and the maximum horiztonal drift does not vary. Therefore, we will focus on the sensitivities of the capacity variables, g and δ_f. The failure probability of connectors 2 and 3 decreases as the slotted gap width increases, and the failure probability decreases as the mean value of the failure deformation increases.

The sensitivities of the limit-state parameters are shown in Table 6.10 for the low hazard level. Decreasing the panel width has the largest effect on decreasing the probability of failure of one panel. The probability can also be decreased by increasing the panel height or increasing the story height. The shape parameter used in the smoothing function of Equation 6.4 has negligible influence on the probability of failure. The trends in sensitivities for the moderate and high hazard levels are similar to the trends of the low hazard level.

6.3.4 FORM and SORM Approximations

The adequacy of the first-order reliability method (FORM) is verified through a comparison with the point-fitting second-order reliability method (SORM). The results of FORM and SORM component reliability analyses of connectors 2 and 3 are computed for the first story and presented in Table 6.11. The results for the other stories follow a similar trend as the first story.

The difference in the failure probability between FORM and SORM is less than 4%. Since an upper bound is not defined for the error in the approximation using the two methods and the results are relatively similar overall, the FORM reliability method is considered suitable for a general approximation of the connector's reliability. The system reliability analysis is therefore based on the FORM component reliability analysis.

6.4 SYSTEM RELIABILITY ANALYSIS

Using the results of the component reliability analyses in Section 6.3, a system reliability analysis is performed to assess the probability of failure of multiple column cover connections. The system consists of 360 column cover connections (4 connectors to each panel, 10 panels in each story, and 9 stories in the building). It is known from Equation 6.1 that for one panel, the deformations in connectors 2 and 3 are equal, and the deformations in connectors 1 and 4 are equal. In addition, the deformations in connectors 2 and 3 are greater than the deformations in connectors 1 and 4. In this study, we will say a panel has failed when two of the panel's connectors have failed. And, since we know from the choice of random variables that the reliability index of connectors 2 and 3 is always lower than the reliability index of connectors 1 and 4, we can reduce the number of limit state functions in the system analysis from 360 to 180 (i.e. we only consider the limit-state functions corresponding to connectors 2 and 3).

If we define the failure of the system as failure of any one panel (failure of connectors 2 and 3), the system is considered a series system. In CalREL, the Sequential Conditioning Importance Sampling method (SCIS) for computing the multinormal probability for system problems is used to calculate the probability of failure. A threshold of coefficient of variation equal to 0.01 is used in the analyses. The probability of failure of any one panel in the system is 69.73% for the low hazard level, 99.74% for the moderate hazard level, and 100% for the high hazard level. These probabilities are extremely high considering that we expect the probability of failure of structural components in buildings to be very low.

Other definitions of failure of the system can be defined using cut sets, a set of components whose joint failure constitutes the failure of the system. For example, to fail any two panels (failure of a panel is failure of connectors 2 and 3), we would need to consider 90!/[(90-2)!*2!] = 4,005 cut sets, which are far too many cut sets to consider. Therefore, the complete multistory system will be divided into one system per story, for a total of nine subsystems. There are ten panels per story, so there are 20 limit-state functions (two critical connections per panel) to consider for each subsystem. Furthermore, from the results of a static nonlinear pushover analysis, it is observed that the cladding connections tend to deform in a symmetric manner. In Fig. 6.14, the relative deformations of the top two connectors in the column covers are shown as circles. As the building is loaded laterally with a reference load vector matching the first mode shape, the deformation in the connections shows vertical symmetry with the largest deformations occurring in the interior column covers. Thus, we can further reduce the number of limit-state functions to 10 per floor by considering just the left or right half of the cladding system (i.e. if one panel fails in a story in the left half, then one panel will fail in the story on the right half for a total of two failed panels in the story). Similarly, the probability of failing four out of ten panels in a story is calculated by computing the probability of failing any two panels out of the five panels in the story in the left half of the building.

With the subsystems described above, we can investigate the probability of failure of different numbers of panels per story. The upper bounds of the probabilities of failing 2, 4, 6, 8, and 10 panels per story are presented in Table 6.12 for the low, moderate, and high hazard levels.

The probabilities of failure in Table 6.12 are shown graphically in Fig. 6.15, Fig. 6.16, and Fig. 6.17. For the low hazard level (Fig. 6.15), the probability of failing 2 panels in story 9 is 44.2%, and the probability of failing all 10 panels in story 9 is 31.6%. Stories 7-9 show large probabilities of failure while stories 1-6 have much lower probabilities of failure.

Similarly, for the moderate hazard level (Fig. 6.16), there is increased probability of failure in the upper stories. The probabilities of failing 2 panels in stories 7-9 are between 60 and 70%, and the probabilities of failing 2 panels in stories 1-6 are between 10 and 30%.

For the high hazard level (Fig. 6.17), the highest probabilities of failure occur in the lower five stories of the building. The probabilities of failing 2 panels in stories 1-5 are between 92 and 100%, and the probabilities of failing 2 panels in stories 6-9 are between 60 and 70%. Interestingly, the probability of failing more panels in story 6 decreases faster than in stories 7, 8, and 9. This behavior is likely due to the fact that the interstory drift demand in story 6 has a much lower standard deviation than the other stories (see Fig. 6.4c).

6.5 CONDITIONAL PROBABILITIES BETWEEN STORIES

The system analyses in Section 6.4 give the probabilities of failure for several different failure scenarios. However, the probability of failure in one story did not directly depend on the probability of failure in any other story. This information would be useful in situations after an earthquake has occurred and we knew that a panel in a certain story has failed. To this end, we can compute the conditional probabilities (or updated probabilities) of the failure of a panel in one story knowing that a panel in another story has failed using Equation 6.7.

$$P(\text{Failure in story i} \mid \text{Failure in story j}) = \frac{\text{P(Failure in story i and j)}}{\text{P(Failure in story j)}} \qquad \text{Eq. 6.7}$$

Using CalREL, the probabilities of failure of one panel each in two different stories are calculated. Then, the conditional probabilities are computed using Equation 6.7 and the probabilities of failure for one panel in Table 6.5, Table 6.6, and Table 6.7. The conditional probabilities of failure are given in Table 6.13.

The probabilities of failing stories 1 through 9 given that one panel in story 1 has failed (column 3 of Table 6.13) are shown in Fig. 6.18, Fig. 6.19, and Fig. 6.20. This information might be useful during post-earthquake reconnaissance, where we could inspect the state of the column cover connections in the first story and use the conditional probabilities to infer the state of the connections in the remaining stories. For the low hazard level (Fig. 6.18), the probabilities of failing one panel in stories 2-6 is up to 18 times higher with the information that a panel in story 1 has failed. The probabilities of failure of one panel in stories 7, 8, and 9 are approximately 4, 3.7, and 2.3 times higher with the information that a panel in story 1 has failed.

For the moderate hazard level (Fig. 6.19), the known failure of a panel in story 1 causes increased probabilities of failure in stories 2-4, decreased probabilities of failure in stories 5 and 6, and increased probabilities of failure in stories 7-9.

For the high hazard level (Fig. 6.20), the known failure of a panel in story 1 causes slightly increased probabilities of failure in the remaining stories. However, since the structure of the building itself may be near collapse for this hazard level, the state of the cladding may be of less concern.

6.6 TOTAL SYSTEM FAILURE PROBABILITY PER STORY

The total failure probability of the cladding system at each story is determined by combining the conditional failure probabilities of the story systems at each hazard level according to their marginal probabilities or equivalent weights. This formulation can be expressed as:

$$P(\mathit{failure}) = \sum_{h} P(\mathit{failure}/H = h) \cdot P_H(h) \qquad \text{Eq. 6.8}$$

where,

H is the seismic hazard level,

h corresponds to the three specific hazard levels considered in the analysis, including the low (50% PE in 50 yrs), moderate (10% PE in 50 yrs), and high (2% PE in 50 yrs) hazard level,

$P(\mathit{failure})$ is the total failure probability of the cladding system at each story,

$P(\mathit{failure}/H = h)$ is the conditional probability of failure of the cladding system at each story, given a hazard level h

$P_H(h)$ is the marginal probability of occurrence of the hazard level, determined for a time period t

The marginal probabilities of the occurrence of the hazard levels come from a probabilistic seismic hazard analysis (PSHA). The annual probability of exceedance of the spectral acceleration $H(s_a)$ can be approximated with the power law relation in Equation 6.9:

$$H(s_a) = P[S_a \geq s_a] = k_o s_a^{-k} \qquad \text{Eq. 6.9}$$

The coefficients k and k_o are calculated using two spectral acceleration values corresponding to two different hazard levels. In this study, the 2% and 50% probability of exceedance in 50 year hazard levels are chosen to determine the coefficients: k = 1.98 and k_o = 2.06 E-04. The results of the PSHA are shown in Table 6.14.

The acceptable performance states for the cladding system are chosen for each hazard level. The acceptable number of failed panels is chosen as 2, 4, and 8 panels in each story for the low, moderate, and high hazard levels, respectively. Using the failure probabilities in Table 6.12 and the marginal probabilities in Table 6.14, the total system probabilities of failure are calculated using Equation 6.8. The total probabilities of failure are given in Table 6.15 and shown graphically in Fig. 6.21. The total probabilities of failure in each story are dominated by the more frequent low hazard event. The system probabilities of failure in the 50 year time period are approximately 4-9% in stories 1-6. In stories 7-9, the system probabilities of failure are 31-48%. Based on these results, there is a relatively strong likelihood of panel failure at low seismic intensities. The probability of more panels failing at higher seismic intensities does not increase very rapidly; however, at these high seismic intensities the probability of structural element failure increases more rapidly (in which case the state of the cladding is less significant).

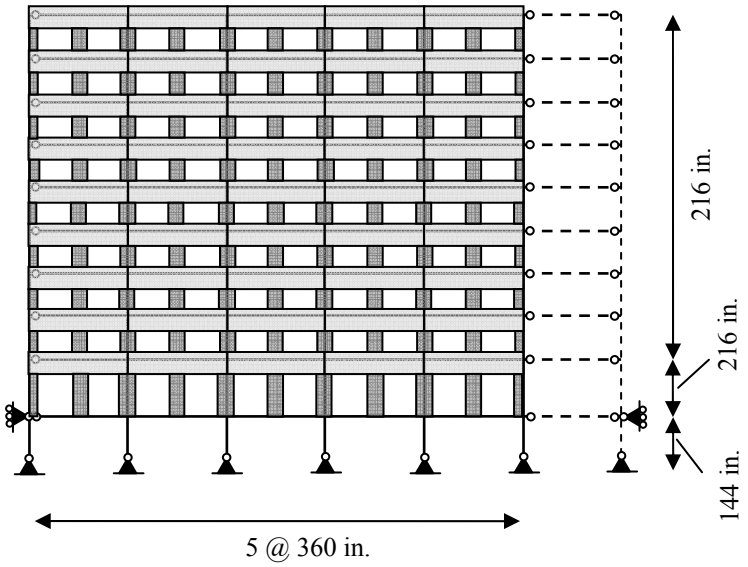

Fig. 6.1 Elevation of the nine-story SAC analytical model C3

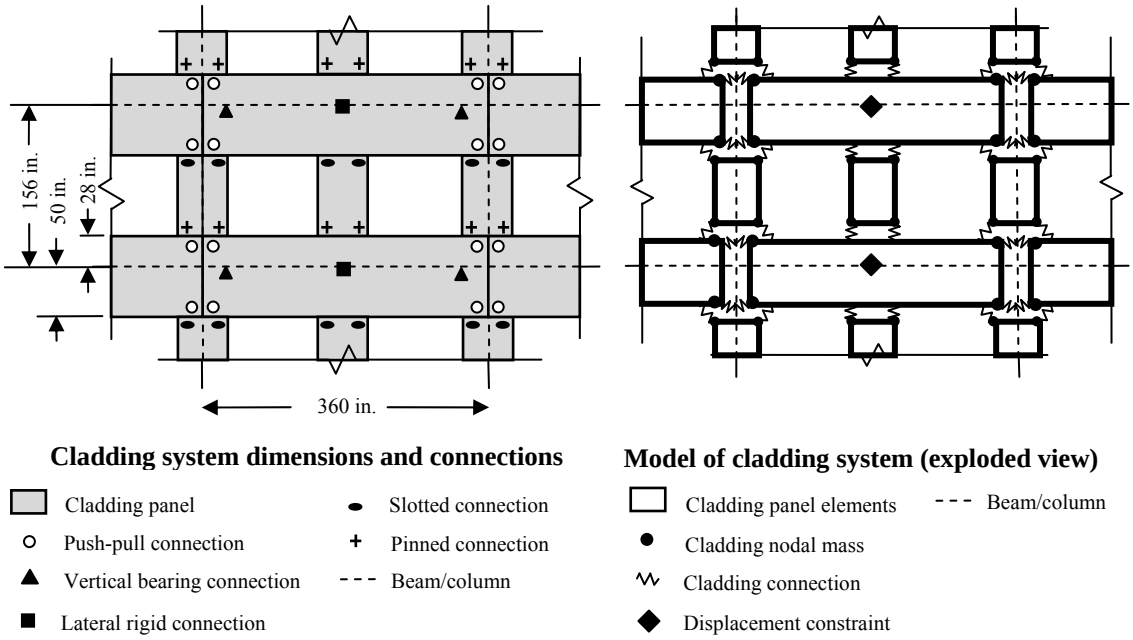

Fig. 6.2 Detailed elevation of cladding type C3

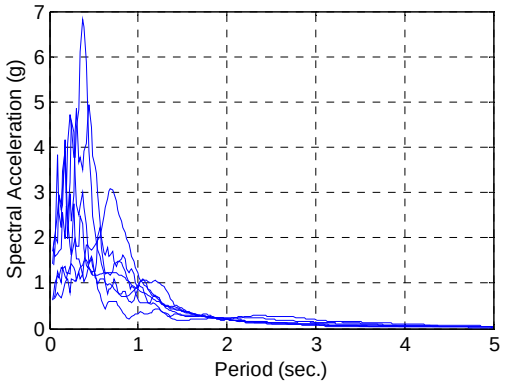

(a) Low Hazard Level, Sa(T_1) = 0.11 g

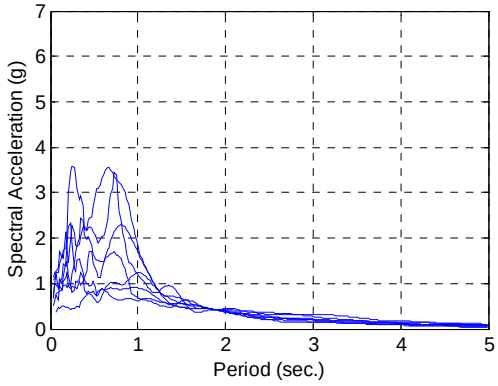

(b) Moderate Hazard Level, Sa(T_1) = 0.34 g

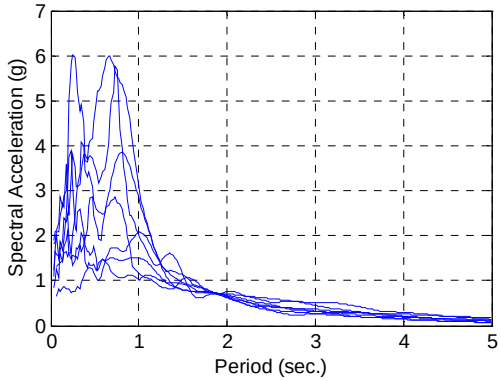

(c) High Hazard Level, Sa(T_1) = 0.65 g

Fig. 6.3 Response spectra for the three hazard levels

Table 6.1 Maximum absolute values of interstory drift

Story	Hazard Level					
	Low (50% PE in 50 yrs)		Moderate (10% PE in 50 yrs)		High (2% PE in 50 yrs)	
	Mean (in.)	Standard Deviation (in.)	Mean (in.)	Standard Deviation (in.)	Mean (in.)	Standard Deviation (in.)
1	2.09	0.51	3.32	0.53	6.35	2.15
2	1.42	0.37	2.19	0.41	5.16	1.28
3	1.50	0.32	2.28	0.36	5.24	1.18
4	1.60	0.34	2.50	0.42	5.28	1.12
5	1.74	0.31	2.53	0.49	4.70	1.18
6	1.74	0.34	2.49	0.37	3.05	0.49
7	2.14	0.57	3.43	1.03	3.59	1.34
8	2.54	0.92	3.53	1.49	3.52	1.51
9	2.81	1.27	3.54	2.01	3.61	2.01

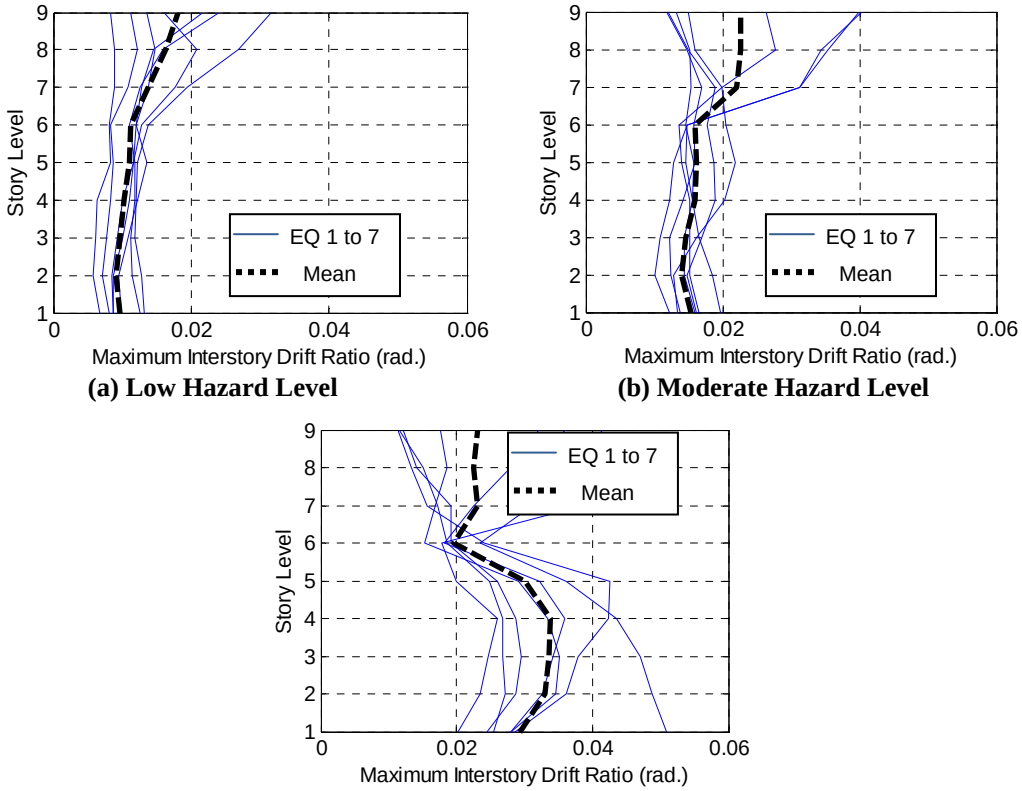

(a) Low Hazard Level **(b) Moderate Hazard Level**

(c) High Hazard Level

Fig. 6.4 Maximum absolute values of interstory drift ratio for the three hazard levels

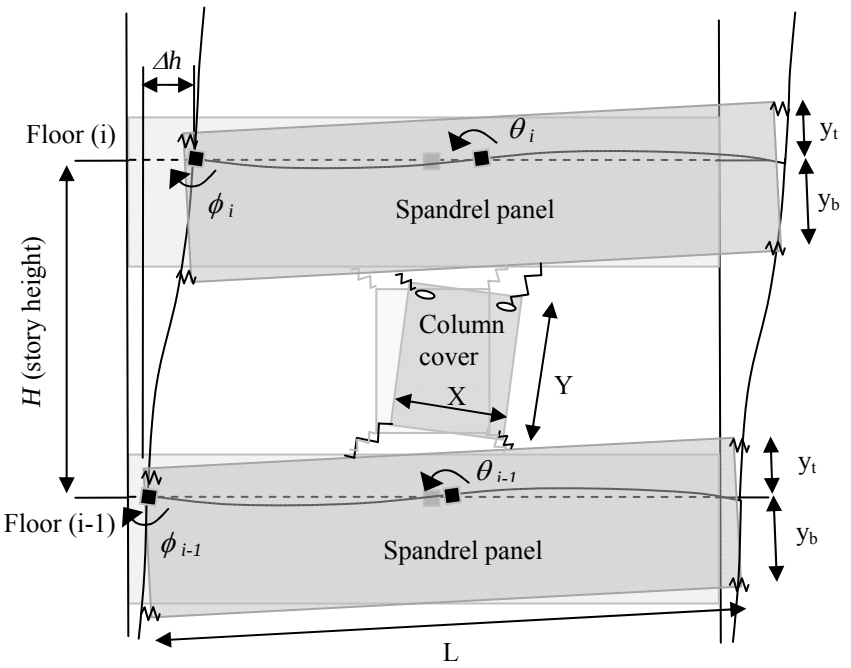

Fig. 6.5 Deformation of column cover connections under lateral drift Δh

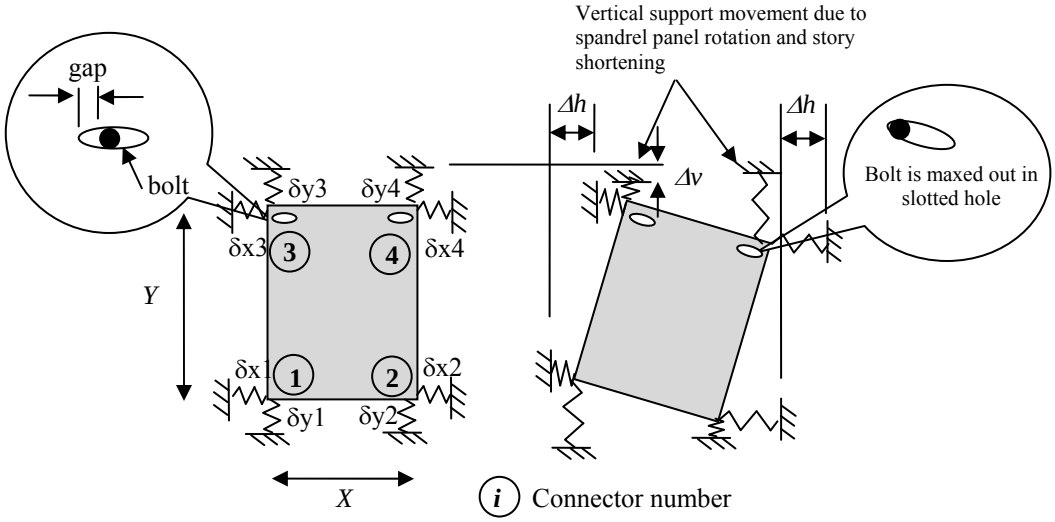

Fig. 6.6 Deformation of connections can be analyzed as a support movement problem

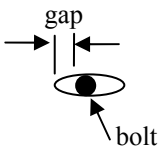

Fig. 6.7 Movement of the connector bolt in the slotted hole.

Table 6.2 Summary of random variables for the low (50% PE in 50 yr.) hazard level

RV	X_i	Description	Distribution	Units	Mean	Std. Dev.	Notes/Reference
Δh_1	1	Floor 1 max. interstory drift	Gumbel	in.	2.09	0.51	Section 2.5
Δh_2	2	Floor 2 max. interstory drift	Gumbel	in.	1.42	0.37	Section 2.5
Δh_3	3	Floor 3 max. interstory drift	Gumbel	in.	1.50	0.32	Section 2.5
Δh_4	4	Floor 4 max. interstory drift	Gumbel	in.	1.60	0.34	Section 2.5
Δh_5	5	Floor 5 max. interstory drift	Gumbel	in.	1.74	0.31	Section 2.5
Δh_6	6	Floor 6 max. interstory drift	Gumbel	in.	1.74	0.34	Section 2.5
Δh_7	7	Floor 7 max. interstory drift	Gumbel	in.	2.14	0.57	Section 2.5
Δh_8	8	Floor 8 max. interstory drift	Gumbel	in.	2.54	0.92	Section 2.5
Δh_9	9	Floor 9 max. interstory drift	Gumbel	in.	2.81	1.27	Section 2.5
$g_{1,1}$	10	Floor 1, panel 1 gap width	Beta	in.	1.63	0.33	Min=0, Max=3.25
$g_{1,2}$	11	Floor 1, panel 2 gap width	Beta	in.	1.63	0.33	Min=0, Max=3.25
…	…	…	…	…	…	…	…
$g_{1,10}$	19	Floor 1, panel 10 gap width	Beta	in.	1.63	0.33	Min=0, Max=3.25
…	…	…	…	…	…	…	…
$g_{9,10}$	99	Floor 9, panel 10 gap width	Beta	in.	1.63	0.33	Min=0, Max=3.25
$(\delta_f)_{1,1}$	100	Floor 1, panel 1 failure deformation	Lognormal	in.	0.34	0.03	Crawford and Kulak (1968)
$(\delta_f)_{1,2}$	101	Floor 1, panel 2 failure deformation	Lognormal	in.	0.34	0.03	Crawford and Kulak (1968)
…	…	…	…	…	…	…	…
$(\delta_f)_{1,10}$	109	Floor 1, panel 10 failure deformation	Lognormal	in.	0.34	0.03	Crawford and Kulak (1968)
…	…	…	…	…	…	…	…
$(\delta_f)_{9,10}$	189	Floor 9, panel 10 failure deformation	Lognormal	in.	0.34	0.03	Crawford and Kulak (1968)

Table 6.3 Correlation coefficients for interstory drifts between floors for different hazard levels

Story	Hazard Level	Correlation Coefficient (low, moderate, high hazard level)								
		1	2	3	4	5	6	7	8	9
1	Low	1.00								
	Moderate	1.00								
	High	1.00								
2	Low	0.98	1.00							
	Moderate	0.98	1.00							
	High	0.95	1.00							
3	Low	0.89	0.94	1.00						
	Moderate	0.69	0.78	1.00						
	High	0.91	0.99	1.00						
4	Low	0.80	0.86	0.98	1.00					
	Moderate	0.12	0.26	0.79	1.00					
	High	0.76	0.89	0.94	1.00					
5	Low	0.66	0.74	0.90	0.95	1.00				
	Moderate	-0.19	-0.04	0.53	0.93	1.00				
	High	0.56	0.74	0.81	0.94	1.00				
6	Low	0.66	0.78	0.86	0.85	0.87	1.00			
	Moderate	-0.35	-0.22	0.36	0.82	0.94	1.00			
	High	0.59	0.61	0.61	0.72	0.73	1.00			
7	Low	0.60	0.72	0.75	0.70	0.62	0.91	1.00		
	Moderate	0.16	0.09	-0.15	-0.41	-0.48	-0.22	1.00		
	High	0.17	-0.01	-0.05	-0.12	-0.38	0.03	1.00		
8	Low	0.72	0.81	0.78	0.71	0.59	0.87	0.98	1.00	
	Moderate	0.23	0.15	-0.21	-0.59	-0.71	-0.53	0.91	1.00	
	High	0.21	0.06	0.04	-0.02	-0.30	-0.08	0.94	1.00	
9	Low	0.96	0.98	0.91	0.84	0.74	0.76	0.71	0.81	1.00
	Moderate	0.24	0.15	-0.19	-0.56	-0.66	-0.48	0.95	0.99	1.00
	High	0.28	0.15	0.13	0.07	-0.21	-0.03	0.92	0.99	1.00

Symmetric

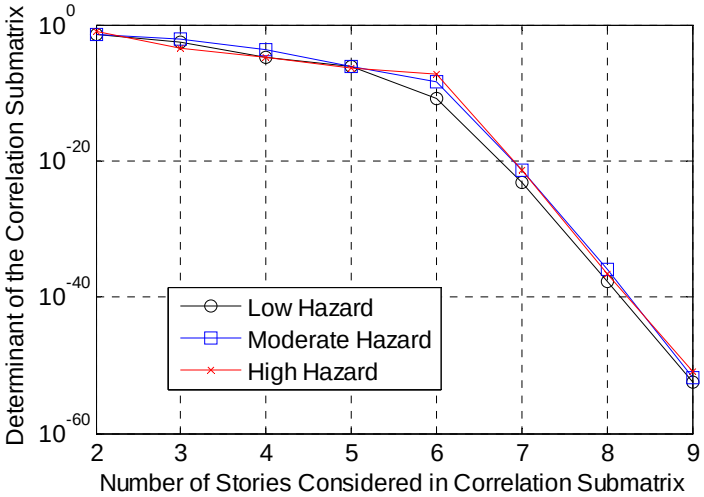

Fig. 6.8 The determinant of the correlation matrix is computed by adding one story to the correlation matrix at a time.

Table 6.4 List of deterministic parameters

Parameter	θ_i	Description	Units	Value
X	θ_1	Column cover width	in.	54
Y (stories 2-9)	θ_2	Column cover height (stories 2-9)	in.	78
Y (story 1)	θ_3	Column cover height (story 1)	in.	166
H (stories 2-9)	θ_4	Story height (stories 2-9)	in.	156
H (story 1)	θ_5	Story height (story 1)	in.	216
y_b	θ_6	Spandrel panel dimension	in.	50
y_t	θ_7	Spandrel panel dimension	in.	28
k	θ_8	Transition parameter for step function approx.	-	10

Table 6.5 Component reliability analysis of one panel for each story level – Low Hazard Level

Story	Connector	β	P_{fl} (%)	x* Design point
1	1 and 4	2.38	0.877	Δh*=[3.57,2.45,2.27,2.31,2.22,2.28,2.93,4.18,6.22], g*=1.37, δ_f*=0.33
	2 and 3	2.21	1.35	Δh*=[3.43,2.36,2.20,2.25,2.18,2.23,2.86,4.03,5.90], g*=1.40, δ_f*=0.33
2	1 and 4	2.43	0.751	Δh*=[3.50,2.48,2.32,2.38,2.30,2.42,3.15,4.47,6.29], g*=1.29, δ_f*=0.33
	2 and 3	2.36	0.907	Δh*=[3.45,2.44,2.29,2.35,2.28,2.40,3.11,4.40,6.16], g*=1.31, δ_f*=0.33
3	1 and 4	2.52	0.584	Δh*=[3.33,2.38,2.42,2.56,2.49,2.54,3.22,4.39,6.01], g*=1.24, δ_f*=0.33
	2 and 3	2.44	0.719	Δh*=[3.28,2.35,2.39,2.52,2.46,2.51,3.18,4.32,5.89], g*=1.26, δ_f*=0.33
4	1 and 4	2.29	1.10	Δh*=[3.01,2.16,2.27,2.46,2.44,2.42,2.99,3.93,5.29], g*=1.28, δ_f*=0.33
	2 and 3	2.21	1.34	Δh*=[2.97,2.13,2.23,2.43,2.41,2.39,2.96,3.88,5.19], g*=1.30, δ_f*=0.33
5	1 and 4	2.22	1.31	Δh*=[2.73,1.96,2.11,2.31,2.42,2.37,2.80,3.53,4.68], g*=1.30, δ_f*=0.33
	2 and 3	2.14	1.62	Δh*=[2.70,1.93,2.08,2.28,2.39,2.34,2.77,3.48,4.60], g*=1.27, δ_f*=0.33
6	1 and 4	2.09	1.81	Δh*=[2.70,1.97,2.05,2.18,2.27,2.48,3.19,4.12,4.65], g*=1.29, δ_f*=0.33
	2 and 3	2.01	2.21	Δh*=[2.67,1.95,2.02,2.15,2.24,2.43,3.14,4.05,4.56], g*=1.31, δ_f*=0.33
7	1 and 4	1.13	12.91	Δh*=[2.32,1.64,1.70,1.79,1.88,2.02,2.68,3.36,3.54], g*=1.47, δ_f*=0.33
	2 and 3	1.05	14.67	Δh*=[2.30,1.62,1.68,1.77,1.87,1.99,2.63,3.29,3.47], g*=1.48, δ_f*=0.33
8	1 and 4	0.49	31.37	Δh*=[2.17,1.49,1.55,1.64,1.76,1.81,2.29,2.79,3.05], g*=1.57, δ_f*=0.34
	2 and 3	0.42	33.87	Δh*=[2.14,1.47,1.54,1.63,1.75,1.79,2.26,2.73,2.99], g*=1.58, δ_f*=0.34
9	1 and 4	0.20	41.91	Δh*=[2.10,1.43,1.50,1.59,1.73,1.73,2.12,2.52,2.84], g*=1.61, δ_f*=0.34
	2 and 3	0.15	44.17	Δh*=[2.07,1.41,1.48,1.58,1.72,1.72,2.10,2.49,2.77], g*=1.62, δ_f*=0.34

Table 6.6 Component reliability analysis of one panel for each story level – Moderate Hazard Level

Story	Connector	β	P_{fl} (%)	x* Design point
1	1 and 4	1.00	15.75	Δh*=[3.71,2.47,2.43,2.46,2.39,2.34,3.37,3.54,3.56], g*=1.47, δ_f*=0.33
	2 and 3	0.75	22.72	Δh*=[3.58,2.37,2.45,2.41,2.36,3.43,3.48,3.47,3.47], g*=1.51, δ_f*=0.33
2	1 and 4	1.29	9.93	Δh*=[3.83,2.60,2.53,2.53,2.45,2.36,3.23,3.47,3.47], g*=1.40, δ_f*=0.33
	2 and 3	1.19	11.71	Δh*=[3.78,2.56,2.50,2.52,2.45,2.37,3.32,3.46,3.45], g*=1.42, δ_f*=0.33
3	1 and 4	1.20	11.42	Δh*=[3.58,2.42,2.59,2.74,2.69,2.55,3.15,3.05,2.91], g*=1.39, δ_f*=0.33
	2 and 3	1.10	13.64	Δh*=[3.54,2.39,2.55,2.71,2.67,2.54,3.16,3.07,2.94], g*=1.41, δ_f*=0.33
4	1 and 4	0.77	22.03	Δh*=[3.26,2.17,2.39,2.69,2.72,2.61,3.04,2.82,2.60], g*=1.48, δ_f*=0.33
	2 and 3	0.66	25.48	Δh*=[3.26,2.17,2.37,2.65,2.68,2.58,3.07,2.88,2.68], g*=1.50, δ_f*=0.34
5	1 and 4	0.66	25.31	Δh*=[3.19,2.12,2.32,2.63,2.72,2.62,3.03,2.77,2.55], g*=1.51, δ_f*=0.34
	2 and 3	0.56	28.82	Δh*=[3.20,2.12,2.31,2.60,2.68,2.59,3.06,2.84,2.65], g*=1.53, δ_f*=0.34
6	1 and 4	0.82	20.68	Δh*=[3.14,2.08,2.30,2.63,2.73,2.66,3.15,2.86,2.69], g*=1.46, δ_f*=0.33
	2 and 3	0.70	24.24	Δh*=[3.15,2.08,2.29,2.60,2.69,2.63,3.16,2.92,2.76], g*=1.63, δ_f*=0.33
7	1 and 4	-0.43	66.77	Δh*=[3.21,2.11,2.24,2.49,2.54,2.46,2.92,2.85,2.59], g*=1.69, δ_f*=0.34
	2 and 3	-0.52	69.94	Δh*=[3.21,2.11,2.25,2.50,2.56,2.47,2.86,2.76,2.47], g*=1.70, δ_f*=0.34
8	1 and 4	-0.33	62.80	Δh*=[3.20,2.11,2.25,2.50,2.56,2.49,3.02,2.89,2.69], g*=1.66, δ_f*=0.34
	2 and 3	-0.39	65.08	Δh*=[3.20,2.10,2.25,2.52,2.58,2.50,2.98,2.82,2.60], g*=1.67, δ_f*=0.34
9	1 and 4	-0.20	57.73	Δh*=[3.22,2.11,2.24,2.47,2.52,2.46,3.11,3.05,2.87], g*=1.64, δ_f*=0.34
	2 and 3	-0.24	59.42	Δh*=[3.21,2.11,2.24,2.48,2.53,2.47,3.07,3.00,2.80], g*=1.65, δ_f*=0.34

Table 6.7 Component reliability analysis of one panel for each story level – High Hazard Level

Story	Connector	β	P_{fl} (%)	x* Design point
1	1 and 4	-1.26	89.56	Δh*=[4.09,3.88,4.09,4.31,3.88,2.69,3.15,2.97,2.73], g*=1.74, δ_f*=0.34
	2 and 3	-1.43	92.30	Δh*=[3.87,3.76,3.98,4.22,3.80,2.66,3.11,2.93,2.66], g*=1.75, δ_f*=0.34
2	1 and 4	-2.29	98.91	Δh*=[3.28,3.27,3.52,3.74,3.28,2.53,3.44,3.16,2.82], g*=1.99, δ_f*=0.35
	2 and 3	-2.43	99.24	Δh*=[3.15,3.19,3.44,3.68,3.22,2.51,3.44,3.15,2.79], g*=2.00, δ_f*=0.35
3	1 and 4	-2.62	99.56	Δh*=[3.17,3.17,3.37,3.58,3.09,2.49,3.57,3.22,2.84], g*=2.08, δ_f*=0.35
	2 and 3	-2.78	99.73	Δh*=[3.03,3.09,3.28,3.51,3.02,2.46,3.59,3.22,2.81], g*=2.09, δ_f*=0.35
4	1 and 4	-2.82	99.76	Δh*=[3.43,3.24,3.40,3.43,2.86,2.40,3.81,3.41,3.05], g*=2.13, δ_f*=0.35
	2 and 3	-2.99	99.86	Δh*=[3.29,3.15,3.32,3.34,2.77,2.37,3.84,3.42,3.03], g*=2.15, δ_f*=0.35
5	1 and 4	-1.84	96.71	Δh*=[4.52,3.84,3.94,3.90,3.18,2.54,4.34,4.11,4.07], g*=1.92, δ_f*=0.35
	2 and 3	-1.97	97.54	Δh*=[4.42,3.77,3.88,3.83,3.11,2.52,4.42,4.19,4.14], g*=1.93, δ_f*=0.35
6	1 and 4	-0.20	57.73	Δh*=[5.83,4.85,4.95,4.99,4.40,2.91,3.37,3.29,3.30], g*=1.67, δ_f*=0.34
	2 and 3	-0.34	63.16	Δh*=[5.71,4.78,4.89,4.91,4.32,2.86,3.36,3.31,3.31], g*=1.70, δ_f*=0.34
7	1 and 4	-0.43	66.68	Δh*=[5.87,4.97,5.08,5.15,4.71,2.97,2.91,2.78,2.65], g*=1.68, δ_f*=0.34
	2 and 3	-0.50	69.18	Δh*=[5.85,4.97,5.08,5.16,4.74,2.97,2.84,2.71,2.56], g*=1.68, δ_f*=0.34
8	1 and 4	-0.31	62.13	Δh*=[5.89,4.94,5.04,5.10,4.62,2.98,3.05,2.89,2.78], g*=1.66, δ_f*=0.34
	2 and 3	-0.37	64.38	Δh*=[5.86,4.94,5.04,5.11,4.64,2.99,2.99,2.82,2.69], g*=1.66, δ_f*=0.34
9	1 and 4	-0.24	59.44	Δh*=[5.87,4.92,5.02,5.08,4.57,2.97,3.12,2.97,2.88], g*=1.65, δ_f*=0.34
	2 and 3	-0.28	61.14	Δh*=[5.85,4.91,5.01,5.07,4.58,2.98,3.08,2.92,2.80], g*=1.65, δ_f*=0.34

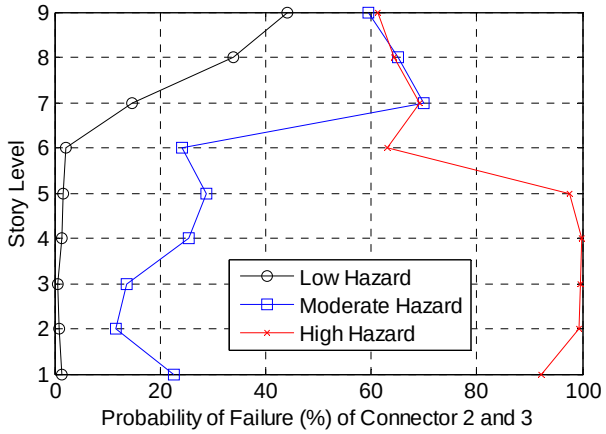

Fig. 6.9 Component reliabilities: probability of failure of connectors 2 and 3 up height of building.

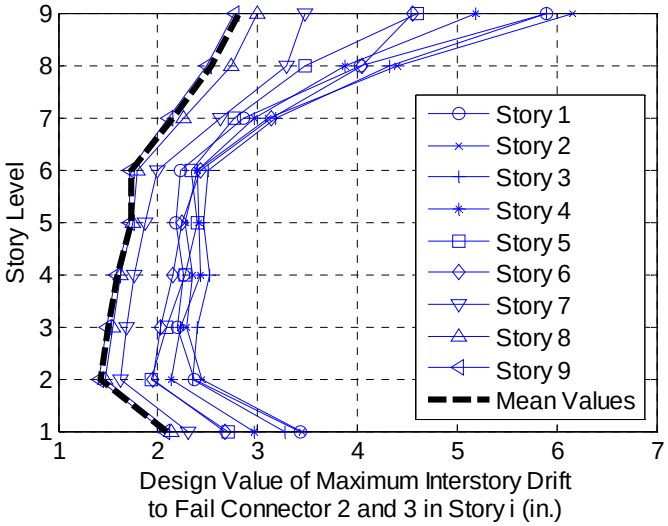

Fig. 6.10 Design values of maximum interstory drift to fail connector 2 and 3 for the low hazard level.

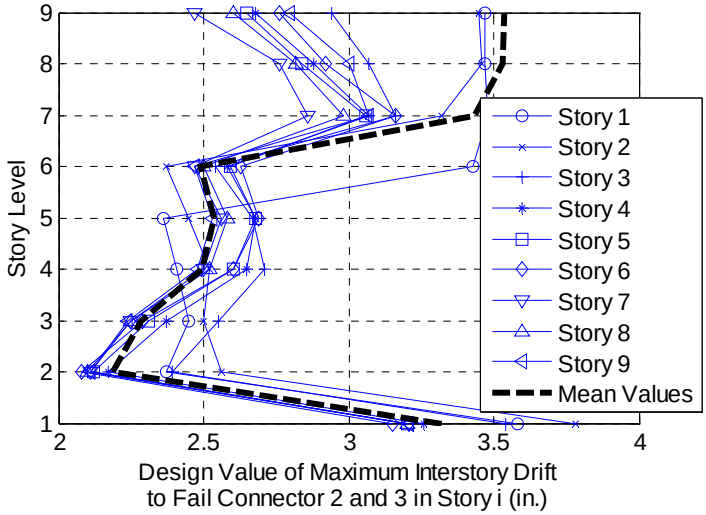

Fig. 6.11 Design values of maximum interstory drift to fail connector 2 and 3 for the moderate hazard level.

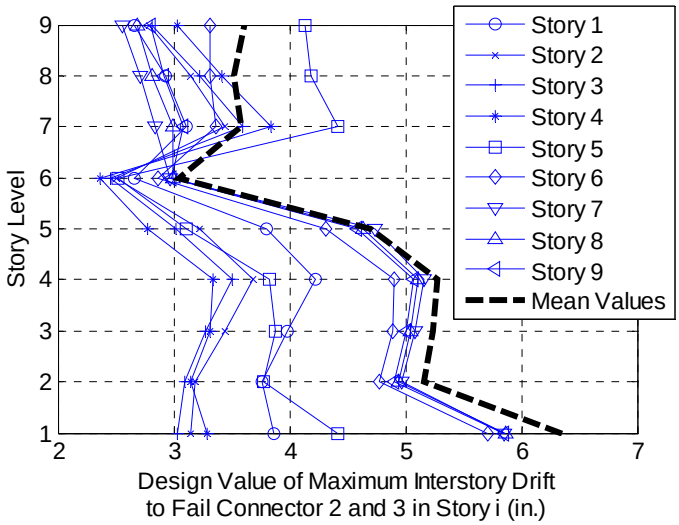

Fig. 6.12 Design values of maximum interstory drift to fail connector 2 and 3 for the high hazard level.

Table 6.8 Importance vectors – connectors 2 and 3, Low Hazard Level

Story	RV	γ (x-space)	δ	η	Classification	Order of Importance
1	Δh_1	0.937	-0.488	-1.283	Demand	1
	g	-0.306	-	-	Capacity	2
	δ_f	-0.170	0.177	-0.079	Capacity	3
2	Δh_2	0.906	-0.461	-1.274	Demand	1
	g	-0.404	-	-	Capacity	2
	δ_f	-0.125	0.129	-0.048	Capacity	3
3	Δh_3	0.883	-0.447	-1.250	Demand	1
	g	-0.449	-	-	Capacity	2
	δ_f	-0.139	0.145	-0.060	Capacity	3
4	Δh_4	0.883	-0.479	-1.153	Demand	1
	g	-0.448	-	-	Capacity	2
	δ_f	-0.139	0.144	-0.055	Capacity	3
5	Δh_5	0.848	-0.484	-1.040	Demand	1
	g	-0.507	-	-	Capacity	2
	δ_f	-0.157	0.164	-0.067	Capacity	3
6	Δh_6	0.867	-0.507	-1.030	Demand	1
	g	-0.476	-	-	Capacity	2
	δ_f	-0.147	0.152	-0.056	Capacity	3
7	Δh_7	0.902	-0.709	-0.604	Demand	1
	g	-0.413	-	-	Capacity	2
	δ_f	-0.126	0.129	-0.028	Capacity	3
8	Δh_8	0.939	-0.909	-0.193	Demand	1
	g	-0.329	-	-	Capacity	2
	δ_f	-0.101	0.102	-0.013	Capacity	3
9	Δh_9	0.961	-1.018	0.035	Demand	1
	g	-0.266	-	-	Capacity	2
	δ_f	-0.082	0.083	-0.008	Capacity	3

Table 6.9 Sensitivity analysis for distribution parameters – Low Hazard Level

Story	RV	Sensitivity in Probability of Failure of Connectors 2 and 3 with Respect to Distribution Parameters					
		μ (mean)	σ (standard deviation)	p_1 (q in Beta distribution)	p_2 (r in Beta distribution)	p_3 (minimum gap width)	p_4 (maximum gap width)
1	Δh_1	3.298 E-02	8.669 E-02	-	-	-	-
	g	-	-	-2.382 E-03	2.083 E-03	-1.789 E-02	-1.355 E-02
	δ_f	-2.039 E-01	9.030 E-02	-	-	-	-
2	Δh_2	3.060 E-02	8.450 E-02	-	-	-	-
	g	-	-	-2.298 E-03	1.896 E-03	-1.788 E-02	-1.204 E-02
	δ_f	-1.055 E-01	3.883 E-02	-	-	-	-
3	Δh_3	2.794 E-02	7.825 E-02	-	-	-	-
	g	-	-	-2.108 E-03	1.689 E-03	-1.672 E-02	-1.060 E-02
	δ_f	-9.633 E-02	3.957 E-02	-	-	-	-
4	Δh_4	4.780 E-02	1.150 E-01	-	-	-	-
	g	-	-	-3.594 E-03	2.942 E-03	-2.811 E-02	-1.863 E-02
	δ_f	-1.648 E-01	6.254 E-02	-	-	-	-
5	Δh_5	6.411 E-02	1.378 E-01	-	-	-	-
	g	-	-	-4.837 E-03	3.884 E-03	-3.830 E-02	-2.441 E-02
	δ_f	-2.210 E-01	8.998 E-02	-	-	-	-
6	Δh_6	7.759 E-02	1.577 E-01	-	-	-	-
	g	-	-	-5.826 E-03	4.803 E-03	-4.536 E-02	-3.050 E-02
	δ_f	-2.674 E-01	9.882 E-02	-	-	-	-
7	Δh_7	2.867 E-01	2.443 E-01	-	-	-	-
	g	-	-	-2.086 E-02	1.919 E-02	-1.522 E-01	-1.277 E-01
	δ_f	-9.869 E-01	2.123 E-01	-	-	-	-
8	Δh_8	3.629 E-01	7.696 E-02	-	-	-	-
	g	-	-	-2.572 E-02	2.516 E-02	-1.814 E-01	-1.724 E-01
	δ_f	-1.248	1.595 E-01	-	-	-	-
9	Δh_9	3.158 E-01	-1.096 E-02	-	-	-	-
	g	-	-	-2.216 E-02	2.212 E-02	-1.547 E-01	-1.532 E-01
	δ_f	-1.086	1.071 E-01	-	-	-	-

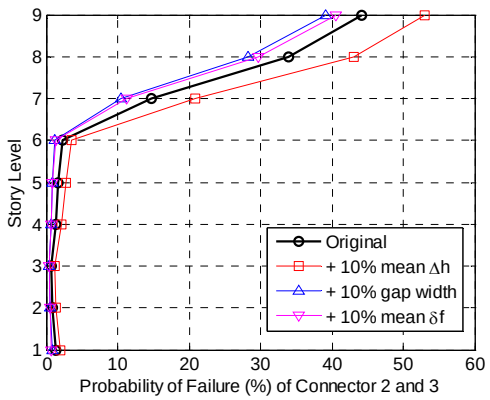

(a) Sensitivity of Random Variables

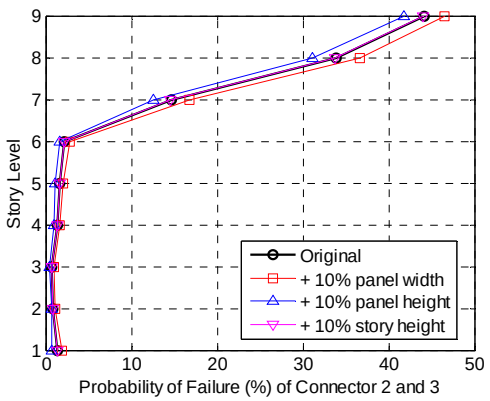

(b) Sensitivity of Deterministic Parameters

Fig. 6.13 Sensitivities of random variable distribution parameters and deterministic parameters for the low hazard level

Table 6.10 Sensitivity analysis for limit-state parameters – Low Hazard Level

Story	Sensitivity in Probability of Failure of Connectors 2 and 3 with Respect to Limit State Parameters			
	X (panel width)	*Y* (panel height)	*L* (story height)	*k* (shape parameter)
1	1.066 E-03	-3.469 E-04	-1.227 E-05	0
2	4.191 E-04	-2.901 E-04	-5.346 E-06	1.160 E-11
3	3.818 E-04	-2.643 E-04	-4.681 E-06	1.128 E-11
4	6.543 E-04	-4.529 E-04	-8.258 E-06	1.842 E-11
5	8.761 E-04	-6.065 E-04	-1.078 E-05	2.577 E-11
6	1.062 E-03	-7.355 E-04	-1.354 E-05	2.948 E-11
7	3.956 E-03	-2.738 E-03	-5.805 E-05	8.701 E-11
8	5.025 E-03	-3.479 E-03	-7.959 E-05	9.756 E-11
9	4.380 E-03	-3.032 E-03	-7.110 E-05	8.159 E-11

Table 6.11 Comparison between FORM and SORM component reliability results

Hazard Level	Story	Description	β_{FORM}	β_{SORM}	$P_{f1,FORM}$ (%)	$P_{f1,SORM}$ (%)
Low	1	Connector 2 and 3	2.212	2.206	1.347	1.368
Moderate	1	Connector 2 and 3	0.748	0.719	22.73	23.60
High	1	Connector 2 and 3	-1.425	-1.432	92.30	92.40

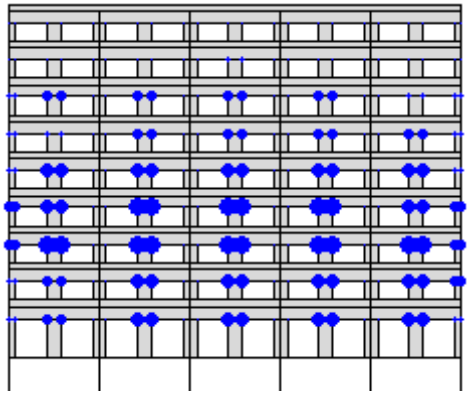

Fig. 6.14 Pushover analysis: relative deformations in the top column cover connections at a global roof drift of 1%. The deformation pattern shows vertical symmetry.

Table 6.12 Probability of failure of the story systems for different failure scenarios and hazard levels

Story	Number of Failed Panels in Story	Hazard Level					
		Low (50% PE in 50 yr)		Moderate (10% PE in 50 yr)		High (2% PE in 50 yr)	
		β	P_{fl} (%)	β	P_{fl} (%)	β	P_{fl} (%)
1	2	2.212	1.35	0.748	22.73	-1.425	92.30
	4	2.365	0.902	0.940	17.36	-1.433	92.40
	6	2.479	0.660	1.102	13.53	-1.325	90.74
	8	2.608	0.456	1.310	9.51	-1.205	88.59
	10	2.721	0.325	1.478	6.97	-1.125	86.98
2	2	2.363	0.907	1.190	11.71	-2.430	99.24
	4	2.533	0.565	1.414	7.87	-2.425	99.23
	6	2.758	0.291	1.668	4.76	-2.354	99.07
	8	2.879	0.199	1.824	3.41	-2.106	98.24
	10	3.016	0.128	2.002	2.26	-1.987	97.65
3	2	2.447	0.719	1.097	13.64	-2.778	99.73
	4	2.697	0.350	1.301	9.66	-2.997	99.86
	6	2.879	0.200	1.597	5.51	-2.614	99.55
	8	3.053	0.113	1.844	3.26	-2.473	99.33
	10	3.206	0.0672	2.061	1.96	-2.353	99.07
4	2	2.214	1.34	0.659	25.48	-2.993	99.86
	4	2.452	0.710	0.884	18.84	-3.153	99.92
	6	2.667	0.383	1.083	13.95	-2.890	99.81
	8	2.804	0.253	1.326	9.24	-2.680	99.63
	10	2.956	0.157	1.511	6.54	-2.557	99.47
5	2	2.138	1.63	0.559	28.82	-1.967	97.54
	4	2.396	0.829	0.756	22.49	-1.917	97.24
	6	2.677	0.372	0.929	17.63	-1.850	96.78
	8	2.835	0.230	1.148	12.54	-1.649	95.04
	10	3.017	0.128	1.323	9.30	-1.506	93.39
6	2	2.012	2.21	0.698	24.24	-0.336	63.16
	4	2.263	1.18	0.955	16.97	-0.315	62.35
	6	2.447	0.720	1.247	10.62	0.088	46.49
	8	2.642	0.412	1.446	7.41	0.266	39.52
	10	2.806	0.251	1.675	4.70	0.472	31.85
7	2	1.051	14.67	-0.523	69.94	-0.501	69.18
	4	1.210	11.32	-0.424	66.43	-0.430	66.65
	6	1.389	8.24	-0.266	60.48	-0.309	62.13
	8	1.509	6.57	-0.163	56.49	-0.224	58.86
	10	1.646	4.98	-0.053	52.12	-0.134	55.32
8	2	0.416	33.87	-0.387	65.08	-0.369	64.38
	4	0.520	30.16	-0.323	62.67	-0.357	63.95
	6	0.607	27.18	-0.251	59.90	-0.241	59.52
	8	0.741	22.95	-0.144	55.71	-0.129	55.12
	10	0.848	19.81	-0.055	52.20	-0.046	51.83
9	2	0.147	44.17	-0.239	59.43	-0.283	61.15
	4	0.172	43.17	-0.186	57.37	-0.236	59.34
	6	0.326	37.21	-0.104	54.14	-0.179	57.11
	8	0.394	34.69	-0.055	52.18	-0.115	54.59
	10	0.480	31.57	-0.004	50.17	-0.043	51.71

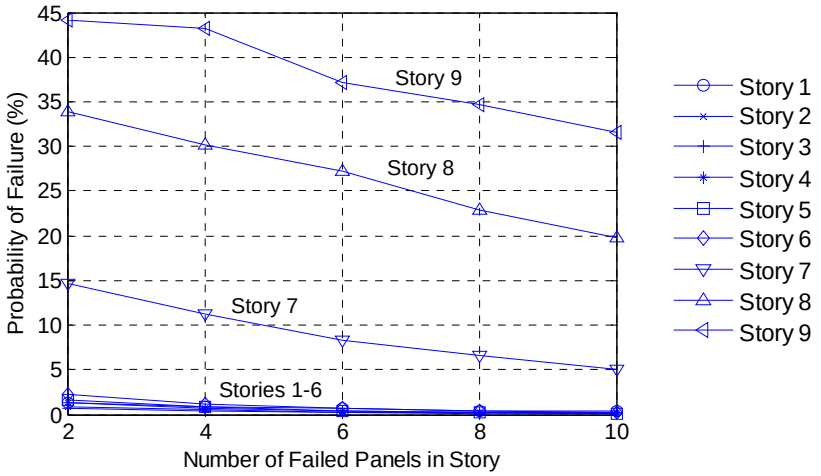

Fig. 6.15 Probability of failure for different number of failed panels in each story – low hazard level (50% PE in 50 yrs).

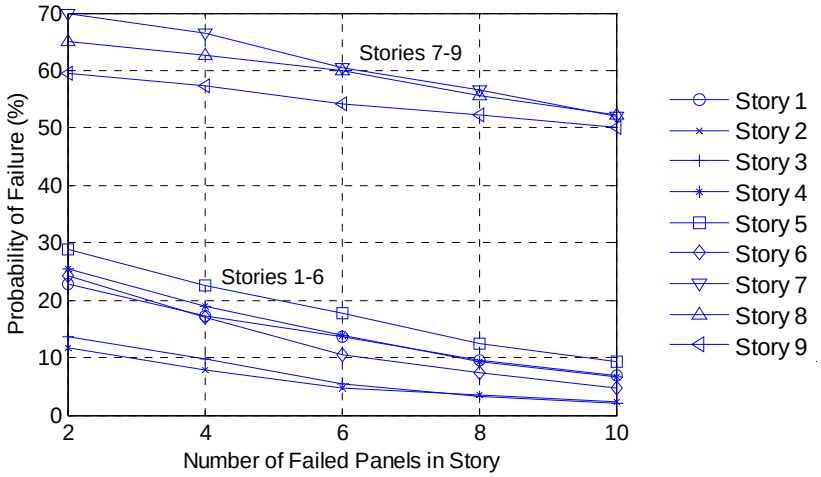

Fig. 6.16 Probability of failure for different number of failed panels in each story – moderate hazard level (10% PE in 50 yrs).

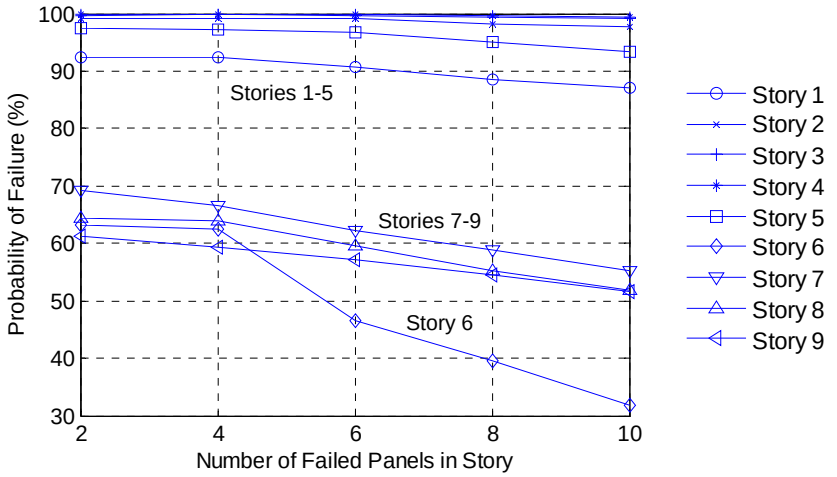

Fig. 6.17 Probability of failure for different number of failed panels in each story – high hazard level (2% PE in 50 yrs).

Table 6.13 Conditional probability of failure of one panel in story *i* given failure of one panel in story *j*

Story *i*	P(Failure of panel in story *i* | Failure of panel in story *j*)									
	Hazard Level	Story *j*								
		1	2	3	4	5	6	7	8	9
1	Low	1.00	0.507	0.400	0.252	0.150	0.140	0.056	0.037	0.031
	Moderate	1.00	0.757	0.489	0.253	0.189	0.144	0.243	0.257	0.263
	High	1.00	0.929	0.925	0.924	0.930	0.963	0.934	0.938	0.947
2	Low	0.341	1.00	0.334	0.211	0.132	0.135	0.046	0.026	0.021
	Moderate	0.390	1.00	0.331	0.160	0.119	0.086	0.1216	0.128	0.131
	High	0.999	1.00	0.993	0.993	0.996	0.998	0.992	0.993	0.994
3	Low	0.212	0.265	1.00	0.233	0.159	0.133	0.038	0.020	0.016
	Moderate	0.294	0.386	1.00	0.295	0.237	0.200	0.126	0.118	0.117
	High	0.999	0.998	1.00	0.998	0.998	0.999	0.997	0.997	0.998
4	Low	0.250	0.312	0.434	1.00	0.271	0.201	0.062	0.036	0.030
	Moderate	0.283	0.347	0.551	1.00	0.531	0.486	0.203	0.161	0.154
	High	0.999	0.999	0.999	1.00	0.999	1.00	0.998	0.999	0.999
5	Low	0.180	0.236	0.357	0.328	1.00	0.218	0.063	0.039	0.035
	Moderate	0.236	0.286	0.491	0.590	1.00	0.585	0.221	0.157	0.149
	High	0.983	0.979	0.977	0.976	1.00	0.993	0.967	0.967	0.968
6	Low	0.229	0.328	0.407	0.332	0.297	1.00	0.121	0.062	0.048
	Moderate	0.154	0.179	0.355	0.463	0.501	1.00	0.219	0.166	0.165
	High	0.659	0.635	0.633	0.632	0.643	1.00	0.634	0.615	0.622
7	Low	0.613	0.744	0.771	0.676	0.568	0.802	1.00	0.392	0.278
	Moderate	0.747	0.726	0.646	0.558	0.546	0.631	1.00	0.886	0.923
	High	0.700	0.692	0.692	0.692	0.686	0.694	1.00	0.910	0.920
8	Low	0.934	0.974	0.962	0.908	0.809	0.955	0.906	1.00	0.607
	Moderate	0.735	0.711	0.562	0.412	0.362	0.447	0.824	1.00	0.930
	High	0.655	0.644	0.644	0.644	0.638	0.626	0.847	1.00	0.928
9	Low	0.998	1.00	0.999	0.991	0.956	0.956	0.836	0.792	1.00
	Moderate	0.688	0.663	0.508	0.359	0.313	0.404	0.784	0.849	1.00
	High	0.627	0.612	0.612	0.612	0.607	0.602	0.813	0.881	1.00

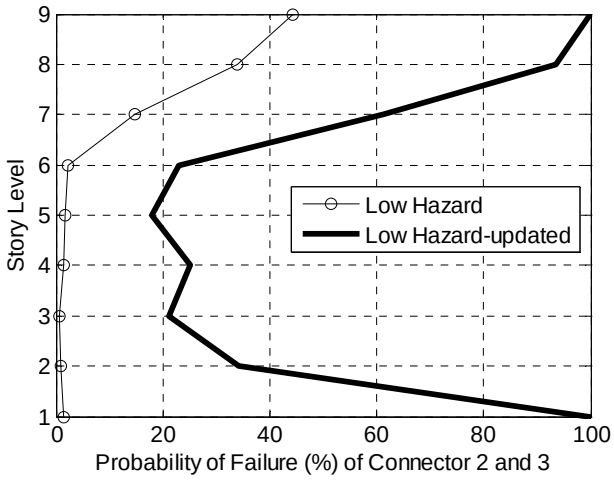

Fig. 6.18 Updated probability of failure of one panel given that a panel in the first story has failed – low hazard level (50% PE in 50 yrs).

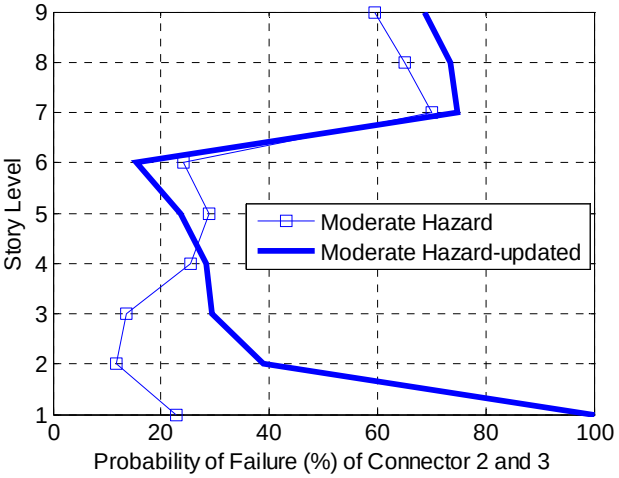

Fig. 6.19 Updated probability of failure of one panel given that a panel in the first story has failed – moderate hazard level (10% PE in 50 yrs).

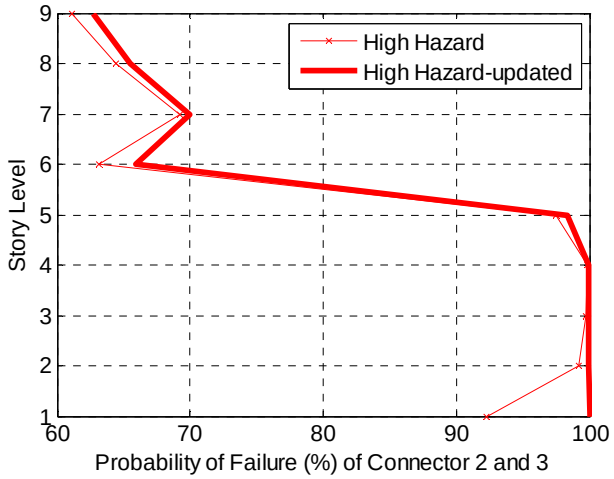

Fig. 6.20 Updated probability of failure of one panel given that a panel in the first story has failed – high hazard level (2% PE in 50 yrs).

Table 6.14 Results of probabilistic seismic hazard analysis

Hazard Level PE in 50 yr	R, Return Period (yr)	$H(S_a) = 1/R$	$Sa(T_1)$ (g)	Slope of Hazard Curve	P_H (h, t=50 yr)	P_H (h, t=1 yr)
Low, 50%	75	0.01333	0.11	-0.17762	0.6781	0.9874
Moderate, 10%	475	0.002105	0.34	-0.013969	0.3121	0.01226
High, 2%	2475	0.000404	0.65	-0.0017194	0.009753	2.897 E-04

Table 6.15 Total story probabilities of failure

Story	P_{fl} (%) t = 50 yrs	P_{fl} (%) t = 1 yr
1	6.29	1.57
2	4.03	1.02
3	4.47	0.86
4	7.76	1.58
5	9.05	1.91
6	7.18	2.40
7	31.25	15.32
8	43.06	34.22
9	48.39	44.33

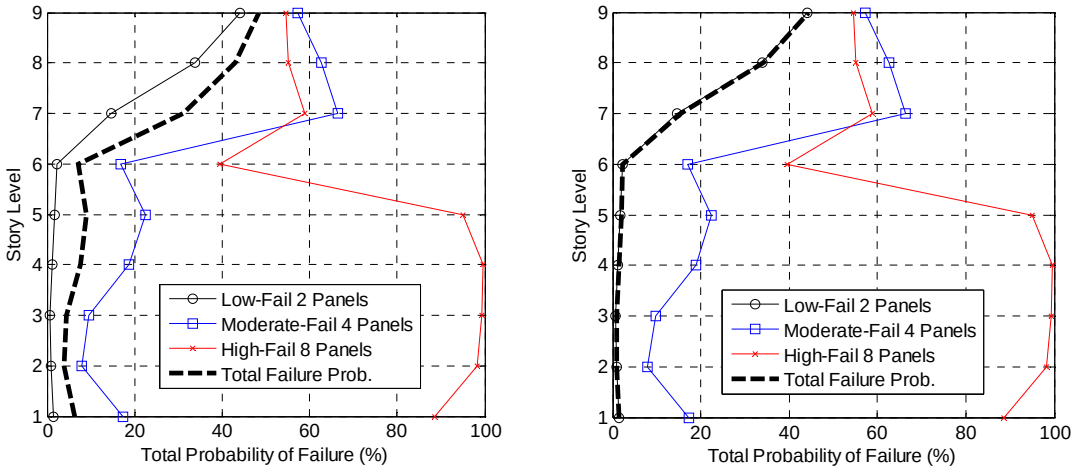

(a) t = 50 years **(b) t = 1 year**

Fig. 6.21 Total system failure probability to fail 2 panels in the low hazard event, 4 panels in the moderate hazard event, and 8 panels in the high hazard event.

Chapter 7: Performance-Based Repair Cost Analysis of Cladding Systems

The seismic response of the cladding systems was evaluated in Chapter 4 using engineering demand parameters (EDPs) such as the maximum interstory drift and the maximum deformations in the cladding connectors. These quantities are useful for engineers and researchers; however, the end-users and decision-makers of the systems are not able to translate these EDPs into a quantity useful for making decisions on post-earthquake repair cost scenarios. In this chapter, the PEER PBEE methodology for calculating post-earthquake repair costs and repair times is used to convert the seismic hazard at the building site into decision variables (repair cost and repair time) that the building owner can more readily understand. In the first two sections, a brief outline is given on the PEER PBEE method, the intermediate models, and the different solution strategies (summarized from Mackie *et al*., 2008a). Then, the PEER method is applied to the nine-story SAC building with the three cladding systems described in Chapter 3. The damage states of the cladding system components, presented as fragility curves, were obtained from previous experimental tests. The repair quantities for each damage state, the unit repair costs, and repair times were obtained from conversations with industry manufacturers of cladding systems.

7.1 PEER PBEE METHODOLOGY

In this section, the performance-based earthquake engineering (PBEE) methodology developed by the Pacific Engineering Earthquake Research (PEER) Center is briefly summarized. This section is not intended to be an all encompassing review of the PEER PBEE method and its solution strategies. The reader is referred to previous reports, such as Yang *et al*. (2006, 2009), Porter and Kiremidjian (2001), Mackie *et al*. (2008a, 2008b), and Mitrani-Reiser (2007) for a background of the PEER PBEE development and details on the formulation, derivations, and solution strategies.

In the last several years, the Pacific Engineering Earthquake Research (PEER) Center has made significant advances in understanding how earthquakes affect the safety and economic losses in buildings and bridges. One of the main goals of the PEER Center has been to develop and implement a modular, performance-based earthquake engineering (PBEE) methodology to quantify the effects that earthquakes have on the safety of our society's built environment. The PEER PBEE method is intended to be a more complete methodology than prescriptive-based approaches and earlier performance-based approaches such as Vision 2000 and FEMA 356. The PEER method allows for the definition of performance objectives under uncertain hazard levels.

The performance objectives are typically defined in terms of thresholds of decision variables (DVs) being exceeded in the seismic hazard. Instead of constructing a probabilistic model directly relating the DVs to intensity measures (IMs) of the seismic hazard, the problem is disaggregated into intermediate probabilistic models developed to address sources of randomness and uncertainty (Mackie *et al*., 2008a). The intermediate models are then combined using total probability theorem. The disaggregation involves the following intermediate variables: seismic hazard intensity measures (IM), engineering demand parameters (EDP), and damage measures (DM). An illustration of the intermediate steps of the PEER methodology is shown in Fig. 7.1. Typical DVs used to evaluate the performance of conventional building structures include repair cost, downtime, and fatalities. DMs can describe the state of damage to the structure as a whole or damage to a particular component (spalling of concrete, cracking of windows, etc.). EDPs are used to quantify the demands in the structural components. Typical EDPs include interstory drifts, strains, floor accelerations, and plastic hinge rotations. Finally, IMs are used to define the intensity of the seismic environment for the structure's site. Typical IMs include first-mode spectral acceleration ($Sa(T_1)$), peak ground acceleration (PGA), and peak ground velocity (PGV).

A common result of the PEER PBEE methodology is a scalar decision fragility curve that defines the conditional probability of exceeding a single (scalar) decision limit state (dv^{LS}) given a seismic intensity value *im*:

$$P(DV > dv^{LS}|IM = im) = \int\int G_{DV|DM}(dv^{LS}|dm)\left|dG_{DM|EDP}(dm|edp)\right|\left|dG_{EDP|IM}(edp|im)\right| \quad \text{Eq. 7.1}$$

The complementary cumulative distribution function (CDF) of intermediate variable X (DV, DM, or EDP) conditioned on intermediate variable Y (DM, EDP, or IM) is written as $G_{X|Y}$. Similarly, the probability density function (PDF) of intermediate variable X conditioned on intermediate variable Y is denoted $dG_{X|Y}$. The lowercase variables in Equation 7.1 represent individual realizations of their capitalized random variable counterparts.

Another common result of the methodology is the mean annual frequency (MAF) of exceeding the same scalar decision limit state (dv^{LS}). The MAF of exceedance, ν, is defined in Equation 7.2.

$$\upsilon_{DV}(dv^{LS}) = \int G_{DV|IM}(dv^{LS}|im)|d\upsilon_{IM}(im)| \quad \text{Eq. 7.2}$$

In this dissertation, the DVs are the post-earthquake repair cost and repair time. There are three main approaches to applying the PEER framework to the problem of building loss modeling, as discussed in Mackie *et al*. (2008a). The third approach discussed in their report, which is a vector approach based on damage model linearization, is used in this research for the PEER framework. This vector approach disaggregates the building into all relevant structural and nonstructural components, denoted as performance groups. The concept of disaggregating structures into performance groups has been investigated previously for buildings by Porter and Kiremidjian (2001) and Yang *et al*. (2006). In the Mackie *et al*. (2008a) approach adopted in this research, it is necessary to consider an additional intermediate probabilistic model into the framework that relates damage to repair quantities (Qs). The repair quantities are multiplied by their respective unit repair costs and repair times for all components, taking into account correlation, before producing the eventual DV.

7.1.1 Seismic Hazard Model

The first step in this approach is to develop the probabilistic seismic hazard model. The seismic hazard model takes into account nearby faults, site distance, source-to-site conditions, and directivity effects. Probabilistic Seismic Hazard Analysis (PSHA) is used to evaluate the mean occurrence rate (mean frequency) of events having an intensity measure (IM) greater than a threshold value, *im*, for a specific site of interest (Cornell, 1968; Kramer, 1996). There are many ways to obtain a site-specific PSHA; however, one of the most common is to use the median seismic curve from the USGS hazard maps. Hazard data should be available for the selected IM (*PGA*, *Sa*, Arias Intensity, etc.). The selection of the IM cannot be made arbitrarily; however, since the selection of the IM determines the efficiency of the EDP-IM relationship (Mackie *et al*., 2008a). Efficiency of the IM is defined in terms of dispersion of the demand model, with 0.35 or less being considered good. The first-mode spectral acceleration is an efficient choice of IM for most structures, especially multistory buildings.

The median seismic hazard curve is generated using the values of the intensity measure at a few selected levels of probability of exceedance. The median hazard curve is assumed to have a power-law form of Equation 7.3 with two unknown parameters, which are determined from the IM data points. The unknown parameters are determined numerically using a least-squares fit in log space, as shown in Equation 7.4.

$$\hat{v}_{IM}(im) = k_o(im)^{-k} \qquad \text{Eq. 7.3}$$

$$\ln\left(\hat{v}_{IM}(im)\right) = \ln(k_o) - k\ln(im) \qquad \text{Eq. 7.4}$$

An example of a seismic hazard curve for a site in Berkeley, California is shown in Fig. 7.2. (Mackie *et al*., 2008a). The IM selected for the plot was the spectral displacement at the first mode period of a bridge.

7.1.2 Demand Model

The second intermediate model is the demand model, which relates the seismic intensity measure (IM) of site-specific ground motions in terms of engineering demand parameters (EDPs) on the structure. The EDPs are generated by using a mathematical computer model of the structural system and a structural analysis method (such as time-history analysis). The computer model is subjected to the selected ground motion acceleration histories, and the EDPs of interest are recorded during the analysis.

The demand model is represented by Equation 7.5 in log space and Equation 7.6 in linear space. The two coefficients in the demand model and the dispersion $\sigma_{EDP|IM}$ are computed using least-squares regression. In linear EDP-IM space, the demand model coefficients become $a = exp(A)$ and $b = B$. The variable $\widehat{EDP}$ is the median, or mean of the natural log of the data points, of the engineering demand parameter.

$$\ln\left(\widehat{EDP}\right) = A + B\ln(IM) \qquad \text{Eq. 7.5}$$

$$\widehat{EDP} = a(IM)^b \quad \text{Eq. 7.6}$$

Several researchers have studied the EDP-IM relationship for buildings (Shome and Cornell (1999); Luco and Cornell (2003); Baker and Cornell (2003); Medina and Krawinkler (2003); Alavi and Krawinkler (2004)).

7.1.3 Damage Model

The third step of the PEER PBEE methodology is the damage analysis. This step uses fragility functions to express the probability that a structural or nonstructural component exceeds a particular damage state as a function of an EDP. The building components are aggregated together into performance groups (PGs), and the damage model describes how the damage to a particular performance group progresses as the EDP increases. A performance group typically consists of components whose damage states (DS) are controlled by the same EDP and have similar repair methods. The different damage states for each performance group are defined considering the repair efforts needed to restore that component to an undamaged state. For example, the damage to a window system can be lumped into one performance group whose damage states are dependent on the interstory drift ratio. The damage states (DS) of the performance group are numbered DS0, DS1, DS2, etc., with higher numbers indicating higher amounts of damage (Mackie *et al*., 2008a). The DS0 state corresponds to the onset of damage and when repair costs begin to accumulate. For this study, the repair cost is \$0 for a performance group with damage below the DS0 level, since damage below this level is assumed to be insignificant and not needing repair. When the damage exceeds the DS0 level, repair costs begin to accrue. For concrete columns, the damage states could be negligible damage with initial cracking (DS0), spalling of cover concrete (DS1), yielding of longitudinal reinforcement (DS2), and fracture of longitudinal reinforcement (DS3). As discussed in Mackie *et al*. (2008a), the moment-based method used to solve the PEER equations assumes that a continuous range of damage exists between the damage states; thus, the definition of the maximum possible repair quantities is needed to maintain an upper limit to the quantities and costs. Appropriately, the upper limit is referred to as DS∞, for which no additional incremental costs are accrued in the performance group. The DS∞ limit corresponds to complete failure of the components in the particular performance group.

The fragility functions that describe the damage states of the performance groups are complied based on experimental tests, analytical simulations, expert opinion, or any combination of these.

$$\ln\left(\widehat{DM}\right) = C + D\ln(EDP) \quad \text{Eq. 7.7}$$

The median relationship between EDP and DM and the associated dispersion, $\sigma_{DM|EDP}$, completely define the damage model. Similar to the demand model, a power-law relationship is used to describe the median relationship, as shown in Equation 7.7. In linear space, the damage model coefficients become $c = exp(C)$ and $d = D$.

7.1.4 Decision Model

The final step in the PEER methodology is to use a decision model to translate the damage measures (DMs) into decision variables (DVs). Common decision variables include post-earthquake repair costs (dollars), repair time (downtime), fatalities (deaths), and building safety tagging. Using the approach by Mackie *et al*. (2008a), the decision model has two parts: one part relates DMs to repair quantities (Q), and one part relates Q to repair cost or repair time. The final product of the decision model is the mean and dispersion of repair costs or repair time for various levels of seismic intensity measure (IM). The data to construct the decision model can come from professional surveys, cost estimators, or repair data from post-earthquake reconstruction (Mackie *et al*., 2008a).

When both the DM and DV are chosen as continuous variables, the median relationship between DM and DV, shown in Equation 7.8, and the dispersion $\sigma_{EDP|IM}$ completely define the decision model.

$$\ln(\widehat{DV}) = E + F\ln(DM) \qquad \text{Eq. 7.8}$$

In linear space, the decision model coefficients become $e = exp(E)$ and $f = F$. The power law relationship is assumed to apply locally in the region of values of interest.

7.2 SOLUTION STRATEGIES

There are several solution methods for implementing and solving the PEER PBEE framework equations. A downloadable toolbox for use in OpenSees Navigator was developed by Yang *et al*. (2006, 2009) to solve for repair costs. In this approach, Monte Carlo simulations are used to generate loss fragilities and mean annual frequencies of exceedance of decision variables. Based on the fragility and repair cost data in Yang *et al*., a graphical user interface program, termed the Performance Assessment Calculated Tool (PACT), was developed to calculated repair costs for different structural and nonstructural components (Rojhana and Hamburger, 2007). This program is available for download over the internet. A similar program for calculating the repair costs of buildings was developed in Matlab by Mitrani-Reiser *et al*. (2006); however, this program was not found to be publically available. Another Matlab-based toolbox was developed by Mackie *et al*. (2008a), in which several solution strategies are pursued. Three solution strategies are presented in their study: closed form, Fourway, and numerical integration. In the closed-form solution method, the intermediate models (CDFs) are assumed to be lognormal, so the DVs (also a lognormal variable) can be conditioned directly on the IM. The Fourway strategy (Mackie and Stojadinovic, 2006) is based on a graphical technique for estimating the parameters of the lognormal distribuition describing the DVs. The numerical integration procedure allows for the use of arbitrary mathematical functions to specify the hazard, demand, damage, and decision models (Mackie *et al*., 2008a). Three approaches of applying the PEER PBEE equations are also discussed in Mackie *et al*. (2008a): a scalar approach and two vector-based approaches. The scalar approach uses the intermediate variables IM-EDP-DM-DV to determine the repair cost ratio (RCR), or ratio of repair cost to replacement cost, to define the losses (DV). In the second approach, a vector-based approach, scalar-type analyses are performed for each performance group and repair item in IM-EDP-DM-Q space.

The third approach, a vector-based approach with damage model linearization, is a more refined application of the first vector-based approach. This approach overcomes the issues of unpredictable behavior of the first-vector approach at demand beyond the last damage state and unrealistically large dispersion values for the repair quantities when there are large changes in repair values between damage states. The repair costs and repair time estimates calculated in this chapter use this third approach along with the closed-form solution method described in Mackie *et al*. (2008a).

7.3 APPLICATION OF PEER METHOD TO THE NINE-STORY SAC BUILDING

Many design firms currently use code documents such as ASCE 7 and FEMA 356 and 450 to design the components of cladding systems. As summarized in Chapter 1, the design the design approaches given in these documents are both force-based and displacement-based. Typically, the design of the connectors of the precast panels follows a force-based approach, while the design of the glazing system follows a displacement-based approach. Performance-based design approaches are starting to be used more often in the design and evaluation process for cladding systems. For example, a flowchart for the damage state analysis of cladding systems used by Mark Hildebrand at Willis Construction is provided in Fig. 7.3.

The PEER PBEE methodology summarized in Section 7.1 is used to calculate the repair costs and repair times for the cladding systems of the nine-story SAC building described in Chapter 3. The vector-based approach with damage model linearization and the closed-form solution method described in Mackie *et al*. (2008a) are used to implement and solve the PEER PBEE equations. Using the PEER PBEE methodology provides the most complete approach to determining the cladding system states of damage and financial losses due to earthquake ground motions.

7.3.1 Probabilistic Seismic Hazard Model

The site for the nine-story SAC building was selected to represent a typical urban location in a highly seismic region of California. The chosen location site is on the UC Berkeley campus in Berkeley, CA (coordinates: 37.87 degrees latitude and -122.26 degrees longitude). This site has the advantage of available high quality geotechnical and seismic hazard data from the UC Berkeley Campus Seismic Guidelines (URS, 2007). The probabilistic seismic hazard model was developed using the approach described in Section 7.1.1. The seismic hazard curve developed in the study is shown in Fig. 7.4. Four data points in the seismic hazard curve corresponding to the 50%, 20%, 10%, and 2% in 50 year probability of exceedance were used to determine the seismic hazard model. The four data points are shown in Table 7.1, and the model coefficients k and k_o that best fit the four data points are shown in Fig. 7.4.

The ground motions selected to represent the seismic hazard model were discussed in Chapter 4. A total of 7 bins of 20 records each were used along with the cloud method of dynamic time-history analysis to obtain the structural analysis results.

7.3.2 Probabilistic Seismic Demand Model

The probabilistic seismic demand models of the nine-story SAC building with various types of cladding were derived in Chapter 4. The EDP-IM relationship was defined using a mathematical model of the structure and cladding system (Chapter 3). The structural model was subjected to 140 ground motions that represented a range of seismic intensities, and engineering demand parameters in the structure were recorded during the analyses. The coefficients that define the power law relationship between EDP and IM discussed in Section 7.1.2 are provided for several different EDPs (interstory drift, floor accelerations, and deformations in the cladding connectors) in the figures of Chapter 4. A total of 1,559 EDPs were tracked during each analysis. Using these EDPs, a total of 54 probabilistic seismic demand models (PSDM) were created for this study, representing the maximum interstory drift, residual interstory drifts, floor accelerations, plastic hinge rotations, connector deformations in the spandrel panels, and connector deformations in the column cover connectors. The choice of IM for use with the EDPs is based on minimizing the dispersion in the EDP-IM relationship. In this study, the first-mode spectral acceleration $Sa(T_1)$ is selected as the IM. However, it is difficult to draw direct comparisons between the PSDMs from buildings with different cladding systems (different first-mode periods) due to the period dependence of the IM. Therefore, the selected IM for all four models (one bare frame model and three different cladded models) is chosen as the first mode spectral acceleration of the bare-frame model ($Sa(T_1 = 2.13$ sec.)).

7.4 DAMAGE STATES AND REPAIR METHODS FOR CLADDING SYSTEM

There are several types of damage states associated with cladding failure, including those related to the caulking between the cladding panels, the components of the window glazing, and the connections between the cladding panels and the structural frame. Little to no damage is expected in the precast panels themselves due to their thickness and rigidity. As such, the panels are modeled to behave as rigid blocks, and the damage to the cladding system is concentrated on the connectors and window glazing system.

The thresholds for each of the damage states and the repair quantities of the cladding system are summarized in the following sections. As discussed in Section 7.1, a lognormal distribution is assumed to describe the cumulative probability of exceeding each damage state. The median values, λ, of the engineering demand parameter (EDP) are given for each damage state along with a shape parameter, β, that represents the logarithmic standard deviation (a larger β represents more uncertainty). The values of β were based on statistical data from experimental tests and engineering judgment. The damage states and repair quantities given in this section apply to each story of the building (i.e. damage and repair is considered on a per story basis).

7.4.1 Caulking

Silicone caulking is used to seal the joints between the various cladding components and provide a watertight and airtight cladding system. Caulking is applied to both the joints between the cladding panels and the joints between the window framing and the panels. The locations in

the cladding system where the caulking is applied are shown in Fig. 7.5. The caulking must accommodate the movements caused by the interstory drift; thus, the EDP that best describes the state of damage to the caulking is interstory drift.

Information about the damage states of typical silicone caulking used in cladding systems was obtained from personal communication with Mark Hildebrand (2009) at Willis Construction, a local precast cladding fabricator. Hildebrand performed experimental tests on the shear stiffness and strength of caulking. The tests consisted of three adjacent rectangular concrete blocks with caulking applied to the vertical joints between each of the blocks. The vertical joints were 0.75 inches wide, which is typical for joints used in cladding system. The two outer blocks were restrained from vertical movement, while the middle block was displaced vertically with an actuator. The vertical movement of the middle block was resisted by the shear strength of the caulking, and the force and displacement were measured to determine when the caulking failed. The caulking showed initial hairline cracking at 0.75 inches of shear displacement (0.48% drift, assuming the story height of 156 inches). This first damage state represents the DS0 level of damage: for interstory drift ratios less than 0.48%, no repair to the caulking is assumed necessary. With further loading, the caulking continued to deform and showed major cracking (failure) after 1.5 inches of shear displacement (0.96% drift). Absent more detailed test information, the logarithmic standard deviations are set to 0.15 for the DS0 state and 0.25 for the DS1 state. The damage states of the caulking are summarized in Table 7.2 and Fig. 7.6.

The repair quantities for each damage state were estimated by Hildebrand (2009). For interstory drift ratios of approximately 0.7%, 1%, and 2% about 25%, 50%, and 75% of the total caulking length in the story would need to be replaced, respectively. The estimates increase rapidly with interstory drift because as more caulking is damaged, more of the adjacent undamaged caulking must be replaced to provide adequate color matching due to long-term fading of the original caulking. The total amount of caulking in the building for each cladding type was given in Chapter 3.

7.4.2 Window Glazing Systems

The window glazing system is made up of several damageable components: glass panes, rubber gaskets, and aluminum framing. The window glazing system can vary significantly from building to building; however, in this study a very common system is implemented for which testing data is available. The information about the damageable states of the glazing system is taken from data by Behr *et al*. (1995a,b) and Behr and Worrell (1998) for in-plane racking capacities of typical glazing systems.

7.4.2.1 Glass Panes

In-plane racking tests of storefront and mid-rise glazing systems were performed by Richard Behr from 1992 to 1997 (Pantelides and Behr, 1994; Behr *et al*., 1995a,b; Behr and Belarbi, 1996; Behr and Worrell, 1998; Behr, 2006). The test results are summarized well in Behr and Worrell (1998). In this dissertation, the discussion of their results is limited to the mid-rise glazing systems: the storefront systems are used in the first story of low-rise buildings, while the mid-rise systems are used in multistory buildings.

The mid-rise glazing system tested was the Kawneer 1600™ wall system, which is a popular glazing system for mid-rise structures. The glazing system was placed in a steel test frame, and an actuator was used to subject the assembly to in-plane dynamic shear motion, simulating interstory drift. The window framing system consisted of aluminum mullions; Fig. 7.7 shows the details of the horizontal sill jamb, the vertical mullion, and the horizontal head jamb (Behr *et al*., 1995a). The glass panes were 5 feet wide and 6 feet tall, which matches the size of the windows used in the SAC buildings. Several glass types were tested in the mid-rise system:

- 6 mm (1/4 in.) annealed monolithic
- 6 mm (1/4 in.) heat-strengthened monolithic
- 6 mm (1/4 in.) fully-tempered monolithic
- 6 mm (1/4 in.) annealed monolithic with 0.1 mm PET film
- 6 mm (1/4 in.) annealed laminated
- 6 mm (1/4 in.) heat-strengthened monolithic spandrel
- 25 mm (1 in.) annealed insulating glass units (IGU)
- 25 mm (1 in.) heat-strengthened insulating glass units (IGU)

In today's construction, the 25 mm (1 in.) annealed insulating glass units (IGUs) and the 25 mm (1 in.) heat-strengthened insulating glass units (IGUs) are typically used in most locations in multistory buildings. The heat-strengthened IGUs are commonly used in safety critical locations (near doors or ground level) because these units do not break into large shards when damaged. In all other locations, the annealed IGUs are assumed.

The glass panes were dry-glazed to the window framing using rubber gaskets, as shown in Fig. 7.7. The window assembly was subjected to "crescendo tests," where the shear displacement was applied cyclically (positive and negative displacements) with gradually increasing amplitudes up to 6 inches. The displacements were recorded for three major events: (1) when the glass pane impacted the surrounding window frame, (2) when cracking developed in the glass pane, and (3) when major cracking and glass fallout occurred. The results are shown in Fig. 7.8 for the three events. Six tests were performed each for annealed and heat-strengthened IGUs; the symbol in the figure represents the mean values, and the error bars show the standard deviation. The test results of the IGUs show that there is no significant difference in the seismic performance of the annealed IGU and the heat-strengthened IGU.

Using the mean and standard deviation values in Fig. 7.8, the median and logarithmic standard deviation values are computed assuming the data follows a lognormal distribution. The median displacement at which the glass impacts the surrounding framing is 0.94 in. (0.006 rad. using a story height of 156 in.). The repairable damage corresponding to this damage state is negligible (DS0 damage state): small, non-critical cracks developed around at the edges of the glass that do not affect the serviceability of the window system. For this damage state, the extent of perimeter cracking was limited to approximately 1.6 in. (0.3%) of the glass perimeter. The edge damage was not sufficient enough to warrant immediate glass replacement; however, the damage may cause long-term serviceability problems, such crack propagation due to thermal and wind stresses.

As interstory drift increases to reach the DS1 damage state, the glass pane is subject to translation and rotation within the glazing pocket. The glass does not become cracked or need replacement; however, the translation and rotation of the glass may cause a reduction or loss of glass bite (the amount of glass that extends into the glazing pocket). A loss of glass bite compromises the water and air integrity of the glazing system, and the window would have to be

deglazed, repositioned, and reglazed to restore glass bite. At 1.7 inches of displacement (0.011 rad.), Behr *et al*. (1995a) report an average horizontal translation at the center of the glass pane of 0.21 inches and an average rotation at the center of the glass panel of 0.22 degrees. These movements result in 0.35 inches of total horizontal movement at one of the corners, which is very close to the initial glass bite of 3/8 inches on all sides. Thus, the corner of the glass is very close to being completely pulled out of the glazing pocket, posing a risk to air and water infiltration. For this damage state, Behr *et al*. (1995a) report that approximately 10% of the IGUs tested experienced total glass bite loss over portions of their perimeters, which requires repositioning of the glass pane.

The DS2 damage state of the glass panes is observable cracking in the field of the pane. The median value of displacement corresponding to this state is 2.48 in. (0.016 rad. using a story height of 156 in.). This damage state affects the serviceability of the window system and requires removal and replacement of the damaged glass pane. Based on photos of damaged windows at this damage state, approximately 20% of the glass panes had observable cracks that warranted replacement. Photos of windows with damage corresponding to DS2 are shown in Fig. 7.9.

The DS3 damage state is major cracking and glass fallout. The median value of displacement corresponding to this state is 3.11 in. (0.020 rad. using a story height of 156 in.). This damage state affects the function and life-safety of the window system and requires removal and replacement of the damaged glass pane. At this level of damage, approximately 40% of the glass panes had major cracking or portions of glass fallout. Photos of windows with damage corresponding to DS3 are shown in Fig. 7.10.

One important detail in the use of these test results is the concept of interstory drift in the cladding system. Many of the researchers who have used the Behr and Worrell (1998) test data have assumed that the interstory drift index given in the paper is the interstory drift ratio for the entire story, which is incorrect. The interstory drift ratio for a story i is calculated as $\theta_{story} = \Delta h_i/H$, where Δh_i is the displacement between adjacent floors and H is the story height (156 inches in this study). The Behr and Worrell interstory drift index, θ_{pane}, is calculated as the shear displacement of the window frame divided by the height of the window, $\theta_{pane} = \delta/H_w$, where δ is the shear displacement and H_w is the height of the window (72 inches in this study). In precast cladding systems with spandrel panels, the interstory displacement, Δh_i, is approximately the same as the displacement of the window framing, δ, because the spandrel panel moves as a rigid block (neglecting the small rotation of the spandrel panel), as shown in Fig. 7.11. Thus, the shear displacements, δ, shown in Fig. 7.8 should be taken equal to interstory displacements, Δh_i, when calculating the interstory drift ratios at which the damage states occur.

7.4.2.2 Gaskets

The glass panes are dry-glazed to the window framing pocket using interior and exterior rubber Santoprene gaskets. The gaskets create a tight seal to ensure water and air tightness of the glazing system. However, during dynamic racking, the seals may become dislodged from their seat or pushed into the glazing pocket from the moving glass. The displacement at which the gaskets became displaced from their original position was recorded by Behr *et al*. (1995a). At 1.7 inches of shear displacement (0.011 rad. of interstory drift, assuming a story height of 156 in.), the movement of the window pane started to dislodge the gaskets. At this level of displacement, the average length of distorted, pulled-out, pushed-in, or shifted gaskets around the perimeter of

the glazing was about 10% of the gasket length (Behr *et al*., 1995b). The gaskets would also need to be replaced on the windows that are repositioned, since the window must be reglazed with new gaskets. A photograph of a window system with dislodged gaskets at 1.7 in. shear displacement is shown in Fig. 7.12.

7.4.2.3 Framing and Mullions

The aluminum framing and mullions are expected to sustain little damage during dynamic racking. Behr *et al*. (1995a) comment that the little damage that occurred was limited to gouging of the aluminum glazing pocket from the corners of the glass panes.

7.4.2.4 Damage States of the Window System

The individual damage states of each component of the window system make up the damage states of the system as a whole. The values of the median and logarithmic standard deviation for each damage state are shown in Table 7.3 and Fig. 7.13.

The results of the tests by Behr *et al*. agree well with the results of glazing tests by Nakata *et al*. (1984). The latter tests include six fixed panes of 5 mm (0.20 in.) glass with elastic sealant (pane width and height were not reported; diagrams suggest dimensions of 2 to 3 ft. by 5 to 6 ft.). Nakata *et al*. report that "cracks were found in fixed windows with elastic sealant when the story drift was around 1/125-1/173," or 0.008 to 0.014 rad. These data are inadequate to construct fragility curves; however, their results provide some validation of the Behr *et al*. test results.

7.4.3 Caulking and Window System: Drift Sensitive Cladding Components

Damage to both the caulking and the window system components are sensitive to interstory drift. Thus, these components are combined into one performance group with interstory drift as its EDP. The damage states for this combined performance group are shown in Table 7.4, and the associated repair items and quantities are shown in Table 7.5. The total amount of window panes and linear feet of gasket per story for each cladding type was given in Chapter 3.

7.4.4 Cladding Connectors

The mechanics of the cladding system and connections are discussed in detail in Chapters 4 and 5. The connectors that sustain most of the damage in the cladding system are the push-pull (threaded rod) connections that attach the spandrel panels to the columns and the top and bottom column cover connectors that attach the column cover panels to the spandrel panels. Thus, the discussion of the damage states, repair methods, and repair costs are limited to the push-pull and column cover connections.

7.4.4.1 Push-Pull Connectors

The push-pull connections are used to connect the spandrel panels to the structural framing. The connections are subjected to shear deformation by lateral displacement and rotation of the spandrel panel relative to the structural framing. The drawings and force-deformation relationship of the push-pull connection used in the SAC building were given in Chapter 3, and the discussion of the mechanics of deformation in the connections was given in Chapter 5.

The push-pull connection assembly used in this research was tested by McMullin *et al*. (2004). The test specimen consisted of four push-pull threaded rod connectors attached to plates on either end. The specimens were tested by a statically increasing load, and the contributions of the different components of the push-pull connections to the total force and displacement were recorded. The connection has an initial stiffness of 6.67 kip/in., yield force of 5.0 kip, yield deformation of 0.75 inches, post-yield stiffness of 2.0 kip/in., deformation at maximum strength of 2.2 inches, and a fracture deformation of 2.8 inches. The DS0 damage state level corresponds to the yield deformation, 0.75 inches, in the threaded rods. For deformations lower than this level, no damage that warranted repair was observed. After the yield point, the threaded rod began to plastify at both ends of the rod as double curvature developed. The DS1 damage state level is set at a shear deformation value of 1.25 inches, which corresponds to a ductility value of 2. The final damage state level, DS2, corresponds to a shear deformation of 2.2 in., the deformation at maximum strength (ductility of approximately 3). Absent better information, a value of 0.25 is assumed for the logarithmic standard deviation for all three damage states. A photograph of a push-pull test specimen that fractured at approximately 2.2 inches of shear deformation is shown in Fig. 7.14. The damage states of the push-pull connection are summarized in Table 7.6 and Fig. 7.15.

The repair methods for the push-pull connectors involve removal of the threaded rod portion of the connection and replacing it with a new rod. The push-pull connections can be accessed through the ceiling space (assuming an acoustical tile system is used, which is common in office buildings). According to Knowles (2010), for both the DS1 and DS2 damage states, the threaded rod would need to be replaced.

There are a total of 340 push-pull connections in the nine-story SAC building, and thus, 340 EDPs would need to be tracked to determine the state of all the push-pull connections. However, a reduction in the required EDPs can be made by considering just a single line of push-pull connectors up the height of the building and inferring the state of all the other connectors based on these selected connectors. The selected (leading) connectors, shown in Fig. 5.9, are in the same locations as the selected connectors in Chapter 5. The relationship between the deformation in the selected connectors and the deformations in the other connectors in a certain story can be obtained from the pushover analysis results. For example, in Fig. 7.17, the deformations of the bottom push-pull connectors are shown for story 3 for the case that the deformation in the selected connector is 1.25 in. (DS1). Based on the pushover analysis results, there are two other connectors that have reached or exceeded 1.25 in. Thus, three bottom push-pull connectors on each building face are replaced when the selected bottom push-pull connector in that story reaches a deformation of 1.25 in. For the DS2 damage state, six connectors reach or exceed a deformation of 2.2 in. when the selected connector reaches the same deformation. Thus, six bottom connectors are replaced on each building face when the selected bottom push-pull connector reaches a deformation of 2.2 in. A similar analysis is performed for the top push-pull

connectors, and the same repair quantities are obtained. The repair items and quantities for each damage state of the push-pull connectors are summarized in Table 7.7.

7.4.4.2 Column Cover Connectors

The column cover panels are connected to the spandrel panels at adjacent floor levels with pin-bolted connections at the bottom and slotted connections at the top. The drawings of the column cover connections are given in Chapter 3. The connections used in the column covers were tested by Crawford and Kulak (1968). The test specimens were 3/4-inch diameter ASTM 325 bolts installed in ASTM A36 steel plates that were 4 inches by 4 inches in size. A total of six identical specimens were tested. The specimens were tested in shear at a load rate of 0.025 inches per minute. The test specimens closely resemble the bottom column cover connection; however, the results can also be applied to the top connector for deformations that cause the bolt in the slotted connection to impact the end of the slotted hole. All test specimens showed failure in shear at the thread run-out portion of the bolt. A photograph of a fractured specimen is shown in Fig. 7.18. The load-deformation curve fitted to the results of the six tests is shown in Fig. 7.19.

The damage states of the column cover connectors are obtained from the test results and force-deformation curve. The DS0 damage state corresponds to the initiation of yielding, which occurs at approximately 50 kips. The median deformation of 0.068 in. at this damage state is calculated from the test data assuming a lognormal distribution. The DS1 damage state is set as the deformation corresponding to a force level 70 kips, representing a force-factor $R = 70/50 = 1.4$. The corresponding median deformation at this damage state is 0.22 in. The DS2 damage state is set as the deformation at maximum (fracture) force, which corresponds to a force-factor $R = 75/50 = 1.5$. The corresponding median deformation at this damage state is 0.33 in. The damage states of the bottom and top column cover connections are summarized in Table 7.8.

The repair methods for the column cover connectors involve removal and replacement of the damaged bolt and plate. The interior wall finish or drywall must be removed to access the connections. According to Knowles (2010), for both the DS1 and DS2 damage states, the column cover connection bolt and plate would need to be replaced.

There are a total of 1,584 column cover connections in the nine-story SAC building, and thus, 1,584 EDPs would need to be tracked to determine the state of all the column cover connections. However, a reduction in the required EDPs can be made by considering just a single line of column cover connectors up the height of the building and inferring the state of all the other connectors based on these selected connectors. The selected (leading) connectors, shown in Fig. 7.21, are in the same locations as the selected connectors in Chapter 5. The relationship between the deformation in the selected connectors and the deformations in the other connectors in a certain story can be obtained from the pushover analysis results. For example, in Fig. 7.22, the deformations of the bottom column cover connectors are shown for story 3 for the case that the deformation in the selected connector is 0.22 in. (DS1). Based on the pushover analysis results, there are five other connectors that have reached or exceeded 0.22 in. Thus, six bottom column cover connectors on each building face are replaced when the selected bottom column cover connector in that story reaches a deformation of 0.22 in. For the DS2 damage state, 13 connectors reach or exceed a deformation of 0.33 in. when the selected connector reaches the same deformation. Thus, 13 bottom connectors are replaced on each building face when the selected bottom column cover connector reaches a deformation of 0.33 in. A similar analysis is

performed for the top column cover connectors, and the same repair quantities are obtained. The repair items and quantities for each damage state of the column cover connectors are summarized in Table 7.9.

7.4.5 Separation of Cladding Repair Methods from Building Repair Methods

When evaluating the repair costs of the cladding separately from the repair costs of the entire building, it is important not to double-count certain repair items that apply to both the cladding and the overall building. For example, the cost of removing a cladding panel to access a moment-frame connection for repair would fall under the building repair costs, not the cladding repair costs. Moreover, if the drywall is damaged in a section where a column cover connection is damaged, then the drywall can be removed, the connection repaired, and new drywall installed. The repair items given in this section are assumed to apply only to the cladding system.

7.5 REPAIR COST AND TIME OF CLADDING SYSTEM

The data for the repair cost and repair time were obtained from personal communication with Ed Knowles (2010) at Walters and Wolf, Inc., a cladding designer, manufacturer, and erector located in Fremont, California. Walters and Wolf designs and fabricates all parts of cladding systems, including the panels, connections, and glazing systems, which made them a valuable resource for obtaining the repair cost and repair time estimates. The data was obtained by presenting hypothetical damage scenarios for which the damage was to be repaired.

7.5.1 Replacement Cost of Cladding System

The total repair cost estimate is a useful data point for making performance-based decisions; however, it is not clear how the magnitude of the repair cost estimate compares to the cost of building a new cladding system (replacement cost). Normalized costs of repair are obtained by calculating the repair cost ratio (RCR) between the total cost of repair and the replacement construction cost (Mackie *et al.*, 2008a). This ratio is useful for comparing the performance of different cladding designs for new construction. For the evaluation of cladding on existing structures, the RCR including demolition costs (which may be substantial) would be more useful. Construction of a new cladding system on an existing building requires both demolition of the cladding system and construction of the new cladding.

The replacement costs of the cladding systems were obtained from Knowles (2010). Knowles gave a cost/SF of cladding surface area of $55-$65 for the three cladding designs C1, C2, and C3. The construction costs for cladding types C1, C2, and C3 are $4,392,000, $4,026,000, and $4,758,000, respectively. These costs does not include the cost of demolition, which is required if the building is saved and the cladding must be replaced. The cost of demolition for the cladding was estimated by Knowles to be approximately $50/SF. The cladding surface area for each of the designs is 150 ft.x122 ft.x4 = 73,200 SF. Thus, the additional cost of demolition for each of the designs is estimated as 73,200 SF x $50 = $3,660,000. These costs are 2010Q1 values.

In Taghavi and Miranda (2003), new construction cost breakdowns of typical commercial buildings are presented. The costs were computed using unit costs from RS Means of over 200 building components. The costs were disaggregated into bins associated with structural components (steel framing, connections, etc.), nonstructural components (partitions, ceilings, floors, etc.), and building contents (computers, equipments, etc.). For a typical 5-10 story office building, the structural components account for 18% of the total cost, the nonstructural components account for 62% of the total cost, and the building contents account for 20% of the total cost. The nonstructural component costs were further disaggregated into their separate components. The costs associated with the exterior enclosure (cladding system) of the 5-10 story office building account for approximately 14% of the total building costs. In this study, the cladding cost (excluding demolition) accounts for up to \$4,758,000/\$40,110,131 = 12% of the total building cost, which agrees well with the data provided in Taghavi and Miranda (2003).

7.5.2 Repair Item Unit Costs

The unit costs for each repair item are given in Table 7.10. The inspection cost is required to determine how much damage occurred to the cladding system. This cost is independent of any inspection of damage to other parts of the building because special equipment and inspectors are necessary for the cladding system. The caulking is the only cladding component that must be accessed from the outside of the building. Thus, rigging and staging (similar to window washing equipment) is required to repair the caulking. The unit costs for the rigging vary depending on how much caulking needs to be removed and replaced. The costs are \$50,000, \$75,000, and \$100,000 for providing the rigging and staging to replace 25%, 50%, and 100% of the caulking, respectively. In the PEER methodology, the unit cost for rigging of \$50,000 is used and the repair quantity can be varied to represent different amounts of rigging needed for different damage states of the caulking. The unit costs for all other repair items can be considered an average representation of the unit cost. These average unit costs were determined considering the effects of economies of scale: a few repairs may be made in isolated locations (higher unit cost) or a large number of repairs made in close proximity to one another (lower unit cost). A 20% coefficient of variation was used to determine the standard deviation of the unit costs.

The unit costs given in Table 7.10 differ from previous repair cost estimates for cladding systems. Repair quantities and unit costs for a typical steel moment-resisting frame building are given in Yang *et al*. (2006, 2009). Their data, which includes repair quantities and unit costs for damage to structural components, nonstructural components, and building contents, were provided by the ATC-58 project participants. The damage states of the cladding system were limited to the windows and precast panels. However, as discussed in this dissertation, the majority of the damage to a heavy precast cladding system is not expected to occur in the panels themselves. Instead, the damage is focused in the cladding connections, caulking, and glazing system. Several other repair cost studies of multistory buildings, which are closely related to one another, include damage to cladding systems (Porter and Kiremidjian, 2001; Beck *et al*., 2002; Mitrani-Reiser, 2007). In these studies, the extent of damage to the cladding system is limited to the windows.

7.5.3 Repair Time

Several different terms have been used to express repair time when using the PEER methodology: downtime, repair duration, and repair effort. Downtime is used to denote the time in which the building, bridge, or component is non-functional after an earthquake because repairs are needed to bring it back into service. Downtime is especially important for bridges because closure of the bridge for repairs after the earthquake may adversely affect the response time of emergency personnel. The downtime of buildings and other structures is less of a concern with regard to life-safety; however, for certain types of buildings, downtimes may impact revenue, employee productivity, manufacturing efficiency, and company image. For example, if a computer chip manufacturer has to close a building after an earthquake for repairs, they will not be able to produce their product, thus affecting future revenue.

Repair duration is the time (in days, weeks) that the required repairs are expected to take to bring the bridge, building, component back into its original operating condition. The repair duration is different from downtime because the repair duration can apply to repairs that are carried out while the building, or part of the building, is still in operation (such as replacing windows, painting, etc.).

Repair effort considers the labor production rate PR_n of each of the repair items. Similar to the unit repair costs, the labor production rates are constant regardless of the repair quantity. Thus, the labor production rate is defined in terms of crew working days (CWD), and not the normalized quantity of CWD over total output (Mackie *et al*., 2008b). Moreover, in the present PEER PBEE methodology, the magnitude of the repair quantity is not used explicitly in the repair time computation, but rather as a trigger for the presence of the repair activity in the total number of CWD required. A repair activity is triggered when the probability is greater than 0.5 that the repair quantity is greater than some small tolerance value. In this study, the tolerance value is set as 3% of the maximum repair quantity. The total expected repair time is then obtained by summing PR_n for all number of repair quantities. The total number of CWD reflects the effort needed to perform the repair and is not the same as total repair duration because it does not include the effect of schedule dependencies, labor availability, and procurement and installation times (Mackie *et al*., 2008b).

In this study, the CWD is used to define the repair time of the cladding system. The labor production rates (CWD) for each of the repair items are given in Table 7.11. The mode, minimum, and maximum values of the repair efforts were given by Knowles (2010). Using these values, the mean and standard deviations were estimated assuming a Beta distribution.

7.5.4 Damage Scenarios

The unit cost and repair time data were collected by presenting three damage scenarios representing a range of damage to the cladding system components. The damage scenarios were constructed for cladding type C3; however, the repair cost and repair time data obtained from the scenarios can be applied to the other cladding designs as well. The scenarios represent light, moderate, and major damage to the cladding system components.

7.5.5 Applicability of Repair Data to Different Cladding Systems

The damage states, repair methods, unit repair costs, and repair efforts were obtained specifically for the components of cladding types C1, C2, and C3. As discussed in Chapter 3, not all components outlined in this chapter are used in the construction of some cladding types. Cladding type C1 consists of spandrel panels with glazing between stories. Thus, the damageable components consist of caulking, the components of the window glazing system, and the push-pull connections. Cladding type C2 consists of spandrel panels that span the full height of the story with windows inside the spandrel panels. Thus, the only damageable components are the caulking and the push-pull connections. The window panes installed within the spandrel panels are surrounding by the rigid panel and protected from the damage caused by interstory drift. Cladding type C3 consists of spandrel panels similar to type C1 with column cover panels spanning between floors. Window glazing is installed between the column cover panels. The damageable components in cladding type C3 include the caulking, window glazing system, push-pull connections, and column cover connections.

The damage states, repair methods, and repair unit costs are listed in this chapter for all damageable components. However, as discussed above, some of the cladding types do not use all of the components, and thus, only their applicable components are included in the repair cost analysis.

7.5.6 Consideration of Additional Repair Cost Data

The repair methods, unit repair costs, and repair effort were obtained from local cladding expert Ed Knowles (2010). Knowles also estimated values for the dispersion of the repair cost and repair effort. However, this is only one data point. Further improvements and refinements can be made by surveying additional cladding manufactures, designers, and installers to obtain a larger sample of repair methods, unit costs, and repair effort. The data structure in this study can be used as a template for future studies if more data is available on cladding repair costs.

7.6 OUTCOMES FOR THE NINE-STORY SAC BUILDING

The PEER methodology summarized in Section 7.1 was applied to the nine-story SAC building models with cladding that were described in Chapter 3. Using the methodology, the probabilistic decision model, or loss model, was constructed considering the seismic hazard model in Section 7.3.1, the demand models in Chapter 4, the damage states and repair quantities in Section 7.4, and unit repair costs and repair time in Section 7.5.

7.6.1 Repair Cost Results of Cladding System

The total repair cost of the cladding system and various repair cost ratios are discussed in the following sections. The total repair cost is calculated by summing the repair cost of all damageable components in the cladding system for a range of seismic intensities.

7.6.1.1 Total Repair Cost of Cladding System

One important result of the PEER methodology is the seismic intensity dependent variation in the total repair cost. The first and second probabilistic moments (mean and standard deviation) of the total repair cost are calculated for each intensity level, and are shown in Fig. 7.23 for the three cladding types C1, C2, and C3. It was assumed that after the summing of all of the costs from each repair quantity, the final repair cost model followed a normal distribution. The total repair costs are intensity dependent, and in this case, a structure-independent IM was selected (spectral acceleration at the first-mode period of the bare frame structure). This allows direction comparison between all three cladding types shown in the plot by simply selecting a target hazard level on the horizontal axis. The total repair costs of all cladding types are similar for intensity levels up to 0.2g. As the seismic intensity increases, the total repair cost of type C2 increases gradually and flattens out with a mean value of approximately $1,000,000. The repair costs of type C2 are the smallest because this cladding type consists of only spandrel panels, and the window systems are installed in the middle of the spandrel panel and are protected from the damage caused by interstory drift. The spandrel panel effectively acts as a rigid shell protecting the windows. Thus, the damageable components of cladding type C2 are limited to the caulking and the push-pull connections.

The repair cost of type C1 increases asymptotically to a mean value of approximately $3,100,000. This cladding system consists of spandrel panels that cover the floor beams with a window glazing system between adjacent floors. The damageable components include all of the items in Table 7.10 except for the column cover connections and drywall access. Because the window system is continuous across one story, there are 50% more window panes in type C1 than in types C2 and C3.

The repair cost of cladding type C3 is similar to type C1 for seismic intensities up to approximately 0.3g. Then, the repair cost of type C3 increases rapidly with increasing IM due to damage to the column cover connections. The repair cost of type C3 reaches a maximum value of approximately $6,000,000.

7.6.1.2 Repair Cost Ratios

A better way to evaluate the repair costs of the cladding systems is to compute normalized repair cost ratios. Typically, the total repair cost is normalized by the replacement cost of the system being evaluated. In this study, the repair cost ratio is computed using three different normalizing quantities. The first repair cost ratio, RCR_1, is computed as the total repair cost of the cladding system normalized by the replacement cost of the cladding system (i.e. cost of demolishing and constructing an entirely new cladding system). The second repair cost ratio, RCR_2, is computed as the total repair cost of the cladding system normalized by the replacement cost of the complete building. The third repair cost ratio, RCR_3, is computed as the total repair cost of the cladding system normalized by the total repair cost of the complete building. This third repair cost ratio gives insight into how large the costs of repairing the cladding system are compared to the costs of the complete building (including all structural and nonstructural components). The three repair cost ratios are summarized in Equations 7.9-7.11. The values of the normalizing factors, RC_{clad}, $RC_{building}$, and $TRC_{building}$, are given in Table 7.12.

$$\text{RCR}_1 = \frac{\text{Total Repair Cost of Cladding System}}{\text{Replacement Cost of Cladding System}} = \frac{TRC_{clad}}{RC_{clad}} \quad \text{Eq. 7.9}$$

$$\text{RCR}_2 = \frac{\text{Total Repair Cost of Cladding System}}{\text{Replacement Cost of Complete Building}} = \frac{TRC_{clad}}{RC_{building}} \quad \text{Eq. 7.10}$$

$$\text{RCR}_3 = \frac{\text{Total Repair Cost of Cladding System}}{\text{Total Repair Cost of Complete Building}} = \frac{TRC_{clad}}{TRC_{building}} \quad \text{Eq. 7.11}$$

The repair cost ratio RCR_1 of the cladding system is shown in Fig. 7.24 for the three cladding types. The figure reveals similar trends as in Fig. 7.23; however Fig. 7.24 shows these trends as the ratio of the total repair costs to the replacement cost of the cladding. At the 50%-in-50 year probability of exceedance hazard level (0.11g), the mean total repair costs amount to 5.4%, 3.7%, and 4.0% of the replacement cost for cladding types C1, C2, and C3, respectively. At the 20%-in-50 year probability of exceedance hazard level (0.22g), the mean total repair costs amount to 13.8%, 7.2%, and 12.7% of the replacement cost for cladding types C1, C2, and C3, respectively. At the 10%-in-50 year probability of exceedance hazard level (0.34g), the mean total repair costs amount to 23.6%, 9.4%, and 25.8% of the replacement cost for cladding types C1, C2, and C3, respectively. At the 2%-in-50 year probability of exceedance hazard level (0.65g), the mean total repair costs amount to 37.6%, 11.9%, and 65.8% of the replacement cost for cladding types C1, C2, and C3, respectively.

The repair cost ratio RCR_2 is the total repair cost of the cladding system divided by the replacement cost of the complete building. The calculation of the replacement cost of the building is given in Appendix B. The replacement cost for the nine-story SAC building located in Berkeley, CA is \$40,110,131, \$39,744,456, and \$40,476,230 for the building with cladding types C1, C2, and C3, respectively. The RCR_2 values for the three cladding types are shown in Fig. 7.25. The trends in the results are the same as in Fig. 7.24; however, the ratios show how much the total repair costs of the cladding are compared to the replacement costs of the complete building. The total repair cost of the cladding can be up to 7.5%, 2.3%, and 13.7% of the replacement cost of the complete building for cladding types C1, C2, and C3, respectively.

The repair cost ratio RCR_3 is the total repair cost of the cladding system divided by the total repair cost of the complete building. The calculation of the total repair cost of the nine-story SAC building is given in Appendix B. The repair quantities and unit costs of the damageable structural and nonstructural components (excluding the cladding system) were determined from the data in Yang *et al*. (2009). The reader is referred to Appendix B for more information. The RCR_3 values for the three cladding types are shown in Fig. 7.26. At the 50%-in-50 year probability of exceedance hazard level (0.11g), the mean total repair costs amount to 12.0%, 7.7%, and 11.1% of the total repair cost for the complete building with cladding types C1, C2, and C3, respectively. At the 20%-in-50 year probability of exceedance hazard level (0.22g), the mean total repair costs amount to 20.0%, 10.7%, and 19.3% of the total repair cost for the complete building with cladding types C1, C2, and C3, respectively. At the 10%-in-50 year probability of exceedance hazard level (0.34g), the mean total repair costs amount to 27.9%, 12.9%, and 31.4% of the total repair cost for the complete building with cladding types C1, C2, and C3, respectively. At the 2%-in-50 year probability of exceedance hazard level (0.65g), the mean total repair costs amount to 29.5%, 11.7%, and 50.4% of the total repair cost for the complete building with cladding types C1, C2, and C3, respectively.

7.6.1.3 Mean Annual Repair Cost

The seismic hazard data in Fig. 7.4 can be used with the total repair cost results in Fig. 7.23 to obtain a mean annual repair cost of each cladding system. The mean annual repair cost is calculated as the product of the mean repair cost of the cladding system conditioned on IM and slope of the hazard curve at each IM, integrated over the range of IM. The mean annual repair costs are presented in Table 7.14 for each cladding type.

The mean annual total repair costs of the cladding system are $39,563, $16,213, and $40,824 for cladding types C1, C2, and C3, respectively. These mean annual costs represent approximately 0.9%, 0.4%, and 0.9% of the total construction cost for cladding systems C1, C2, and C3, respectively. Thus, in terms of mean annual repair costs, cladding system C2 is the most cost-effective cladding design, while cladding types C1 and C3 are the most expensive. The mean annual repair costs can be used along with a discount rate and a time period of interest to determine the present value lump sum of the annual repair costs. The present value of the annual repair costs can be added to the new construction cost to determine the total cost of a particular cladding design. However, in this case, since the new construction costs of the three cladding systems are very similar, the most effective cladding system (type C2) can be determined from the mean annual repair costs.

7.6.1.4 Disaggregation of Total Repair Cost by Repair Quantity

Because of the assembly-based nature of the methodology used to solve the PEER equations, it was possible to disaggregate the total repair costs into individual contributions from each repair quantity. The total expected cost of each repair quantity is shown in Fig. 7.27, Fig. 7.28, and Fig. 7.29 for cladding types C1, C2, and C3, respectively. For cladding type C1 (Fig. 7.27), the peak contribution for intensities less than 0.15g is the cost of inspection after the earthquake to determine the level of damage to the cladding. For larger intensities, replacing damaged windows and dislodged gaskets constitute the majority of the repair costs. The costs of replacing the caulking and push-pull connections are significantly less than the other costs.

For cladding type C2 (Fig. 7.28), the inspection costs are the top contributor to the total repair costs for spectral accelerations less than 0.3g. For intensities larger than 0.3g, the cost of replacing the caulking and replacing the push-pull connections exceed the inspection costs. In cladding type C2, the height of the spandrel panels extend from story to story, and thus, the demands in the push-pull connections are larger than those in cladding type C1. Consequently, the cost of replacing the push-pull connections is larger in type C2 than in type C1.

The breakdown of the total repair costs for cladding type C3 (Fig. 7.29) is similar to type C1 for intensities less than 0.2g. For larger intensities, the repair costs of the column cover connections and associated drywall access costs dominate the repair costs. The high level of sensitivity of the column cover connections to seismic intensity, which was discussed in Chapter 6, is even more apparent in terms of repair costs.

A similar presentation of the disaggregation of expected repair cost by repair quantity can be made by selecting discrete hazard levels of interest and plotting repair quantity contributions in the form of a pie chart. The breakdown of expected costs at the four hazard levels of 2%-, 10%-, 20%-, and 50%-in-50 years exceedance probabilities is shown in Fig. 7.30, Fig. 7.31, and Fig. 7.31 for cladding type C1, C2, and C3, respectively. Similar to the approach in Mackie *et al*.

(2008a), the charts have been constructed so that the repair quantities that contribute a total of 10% or less to the total repair cost are lumped together in a group named "Other." For cladding type C1 (Fig. 7.30), the inspection costs contribute approximately 40% of the total repair costs at the 50%-in-50 year probability of exceedance level. The costs of the rigging, repair of the caulking, and repair of the gaskets each account for approximately 10-15% of the total repair cost. At the 20%-in-50 year probability of exceedance level, the peak contribution to the total repair cost is the replacement of the window gaskets (about 30% contribution). Approximately 20% of the repair costs are attributed to the replacement of cracked windows. In the 10%- and 2%-in-50 year probability of exceedance levels, the repair of the windows dominate the total repair costs of cladding type C1.

For cladding type C2 (Fig. 7.31), the cost of inspecting the cladding system after an earthquake has a large contribution to the total repair cost in all four hazard levels. The inspection cost contribution is approximately 40%, 30%, 25%, and 20% for the 50%-, 20%-, 10%-, and 2%-in-50 year probability of exceedance levels, respectively. In the 10%-in-50 year probability of exceedance level, the cost of repairing the caulking and the cost of replacing the push-pull connections each account for approximately 30% of the total repair costs. For the 2%-in-50 year probability of exceedance level, the replacement of the push-pull connections contributes about 40% to the total repair costs.

For cladding type C3 (Fig. 7.32), the inspection costs account for approximately 55% of the total repair cost in the 50%-in-50 year probability of exceedance level. The rigging cost and the repair of the caulking each account for approximately 20% of the total repair cost. For the 20%-in-50 year probability of exceedance level, the repair of the column cover connection (and the associated removal and replacement of the drywall to access the connections) is the major contributor to the total repair cost. This remains true for the 10%- and 2%-in-50 year probability of exceedance levels. For the 2%-in-50 year probability of exceedance level, the repair costs of the column cover connections and removal and replacement of the drywall total to approximately 70% of the total repair costs.

It is clear that the damage to the column cover connections are the culprit for the high repair costs in cladding type C3. The column cover connections are difficult to access and replace, prompting a need for better cladding designs. A system similar to cladding type C2 would be a better alternative, since the repair costs for this type are much lower.

7.6.1.5 Disaggregation of Total Repair Cost by Performance Group

The total repair costs were also disaggregated by performance group (i.e. maximum interstory drift, push-pull deformations, etc.). This way, the contribution of engineering demand parameters in certain stories to the total repair cost can be evaluated. The breakdown of the total repair cost by performance group is shown in Fig. 7.33, Fig. 7.34, and Fig. 7.35 for cladding types C1, C2, and C3, respectively. For cladding type C1 (Fig. 7.33), the damage driven by maximum interstory drift dominates the repair costs for all levels of seismic intensity. By comparison, the contributions from the push-pull deformations are very small. The individual contributions of interstory drift in each story vary over the range of seismic intensity. For spectral accelerations less than 0.3g, the maximum interstory drift in stories 7, 8, and 9 contribute the most to the total repair costs. For larger spectral accelerations, the maximum interstory drift in stories 3, 4, and 5 contribute the most to the total repair costs. This behavior is

due to the fact that for larger intensity earthquakes, there are larger drift demands in the lower stories, as explained in Chapter 4.

For cladding type C2 (Fig. 7.34), the damage is primarily driven by maximum interstory drift, followed by the maximum deformation of the bottom push-pull connectors. The maximum deformation at the top push-pull connectors contributes the smallest amount. In this cladding type, the maximum interstory drift only causes damage to the caulking. The contributions of the maximum interstory drift in the individual stories converge to approximately $65,000 at an intensity of 0.45g.

For cladding type C3 (Fig. 7.35), the performance group that is the main contributor to the total repair cost varies on the intensity level. For spectral accelerations less than 0.4g, the damage caused by maximum interstory drift contributes the most to the total repair cost, and for spectral accelerations greater than 0.4g, the damage caused by maximum column cover deformation contributes the most to the total repair cost. The contribution the of costs from the damage caused by maximum interstory drift accumulates much more gradually in cladding type C3 than in cladding type C1. The maximum push-pull deformations have the smallest contribution to the total repair cost. The contributions from the maximum deformation in the column cover connection are triggered at approximately 0.15g, a relatively low seismic intensity.

7.6.2 Repair Time Results of Cladding System

The repair times are calculated using the labor production rates (CWD) for each repair item. The total number of CWD represents the effort needed to perform the repair and is not the same total repair duration because it does not include the effects of schedule dependencies, labor availability, and procurement and installation times (Mackie *et al*., 2008b). The total repair time using the labor production rates of each of the cladding systems are shown in Fig. 7.36. The total repair time jumps to approximately 60 CWD, due to the inspection time required to determine the amount of damage to the cladding system. This repair item accounts for the majority of the repair efforts. For cladding type C2, the repair time does not change significantly, since the labor production rates for the other damageable components in this cladding system (caulking and push-pull connections) are very low. For cladding type C1, the repair time jumps to approximately 62 CWD at 0.12g because of the repair efforts needed for the damaged window system. For cladding type C3, the repair time jumps to approximately 67 CWD at 0.23g because additional repair efforts are needed to remove and replace the column cover connections (and drywall for access).

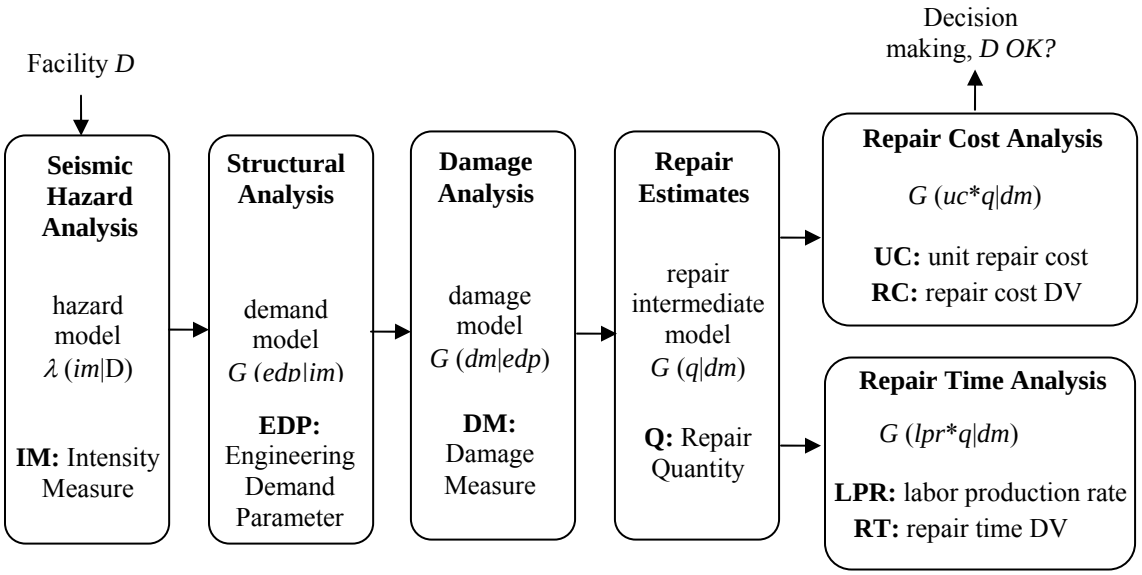

Fig. 7.1 Schematic of PEER methodology (adapted from Mitrani-Reiser, 2007)

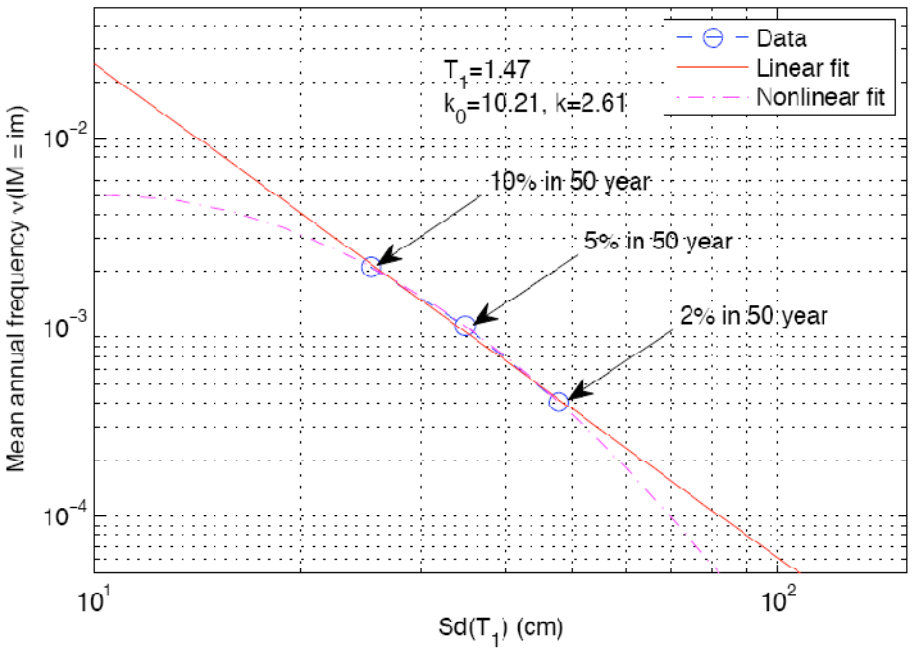

Fig. 7.2 Annual seismic hazard curve for T_1 = 1.47 sec in Berkeley, CA showing three hazard data points sampled from USGS maps and the linear fit (from Mackie *et al.*, 2008a)

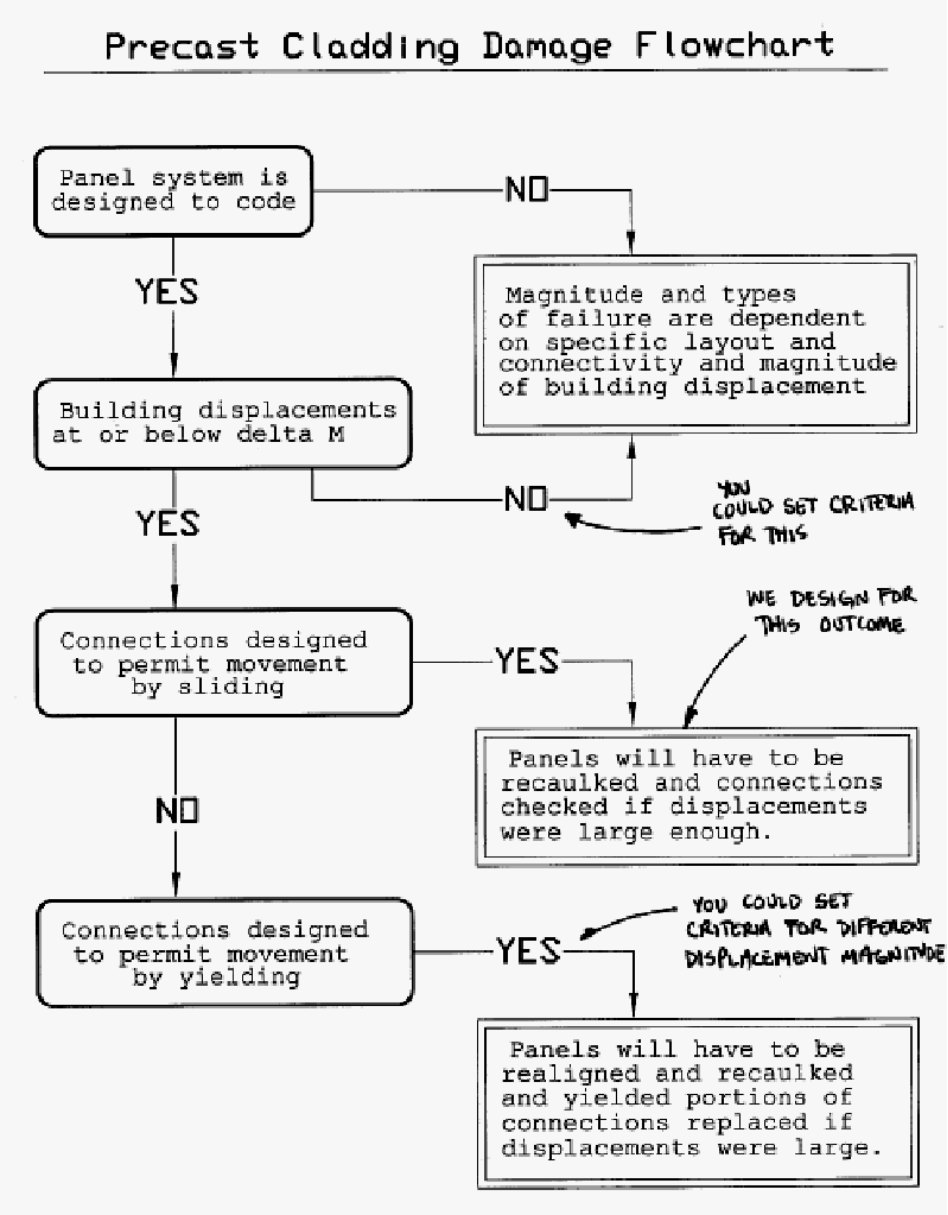

Fig. 7.3. Damage flowchart for precast cladding systems to determine damage and repair methods (as used by Mark Hildebrand at Willis Construction, 2009)

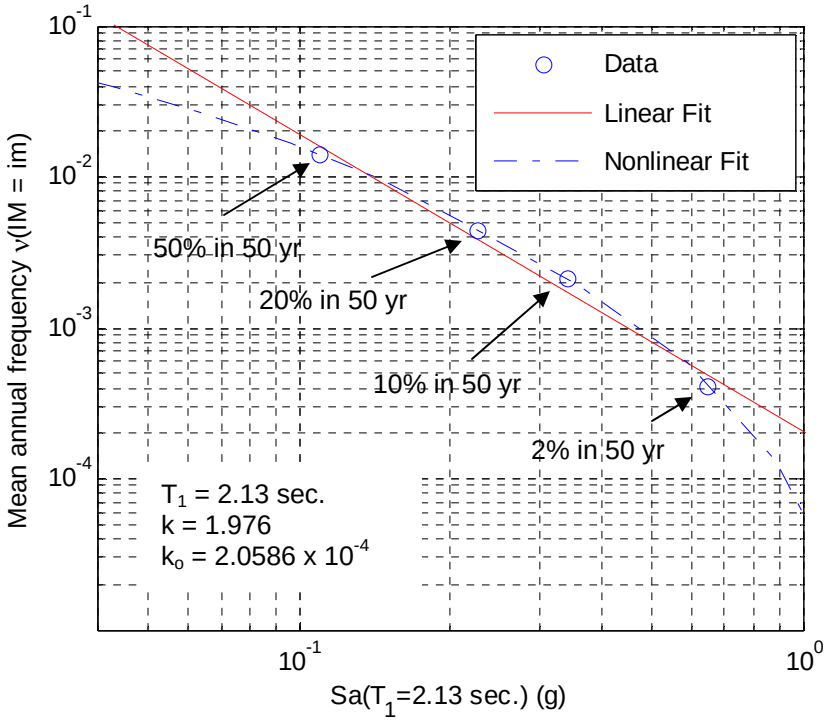

Fig. 7.4 Annual seismic hazard curve for T_1 = 2.13 sec. at UC Berkeley Campus showing four hazard data points sampled from URS (2007)

Table 7.1 Seismic hazard data points at four selected hazard levels

Hazard Level	Return Period (years)	First-mode spectral acceleration (T_1 = 2.13 sec.) (g)
50% PE in 50 yrs	72	0.11
20% PE in 50 yrs	225	0.22
10% PE in 50 yrs	475	0.34
2% PE in 50 yrs	2475	0.65

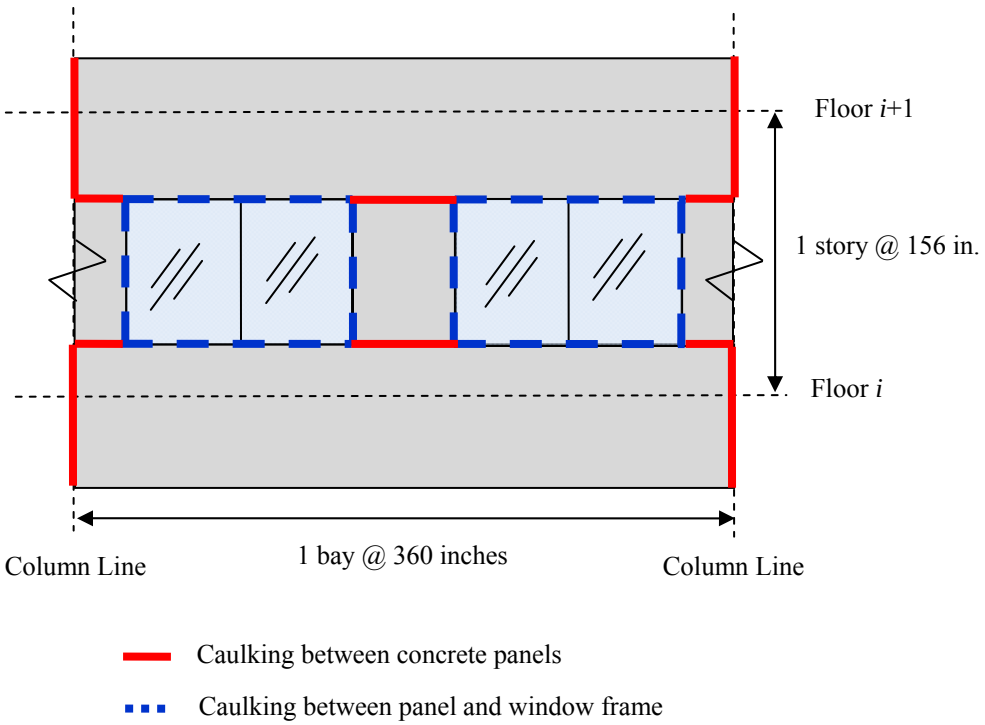

Fig. 7.5 Detailed elevation of cladding system C3 showing locations of caulking

Table 7.2 Damage states for caulking in cladding systems

Damage State (DS)	Description	λ (rad.)	β
DS0	Initial cracking	0.0048	0.15
DS1	Failure	0.0096	0.25

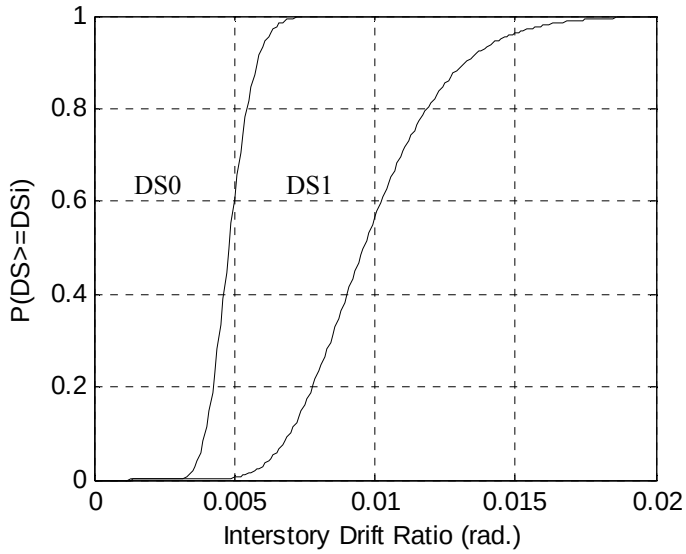

Fig. 7.6 Damage states for the caulking

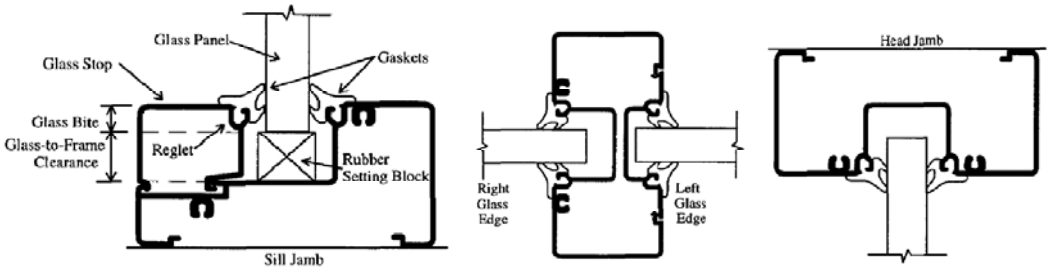

Fig. 7.7 Cross-sections of window system: horizontal/sill (left), mullion (middle), and horizontal/head (right) (Behr *et al*., 1995a)

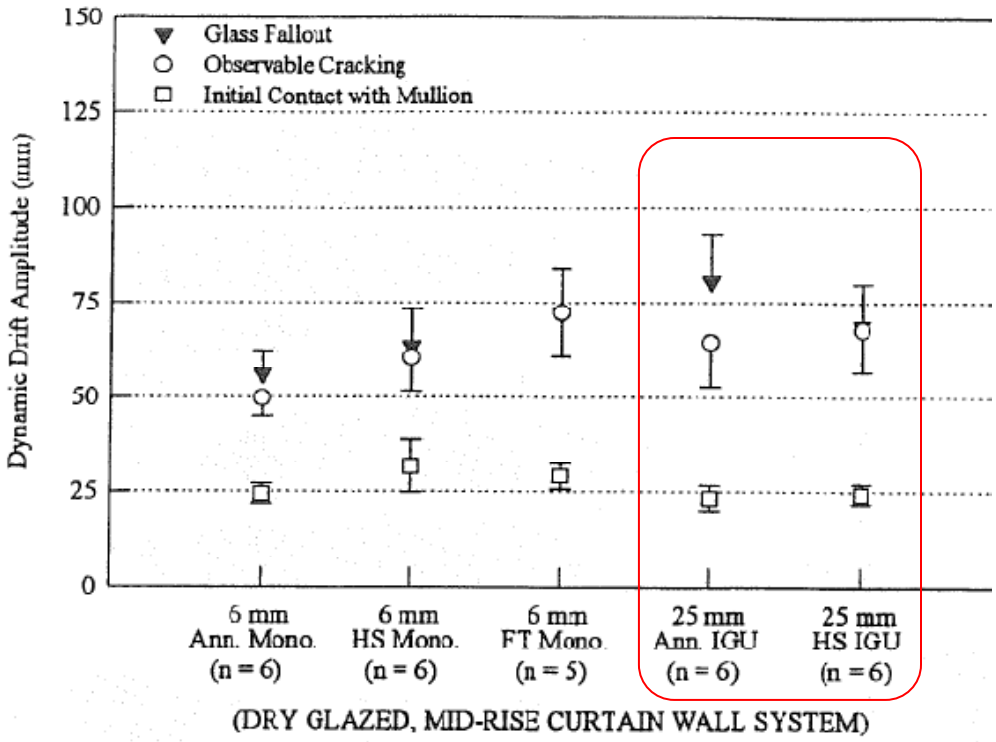

Fig. 7.8 Shear displacements for three levels of damage to the window pane (Behr and Worrell, 1998)

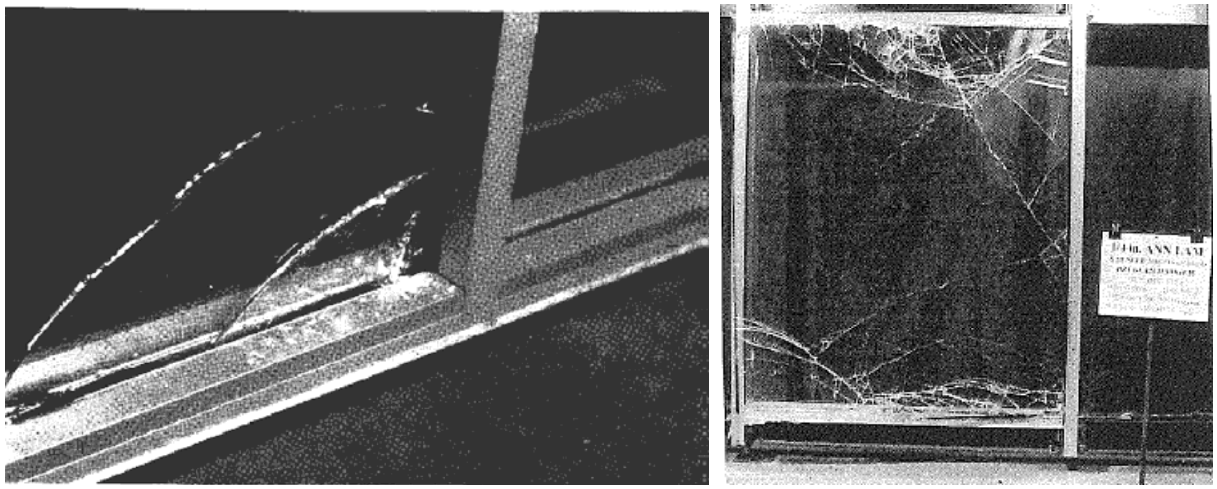

Fig. 7.9 Observed cracking in glass panes (Behr *et al.*, 1995a)

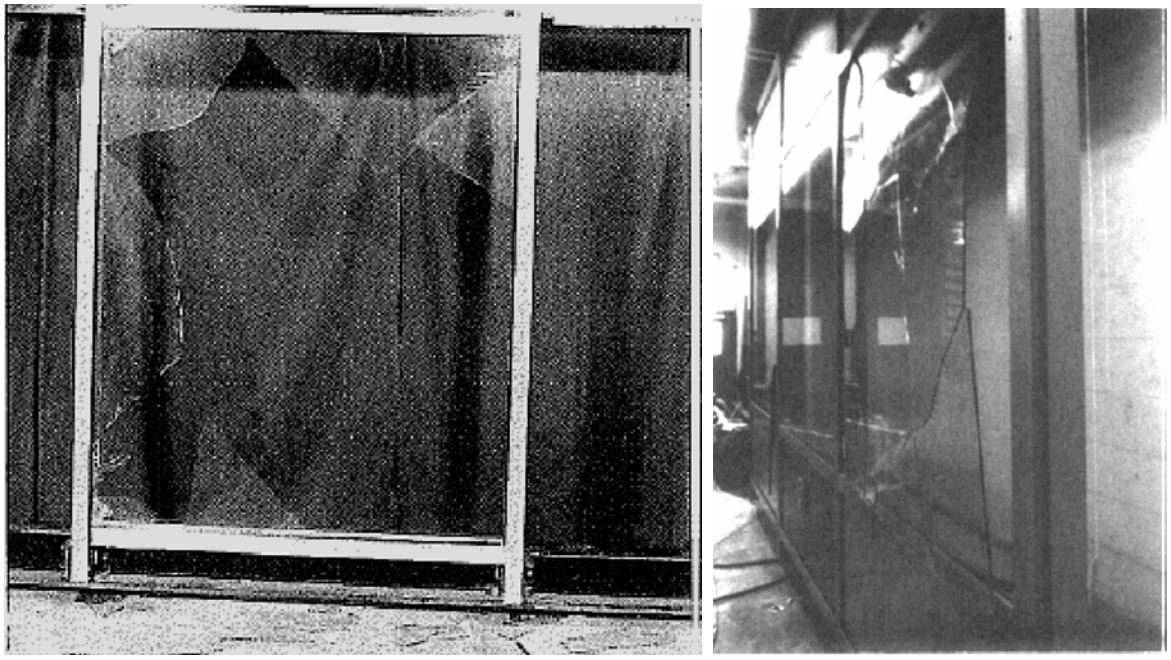

Fig. 7.10 Glass fallout from window glazing system (Pantelides and Behr, 1994)

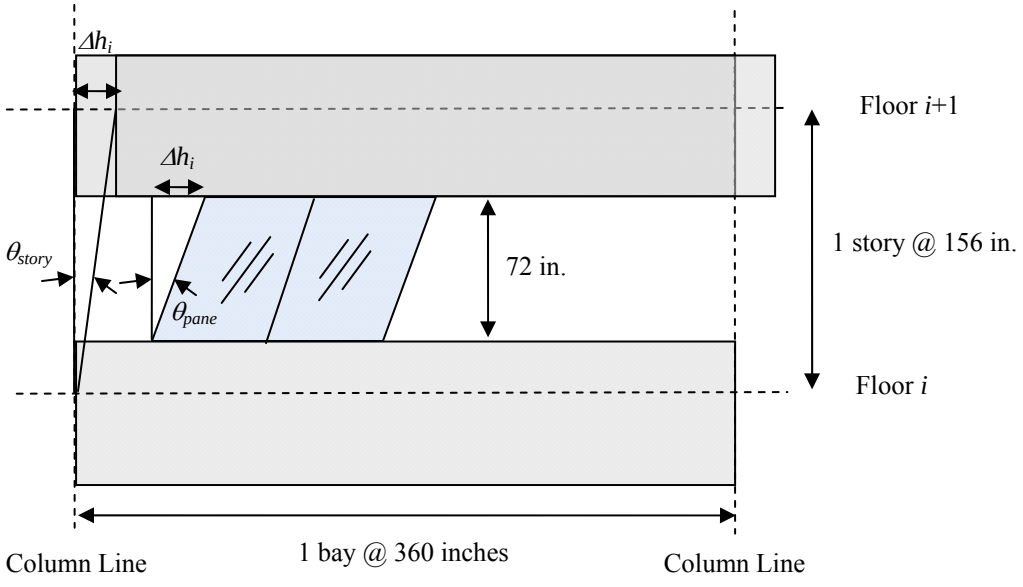

$\theta_{story} = \Delta h_i / 156$
$\theta_{pane} = \Delta h_i / 72$

Fig. 7.11 For cladding systems with precast panels, the drift ratio for the window pane is greater than the drift ratio for the story

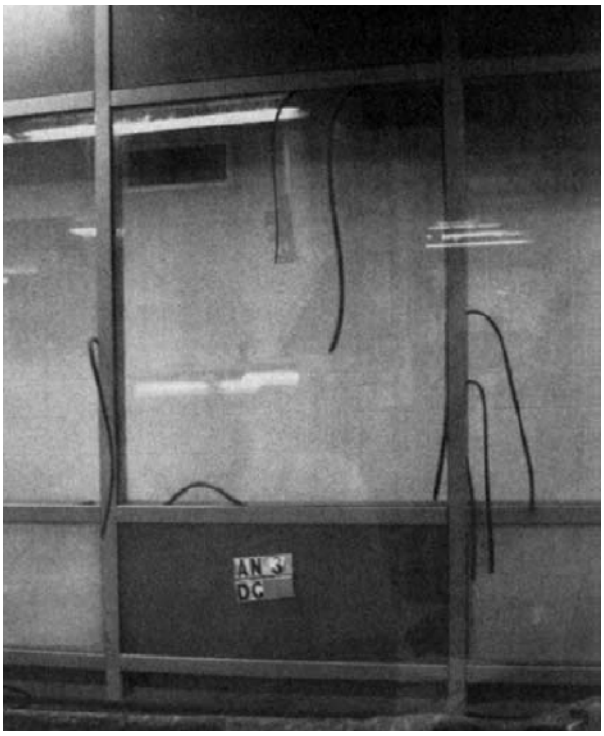

Fig. 7.12 Gaskets dislodged from window glazing system (Pantelides and Behr, 1994)

Table 7.3 Damage states for window glazing system

Damage State (DS)	Description	λ (rad.)	β
DS0	Glass pane contact and small cracking at perimeter	0.006	0.12
DS1	Glass translation and gasket pull-out	0.011	0.20
DS2	Observable cracking in glass	0.016	0.19
DS3	Major cracking and glass fallout	0.020	0.16

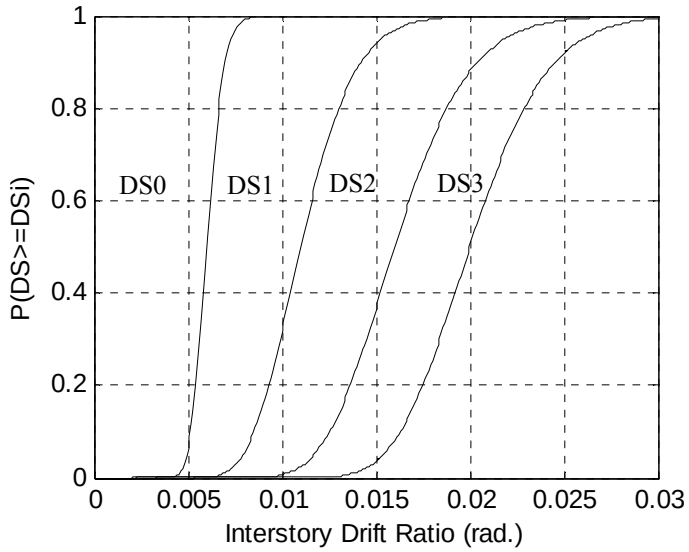

Fig. 7.13 Damage states for the window glazing system

Table 7.4 Damage states for drift sensitive components: caulking and window system

Damage State (DS)	Description	λ (rad.)	β
DS0	Initial cracking in caulking	0.0048	0.15
DS1	Glass pane contact and small cracking in pane at perimeter	0.006	0.12
DS2	Caulking failure	0.0096	0.25
DS3	Glass translation and gasket pull-out	0.011	0.20
DS4	Observable cracking in glass	0.016	0.19
DS5	Major cracking and glass fallout	0.020	0.16

Table 7.5 Repair items for drift sensitive components: caulking and window system

Damage State (DS)	Repair Item	Quantity
DS1	*Glass pane contact* Provide rigging/staging to access caulking (EA) Remove and replace caulking in cladding (LF)	 1 25% of caulking length
DS2	*Caulking failure* Provide rigging/staging to access caulking (EA) Remove and replace caulking in cladding (LF) Deglaze and reposition window (EA) Replace gaskets for repositioned windows (LF)	 1 25% of caulking length 5% of windows 5% of gasket length
DS3	*Glass translation and gasket pull-out* Provide rigging/staging to access caulking (EA) Remove and replace caulking in cladding (LF) Deglaze and reposition window (EA) Replace gaskets for repositioned windows (LF) Replace gaskets that have become dislodged (LF)	 1.5 50% of caulking length 10% of windows 10% of gasket length 10% of gasket length
DS4	*Observable cracking in glass* Provide rigging/staging to access caulking (EA) Remove and replace caulking in cladding (LF) Deglaze and reposition window (EA) Remove and replace window (EA) Replace gaskets for repositioned windows (LF) Replace gaskets that have become dislodged (LF)	 1.5 50% of caulking length 20% of windows 20% of windows 20% of gasket length 15% of gasket length
DS5	*Major cracking and glass fallout* Provide rigging/staging to access caulking (EA) Remove and replace caulking in cladding (LF) Deglaze and reposition window (EA) Remove and replace window (EA) Replace gaskets for repositioned windows (LF) Replace gaskets that have become dislodged (LF)	 2 75% of caulking length 30% of windows 40% of windows 30% of gasket length 20% of gasket length
DS∞	*Complete replacement of all components* Provide rigging/staging to access caulking (EA) Remove and replace caulking in cladding (LF) Deglaze and reposition window (EA) Remove and replace window (EA) Replace gaskets for repositioned windows (LF)	 2 100% of caulking length 30% of windows 70% of windows 30% of gasket length

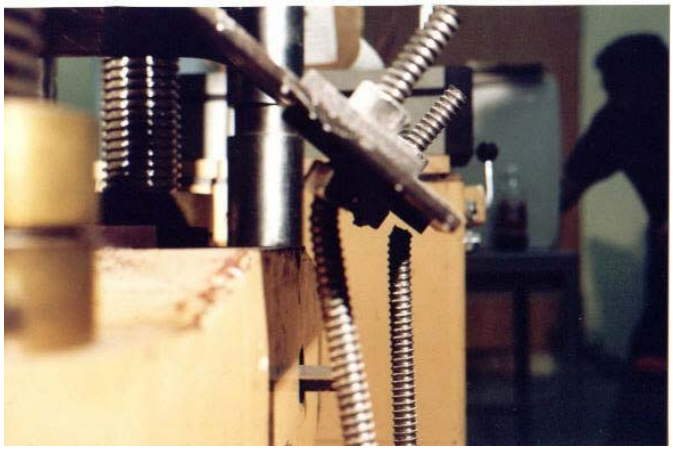

Fig. 7.14. Photograph of fracture of threaded rod in push-pull connection (McMullin *et al.*, 2004)

Table 7.6 Damage states for bottom and top push-pull connectors

Damage State (DS)	Description	λ (in.)	β
DS0	Negligible damage with onset of yielding of threaded rod	0.75	0.25
DS1	Significant yielding	1.25	0.25
DS2	Fracture of threaded rod	2.2	0.25

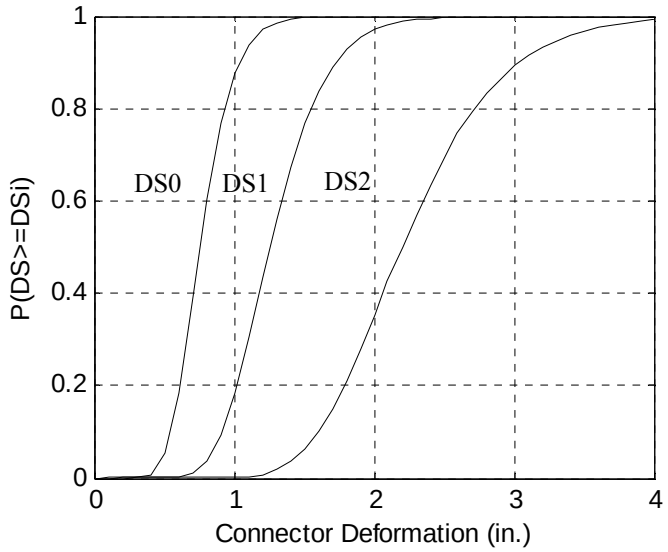

Fig. 7.15. Damage states for the push-pull connectors

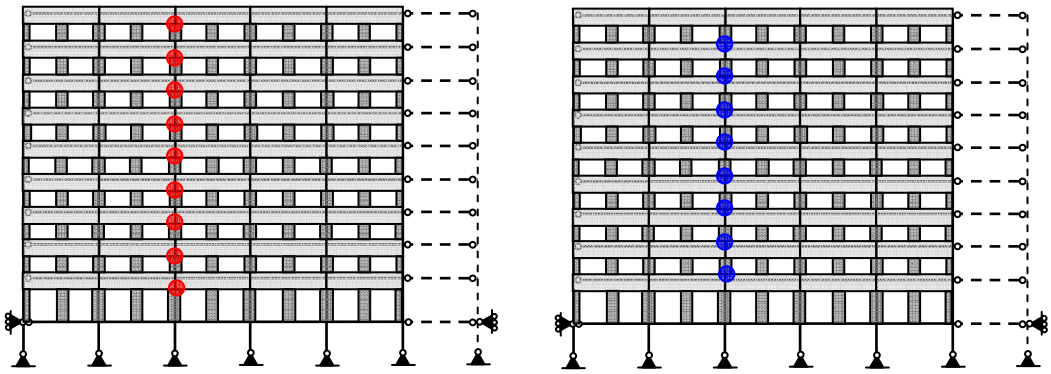

Bottom push-pull connector in center spandrel panel

Top push-pull connector in center spandrel panel

Fig. 7.16 Location of representative push-pull connectors

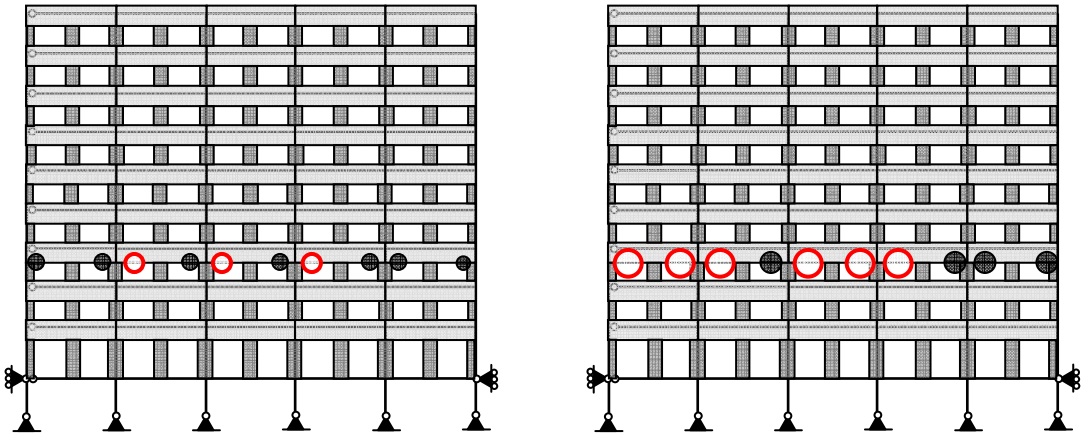

DS1: bottom connectors in story 3 with deformations at least 1.25 in. during pushover analysis

DS2: bottom connectors in story 3 with deformations at least 2.2 in. during pushover analysis

Fig. 7.17 Repair quantities for damage states of bottom push-pull connectors in story 3

Table 7.7 Repair items for bottom and top push-pull connectors

Damage State (DS)	Repair Item	Quantity
DS1	*Significant yielding* Remove and replace threaded rod (EA)	30% of bottom or top push-pull connectors
DS2	*Fracture of threaded rod* Remove and replace threaded rod (EA)	60% of bottom or top push-pull connectors
DS∞	*Complete replacement of all components* Remove and replace threaded rod (EA)	100% of bottom or top push-pull connectors

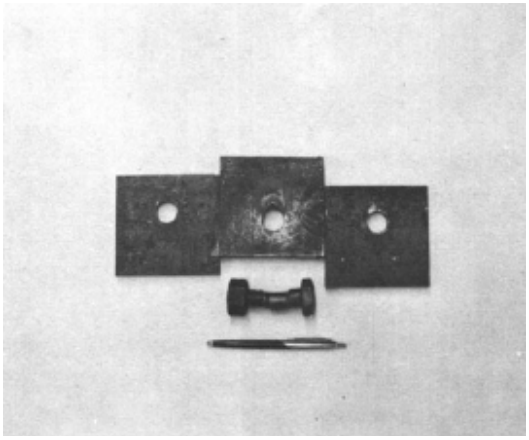

Fig. 7.18. Photograph of fractured bolt in column cover connection (Crawford and Kulak, 1968)

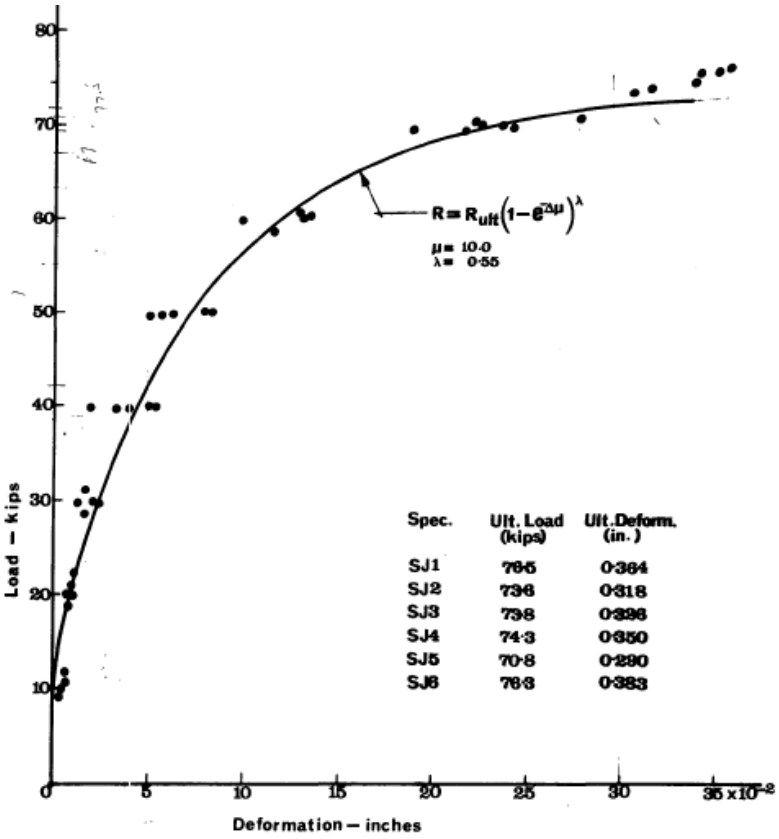

Fig. 7.19. Force-deformation curve for column cover connections determined by Crawford and Kulak (1968)

Table 7.8 Damage states for bottom and top column cover connectors

Damage State (DS)	Description	λ (in.)	β
DS0	Negligible damage with onset of yielding of bolt	0.068	0.19
DS1	Significant yielding	0.22	0.11
DS2	Fracture of connection	0.33	0.10

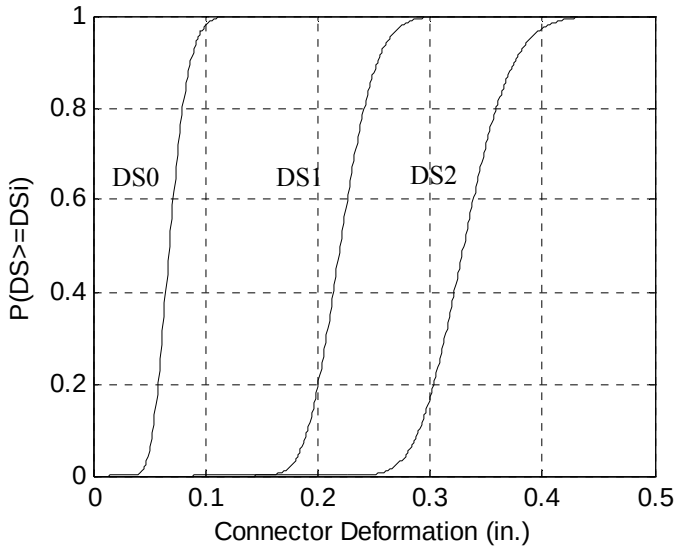

Fig. 7.20. Damage states for the column cover connectors

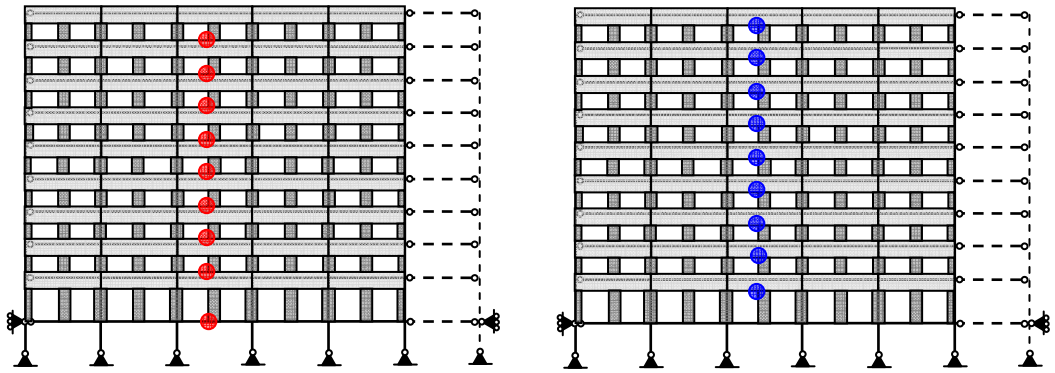

Bottom column cover connector in center column cover panel

Top column cover connector in center column cover panel

Fig. 7.21 Location of representative column cover connectors

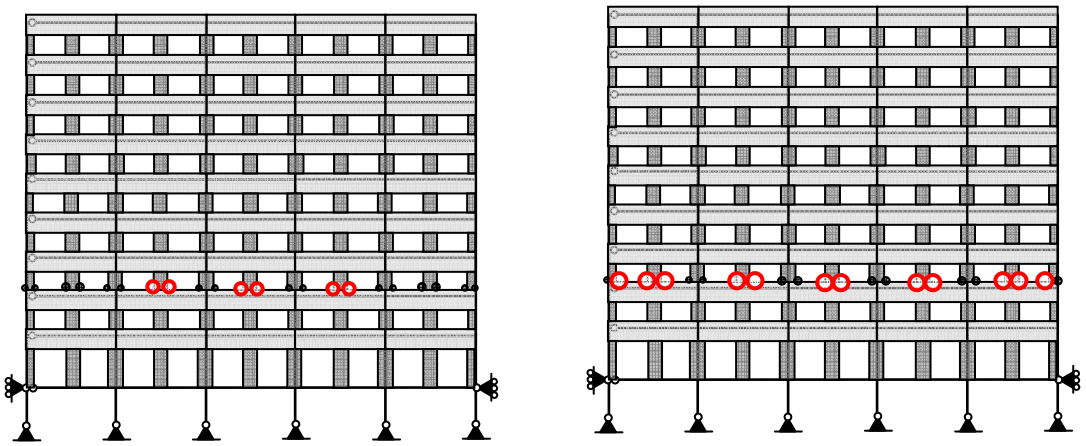

DS1: bottom connectors in story 3 with deformations at least 0.22 in. during pushover analysis

DS2: bottom connectors in story 3 with deformations at least 0.33 in. during pushover analysis

Fig. 7.22 Repair quantities for damage states of bottom column cover connectors in story 3

Table 7.9 Repair items for bottom and top column cover connectors

Damage State (DS)	Repair Item	Quantity
DS1	*Significant yielding* Remove and replace drywall for access (EA conn.) Remove and replace bolted connection (EA)	 27% of connectors 27% of connectors
DS2	*Fracture of bolted connection* Remove and replace drywall for access (EA conn.) Remove and replace bolted connection (EA)	 59% of connectors 59% of connectors
DS∞	*Complete replacement of all components* Remove and replace drywall for access (EA conn.) Remove and replace bolted connection (EA)	 100% of connectors 100% of connectors

Table 7.10 Repair item unit costs

Item name	Unit	Mean unit cost	Standard deviation (using 20% coeff. of variation)	Notes
Inspection after seismic event	EA	$180,000.00	$36,000.00	Check all cladding elements for damage
Rigging and staging for caulking	EA	$50,000.00	$10,000.00	Based on replacing 25% of total caulking
Remove and replace caulking	LF	$15.00	$3.00	
Deglaze and reposition window	EA	$800.00	$160.00	For undamaged windows that have shifted, does not include cost of gaskets
Remove and replace window	EA	$2,100.00	$420.00	Includes cost of gaskets
Replace gaskets	LF	$50.00	$10.00	For gaskets that have dislodged or shifted out of place
Replace threaded rod connection	EA	$850.00	$170.00	Access through ceiling space
Replace bolted column cover connection	EA	$1,750.00	$350.00	Remove drywall for access to connection
Remove and replace drywall for access	EA	$1,450.00	$290.00	For each bolted column cover replaced

Table 7.11 Labor production rates for each repair item

Item name	Unit(a)	Mean[(b)]	Standard deviation[(c)]	Mode	Min	Max
Inspection after seismic event (EA)	CWD	55.0	11.67	50	30	100
Rigging and staging for caulking (EA)	CWD	2.17	0.5	2.0	1.0	4.0
Remove and replace caulking (LF)	CWD	0.75	0.25	0.5	0.5	2.0
Deglaze and reposition window (EA)	CWD	0.75	0.25	0.5	0.5	2.0
Remove and replace window (EA)	CWD	1.33	0.33	1.0	1.0	3.0
Replace gaskets (LF)	CWD	0.75	0.25	0.5	0.5	2.0
Replace threaded rod connection (EA)	CWD	1.08	0.25	1.0	0.5	2.0
Replace bolted column cover connection (EA)	CWD	1.33	0.33	1.0	1.0	3.0
Remove and replace drywall for access (EA)	CWD	4.0	0.67	4.0	2.0	6.0

(a) CWD = labor production rate
(b) Mean = (max + 4*mode + min)/6
(c) Standard deviation = (max - min)/6

Table 7.12 Normalizing factors for RCR

Repair Cost Ratio	Description	Cladding Type	Cost
RCR_1	RC_{clad} = demo and replacement cost of cladding (assuming rest of building will be saved)	C1 C2 C3	\$8,052,000 \$7,686,000 \$8,418,000
RCR_2	$RC_{building}$ = replacement cost of building	C1 C2 C3	\$40,110,131 \$39,744,456 \$40,476,230
RCR_3	$TRC_{building}$ = total repair cost of building	C1 C2 C3	varies with IM (Appendix B)

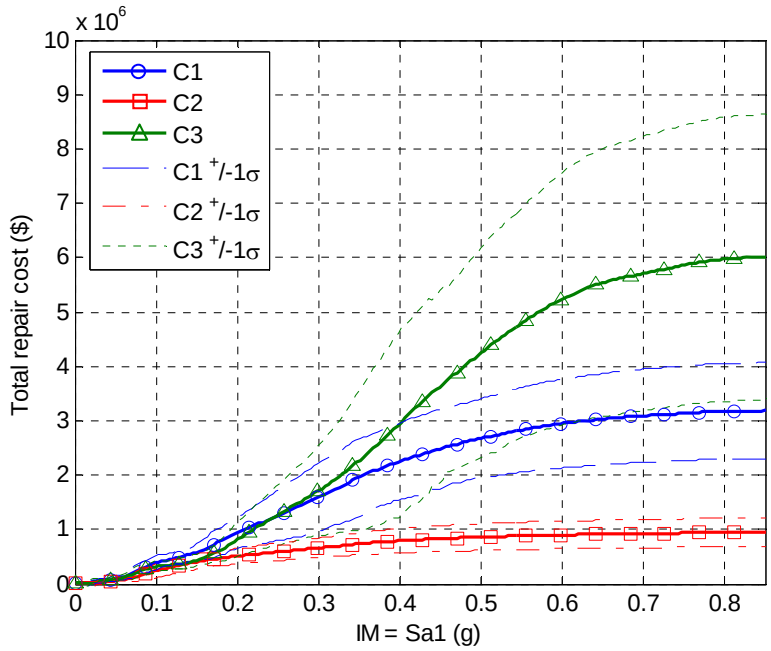

Fig. 7.23 Comparison of total repair cost of the cladding system as a function of intensity for three different cladding types

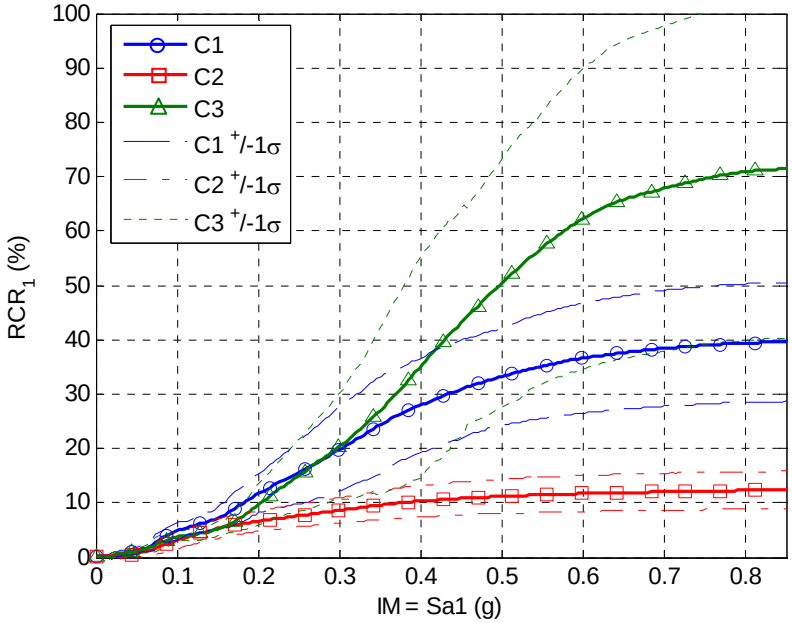

Fig. 7.24 Comparison of RCR_1, the total repair cost of the cladding system normalized by the replacement cost of the cladding system, for three different cladding types

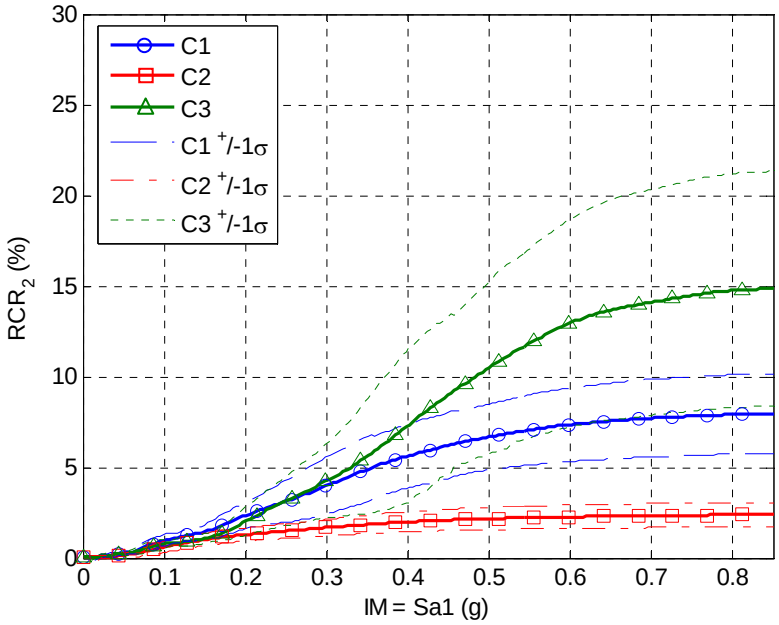

Fig. 7.25 Comparison of RCR_2, the total repair cost of the cladding system normalized by the replacement cost of the complete building, for three different cladding types

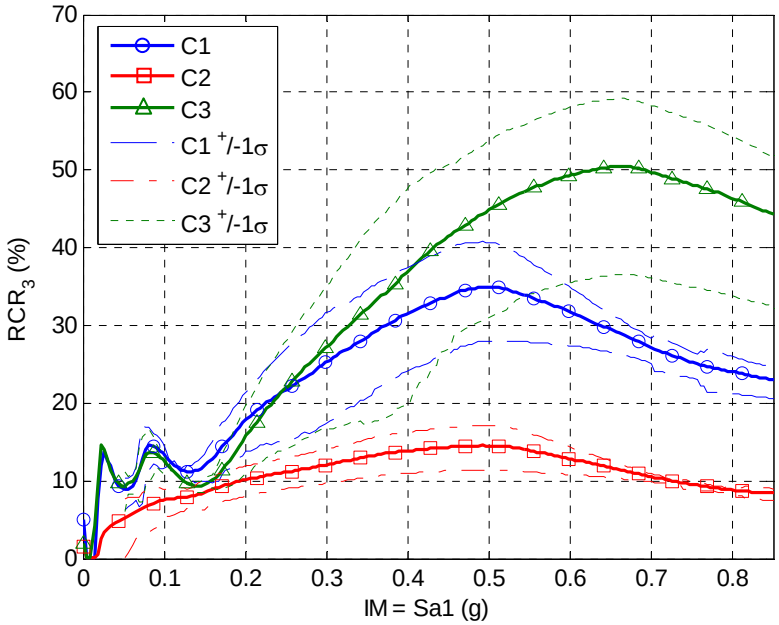

Fig. 7.26 Comparison of RCR_3, the total repair cost of the cladding system normalized by the total repair cost of the complete building, for three different cladding types

Table 7.13 Comparison of expected repair cost ratios for different cladding systems

Repair Cost Ratio	Cladding Type	Expected Repair Cost Ratio for Different Hazard Levels			
		50% PE in 50 years	20% PE in 50 years	10% PE in 50 years	2% PE in 50 years
RCR_1	C1	5.4%	13.8%	23.6%	37.6%
	C2	3.7%	7.2%	9.4%	11.9%
	C3	4.0%	12.7%	25.8%	65.8%
RCR_2	C1	1.1%	2.8%	4.7%	7.5%
	C2	0.7%	1.4%	1.8%	2.3%
	C3	0.8%	2.6%	5.4%	13.7%
RCR_3	C1	12.0%	20.0%	27.9%	29.5%
	C2	7.7%	10.7%	12.9%	11.7%
	C3	11.1%	19.3%	31.4%	50.4%

Table 7.14 Comparison of mean annual repair costs for different cladding systems

Value	Cladding Type		
	C1	C2	C3
Cost of new construction (excluding demo cost of existing cladding)	$4,392,000	$4,026,000	$4,758,000
Mean annual repair cost	$39,563	$16,213	$40,824
Mean annual repair cost ratio	0.9%	0.4%	0.9%

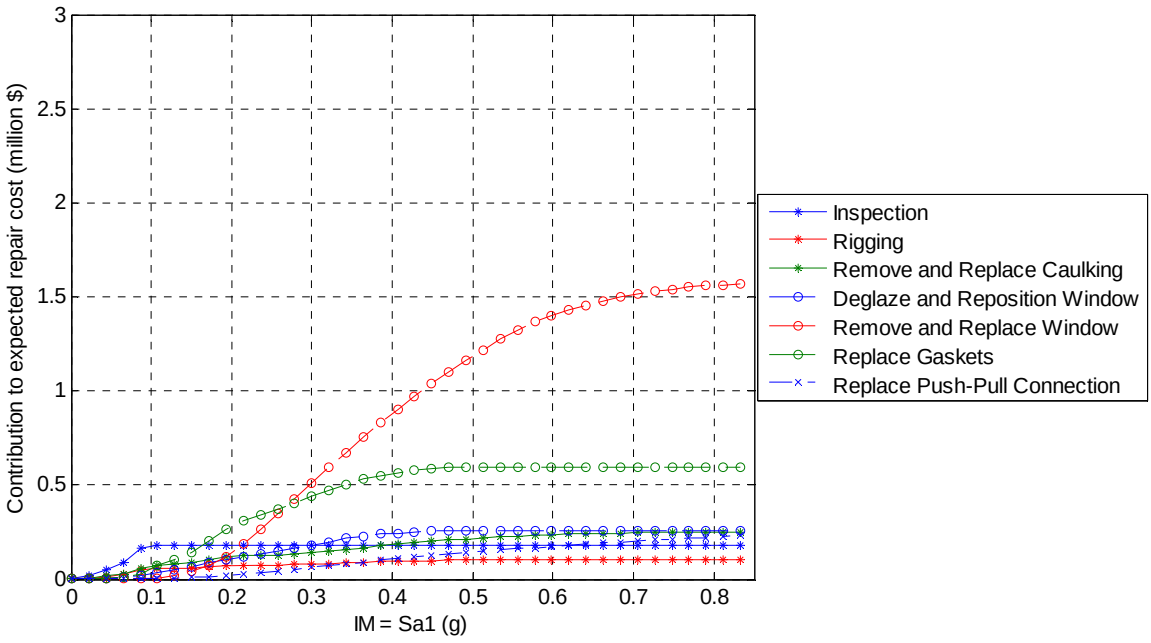

Fig. 7.27 Disaggregation of total repair cost of cladding type C1 by repair quantity

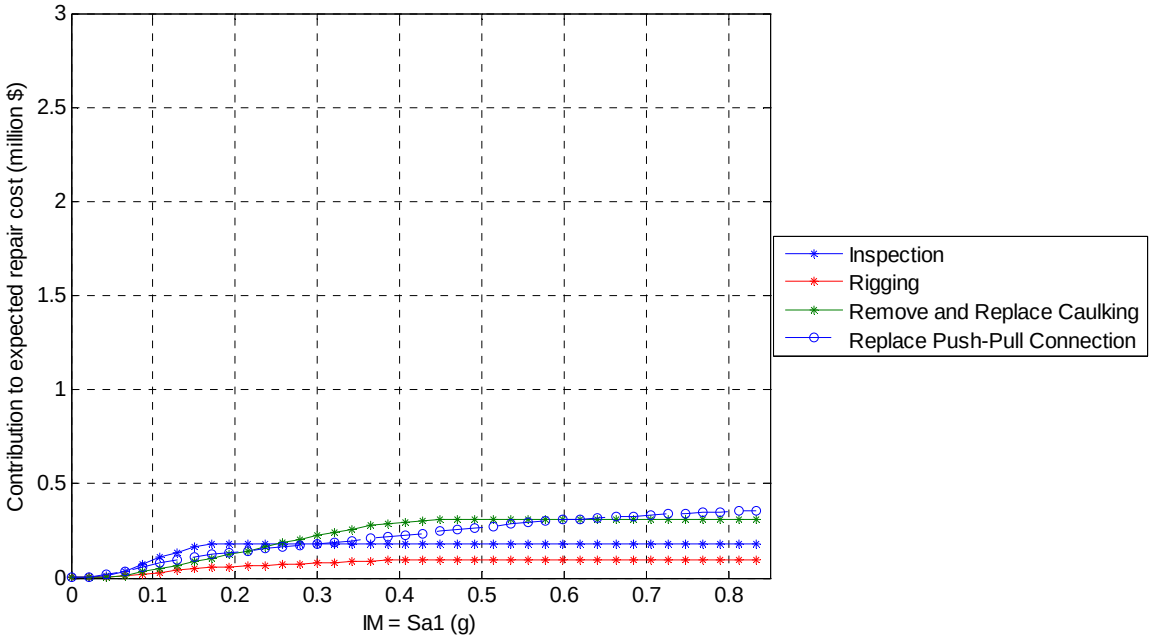

Fig. 7.28 Disaggregation of total repair cost of cladding type C2 by repair quantity

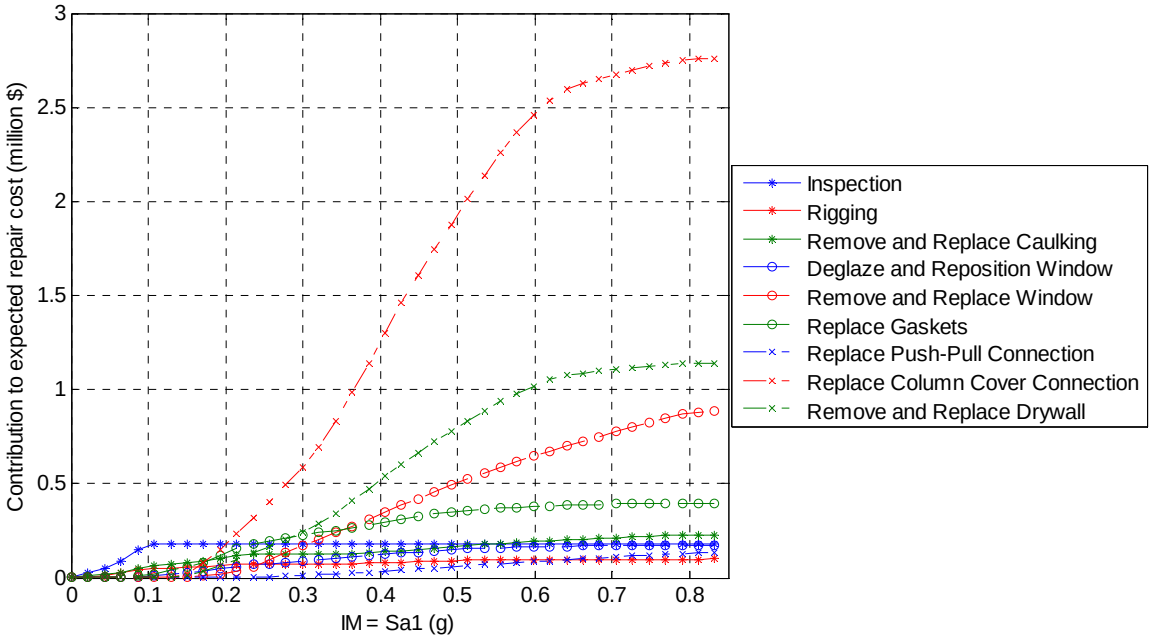

Fig. 7.29 Disaggregation of total repair cost of cladding type C3 by repair quantity

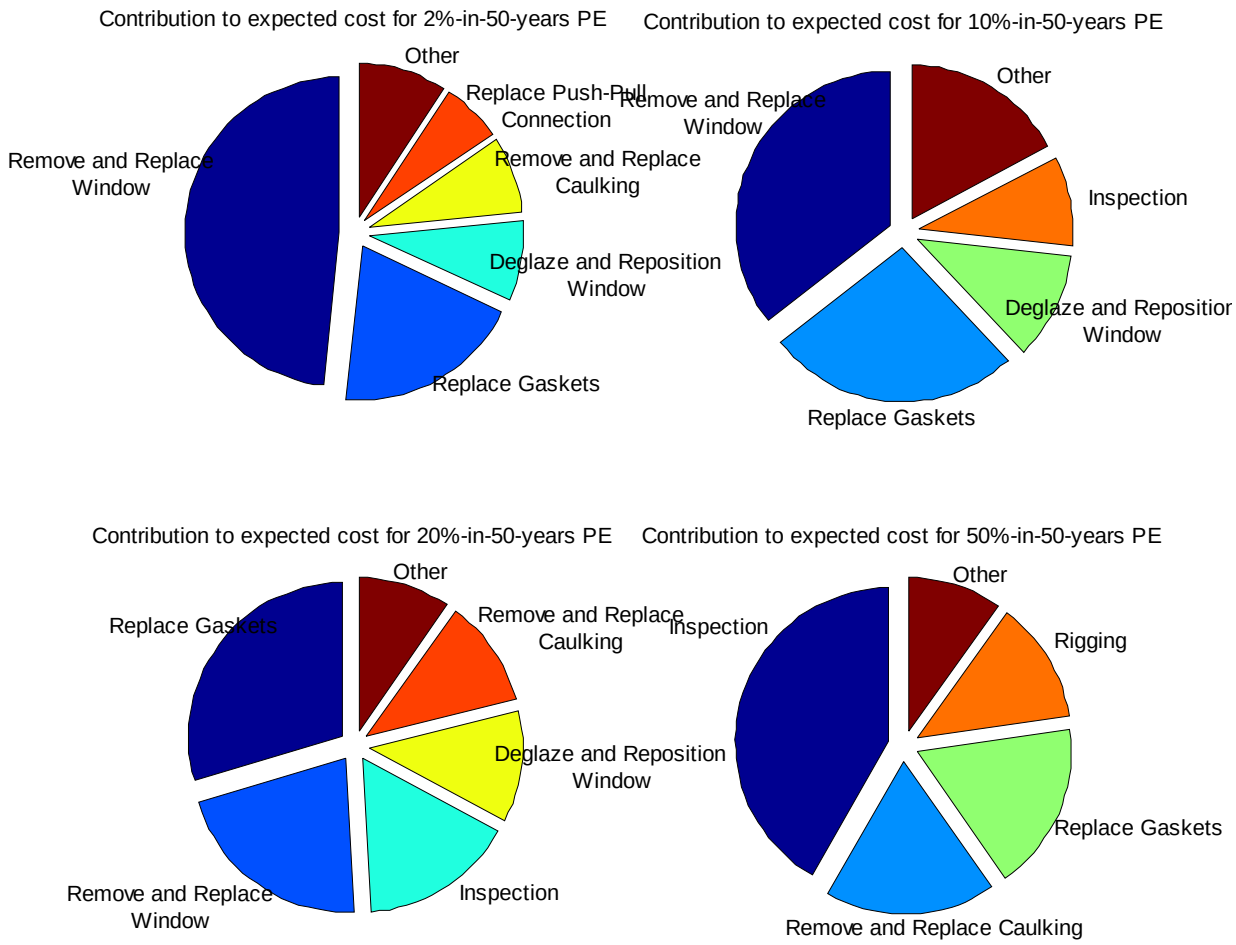

Fig. 7.30 Disaggregation of total repair cost of cladding type C1 by repair quantity for 4 discrete hazard levels

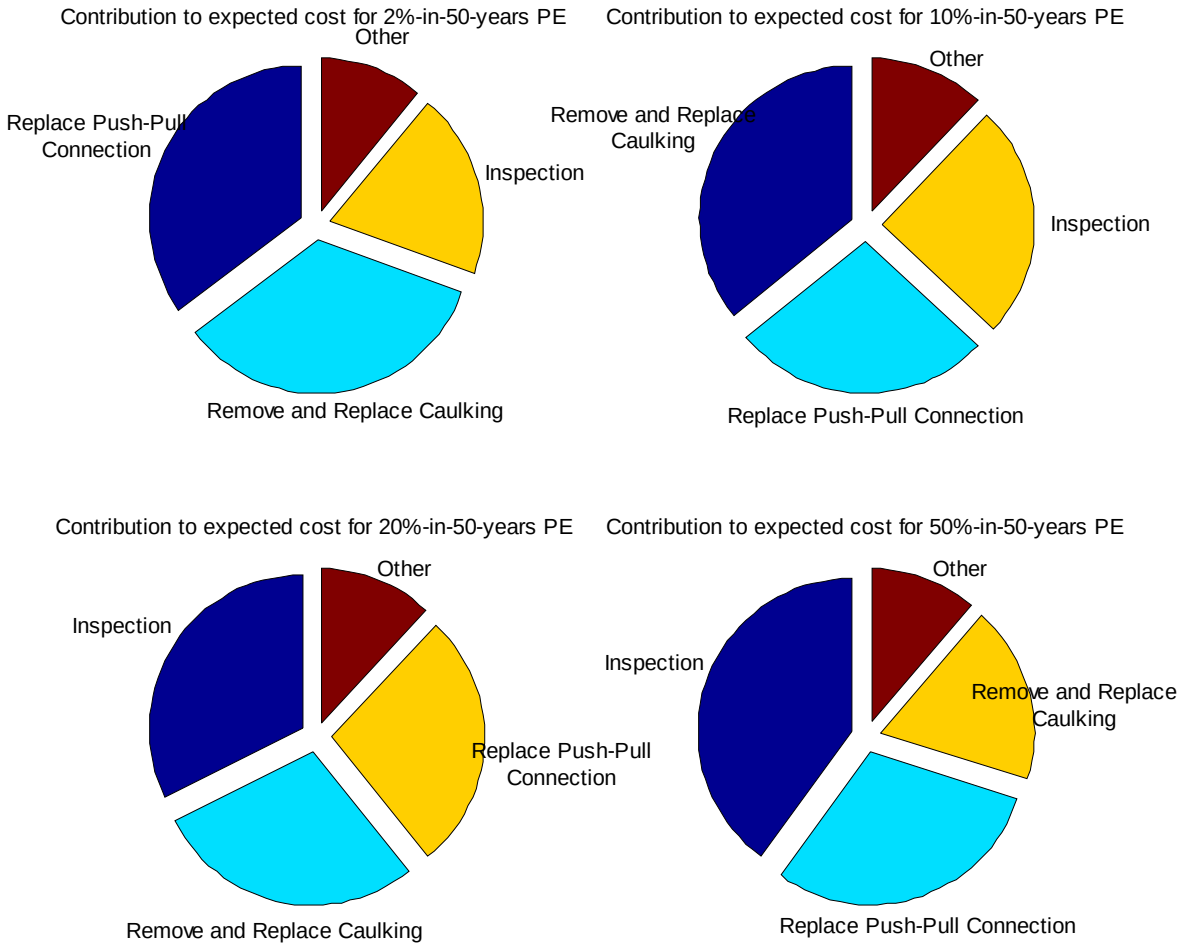

Fig. 7.31 Disaggregation of total repair cost of cladding type C2 by repair quantity for 4 discrete hazard levels

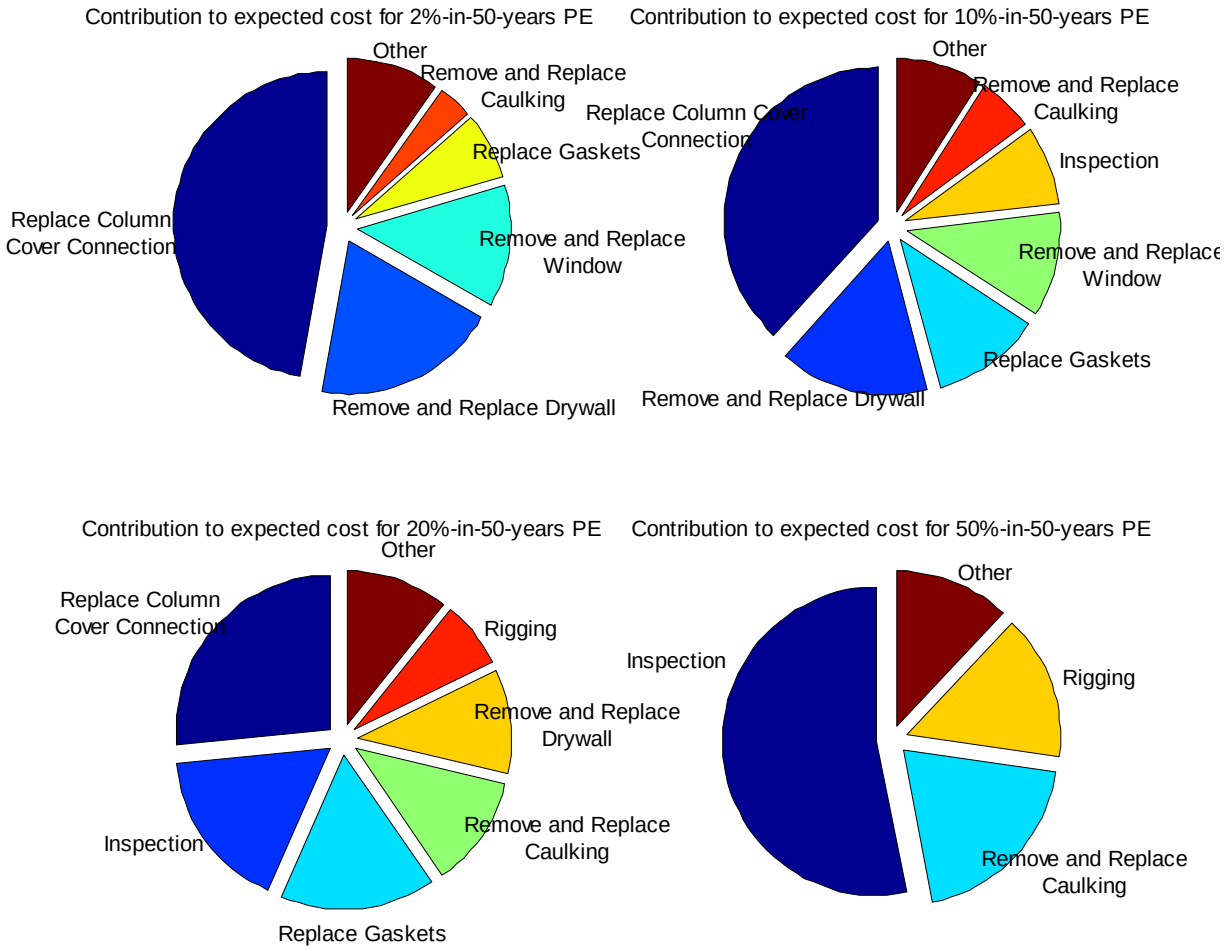

Fig. 7.32 Disaggregation of total repair cost of cladding type C3 by repair quantity for 4 discrete hazard levels

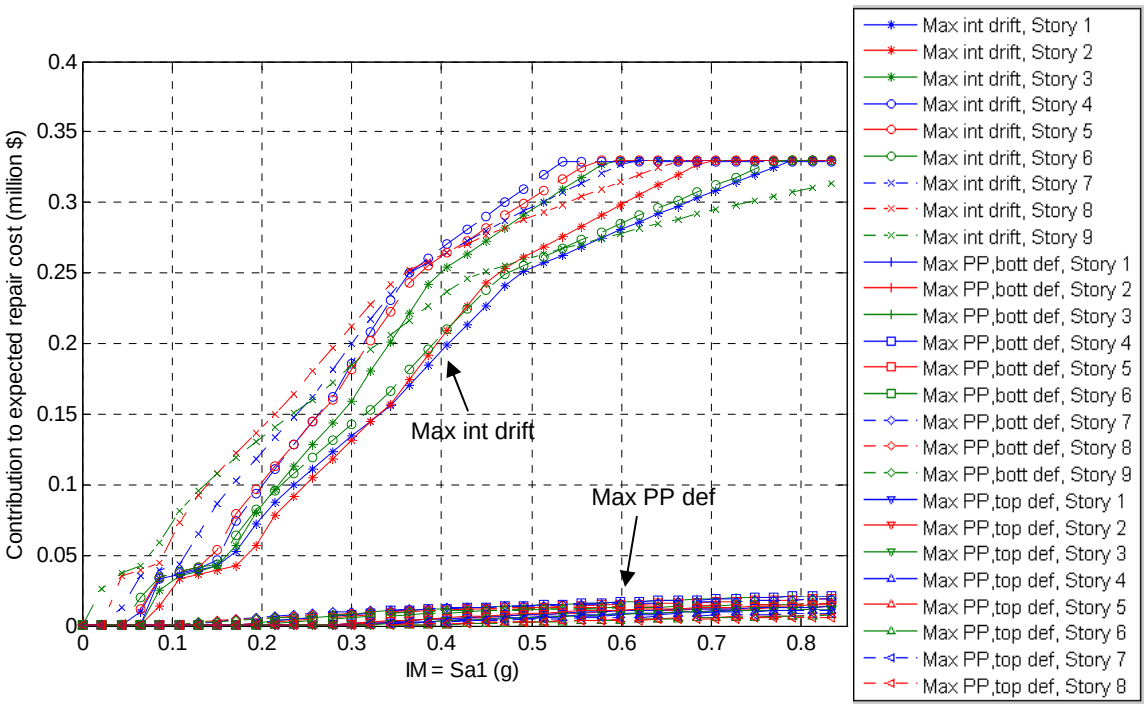

Fig. 7.33 Disaggregation of total repair cost of cladding type C1 by performance group

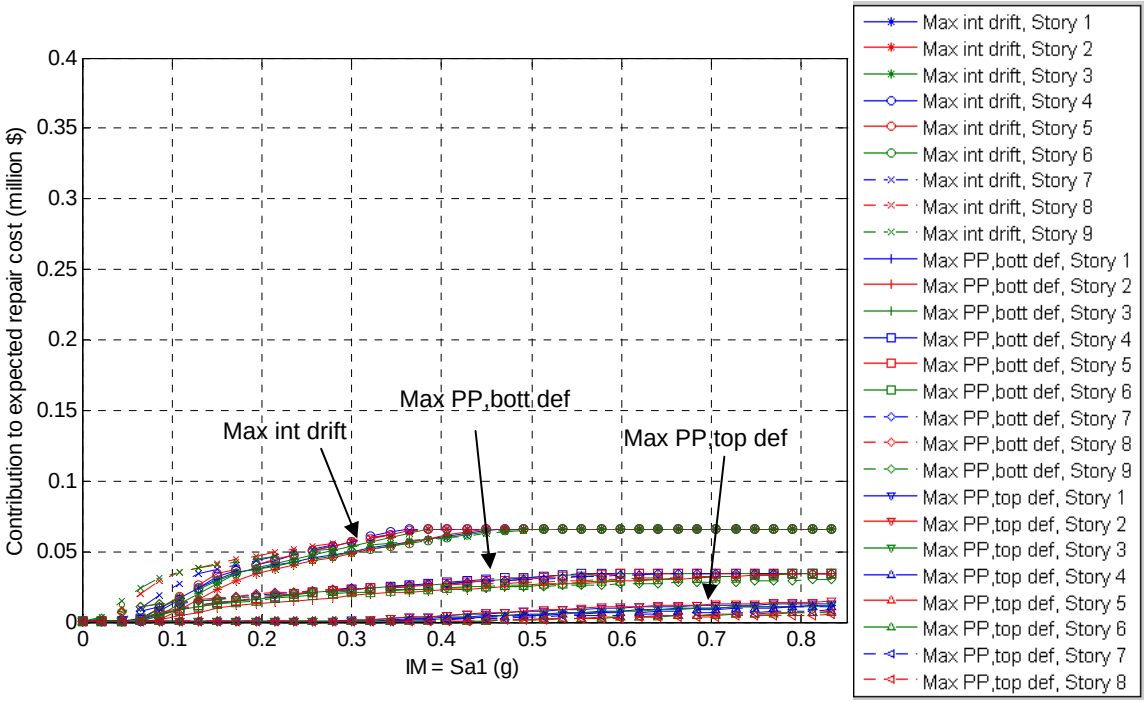

Fig. 7.34 Disaggregation of total repair cost of cladding type C2 by performance group

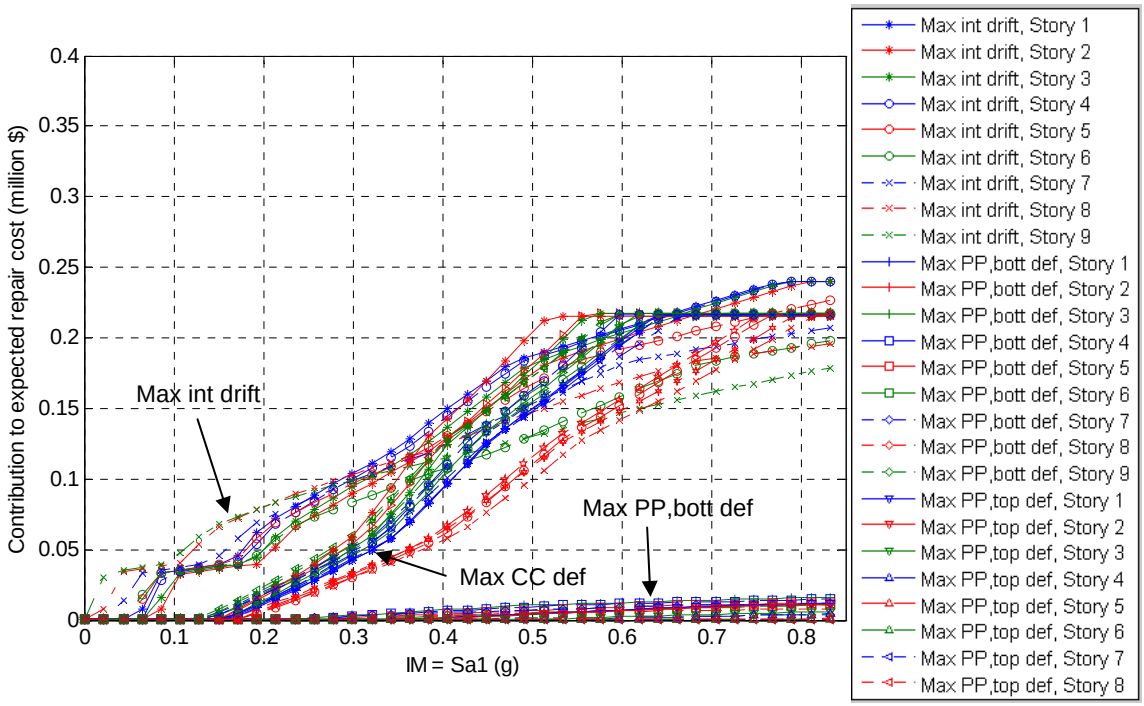

Fig. 7.35 Disaggregation of total repair cost of cladding type C3 by performance group

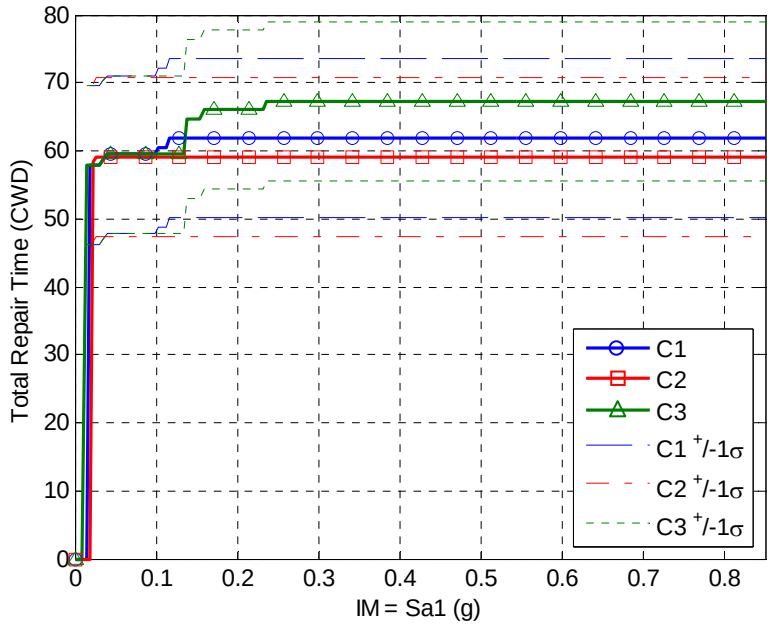

Fig. 7.36 CWD as a function of Sa(T_1) for three different cladding systems

Chapter 8: Conclusions and Future Work

In this chapter, the main results and conclusions of the research in this dissertation are summarized. The results of this research are used to form recommendations for the design of cladding systems. In addition, an experimental test program to study the three-dimensional behavior of a corner cladding system is outlined for future work.

8.1 CONCLUSIONS

Analytical and experimental studies have shown that exterior cladding panels have a major influence on structural behavior (i.e. Henry and Roll, 1986; Goodno *et al*., 1983; Wolz *et al*., 1992; Hunt and Stojadinovic, 2008). However, in seismic analysis and design, engineers typically ignore the additional stiffness and damping that the cladding system may provide, which could prove to be beneficial or detrimental to the building's seismic performance. The notion of advanced cladding connections developed by previous researchers was created to take advantage of energy dissipation due to the relative movement of the cladding panels and structural frame. However, these systems require cladding systems to undergo significant movements to create any significant effects; therefore, the appearance, water tightness, and air tightness due to the relative panel-structure movement could be jeopardized. Thus, these advanced connections have yet to be shown feasible; today, sound design of conventional cladding systems is more favorable.

The purpose of the research discussed in this dissertation was to study the effect that cladding has on the structural response of multistory buildings, develop analytical equations to estimate the seismic demand in the cladding connections, calculate the probability of failure of typical cladding connections, and determine the post-earthquake repair costs and repair times of typical cladding systems. These topics are summarized in the following sections.

8.1.1 Analytical Models of Buildings with Cladding

Analytical models were created in OpenSees to study the effect that typical cladding systems have on the seismic response of multistory buildings. The nine-story LA SAC building (Foutch, 2000) was selected as the study building, and a two-dimensional, nonlinear model was developed of the bare-frame structure. The steel moment-resisting frame of the bare structure was modeled using nonlinear force beam-column line elements capable of representing distributed plasticity along their length. The sections of the beam-column elements were modeled using fiber elements to capture the distribution of stress and strain in the section. The

corotational transformation method was used when translating the local degrees of freedom to global degrees of freedom to capture the secondary effects due to large displacements and P-Δ effects. The steel moment-resisting frame connections were reduced-beam section (RBS) moment connections, and their cyclic moment-rotation behavior was assigned to the model based on experimental test results of the connection. The effects of the floor slab on the strength of the floor beams were modeled using a composite beam section with an effective wide of concrete slab. The rigidity of the shear (simple) connections in the gravity framing was modeled using semi-rigid connections. The stiffness and strength of the gravity framing and weak-axis moment-resisting framing were lumped into a dummy frame, which was attached to the model with rigid links. The seismic mass of the building was distributed to the beam-column nodes.

Analytical models of three different precast cladding designs were applied to the bare-frame structure to study their effect on the building's seismic response. The three cladding designs represent common systems used in regular multistory buildings in modern construction. The first cladding design, cladding type C1, consisted of alternating horizontal bands of spandrel panels (covering the exterior floor beams) and glazing. The spandrel panels extend the full width of the bay. The second cladding design, cladding type C2, consisted of spandrel panels that extend the full height of the story with rectangular window openings "punched" into their surface. The third cladding design, cladding type C3, consisted of the same spandrel panels as in type C1 with column cover panels spanning between adjacent spandrel panels.

The precast panels themselves were five inches thick and were not expected to sustain major damage due to interstory drift. Thus, the precast panels in all cladding types were modeled as rigid blocks using rigid elastic beam-column elements. The spandrel panels were connected at their corners to the columns with push-pull connections that transmit shear forces between the cladding and frame by bending of a threaded rod. The middle of the spandrel panels were connected to the beams with rigid lateral connections (rigid plates) that prevent relative horizontal displacement between the spandrel panel and the supporting beam. There were two vertical bearing connections in the spandrel panels that provided a rigid connection in compression but no tension or lateral force resistance. The column covers span the gap between the spandrel panels, and they were attached to the spandrel panels with two slotted connections at their tops and two pinned connections at their bottoms. The connections cladding connections were modeled using nonlinear zero-length elements. The force-deformation curves of the connections used in the model were obtained from experimental tests of push-pull connections and column cover connections. The total seismic mass of the models with the cladding systems was the same as the total seismic mass of the bare-frame model. However, in the models with cladding, the seismic mass was distributed between the beam-column nodes and the nodes of the cladding system according to their respective tributary weights.

8.1.2 Analysis Results

The effects of the cladding on the seismic response of the bare-frame structure were studied by performing modal analyses, static pushover analyses, and dynamic time-history analyses of the analytical models.

The fundamental period of the bare frame structure was 2.13 sec., while the fundamental periods of the models with cladding type C1, C2, and C3 were 2.11 sec., 2.05 sec., and 2.09 sec., respectively. Thus, the cladding systems decreased the fundamental period by a maximum of 4%

compared to the bare-frame structure. The mode shapes and effective modal mass percentages were also not significantly affected by the cladding systems.

A static nonlinear pushover analysis was performed for the bare frame model and the models with cladding. The pushover analyses were started after first applying the gravity loads, and the applied lateral force distribution was proportional to the first mode shapes (approximately linear). The pushover curves (roof drift ratio versus base shear) for the bare-frame structure and models with cladding all had approximately the same initial stiffness. The bare-frame model, model with cladding type C1, and model with cladding type C2 also had approximately the same post-yield response: the global yield base shear was approximately 17% of the building weight at 0.012 rad. roof drift, and the maximum base shear was 19% of the building weight at 0.025 rad. roof drift. The post-yield strength of the model with cladding type C3 was approximately 25% larger than the post-yield strength of the other models. The plastic hinge rotations of the beam-column connections were recorded during the pushover analysis to study the effect of the cladding on the element demands. For most levels of roof drift, the results showed that the plastic hinge rotations are very similar between the bare-frame model and the models with cladding. However, as the building undergoes more significant drift, the plastic hinges increase in the lower stories and are 25% larger in model C3 at 0.025 rad. roof drift. In addition, the plastic hinges start to redistribute in model C3 and column hinging may develop. The deformations in the push-pull connections and the column cover connections were also recorded during the pushover analysis. The performance levels of the deformations in the push-pull connections were set at 0.5 in. for Immediate Occupancy, 1.25 in. for Life Safety, and 2.2 in. for Collapse Prevention. At 0.007 rad. roof drift, the maximum push-pull deformations were approximately 0.7 in., 1.4 in., and 0.6 in. in the models with cladding types C1, C2, and C3, respectively. At 0.025 rad. roof drift, the maximum push-pull deformations were approximately 2.2 in., 5.5 in., and 3.8 in. in the models with cladding types C1, C2, and C3, respectively. Finally, at 0.05 rad. roof drift, the maximum push-pull deformations were approximately 4.3 in., 10.5 in., and 7.5 in. in the models with cladding types C1, C2, and C3, respectively. The performance levels of the deformations in the column cover connections were set at 0.06 inches for Immediate Occupancy, 0.12 in. for Life Safety, and 0.25 in. for Collapse Prevention. For the model with cladding type C3, the maximum column cover deformations were approximately 0.04 in., 0.5 in., and 0.6 in. at roof drift ratios of 0.007 rad., 0.025 rad., and 0.05 rad., respectively.

Time-history analyses were performed to evaluate the nonlinear dynamic response of the frames to ground motions with a wide range of intensities. Seven bins of 20 ground motions each (140 motions total) were selected to perform the time-history analyses. The ground motions in each bin were scaled by a common factor (cloud method with constant scaling) to ensure nonlinear response was captured. The parameters recorded during the analyses include the maximum interstory drifts, residual interstory drifts, maximum floor accelerations, maximum plastic hinge rotations, and maximum deformations in the cladding connectors. The time-history results were plotted in log-log space, and a linear trend line was fitted to the data to represent the mean maximum response values.

The time-history results revealed that the addition of cladding reduces the mean maximum interstory drift ratios by up to 22%, 28%, and 33% for the 50%-, 10%-, and 2%-in-50 year probability of exceedance levels, respectively. The reductions in interstory drift were the largest for cladding type C3 and smallest for cladding type C1. The mean residual interstory drifts were small for all levels of intensity and were not significantly affected by the cladding.

The mean maximum floor accelerations were not significantly affected by cladding types C1 and C2: the mean values of maximum floor accelerations in the bare frame structure were reduced by only 8% for these two cladding types. On the other hand, the mean values of the maximum acceleration at the roof level in the model with cladding type C3 were up to 35%, 63%, and 97% larger than the values in the bare frame structure for the 50%-, 10%-, and 2%-in-50 year probability of exceedance levels, respectively. The plastic hinge demands were small for the 50%- and 10%-in-50 year probability of exceedance levels. For the 2%-in-50 year probability of exceedance level, the mean values of the maximum plastic hinge rotation in the models with cladding types C1, C2, and C3 were up to 15%, 33%, and 32% smaller than the values in the bare frame structure, respectively. The maximum reductions occurred in the upper stories.

The mean maximum deformations in the push-pull connectors were calculated from the time-history analyses. The mean maximum deformations for 50%-in-50 year probability of exceedance level were up to 0.9 in., 1.9 in., and 0.7 in. for the models with cladding type C1, C2, and C3, respectively. For the 10%-in-50 year probability of exceedance level, the mean maximum deformations were up to 1.3 in., 2.8 in., and 1.0 in. for the models with cladding type C1, C2, and C3, respectively. For the 2%-in-50 year probability of exceedance level, the mean maximum deformations were up to 2.0 in., 4.7 in., and 1.5 in. for the models with cladding type C1, C2, and C3, respectively. For the column cover connections in cladding type C3, the mean maximum deformations were up to 0.09 in., 0.23 in., and 0.70 in. for the 50%-, 10%-, and 2%-in-50 year probability of exceedance level, respectively.

The differences in the results from the pushover analyses and time-history analyses highlight the importance of knowing their limitations. The pushover analyses give insight into how the building and cladding system respond due to a statically applied force distribution, while the time-history analyses give insight into how the building and cladding system respond due to earthquake ground motions. The effects of nonlinear yielding, energy dissipation, and damping of the cladding system are better understood through time-history analyses.

8.1.3 Analytical Equations for Estimating Connector Demands in the Cladding System Connections

The models developed in Chapter 3 and analyzed in Chapter 4 were time-consuming to create and computationally demanding to analyze. Thus, analytical equations were derived to describe the mechanisms for deformation in the cladding connectors. The input variables are the response quantities of the bare-frame (BF) structure and the geometry of the cladding system. The output of the equations is an estimation of the maximum deformations in the push-pull and column cover connectors. The maximum deformations estimated from the equations were compared to the maximum deformations recorded from the time-history analyses.

The analytical equations provided good estimates of the actual maximum deformations in the push-pull connectors from the time-history analyses. For the LA50 and LA10 ground motion bins, the percent error between in the median value of the maximum deformation estimated by the equations was less than 10% in most stories. For the LA2 ground motion bin, the percent error was less than 27%. For the column cover connectors, the estimates from the analytical equations were more accurate for moderate to higher intensity ground motions than low intensity ground motions. This result is due to the fact that the analytical equations were derived for the higher intensity ground motion levels. The low intensity ground motions do not create significant

deformations in the column cover connectors. For the LA10 bin, the percent error between in the median value of the maximum deformation estimated by the equations was less than 22% in most stories. For the LA2 ground motion bin, the percent error was less than 12%. Since the median value of the maximum deformations estimated from the equations overestimate the median values from the time-history analyses, the analytical equations can be used as conservative estimates of deformation for the seismic design of similar cladding connectors.

8.1.4 Probabilistic Analysis of the Column Cover Connections

The analysis results in Chapter 4 and the estimations from the analytical equations in Chapter 5 show that significant deformations develop in the column cover connections in moderate earthquakes. The deformations exceed the life-safety, and in some cases, the collapse prevention performance criteria. Thus, the failure probabilities of the column cover connections subject to multiple hazard levels were investigated using structural reliability theorem. The two-dimensional nonlinear analytical model of SAC building with cladding type C3 was used, and three suites of nonlinear time-history analyses (corresponding to three hazard levels) were performed to obtain the mean values and standard deviations of the maximum interstory drifts. The analytical equations derived in Chapter 5 for estimating the deformations in the column cover connectors were used to construct the limit-state function describing the structural reliability of the connectors. The random variables consisted of the maximum interstory drift, the gap width in the slotted connections, and the failure shear deformation in the connectors. The deterministic parameters in the limit-state functions were the panel dimensions and the story height. The correlation coefficients were calculated for the maximum interstory drifts between different stories.

The components of the column covers consist of four connectors (one in each corner). The component failure probabilities (calculated using FORM) were as high as 44.2%, 70.0%, and 100% for the low, moderate, and high hazard levels. The maximum interstory drift was found to be the most important (had the largest effect on the results) random variable, and the gap width was the most important capacity or design variable. Increasing the gap width in the slotted connection reduces the probability of failure. Regarding the deterministic parameters, decreasing the panel width has the largest effect on decreasing the probability of failure of one panel. The probability of failure can also be decreased by increasing the panel height or increasing the story height. However, increasing the story height may increase the building's fundamental period and interstory drifts.

Story system reliabilitiy analyses were performed to investigate the probability of failure of multiple panels per story. For each story, the total probability theorem was used to calculate the total probability of failure of 2 panels in the low hazard event, 4 panels in the moderate hazard event, and 8 panels in the high hazard event. The total probabilities of failure were as high as 48.4% for a lifetime of 50 years of the building, with the largest probabilities at the top three stories of the building. Compared to common structural systems, which have probabilities of failure often less than 1%, the total failure probabilities of column cover connections are very large. The cost of the cladding system accounts for a large portion of the total cost of a new building, and their unreliable connections pose risks to the life safety of the occupants and increases the building repair costs after an earthquake.

8.1.5 Repair Cost Analysis of the Cladding System

To gain additional insight on the seismic performance of multistory buildings with cladding, post-earthquake repair cost analyses were performed on the analytical models using the performance-based earthquake engineering (PBEE) methodology developed by the Pacific Engineering Earthquake Research (PEER) Center. The PEER PBEE method is a modular framework for translating the seismic intensity hazards at the building site into decision variables (repair cost and repair time). The seismic hazard curve for the nine-story SAC building was established based on the seismic guidelines of the UC Berkeley campus. The seismic intensity measure (IM) used to quantify the hazard levels was the spectral acceleration at the fundamental period of the bare frame structure, $Sa(T_1 = 2.13$ sec.). This IM can be considered a structure independent period because none of the analyzed models with cladding have this period. Then, the demand model, or engineering demand parameter (EDP) versus intensity measure (IM) relationship, was constructed based on the time-history analyses results of Chapter 4. The damage state fragility curves of the cladding components (i.e. cracking of window panes, yielding of connectors, etc.) were determined from experimental and analytical test results to define the damage model (DM). The repair methods and repair quantities for each damage state were obtained from local cladding manufacturers. Finally, the unit repair costs and unit repair efforts for each repair method, also determined from the cladding manufacturers, were used to determine the decision variables (DVs), total repair cost and repair effort.

The total repair cost of each of the three cladding types was expressed in terms of three different repair cost ratios. The three different repair cost ratios each give a different measure of the total repair costs of the cladding system. The first repair cost ratio was calculated as the total repair cost of the cladding system divided by the replacement cost of the cladding system. At a spectral acceleration of 0.11g, the ratios were 5.4%, 3.7%, and 4.0% for cladding types C1, C2, and C3, respectively. At a spectral acceleration of 0.65g, the ratios were 37.6%, 11.9%, and 65.8% for cladding types C1, C2, and C3, respectively. The second repair cost ratio was calculated as the total repair cost of the cladding system divided by the replacement cost of the complete building. At a spectral acceleration of 0.11g, the ratios were 1.1%, 0.7%, and 0.8% for cladding types C1, C2, and C3, respectively. At a spectral acceleration of 0.65g, the ratios were 7.5%, 2.3%, and 13.7% for cladding types C1, C2, and C3, respectively. The third repair cost ratio was calculated as the total repair cost of the cladding system divided by the total repair cost of the complete building. At a spectral acceleration of 0.11g, the ratios were 12.0%, 7.7%, and 11.1% for cladding types C1, C2, and C3, respectively. At a spectral acceleration of 0.65g, the ratios were 29.5%, 11.7%, and 50.4% for cladding types C1, C2, and C3, respectively.

The mean annual repair costs were calculated as the product of the mean repair cost of the cladding system conditioned on IM and slope of the hazard curve at each IM, integrated over the range of IM. The mean annual total repair costs of the cladding system were $39,563, $16,213, and $40,824 for cladding types C1, C2, and C3, respectively.

Based on the repair cost analyses, it is apparent that cladding type C2 is the most cost-effective cladding design. Because the cladding panels have window punch-outs, the window panes are protected from damage due to interstory drift. In addition, cladding type C2 does not use the highly damageable column cover connections that are expensive to repair.

8.1.6 Implications for Cladding Design

The results of this research highlight several important issues in cladding design. First, the cladding system should be carefully designed in consultation with the structural engineer to ensure that the cladding system does not significantly impact the structural response of the building structure. As shown by the results in Chapters 4 and 5, the selected cladding type determines how much the cladding affects the structural response of the building. The addition of cladding to the bare-frame model reduced the interstory drifts significantly; however, this does not necessarily mean that the cladding should be used as a response modification mechanism. Instead, this result implies that a more accurate consideration of cladding may lead to a refined estimate of the displacement demands, which may provide the engineer with more margin against the considered limit states. The addition of cladding type C3 to the bare-frame model increased the floor accelerations significantly. In this cladding type, the spandrel panels and column covers create a "spine" up the height of the building such that the building is more rigid when subjected to sudden changes in the direction of motion, which causes increased floor accelerations. These increased accelerations are important when considering the design of nonstructural components and building contents.

The analytical equations developed to approximate the demands in the cladding connections are useful for the design engineer to predict the deformations in the connectors without explicitly modeling the cladding system. The analysis of the code equations for window glazing systems revealed that windows with narrow aspect ratios (height greater than width) and generous clearances between the glass and surrounding window framing provide significantly better seismic drift capacity before cracking and glass fallout occurs. The results of the post-earthquake repair cost analyses of typical cladding systems showed that cladding systems with full-story height spandrel panels with window cutouts incur the lowest repair costs. The cladding systems using spandrel panels and column cover panels sustain more damage and are more expensive to repair.

8.2 FUTURE WORK

The research discussed in this dissertation has attempted to answer the important questions related to the seismic behavior and expected damage states of typical precast concrete cladding systems in multistory buildings. However, more research in this field will provide results for a wider array of structural geometries, cladding configurations, and connection types.

Detailed analytical models of the cladding systems were constructed in Chapter 3. The force-deformation relationship of the cladding connectors were obtained from the results of a limited amount of experimental tests. To improve the computer models, more experimental tests should be performed on the various types of cladding connectors typically found in construction.

The analytical equations derived in Chapter 5 provide the engineer with a simple way of computing the maximum deformations in the cladding connectors using the response quantities of a bare-frame model. However, these equations were developed for the two-dimensional motion of regular structures. Thus, more research on the structural response of non-regular structures (with height and plan irregularities) due to two-dimensional and three-dimensional motion is warranted.

The structural reliability analyses discussed in Chapter 6 provide a method of determining the probabilities of failure of the column cover connections. However, the column cover panels analyzed in this research were symmetric panels, and the analyses were performed considering only two-dimensional motion. More research on the response of different panel sizes and shapes due to two-dimensional and three-dimensional motion would provide the necessary data for the structural reliability of different panel types.

The probabilistic repair cost analyses discussed in Chapter 7 detail the damage states, post-earthquake repair costs, and repair times of typical cladding systems. The data used for these analyses is based on limited analytical and experimental tests of the cladding system components. Thus, more experimental tests of the many cladding components found in existing and new construction will provide more statistical data (median and standard deviation EDPs for damage states) for the repair cost analyses. In addition, more discussions with cladding manufacturers and contractors will provide additional data on the unit repair costs and repair times corresponding to the different repair methods. Overall, the use of the design equations in Chapter 5, the probabilities of failure in Chapter 6, and the repair cost analyses in Chapter 7 provide a rational framework for selecting a cladding type, designing the cladding connections, and/or designing new cladding systems.

8.3 PROPOSED EXPERIMENTAL TEST PROGRAM

The majority of the research in this dissertation focused on computer simulations of cladding systems, reliability studies, and repair cost analyses. The next step in understanding the behavior of cladding systems is to perform experimental testing of typical cladding system components. The next sections outline a proposed testing program to investigate the lateral response of a full-scale portion of a cladding system. The goals of the tests are to understand how the cladding system components interact together as a unit and to monitor the progression of damage. The results of the tests should provide some validation to the analytical results presented in this dissertation.

8.2.1 Test Setup

The proposed experimental testing program will provide insight into the three-dimensional behavior of the cladding system. Three full-scale cladding assemblies measuring 30 feet (one bay) long by 15 feet (one half bay) wide by 18 feet (one story) tall will be tested to investigate the interaction of the cladding panels in plane and out of plane, determine the locations of damage, and identify the failure modes of the connections. The current details of the tests are presented in this section (more detailed information can be found in McMullin and Nguyen, 2008).

Three specimens will be tested: two are to be tested according to the ATC 58 loading protocol, and one specimen will be tested with the hybrid simulation testing method. In plan the specimen is “L-shaped.” The cladding panels are attached to a reusable steel frame with pinned connections so that the frame provides no lateral resistance.

Two quasi-statically tested specimens are expected to provide information about the behavior of the connectors, the interaction of panels at the corners, and the progression of

damage. The hybrid simulation, on the other hand, is designed to provide insight into how panels and connectors behave during an earthquake along the entire height of the building and to validate the analytical models developed in OpenSees. In order to investigate the response of essentially identical cladding sub-assemblies along the height of the building, the physical L-shaped first-story cladding sub-assembly will be used as the leading element. Thus, the physical test will provide not only the forces to be assembled into the hybrid model equation of motion, but also the data to re-calibrate on-the-fly the properties of the OpenSees models for the cladding at higher stories. Development of suitable identification and integration algorithms is under way.

8.3.2 Specimen Design

The nine-story SAC Los Angeles building will again be used as the study building for the experimental tests. The building is indicative of mid-rise, moment frame structures common in commercial real estate. The cladding design, connection types, and connection locations are the same as discussed in this dissertation.

The structural steel frame is reusable and is constructed with pinned connections so that the frame provides no lateral resistance. The beams and columns of the steel frame are box sections. A sketch of the south elevation of the specimen is shown in Fig. 8.1 in the undeformed and deformed states after lateral movement.

The test specimen does not represent all of the cladding panels on the nine-story building; however, the full-scale corner subassembly has the following benefits for testing, according to McMullin and Nguyen (2008):

1. "It includes the largest interstory height and therefore has the tallest column cover panels."
2. "It covers the story levels of the building that analysis has shown to experience the largest post-yield drifts during seismic loading."

In addition, the corner specimen provides a unique opportunity to investigate the interaction between the cladding panels as the frame moves in the direction orthogonal to the spandrel-panel plane. Contacts between the orthogonal panels may induce additional forces in panel connections that are difficult to model analytically.

8.3.3 Specimen Terminology

As described in Chapter 1, cladding designers use a common glossary to define the components. These terms help the engineers, architects, and contractors communicate clearly about the cladding design (McMullin and Nguyen, 2008). The terminology that applies to the test specimen is explained below.

The test specimen represents a corner of the SAC nine-story building, shown in Fig. 8.2a. The system is represented as opaque cladding panels (Fig. 8.2a) and window glazing (Fig. 8.2b). The largest panel in the cladding system is the spandrel panel, shown in Fig. 8.3. There are two types of spandrel panels in the test specimen: Fig. 8.3a shows the spandrel panel for the in-plane loading direction, and Fig. 8.3b shows the spandrel return panel on the opposite edge that wraps around the building edge.

The column cover panels are used to cover the vertical elements in the supporting frame. There are three types of column covers in the test specimen, as shown in Fig. 8.4: Fig. 8.4a shows the column cover panel for the in-plane loading direction, Fig. 8.4b shows the half column cover panel for the in-plane loading direction, and Fig. 8.4c shows the corner column cover panel that wraps around the building edge.

Horizontal and vertical gaps between the different types of panels are maintained to facilitate installation and construction tolerance (McMullin and Nguyen, 2008). The typical vertical gaps are shown in Fig. 8.5a, and the typical horizontal gaps are shown in Fig. 8.5b. These gaps are usually 0.75 inches in U.S. construction practice. The vertical seismic joint, shown in Fig. 8.5c, separates the two-dimensional panels on the in-plane face and the three-dimensional panels on the opposite face. The vertical seismic gap is typically 2 inches wide to prevent panel-to-panel contact during extreme interstory drifts.

8.3.4 Expected Damage States

The damage to the cladding system is caused by excessive interstory drift levels in the supporting frame. According to McMullin and Nguyen (2008), the expected damage states include:

- "Loss of air seal at joints"
- "Closing of the slip connection at the top of column cover panels"
- "Damage to the corners of concrete panels when excessive rotation results in the contact between adjoining panels"
- "Damage, including possible bolt fracture, to the pin connections at the base of the column cover panels"
- "Cracking of the window glass due to crushing"
- "Damage to the connections supporting the return panels resulting in potential instability of panels"

These damage states are slightly different than the damage states discussed in Chapter 7: the damage states in Chapter 7 correspond to in-plane two-dimensional motion, while the damage states for the experimental test correspond to the three-dimensional interaction of the components at the corner of the building. The corner of the cladding system creates additional problems with the compatibility of lateral movement between the two spandrel panels. Arnold (2008) shows this "cladding corner problem" in Fig. 8.6. The undeformed state of the spandrel panels at the corner of the building is shown in Fig. 8.6a. After a certain amount of drift, the spandrel panel in-plane with the structural drift contacts the out-of-plane spandrel panel and causes damage, as shown in Fig. 8.6b. To relieve the cladding corner problem, Arnold suggests mitering the panel edges so that the adjacent panels do not contact each other under significant drifts. The proposed solution is shown in Fig. 8.7.

8.3.5 Hybrid Simulation

A hybrid simulation test will be conducted on one of the test specimens using OpenSees. The hybrid model combines the physical cladding system at the corners of the building and analytical elements to study the system response of the nine-story SAC building. The connector

response and panel interaction at the corners of the building are difficult to understand; therefore, this subassembly was selected as the test specimen. The beams and columns will be modeled with nonlinear force beam-column elements, and the cladding panels will be modeled as elastic (rigid) beam-column elements. The cladding connectors will be modeled as nonlinear zero-length experimental elements with their force-deformation relationship defined from the quasi-static tests. The test specimen physically represents only the corner on the lowest story of the building; however, the cladding connections are expected to behave in a similar manner along the height of the building. A weighting function or learning algorithm will be developed to relate the response of the connectors at the lower story of the building to the response of the connectors along the height of the building.

The differential equation governing the system dynamics at time t_n is shown in Eq. 8.1:

$$M(\ddot{u}_n) + C(\dot{u}_n) + P_r(u_n, \dot{u}_n) = -M\iota\ddot{u}_{g,n} \qquad \text{Eq. 8.1}$$

The variable M is the mass matrix of the structure, and C is the damping matrix of the structure. The variables $u_n, \dot{u}_n, \ddot{u}_n$ are the displacement, velocity, and acceleration vectors at time t_n. The variable $\Pr(u, \dot{u})$ is the resisting force vector at the element degrees of freedom (dof) at time t_n. The resisting force vector is assembled from the analytical and experimental elements. Vector ι is the influence vector that relates the dof at the ground excitation to the element dof, and $\ddot{u}_{g,n}$ is the ground acceleration at time t_n.

The Newmark time step integration method with constant acceleration and Newton-Raphason initial stiffness is used to solve this system of nonlinear differential equations. The process of the hybrid simulation test starts with the integrator calculating the structural deformation due to the external excitation at the beginning of each time step. Then, the actuators in the test setup apply the computed displacements on the test specimen, and the force is measured in the connectors. The measured forces in the connectors of the physical specimen are used to re-calculate the properties of the connector models in Opensees for the remainder of the building. To prevent sudden changes in properties, a weighted function will be used up to the point of failure of the connectors. Once the new properties are calculated, the force states in the analytical elements in OpenSees are calculated at the given displacement state. The force feedbacks from the experimental and analytical elements and the external excitation are combined in OpenSees to calculate the structural deformations at the next time step. The whole process is repeated until the entire time-history analysis is complete. A schematic of the hybrid simulation test setup is shown in Fig. 8.8.

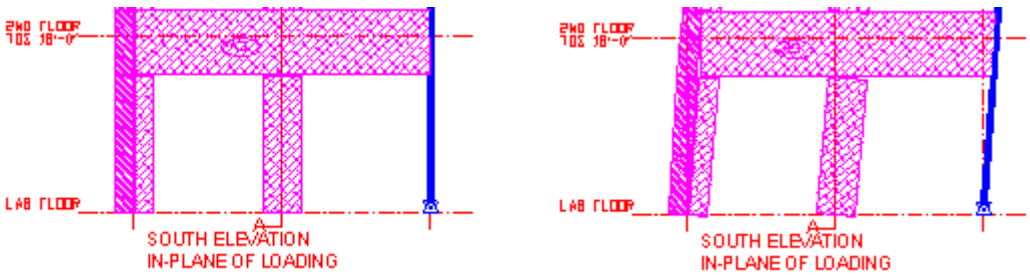

(a) undeformed state *(b) deformed state*

Fig. 8.1 Cladding system before and after lateral movement (McMullin and Nguyen, 2008)

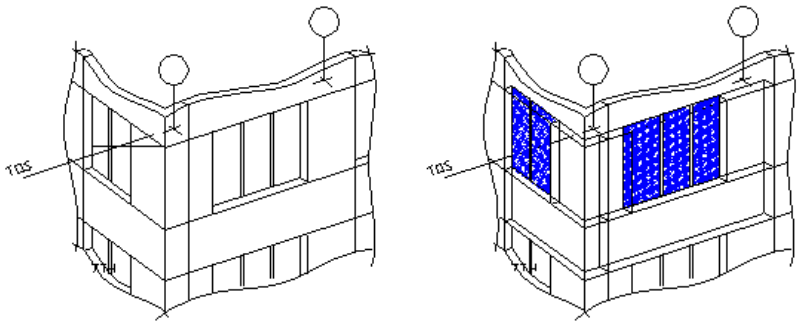

(a) corner cladding system *(b) glazing system*

Fig. 8.2 Corner cladding system (McMullin and Nguyen, 2008)

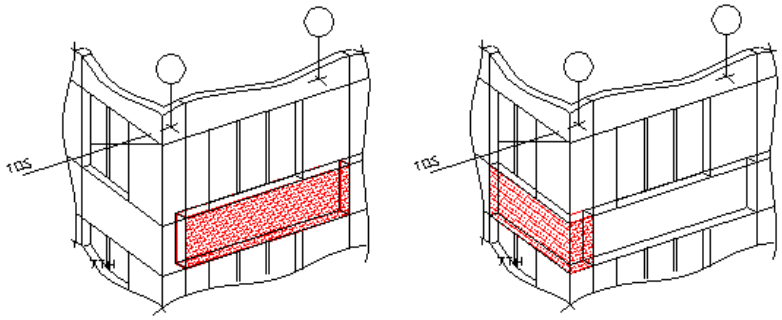

(a) spandrel panel *(b) spandrel return panel*

Fig. 8.3 Spandrel panels (McMullin and Nguyen, 2008)

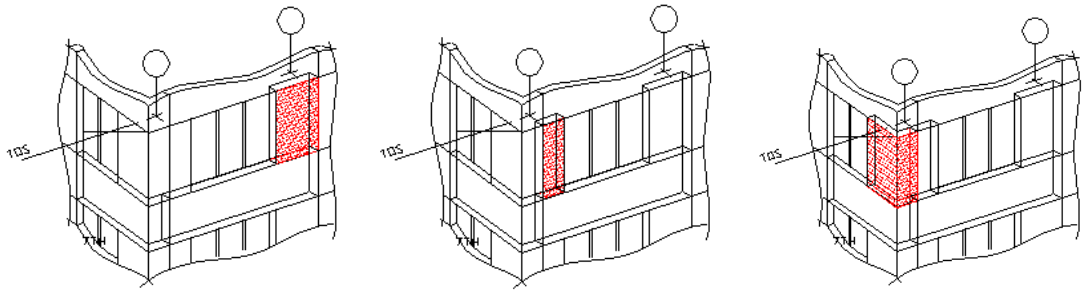

(a) column cover panel *(b) half column cover panel* *(c) corner column cover panel*

Fig. 8.4 Column cover panels (McMullin and Nguyen, 2008)

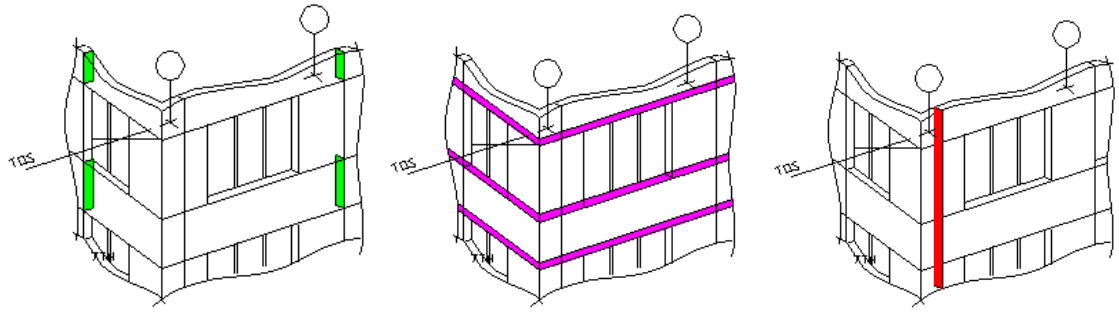

(a) vertical cladding joints *(b) horiz. cladding joints* *(c) vertical seismic joint*

Fig. 8.5 Cladding panel joints (McMullin and Nguyen, 2008)

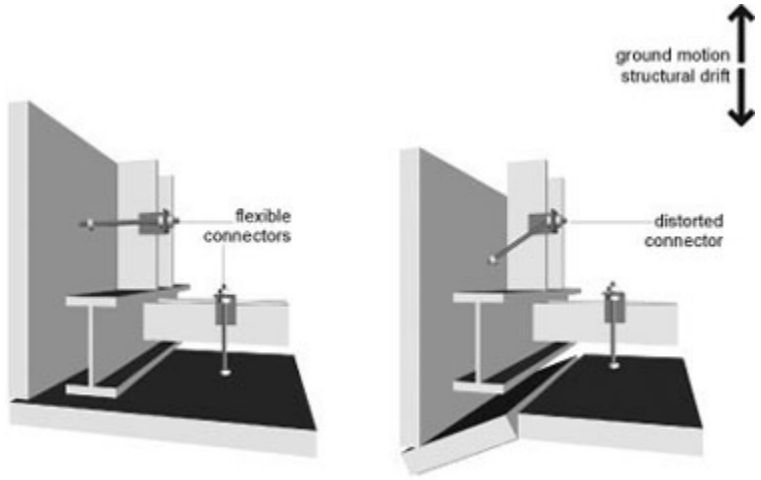

(a) undeformed state *(b) deformed/damaged state*

Fig. 8.6 The cladding corner problem, view from above (Arnold, 2008)

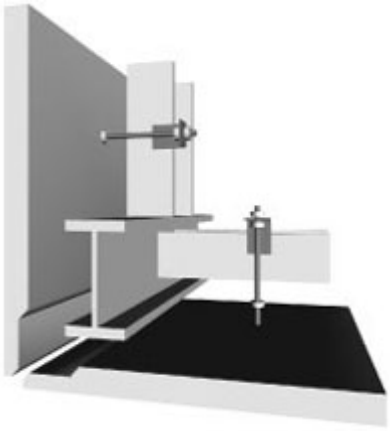

Fig. 8.7 Mitered panels to address corner panel problem (Arnold, 2008)

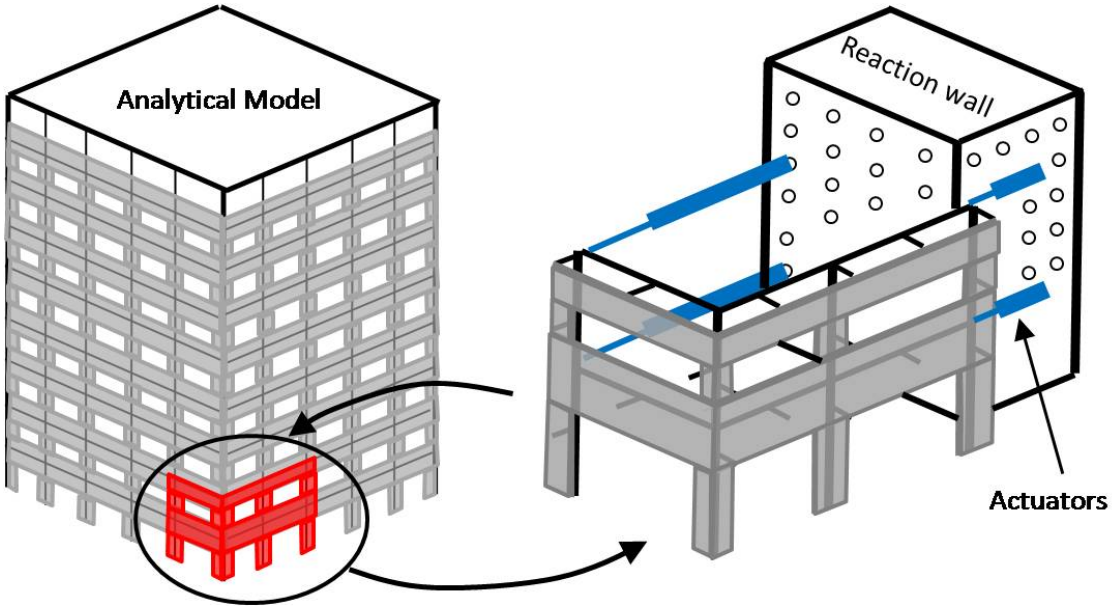

Fig. 8.8 Hybrid simulation test setup schematic (Hunt *et al.*, 2008)

References

Alavi, B. and Krawinkler, H. 2004. Behavior of Moment-Resisting Frame Structures Subjected to Near-Fault Ground Motions, *Earthquake Engineering and Structural Dynamics*, 33(6): 687–706.

Arnold, C. 1989. Cladding Design: Recent Architectural Trends and Their Impact on Seismic Design. In *Architectural Precast Concrete Cladding – Its Contribution to Lateral Resistance of Buildings*, PCI, Chicago, Illinios, pp.14-31, Nov. 8-9.

Arnold, C. 2008. Seismic Safety of the Building Envelope. *Whole Building Design Guide*: http://www.wbdg.org/resources/env_seismicsafety.php?r=envelope. Article sponsored by the Building Enclosure Council. Last updated on 05/23/2008.

Astaneh-Asl, A. 2005. Design of Shear Tab Connections for Gravity and Seismic Loads. *Steel Tips*, Structural Engineering Council, June.

Baker, J.W. and Cornell, C.A. 2003. Uncertainty Specification and Propagation for Loss Estimation using FOSM Methods, *Report No. 2003/07*, University of California, Pacific Earthquake Engineering Research Center, Berkeley CA.

Behr, R.A.; Belarbi, A.; and Brown, A.T. 1995a. Seismic Performance of Architectural Glass in a Storefront Wall System, *Earthquake Spectra*, Vol. 11, No. 3, August.

Behr, R.A.; Belarbi, A; and Culp, J.H. 1995b. Dynamic Racking Tests of Curtain Wall Glass Elements with In-Plane and Out-of-Plane Motions, *Earthquake Engineering and Structural Dynamics*, Vol. 24, pp. 1-14.

Behr, R.A. and Belarbi, A. 1996. Seismic Test Methods for Architectural Glazing Systems, *Earthquake Spectra*, Vol. 12, No. 1, February, pp. 129-143.

Behr, R.A. and Worrell, C.L. 1998. Limit States for Architectural Glass Under Simulated Seismic Loadings, in *Proc. Seminar on Seismic Design, Retrofit, and Performance of Nonstructural Components*, ATC 29-1, January 22-23, 1998, San Francisco, Redwood City, CA, Applied Technology Council, pp. 229-240.

Behr, R.A. 2006. Design of Architectural Glazing to Resist Earthquakes, *Journal of Architectural Engineering*, ASCE, Vol. 12, No. 3, September, pp.122-128..

Bouwkamp J.G. and Meehan, J.F. 1960. Drift Limitations Imposed by Glass, *Proceedings of the Second World Conference on Earthquake Engineering*, Tokyo, Japan, pp. 1763-1778.

Carpenter, L.D. 2004. High-Rise Building Cladding Drift Accomodation, *Struc. Design Tall Spec. Build.*, 13, pp. 439-456.

Charney, F.A.; and Harris, J.R. 1989. The Effect of Architectural Precast Concrete Cladding on the Lateral Response of Multistory Buildings. In *Architectural Precast Concrete Cladding – Its Contribution to Lateral Resistance of Buildings*, PCI, Chicago, Illinios, pp. 80-96, Nov. 8-9.

Cohen, J.M. 1995. *Literature Review on Seismic Performance of Building Cladding System*. Report NIST GCR 95-681. National Institute of Standards and Technology, United States Department of Commerce.

Cornell, C.A. 1968. Engineering Seismic Risk Analysis, *Bulletin of Seismological Society of America* 58: pp. 1583-1606.

Craig, J.I.; Goodno, B.J.; Keister, M.J.; and Fennell, C.J. 1986. Hysteretic Behavior of Precast Cladding Connections. *Dynamic Response of Structures*, Ed. by G.C. Hart and R.B. Nelson, In Third Conference of Engineering Mechanics Division, ASCE, Los Angeles, CA, pp. 817-826, March 31-April 2.

Craig, J.I.; Leistikow, R.; and Fennell, C.J. 1988. Experimental Studies of the Performance of Precast Concrete Cladding Connections. In *Ninth World Conference on Earthquake Engineering*, Tokyo-Kyoto, Japan, Vol. 6, pp. 201-206, Aug. 2-9.

Crawford, S.F.; and Kulak, G.L. 1968. Studies in Structural Engineering: Behavior of Eccentrically Loaded Bolted Connections, *Report No. 4*, Department of Civil Engineering, Nova Scotia Technical College.

El-Gazairly, L.F.; and Goodno, B.J. 1989. Dynamic Analysis of a High-Rise Building Damaged in the Mexico Earthquake including Cladding-Structure Interaction. In *Architectural Precast Concrete Cladding – Its Contribution to Lateral Resistance of Buildings*, PCI, Chicago, Illinios, pp. 257-286, Nov. 8-9.

Elsesser, E. 1986. Survey of Seismic Structural Systems and Design Implications. In *ATC-17 Seminar and Workshop on Base Isolation and Passive Energy Dissipation*, ATC, San Francisco, CA, pp. 51-62, March 12-14.

Engelhardt, M.; Fry, G.T.; Jones, S.L.; Venti, M.J.; and Holliday, S.D. 2000. Behavior and Design of Radius Cut Reduced Beam Section Connections, *SAC Background Document, Report No. SAC/BD-00/17*, SAC Joint-Venture, Richmond, CA.

Facades: Errors can be Expensive, *Engineering News Record*, Vol. 204, No. 5, January 24, 1980, pp. 30-34.

FEMA-356. 2000. Prestandard and Commentary for the Seismic Rehabilitation of Buildings, *Report No. FEMA 356*, Federal Emergency Management Agency, Washington, DC.

Foutch, D.A.; Goel, S.C.; and Roeder, C.W. 1986. Preliminary Report on Seismic Testing of a Full-Scale Six-Story Steel Building, Ch. 6 on Phase III and Phase IV – Moment Frame Test and Nonstructural Component Test, *UILU-ENG-86-2009*, Structural Research Series No. 527, Civil Engrg. Studies, Univ. of Illinois, Nov. 1986.

Foutch, D.A. 2000. State of the Art Report on Performance Prediction and Evaluation of Steel Moment-Frame Buildings. *SAC Report No. FEMA 355F*. Federal Emergency Management Agency. Washington, D.C.

Gaiotti, R.; and Smith, B.S. 1992. Stiffening of Moment-Resisting Frame by Precast Concrete Cladding. *PCI Journal*, PCI, Vol. 37, No. 5, pp. 80-92, Sept./Oct.

Gjelvik, A. 1973. Interaction between Frames and Precast Wall Panels. *Journal of the Structural Division*, ASCE, Vol. 100, No. ST2, pp. 405-426, Feb.

Goel, R.K. and Chopra, A.K. 1997. Vibration Properties of Buildings Determined from Recorded Earthquake Motions, *Report No. UCB/EERC-97/14*, Earthquake Engineering Research Center, University of California, Berkeley, December.

Goodno, B.J.; and Craig, J.I. 1989. Historical Overview of Studies on the Contribution of Cladding to Lateral Resistance of Buildings. In *Architectural Precast Concrete Cladding –*

Its Contribution to Lateral Resistance of Buildings, PCI, Chicago, Illinios, pp. 36-47, Nov. 8-9.

Goodno, B.J.; Will, K.M.; and Palsson, H. 1980. Effect of Cladding on Building Response to Moderate Ground Motion. In *Seventh World Conference on Earthquake Engineering*, Istanbul, Turkey, Vol. 2, pp. 449-456, Sept.

Goodno, B.J.; and Palsson, H. 1981. Torsional Response of Partially Clad Structures. In *Conference on Earthquakes and Earthquake Engineering: The Eastern U.S.*, Knoxville, TN, Vol. 2, pp. 859-877, Sept.

Goodno, B.J.; Craig, J.I.; and Meyyappa, M. 1983. *Cladding-Structure Interaction in High-Rise Buildings*. Report No. CEE-7704269, Georgia Institute of Technology, Atlanta, GA, January.

Goodno, B.J.; and Palsson, H. 1986. Analytical Studies of Building Cladding. *Journal of Structural Engineering*, ASCE, Vol. 112, No. 4, pp. 665-676, April.

Goodno, B.J.; Palsson, H.; and Pless, D.G. 1984. Localized Cladding Response and Implications for Seismic Design. In Eighth World Conference on Earthquake Engineering, San Francisco, CA, Vol. 5, pp. 1143-1150, July 21-28.

Goodno, B.J.; Meyyappa, M.; and Nagarajaiah, S. 1988. A Refined Model for Precast Concrete Cladding and Connections, In *Proceedings of the Ninth World Conference on Earthquake Engineering*, Tokyo-Kyoto, Japan, VI:195-200, Aug. 2-9.

Goodno, B.J.; Craig, J.; Zeevaert-Wolf, A. 1989. The Mexico Earthquake of September 19, 1985 – Behavior of Heavy Cladding Components, *Earthquake Spectra*, Vol. 5, No. 1.

Goodno, B.J.; Craig, J.I.; and Hsu, C.C. 1991. Experimental Studies and Analytical Evaluation of Ductile Cladding Connections. In *Pacific Conference on Earthquake Engineering*, New Zealand, National Society for Earthquake Engineering, Auckland, New Zealand, Vol. 2, pp. 43-54, 20-23 Nov.

Gupta, A. and Krawinkler, H. 1999. Seismic Demands for Performance Evaluation of Steel Moment Resisting Frame Structures, *Report No. 132*, The John A. Blume Earthquake Engineering Center, Dept. of Civil and Env. Engrg., Stanford University, Stanford, CA, June.

Hareer, R.W. 2007. Seismic Response of Building Façade System with Energy Absorbing Connections, *Doctoral Thesis*, Centre for Built Environment and Engineering Research, Queensland University of Technology.

Hegle, R.L. 1989. Connection of Cladding to Multi-Story Structures. In *Architectural Precast Concrete Cladding – Its Contribution to Lateral Resistance of Buildings*, PCI, Chicago, Illinios, pp.192-201, Nov. 8-9.

Henry, R.M.; Goodspeed, C.H.; and Calvin, D.L. 1989. In *Architectural Precast Concrete Cladding – Its Contribution to Lateral Resistance of Buildings*, PCI, Chicago, Illinios, pp. 62-79, Nov. 8-9.

Henry, R.M.; and Roll, F. 1986. Cladding-Frame Interaction. *Journal of Structural Engineering*, ASCE, Vol. 112, No. 4, pp. 815-834, April.

Hildebrand, M. 2009. Personal Communication.

Hunt, J.; Stojadinovic, B.; and McMullin, K. 2008. Modeling the Effect of Non-structural Cladding in Buildings, In *Sixth Annual NEES Meeting: The Value of Earthquake Engineering Research*, Portland, Oregon, June 18-20.

Hunt, J. and Stojadinovic, B. 2008. Nonlinear Dynamic Model for Seismic Analysis of Non-structural Cladding, In *Proceedings of the Fourteenth World Conference on Earthquake Engineering*, Beijing, China, October 12-17.

Iverson, J.K. 1989. Concrete Cladding Connections in Earthquake Country. In *Architectural Precast Concrete Cladding – Its Contribution to Lateral Resistance of Buildings*, PCI, Chicago, Illinios, pp.202-216, Nov. 8-9.

Kato, B.; Aoki, H.; and Tagawa, Y. 1984. Seismic Behavior of Steel Frames with Composite Girders, In *Proceedings, 8th World Conference on Earthquake Engineering*, San Francisco, Vol. VI.

Kemeny, Z.A.; and Lorant, J. 1989. Energy Dissipating Elastomeric Connections. In *Architectural Precast Concrete Cladding – Its Contribution to Lateral Resistance of Buildings*, PCI, Chicago, Illinios, pp. 287-299, Nov. 8-9.

Knowles, E. 2010. Personal Communication.

Korista, D.S. 1989. Exterior Façade System – Building Structure System: Load-Deformation Behavioral Inter-Relationships. *Exterior Claddings on High Rise Buildings*. Report No. 12, Chicago, Illinois, pp. 47-86, June.

Kramer, S.L. 1996. *Geotechnical Earthquake Engineering*, Upper Saddle River, NJ: Prentice Hall.

Krawinkler, H. 2000. State of the Art Report on Systems Performance of Moment Resisting Steel Frames Subject to Earthquake Ground Shaking, SAC Report, Report No. FEMA 355C, Federal Emergency Management Agency, Washington, DC.

Kunnath, S.K., *Ed*. 2006. Application of the PEER PBEE Methodology to the I-880 Viaduct, *Report No. 2006/10*, University of California Berkeley, Pacific Earthquake Engineering Research Center, Berkeley CA.

Lee, K. and Foutch, D.A. 2000. Performance Prediction and Evaluation of Steel Special Moment Frames for Seismic Loads, SAC Background Document, Report No. SAC/BD-00/25, SAC Joint-Venture, Richmond, CA.

Lee, K. and Foutch, D.A. 2002. Performance Evaluation of New Steel Frame Buildings for Seismic Loads, *Earthquake Engineering and Structural Dynamics*, 31:653-670.

Luco, N. and Cornell, C. A. 2003. Structure-Specific Scalar Intensity Measures for Near-Source and Ordinary Earthquake Ground Motions, *Earthquake Spectra*, Vol. 23, Issue 2, pp. 357-392.

Mackie, K.R. and Stojadinovic, B. 2006. Fourway: A Graphical Tool for Performance-Based Earthquake Engineering, *Journal of Structural Engineering*, 132(8): 1274–1283.

Mackie, K.R., Wong, J.M., and Stojadinovic, B., 2008a. Integrated Probabilistic Performance-Based Evaluation of Benchmark Reinforced Concrete Bridges, *Technical Report PEER 2007/09*, Pacific Earthquake Engineering Research Center, University of California, Berkeley, California, January.

Mackie, K.R., Wong, J.M., and Stojadinovic, B., 2008b. Probabilistic Methodologies for Prediction of Post-Earthquake Bridge Repair Costs and Repair Times, In *Proceedings of the 14th World Conference on Earthquake Engineering,* Oct. 12-17, Beijing, China.

Masek, J. and Ridge, R. 2009. Identification of Methods to Achieve Successful Implementation of Nonstructural and Equipment Seismic Restraints, *Earthquake Engineering Research Institute Technical Report*.

McCann, R.A. 1991. Architectural Precast Concrete Cladding Connections. Implementation and Performance of Structural Details. 1991 Fall Seminar, Session 2, Struct. Engrs. Assoc. of Northern CA, 21 pp., 31 Oct.

McMullin, K.; Wong, Y.; Choi, C.; Chan, K. 2004. Seismic Performance States of Precast Concrete Cladding Connections. In *Thirteenth World Conference on Earthquake Engineering*, Vancouver, B.C., Canada, Paper No. 3379, Aug. 1-6.

McMullin, K; and Nguyen, H. 2008. Drift Controlled Damage to Precast Concrete Cladding Panels – Expected Damage Patterns, *In Sixth Annual NEES Meeting: The Value of Earthquake Engineering Research*, Portland, Oregon, June 18-20.

Medina, R.A. and Krawinkler, H. 2003. Seismic Demands for Nondeteriorating Frame Structures and Their Dependence on Ground Motions. *Report No. 144*, The John A. Blume Earthquake Engineering Center, Dept. of Civil and Env. Engrg., Stanford University, Stanford, CA, December.

Meyyappa, M.; Palsson, H.; and Craig, J.I. 1981. Modal Parameter Estimation for a Highrise Building Using Ambient Response Data Taken During Construction, *Proc. 2nd Specialty Conf. Dyn. Resp. Struct.: Experimentation, Observation, Prediction, and Control*, Atlanta, Georgia, pp. 141-151.

Mitrani-Reiser, J. 2007. An Ounce of Prevention: Probabilistic Loss Estimation for Performance-Based Earthquake Engineering, *Report No. EERL 2007-01*, Earthquake Engineering Research Laboratory, California Institute of Technology, Pasadena, CA, January.

Nakata, S.H.; Itoh, A.; Baba, A.; and Okamoto, S. 1984. U.S.-Japan Cooperative Research on R/C Full-Scale Building Test, *Proceedings of the Eight World Conference on Earthquake Engineering, July 21-28, San Francisco, CA*, Englewood Cliffs NJ: Prentice-Hall, Inc. Vol. VI, pp.611-618.

Oppenheim, I.J. 1973. Dynamic Behavior of Tall Buildings with Cladding. In *Fifth World Conference on Earthquake Engineering*, Rome, Italy, pp. 2769-2773, June.

Pall, A.S. 1989. Friction-Damped Connections for Precast Concrete Cladding. In *Architectural Precast Concrete Cladding – Its Contribution to Lateral Resistance of Buildings*, PCI, Chicago, Illinios, pp. 300-309, Nov. 8-9.

Palsson, H.; and Goodno, B.J. 1982. A Degrading Stiffness Model for Precast Concrete Cladding. In *Seventh European Conference of Earthquake Engineering*, Athens, Greece, Vol. 5, pp. 135-142, Sept. 20-25.

Palsson, H.; Goodno, B.J.; Craig, J.I.; and Will, K.M. 1984. Cladding Influence on Dynamic Response of Tall Buildings. *Earthquake Engineering and Structural Dynamics*, Vol. 12, No. 2, pp. 215-228.

Palsson, H.; and Goodno, B.J. 1988. Influence of Interstory Drift on Cladding Panels and Connections. In *Ninth World Conference on Earthquake Engineering*, Tokyo-Kyoto, Japan, Vol. 6, pp. 213-218, Aug. 2-9.

Pantelides, C.P. and Behr, R.A. 1994. Dynamics In-Plane Racking Tests of Curtain Wall Glass Elements, *Earthquake Engineering and Structural Dynamics*, Vol. 23, pp. 211-228.

PCI. 1989. *Architectural Precast Concrete*. 2nd Edition, First Printing. PCI Architectural Precast Concrete Manual Committee, 175 W. Jackson Blvd., Chicago, Illinois, 340 pp.

PCI. 2007. *Architectural Precast Concrete*. 3rd Edition, First Printing. PCI Architectural Precast Concrete Manual Committee, 175 W. Jackson Blvd., Chicago, Illinois, 340 pp.

Pinelli, J.P.; and Craig, J.I. 1989. Experimental Studies on the Performance of Mexican Precast Cladding Connections. In *Architectural Precast Concrete Cladding – Its Contribution to Lateral Resistance of Buildings*, PCI, Chicago, Illinios, pp.159-176, Nov. 8-9.

Pinelli, J.P.; Craig, J.I.; and Goodno, B.J. 1992. Development of Advanced Connection Concepts for Precast Concrete Cladding. In *ATC-29 Seminar and Workshop on Seismic Design and*

Performance of Equipment and Nonstructural Elements in Buildings and Industrial Structures, ATC, pp. 341-351, Oct. 3-5.

Pinelli, J.P.; Craig, J.I.; and Goodno, B.J.; and Hsu, C.C. 1993. Passive Control of Building Response Using Energy Dissipating Cladding Connections. *Earthquake Spectra*, Theme Issue: Passive Energy Dissipation, EERI, Vol. 9, No. 3, pp. 529-546, Aug.

Pinelli, J.P.; Craig, J.I.; and Goodno, B.J. 1995. Energy-Based Seismic Design of Ductile Cladding Systems. *Journal of Structural Engineering*, Vol. 121, No. 3, March, Paper No. 7840.

Porter, K.A. and Kiremidjian, A.S. 2001. Assembly-Based Vulnerability of Buildings and its Uses in Seismic Performance Evaluation and Risk Management Decision-Making, *Report No. 139*, The John A. Blume Earthquake Engineering Center, Dept. of Civil and Env. Engrg., Stanford University, Stanford, CA, February.

Rihal, S.S. 1988. Earthquake Resistance and Behavior of Heavy Facades/Cladding and Connections in Medium-Rise Steel-Framed Buildings. In *Ninth World Conference on Earthquake Engineering*, Tokyo-Kyoto, Japan, Vol. 6, pp. 207-212, Aug. 2-9.

Rihal, S.S. 1989. Earthquake Resistance and Behavior of APCC and Connections. In *Architectural Precast Concrete Cladding – Its Contribution to Lateral Resistance of Buildings*, PCI, Chicago, Illinios, pp.110-140, Nov. 8-9.

Rojhann, C. and Hamburger, R.O. 2007. Guidelines for Seismic Performance Assessment of Buildings, *ATC 58 35% Draft*, Applied Technology Council.

RS Means. 2009. *Square Foot Costs: Residential, Commercial, Industrial, Institutional*, 18th Annual Edition, Kingston, MA: RS Means, Co.

Sack, R.L.; Beers, R.J.; and Thomas, D.L. 1989. Seismic Behavior of Architectural Precast Concrete Cladding. In *Architectural Precast Concrete Cladding – Its Contribution to Lateral Resistance of Buildings*, PCI, Chicago, Illinios, pp.141-158, Nov. 8-9.

Seike, Tsuyoshi, and Sakamoto, I. 1997. A Report of the Damage of Precast Concrete Curtain Walls by the 1995 Hyogo-ken Nanbu Earthquake, In *Proceedings of the International Conference on the Building Envelope Systems and Technology*, UK.

Shome, N. and Cornell, C.A. 1999. Probabilistic Seismic Demand Analysis of Nonlinear Structures. *Report No. RMS 35*, Stanford University, Department of Civil and Environmental Engineering, Stanford, CA.

Smith, B.S.; and Gaiotti, R. 1989. Interaction of Precast Concrete Cladding with a Story-Height Frame Module. In *Architectural Precast Concrete Cladding – Its Contribution to Lateral Resistance of Buildings*, PCI, Chicago, Illinios, pp.48-61, Nov. 8-9.

Somerville, P.G. and SAC Phase 2 Participants. 1997. Develop Suites of Time Histories, SAC Joint Venture Steel Project Phase 2, *Project Task: 5.4.1*, March 21.

Somerville, P.G. 2001. Ground Motion Time Histories for the UC Lab Building, within the *UC Berkeley Seismic Guidelines*, University of California, Berkeley.

Sproken, J.R. 1989. Detailing of Cladding for Deformations. In *Architectural Precast Concrete Cladding – Its Contribution to Lateral Resistance of Buildings*, PCI, Chicago, Illinios, pp. 184-191, Nov. 8-9.

Stockbridge, J.G. 1990. Lessons Learned from Cladding Failures. *Exterior Claddings on High Rise Buildings*, The 1989 Fall Symposium, The Chicago Committee on High Rise Buildings, Report No. 12, Chicago, Illinois, pp. 283-294, June.

Stojadinovic, B., Sapcone E., Goel, S.C. and Kwon, M. 1998. Influence of Semi-rigid Column Base Models on the Response of Steel MRF Buildings. *Proceedings of the 6th U.S. National*

Conference on Earthquake Engineering, Seattle, WA, May 31-June 4, 1998, Earthquake Engineering Research Institute, Oakland, CA.

Taghavi, S., and Miranda, E. 2003. Response Assessment of Nonstructural Building Elements, *Technical Report PEER 2003/05*, Pacific Earthquake Engineering Research Center, University of California, Berkeley, California.

Thiel, C.C; Elsesser, E.; Lindsay, J.; Kelly, T.; Bertero, V.V.; Filippou, F.; and McCann R. 1986. Seismic Energy Absorbing Cladding System: A Feasibility Study. In *ATC-17 Seminar and Workshop on Base Isolation and Passive Energy Dissipation*, ATC, San Francisco, CA, March 12-14, pp. 251-260.

UBC, 1994. *Uniform Building Code*, International Conference of Building Officials, Whittier, California.

URS, 2007. Updated Probabilistic Seismic Hazard Evaluation and Development of Seismic Design Ground Motions for the University of California, Berkeley and Lawrence Berkeley National Laboratory, *Draft Report*, 12 December.

Vamvatsikos, D. and Cornell, C.A. 2002. Incremental Dynamic Analysis, *Earthquake Engineering and Structural Dynamics*, 31(3): 491–512.

Wang, M.L. 1986. Nonstructural Element Test Phase: U.S.-Japan Cooperative Research Project on a Full-Scale Steel Test Frame, Center of Environmental Design Research, U.C. Berkeley, 140 pp.

Wang, M.L. 1987. Cladding Performance on a Full Scale Test Frame. *Earthquake Spectra*, EERI, Vol. 3, No. 1, pp. 119-173, Feb.

Wang, M.L. 1992. Design of Cladding for Earthquakes, *Cladding*, Ch. 4, Tall Building Systems and Concepts, Council on Tall Buildings and Urban Habitat, Committee 12A, pub. by McGraw-Hill, Inc., New York.

Weidlinger, P. 1973. Shear Field Panel Bracing. *Journal of the Structural Division*, ASCE, Vol. 99, No. ST7, pp. 1615-1631, July.

Wolz, M.W.; Hsu, C.C.; and Goodno, B.J. 1992. Nonlinear Interaction between Building Structural Systems and Nonstructural Cladding Components. In *ATC-29 Seminar and Workshop on Seismic Design and Performance of Equipment and Nonstructural Elements in Buildings and Industrial Structures*, ATC, pp. 329-340, Oct. 3-5.

Wothke, W. 1993. Nonpositive Definite Matrices in Structural Modeling. In K. A. Bollen & J. S. Long (Eds.), *Testing Structural Equation Models* (pp. 256-93), Newbury Park, CA: Sage.

Yang, T.Y., Moehle, J., Stojadinovic, B., and Der Kiureghian, A. 2006. An Application of the Peer Performance-Based Earthquake Engineering Methodology. In *Proc., 8th National Conference on Earthquake Engineering*, San Francisco, April 18-22.

Yang, T.Y., Moehle, J., Stojadinovic, B., 2009. Integrated Performance Evaluation of Innovative Steel Braced Frames, *Technical Report PEER 2009/103*, Pacific Earthquake Engineering Research Center, University of California, Berkeley, California.

Yun, S.Y. and Foutch, D.A. 2000. Performance Prediction and Evaluation of Low Ductility Steel Moment Frames for Seismic Loads. SAC Background Document. *Report No. SAC/BD-00/26*, SAC Joint-Venture, Richmond, CA.

Appendix A: Structural Analysis of the Column Cover Connections

Initial deformations, Vd, due to support movements:

$$Vd(\Delta h, g, \theta_b, \theta_t, y_t, y_b, X, H) := \begin{pmatrix} 0 & y_t & 0 & 0 \\ 0 & \frac{X}{2} & 0 & 0 \\ 0 & -y_t & 0 & 0 \\ 0 & \frac{-X}{2} & 0 & 0 \\ -1 & 0 & -y_b & 0 \\ 0 & 0 & \frac{-X}{2} & -1 \\ 1 & 0 & y_b & 0 \\ 0 & 0 & \frac{X}{2} & -1 \end{pmatrix} \cdot \begin{pmatrix} \Delta h - g \\ \theta_b \\ \theta_t \\ \frac{\Delta h^2}{2 \cdot H} \end{pmatrix}$$

$$Vd(\Delta h, g, \theta_b, \theta_t, y_t, y_b, X, H) \text{ simplify } \rightarrow \begin{pmatrix} y_t \cdot \theta_b \\ \frac{1}{2} \cdot X \cdot \theta_b \\ -y_t \cdot \theta_b \\ \frac{-1}{2} \cdot X \cdot \theta_b \\ -\Delta h + g - y_b \cdot \theta_t \\ \frac{-1}{2} \cdot \frac{X \cdot \theta_t \cdot H + \Delta h^2}{H} \\ \Delta h - g + y_b \cdot \theta_t \\ \frac{1}{2} \cdot \frac{X \cdot \theta_t \cdot H - \Delta h^2}{H} \end{pmatrix}$$

Element stiffness matrix:

$$Ks(kl) := \begin{pmatrix} kl & 0 & 0 & 0 & 0 & 0 & 0 & 0 \\ 0 & kl & 0 & 0 & 0 & 0 & 0 & 0 \\ 0 & 0 & kl & 0 & 0 & 0 & 0 & 0 \\ 0 & 0 & 0 & kl & 0 & 0 & 0 & 0 \\ 0 & 0 & 0 & 0 & kl & 0 & 0 & 0 \\ 0 & 0 & 0 & 0 & 0 & kl & 0 & 0 \\ 0 & 0 & 0 & 0 & 0 & 0 & kl & 0 \\ 0 & 0 & 0 & 0 & 0 & 0 & 0 & kl \end{pmatrix}$$

Applied force vector:

$$P := \begin{pmatrix} 0 \\ 0 \\ 0 \end{pmatrix}$$

Structural compatibility matrix:

$$Af(X, Y) := \begin{pmatrix} 1 & 0 & \frac{-Y}{2} \\ 0 & -1 & \frac{X}{2} \\ -1 & 0 & \frac{Y}{2} \\ 0 & -1 & \frac{-X}{2} \\ 1 & 0 & \frac{Y}{2} \\ 0 & 1 & \frac{-X}{2} \\ -1 & 0 & \frac{-Y}{2} \\ 0 & 1 & \frac{X}{2} \end{pmatrix}$$

Initial force vector:

$$\mathbf{Po}(X, Y, k1, \Delta h, g, \theta_b, \theta_t, y_t, y_b, H) := Af(X, Y)^T \cdot Ks(k1) \cdot Vd(\Delta h, g, \theta_b, \theta_t, y_t, y_b, X, H)$$

$$\mathbf{Po}(X, Y, k1, \Delta h, g, \theta_b, \theta_t, y_t, y_b, H) \text{ simplify } \rightarrow \begin{bmatrix} 2 \cdot k1 \cdot y_t \cdot \theta_b - 2 \cdot k1 \cdot \Delta h + 2 \cdot k1 \cdot g - 2 \cdot k1 \cdot y_b \cdot \theta_t \\ -k1 \cdot \frac{\Delta h^2}{H} \\ \frac{1}{2} \cdot k1 \cdot \left(-2 \cdot Y \cdot y_t \cdot \theta_b + X^2 \cdot \theta_b - 2 \cdot Y \cdot \Delta h + 2 \cdot Y \cdot g - 2 \cdot Y \cdot y_b \cdot \theta_t + X^2 \cdot \theta_t\right) \end{bmatrix}$$

Global stiffness matrix:

$$\mathbf{Kf}(X, Y, k1) := Af(X, Y)^T \cdot Ks(k1) \cdot Af(X, Y)$$

$$Kf(X, Y, k1) \text{ simplify } \rightarrow \begin{pmatrix} 4 \cdot k1 & 0 & 0 \\ 0 & 4 \cdot k1 & 0 \\ 0 & 0 & Y^2 \cdot k1 + X^2 \cdot k1 \end{pmatrix}$$

Global displacements:

$$\mathbf{Uf}(X, Y, k1, \Delta h, g, \theta_b, \theta_t, y_t, y_b, H) := Kf(X, Y, k1)^{-1} \cdot (P - Po(X, Y, k1, \Delta h, g, \theta_b, \theta_t, y_t, y_b, H))$$

$$\mathbf{Uf}(X, Y, k1, \Delta h, g, \theta_b, \theta_t, y_t, y_b, H) \text{ simplify } \rightarrow \begin{pmatrix} \frac{-1}{2} \cdot y_t \cdot \theta_b + \frac{1}{2} \cdot \Delta h - \frac{1}{2} \cdot g + \frac{1}{2} \cdot y_b \cdot \theta_t \\ \frac{1}{4} \cdot \frac{\Delta h^2}{H} \\ \frac{-1}{2} \cdot \frac{-2 \cdot Y \cdot y_t \cdot \theta_b + X^2 \cdot \theta_b - 2 \cdot Y \cdot \Delta h + 2 \cdot Y \cdot g - 2 \cdot Y \cdot y_b \cdot \theta_t + X^2 \cdot \theta_t}{Y^2 + X^2} \end{pmatrix}$$

Connector element defcrmations:

$$Vf(X, Y, k1, \Delta h, g, \theta_b, \theta_t, y_t, y_b, H) := Af(X, Y) \cdot Uf(X, Y, k1, \Delta h, g, \theta_b, \theta_t, y_t, y_b, H) + Vd(\Delta h, g, \theta_b, \theta_t, y_t, y_b, X, H)$$

$$Vf(X, Y, k1, \Delta h, g, \theta_b, \theta_t, y_t, y_b, H) \text{ simplify } \rightarrow \begin{bmatrix} \frac{-1}{4} \cdot X^2 \cdot \frac{-2 \cdot y_t \cdot \theta_b - 2 \cdot \Delta h + 2 \cdot g - 2 \cdot y_b \cdot \theta_t - Y \cdot \theta_b - Y \cdot \theta_t}{Y^2 + X^2} \\ \frac{-1}{4} \cdot \frac{\Delta h^2 \cdot Y^2 + \Delta h^2 \cdot X^2 - 2 \cdot X \cdot H \cdot Y \cdot y_t \cdot \theta_b - X^3 \cdot H \cdot \theta_b - 2 \cdot X \cdot H \cdot Y \cdot \Delta h + 2 \cdot X \cdot H \cdot Y \cdot g - 2 \cdot X \cdot H \cdot Y \cdot y_b \cdot \theta_t + X^3 \cdot H \cdot \theta_t - 2 \cdot X \cdot \theta_b \cdot H \cdot Y^2}{(Y^2 + X^2) \cdot H} \\ \frac{1}{4} \cdot X^2 \cdot \frac{-2 \cdot y_t \cdot \theta_b - 2 \cdot \Delta h + 2 \cdot g - 2 \cdot y_b \cdot \theta_t - Y \cdot \theta_b - Y \cdot \theta_t}{Y^2 + X^2} \\ \frac{1}{4} \cdot \frac{-\Delta h^2 \cdot Y^2 - \Delta h^2 \cdot X^2 - 2 \cdot X \cdot H \cdot Y \cdot y_t \cdot \theta_b - X^3 \cdot H \cdot \theta_b - 2 \cdot X \cdot H \cdot Y \cdot \Delta h + 2 \cdot X \cdot H \cdot Y \cdot g - 2 \cdot X \cdot H \cdot Y \cdot y_b \cdot \theta_t + X^3 \cdot H \cdot \theta_t - 2 \cdot X \cdot \theta_b \cdot H \cdot Y^2}{(Y^2 + X^2) \cdot H} \\ \frac{1}{4} \cdot X^2 \cdot \frac{-2 \cdot y_t \cdot \theta_b - 2 \cdot \Delta h + 2 \cdot g - 2 \cdot y_b \cdot \theta_t - Y \cdot \theta_b - Y \cdot \theta_t}{Y^2 + X^2} \\ \frac{1}{4} \cdot \frac{-\Delta h^2 \cdot Y^2 - \Delta h^2 \cdot X^2 - 2 \cdot X \cdot H \cdot Y \cdot y_t \cdot \theta_b + X^3 \cdot H \cdot \theta_b - 2 \cdot X \cdot H \cdot Y \cdot \Delta h + 2 \cdot X \cdot H \cdot Y \cdot g - 2 \cdot X \cdot H \cdot Y \cdot y_b \cdot \theta_t - X^3 \cdot H \cdot \theta_t - 2 \cdot X \cdot \theta_t \cdot H \cdot Y^2}{(Y^2 + X^2) \cdot H} \\ \frac{-1}{4} \cdot X^2 \cdot \frac{-2 \cdot y_t \cdot \theta_b - 2 \cdot \Delta h + 2 \cdot g - 2 \cdot y_b \cdot \theta_t - Y \cdot \theta_b - Y \cdot \theta_t}{Y^2 + X^2} \\ \frac{-1}{4} \cdot \frac{\Delta h^2 \cdot Y^2 + \Delta h^2 \cdot X^2 - 2 \cdot X \cdot H \cdot Y \cdot y_t \cdot \theta_b + X^3 \cdot H \cdot \theta_b - 2 \cdot X \cdot H \cdot Y \cdot \Delta h + 2 \cdot X \cdot H \cdot Y \cdot g - 2 \cdot X \cdot H \cdot Y \cdot y_b \cdot \theta_t - X^3 \cdot H \cdot \theta_t - 2 \cdot X \cdot \theta_t \cdot H \cdot Y^2}{(Y^2 + X^2) \cdot H} \end{bmatrix}$$

An example: $Vf(54, 78, 100, 2.0, 1.5, 0.0027, 0.0027, 28, 50, 156) = \begin{pmatrix} 0.149 \\ 0.209 \\ -0.149 \\ -0.222 \\ -0.149 \\ -0.222 \\ 0.149 \\ 0.209 \end{pmatrix}$ inches

Total connector deformation is calculated as the vector sum of the horizontal and vertical deformations:

$$Vf_{total}(X, Y, k1, \Delta h, g, \theta_b, \theta_t, y_t, y_b, H) := \begin{bmatrix} \sqrt{(Vf(X, Y, k1, \Delta h, g, \theta_b, \theta_t, y_t, y_b, H)1)^2 + (Vf(X, Y, k1, \Delta h, g, \theta_b, \theta_t, y_t, y_b, H)2)^2} \\ \sqrt{(Vf(X, Y, k1, \Delta h, g, \theta_b, \theta_t, y_t, y_b, H)3)^2 + (Vf(X, Y, k1, \Delta h, g, \theta_b, \theta_t, y_t, y_b, H)4)^2} \\ \sqrt{(Vf(X, Y, k1, \Delta h, g, \theta_b, \theta_t, y_t, y_b, H)5)^2 + (Vf(X, Y, k1, \Delta h, g, \theta_b, \theta_t, y_t, y_b, H)6)^2} \\ \sqrt{(Vf(X, Y, k1, \Delta h, g, \theta_b, \theta_t, y_t, y_b, H)7)^2 + (Vf(X, Y, k1, \Delta h, g, \theta_b, \theta_t, y_t, y_b, H)8)^2} \end{bmatrix}$$

$$Vf_{total}(54, 78, 100, 2.0, 1.5, 0.0027, 0.0027, 28, 50, 156) = \begin{pmatrix} 0.2569 \\ 0.2675 \\ 0.2675 \\ 0.2569 \end{pmatrix}$$ inches

Appendix B: Repair Cost Analysis of the Nine-Story LA SAC Building

In this section, the replacement cost and total repair costs of the nine-story LA SAC building are computed. The replacement cost is determined from RS Means Square Foot Costs (2009), and the repair costs are computed using the adjusted repair quantities and unit costs from Yang *et al.* (2009).

B.1 TOTAL REPLACEMENT COST OF NINE-STORY SAC BUILDING

The total replacement cost of the nine-story SAC building (including excavation, materials, labor, contractor fees, and architect fees) was determined from RS Means Square Foot Costs (2009). The cost per square foot was determined from the tables for multistory office buildings 5-10 stories in height with exterior precast concrete panels (similar to cladding type C1) and a steel-moment resisting frame. The items considered in the cost calculation are shown in Table B.1. The SAC nine-story building has a total square footage of floor area of 202,500 SF and a perimeter of 600 LF. Thus, the square foot cost for elevated floors is $164.15. The cost for basement levels is given at $36.40 per square foot of basement area; therefore, the total replacement cost is 202,500 x $164.15 + 45,000 x $36.40 = $34,878,375. This cost represents an average cost for the United States. The location factor given in RS Means for Berkeley, California is 1.15. Thus the total replacement cost for the nine-story SAC building in Berkeley, CA is $34,878,375 x 1.15 = $40,110,131. This total cost best represents the cost of the building with cladding type C1. The total replacement cost is adjusted for the building with cladding types C2 and C3 by considering the cost of their respective cladding systems. Thus, the total replacement costs for the building with cladding types C2 and C3 are $39,744,456 and $40,476,230, respectively. These costs are 2010Q1 values.

Table B.1 Components considered in the calculation of total replacement cost of the nine-story SAC building

A. Substructure		
1010	Standard Foundations	Poured concrete; strip and spread footings
1020	Special Foundations	N/A
1030	Slab on Grade	4" reinforced concrete with vapor barrier and granular base
2010	Basement Excavation	Site preparation for slab and trench for foundation wall and footing
2020	Basement Walls	4' foundation wall
B. Shell		
	B10 Superstructure	
1010	Floor Construction	Concrete slab with metal deck and beams

1020	Roof Construction	Metal deck, open web steel joists, interior columns
	B20 Exterior Enclosure	
2010	Exterior Walls	Precast concrete panels (80% of wall)
2020	Exterior Windows	Vertical pivoted steel (20% of wall)
2030	Exterior Doors	Double aluminum and glass doors and entrance with transoms
	B30 Roofing	
3010	Roof Coverings	Built-up tar and gravel with flashing; perlite/EPS composite insulation
3020	Roof Openings	N/A
C. Interiors		
1010	Partitions	Gypsum board on metal studs
1020	Interior Doors	Single leaf hollow metal
1030	Fittings	Toilet partitions
2010	Stair Construction	Concrete filled metal pan
3010	Wall Finishes	60% vinyl wall covering, 40% paint
3020	Floor Finishes	60% carpet, 30% vinyl composition tile, 10% ceramic tile
3030	Ceiling Finishes	Mineral fiber tile on concealed zee bars
D. Services		
	D10 Conveying	
1010	Elevators & Lifts	Four general passenger elevators
1020	Escalators & Moving Walks	N/A
	D20 Plumbing	
2010	Plumbing Fixtures	Toilet and service fixtures, supply and drainage (1 fixture/1370 S.F. floor)
2020	Domestic Water Distribution	Gas fired water heater
2040	Rain Water Drainage	Roof drains
	D30 HVAC	
3010	Energy Supply	N/A
3020	Heat Generating Systems	Included in D3050
3030	Cooling Generating Systems	N/A
3050	Terminal & Package Units	Multizone unit gas heating, electric cooling
3090	Other HVAC Sys. & Equipment	N/A
	D40 Fire Protection	
4010	Sprinklers	Wet pipe sprinkler system
4020	Standpipes	Standpipes and hose systems
	D50 Electrical	
5010	Electrical Service/Distribution	1600 ampere service, panel board and feeders
5020	Lighting & Branch Wiring	High efficiency fluorescent fixtures, receptacles, switches, and A.C.
5030	Communications & Security	Addressable alarm systems, internet and phone wiring, emergency lighting
5090	Other Electrical Systems	Emergency generator, 100kW, uninterruptible power supply

B.2 TOTAL REPAIR COSTS OF NINE-STORY SAC BUILDING

The total repair costs of the nine-story SAC building were calculated using the repair quantities and unit costs determined by the ATC-58 project team and reported in Yang *et al*. (2009). The study building in their report was a multistory office similar to the SAC building in this report. The square footage of one floor was 22,736 SF, which is very similar (within 1%) of the square footage of one floor in the nine-story SAC building (22,500 SF). The building consists of a steel frame and exterior precast concrete panels similar to the SAC building. The damage states, repair quantities, and unit costs are given in Yang *et al*. (2009) for the structural components, nonstructural components, and building contents.

B.2.1 Damage States

The damage states of the components of the building are divided into several performance groups: structural lateral system, interior nonstructural components (drift sensitive), interior nonstructural components (acceleration sensitive), interior building contents (acceleration sensitive), caulking and window system, and cladding connections. The damage states are summarized in Table B.2. The damage states of the building components are taken from Yang *et al*. (2009), and the damage states of the caulking, window system, and cladding connections are taken from Chapter 7 of this dissertation.

Table B.2 Damage states of nine-story SAC building

PG #	EDP	Components	Param.	DS0	DS1	DS2	DS3	DS4	DS5
1-9	Int. drift ratio (rad.)	Structural lateral system	λ	0.01	0.015	0.025	0.035		
			β	0.25	0.25	0.30	0.30		
10-18	Int. drift ratio (rad.)	Interior nonstructural	λ	0.002	0.0039	0.0085			
			β	0.15	0.17	0.23			
19-27	Floor acc. (g)	Interior nonstructural	λ	0.5	1.0	1.5	2.0		
			β	0.15	0.15	0.20	0.20		
28-36	Floor acc. (g)	Interior Contents	λ	0.2	0.3	0.7	3.5		
			β	0.20	0.20	0.22	0.25		
36-45	Int. drift ratio (rad.)	Caulking + window glazing system	λ	0.0048	0.006	0.0096	0.011	0.016	0.02
			β	0.15	0.12	0.25	0.20	0.19	0.16
46-54	Push-pull def. (in.)	Bott. & top push-pull conn.	λ	0.75	1.25	2.2			
			β	0.25	0.25	0.25			
54-63	Column cover def. (in.)	Bott. & top col. cover conn.	λ	0.068	0.22	0.33			
			β	0.19	0.11	0.10			

B.2.2 Repair Quantities

The repair quantities of the structural lateral system, interior nonstructural components, and interior building contents are taken from Yang *et al*. (2009). The repair quantity values were modified so that they fit into the approach described in Chapter 7 (i.e. DS0 and DS∞ limit states were defined). The repair quantities for the cladding system were taken from Chapter 7. The repair quantities for each damage state are summarized in Table B.3-Table B.8. As discussed in Chapter 7, not all repair items of the cladding system are applicable for some cladding systems.

Table B.3 Repair quantities for structural lateral system: drift sensitive

Repair Item	Unit	DS1	DS2	DS3	DS∞
Demolition/Access					
Finish protection	sf	6000	6000	6000	6000
Ceiling system removal	sf	2000	3000	5000	5000
Drywall assembly removal	sf	800	800	6000	6000
Miscellaneous MEP	loc	2	4	6	6
Remove exterior skin (salvage)	sf	0	0	5600	5600
Repair					
Welding protection	sf	1500	1500	1500	1500
Shore beams below & remove	loc	0	0	12	12
Cut floor slab at damaged connection	sf	70	150	1600	1600
Carbon arc out weld	lf	40	50	50	50
Remove portion of damaged beam/col	sf	0	100	100	100
Replace weld – from above	lf	40	40	40	40
Remove/replace connection	lb	0	0	3000	3000
Replace slab	sf	70	70	1600	1600
Put-back					
Miscellaneous MEP and clean-up	loc	2	4	6	6
Wall framing (studs, drywall, tape, paint)	sf	800	800	6000	6000
Replace exterior skin (from salvage)	sf	0	0	5600	5600
Ceiling system	sf	2000	3000	5000	5000

Table B.4 Repair quantities for interior nonstructural components: drift sensitive

Repair Item	Unit	DS1	DS2	DS∞
Demolition/Access				
Finish protection	sf	5000	10000	10000
Remove furniture	sf	5000	10000	10000
Carpet and rubber base removal	sf	0	10000	10000
Drywall construction removal	sf	0	10000	10000
Door and frame removal	ea	8	8	8
Interior glazing removal	sf	100	100	100
Ceiling system removal	sf	0	5000	5000
MEP removal	sf	0	1000	1000
Remove casework	lf	0	200	200
Interior Construction				
Drywall construction/paint	sf	0	10000	10000
Doors and frames	ea	8	25	25
Interior glazing	sf	100	400	400
Carpet and rubber base	sf	0	10000	10000
Patch and paint interior partitions	sf	5000	5000	5000
Replace ceiling tiles	sf	0	0	0
Replace ceiling system	sf	0	5000	5000
MEP replacement	sf	0	1000	1000
Replace casework	lf	0	200	200

Table B.5 Repair quantities for interior nonstructural components: acceleration sensitive

Repair Item	Unit	DS1	DS2	DS3	DS∞
General clean-up					
Water damage	sf	0	10000	20000	20000
Demolition/Access					
Finish protection	sf	4000	10000	20000	20000
Remove furniture	sf	4000	10000	20000	20000
Ceiling system removal	sf	0	0	20000	20000
MEP removal	sf	0	500	2000	2000
Interior Construction					
Replace ceiling tiles	sf	2500	8000	8000	8000
Replace ceiling system	sf	0	0	20000	20000
MEP replacement	sf	0	500	2000	2000

Table B.6 Repair quantities for interior building contents: acceleration sensitive

Repair Item	Unit	DS1	DS2	DS3	DS∞
General clean-up					
Office papers/books	sf	0	10000	10000	10000
Office equipment	sf	5000	10000	10000	10000
Loose furniture/file drawers	sf	10000	20000	20000	20000
Contents					
Conventional office	sf	0	0	20000	20000

Table B.7 Repair quantities for caulking and window glazing system: drift sensitive

Repair Item	Unit	DS1	DS2	DS3	DS4	DS5	DS∞
Cladding inspection	ea	1	1	1	1	1	1
Rigging	ea						
Remove and replace caulking	lf	0	469	938	1407	1407	1876
Deglaze and reposition window	ea	0	4	8	16	24	24
Remove and replace window	ea	0	0	0	16	32	56
Replace gaskets	lf	0	88	352	616	880	880

Table B.8 Repair quantities for cladding connections

Repair Item	Unit	DS1	DS2	DS∞
Replace push-pull connections	ea	12	24	40
Replace column cover connection	ea	24	52	88
Remove and replace drywall (access)	ea	12	26	44

B.2.3 Unit Repair Costs

The unit costs for each repair quantity are given in Table B.9. The repair unit costs for the repair items of structural lateral system, interior nonstructural components, and interior building contents were taken from Yang *et al*. (2009). The unit costs in their report were adjusted for inflation using the historical price indexes given in RS Means Square Foot Costs (2009). The unit costs given in Yang *et al*. (2009) are Jan. 2005 cost values; thus, the costs were adjusted for Jan. 2010 by multiplying the Yang *et al*. unit costs by the factor $Index_{2009}/Index_{2005}$ = 228.1/179.7 = 1.27. As discussed in Chapter 7, not all unit costs of the cladding system repair items are applicable for some of cladding systems.

Table B.9 Unit repair costs

Repair Item	Unit	Mean Cost ($)	Standard deviation ($)
Office papers/books	sf	0.10	0.02
Office equipment	sf	0.06	0.01
Loose furniture/file drawers	sf	0.05	0.01
Water damage	sf	0.16	0.03
Conventional office	sf	29.21	5.84
Finish protection	sf	0.29	0.06
Ceiling system removal	sf	2.06	0.41
Drywall assembly removal	sf	2.54	0.51
Miscellaneous MEP	loc	222.25	44.45
Remove exterior skin	sf	34.92	6.99
Welding protection	sf	1.59	0.32
Shore beams	loc	2349.50	469.90
Cut floor slab at damaged conn	sf	222.25	44.45
Carbon arc out weld	lf	15.88	3.18
Remove portion of damaged beam col	sf	82.55	16.51
Replace weld from above	lf	57.15	11.43
Remove replace connection	lb	6.99	1.40
Replace slab	sf	22.86	4.57
Miscellaneous MEP cleanup	loc	317.5	63.50
Wall framing	sf	12.7	2.54
Replace exterior skin (from salvage)	sf	41.28	8.26
Ceiling system	sf	8.26	1.65
Remove furniture	sf	2.06	0.41
Carpet and rubber base removal	sf	1.59	0.32
Drywall construction removal	sf	2.54	0.51
Door and frame removal	ea	41.28	8.26
Interior glazing removal	sf	2.86	0.57
MEP removal	sf	34.93	6.99
Remove casework	lf	22.23	4.45
Drywall construction paint	sf	12.70	2.54
Doors and frames	ea	635.00	127.00
Interior glazing	sf	47.63	9.53
Carpet and rubber base	sf	6.35	1.27
Patch and paint interior partitions	sf	2.86	0.57
Replace ceiling tiles	sf	2.22	0.44
Replace ceiling system	sf	3.49	0.70
MEP replacement	sf	88.90	17.78
Replace casework	lf	76.20	15.24
Site clean up	sf	1.43	0.29
Cladding inspection	ea	180000.00	36000.00
Rigging for cladding	ea	50000.00	10000.00
Remove and replace caulking	lf	15.00	3.00
Deglaze and reposition window	ea	800.00	160.00
Remove and replace window	ea	2100.00	420.00
Replace gaskets	lf	50.00	10.00
Replace push-pull connection	ea	850.00	170.00
Replace column cover connection	ea	1750.00	350.00
Remove and replace drywall	ea	1450.00	290.00

B.2.4 Repair Cost Ratio

Using the PEER methodology discussed in Chapter 7, the total repair cost ratio (total repair cost of the complete building divided by the replacement cost of the complete building) was calculated as a function of seismic intensity (spectral acceleration at the first mode period of the bare structure). The mean and standard deviation of the total repair cost ratio is shown in Fig. B.1 for the building with three different cladding types. The choice of cladding type has a significant impact on the total repair cost ratio of the building. The repair cost ratio is very similar for the three types up to spectral accelerations of 0.2g. After this point, the repair cost of the building with cladding type C2 flattens out to approximately 15% at 0.5g. After 0.5g, the repair cost ratio of cladding type C2 increases to 27% at 0.8g. The repair cost ratios for the building with cladding type C1 are approximately 20% larger than the repair cost ratios for the building with cladding type C2. Finally, the repair cost ratio of the building with cladding type C3 is the highest among the cladding types: the repair cost ratios are up to 67% larger than the repair cost ratios of the building with cladding type C2 (for the range of spectral accelerations between 0.4-0.65g). The ratios shown in Fig. B.1 are the normalizing ratios for the RCR_3 repair cost ratios in Chapter 7.

B.2.5 Disaggregation of Total Repair Cost by Repair Quantity

The total repair cost of the building is disaggregated by repair quantity for the three cladding types. The breakdown of the total repair cost is shown in Fig. B.2, Fig. B.3, and Fig. B.4, for the building with cladding type C1, C2, and C3, respectively.

The disaggregation of the total repair cost is also shown in the form of a pie chart for four selected hazard levels in Fig. B.5, Fig. B.6, and Fig. B.7, for the building with cladding type C1, C2, and C3, respectively.

B.2.6 Disaggregation of Total Repair Cost by Performance Group

The total repair cost of the building is disaggregated by performance group for the three cladding types. The breakdown of the total repair cost is shown in Fig. B.8, Fig. B.9, and Fig. B.10, for the building with cladding type C1, C2, and C3, respectively.

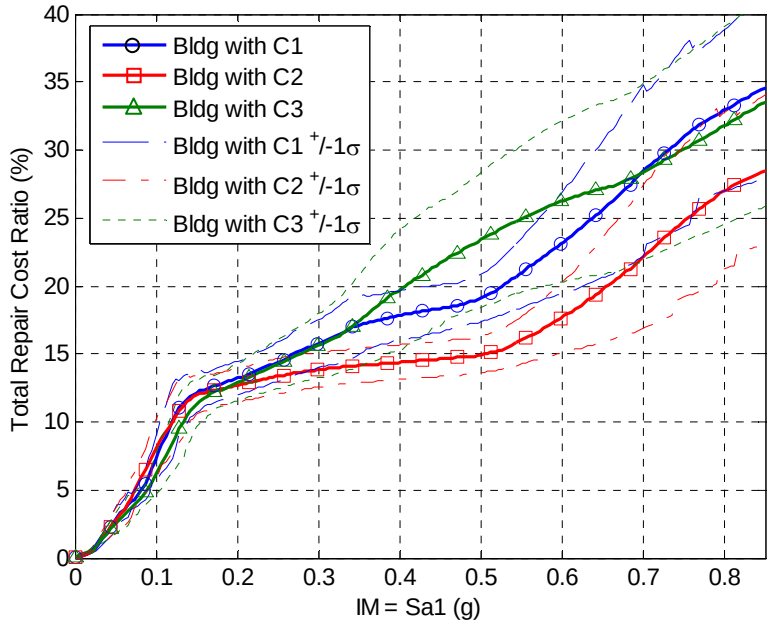

Fig. B.1 Comparison of total repair cost ratios of nine-story SAC building with three different cladding types

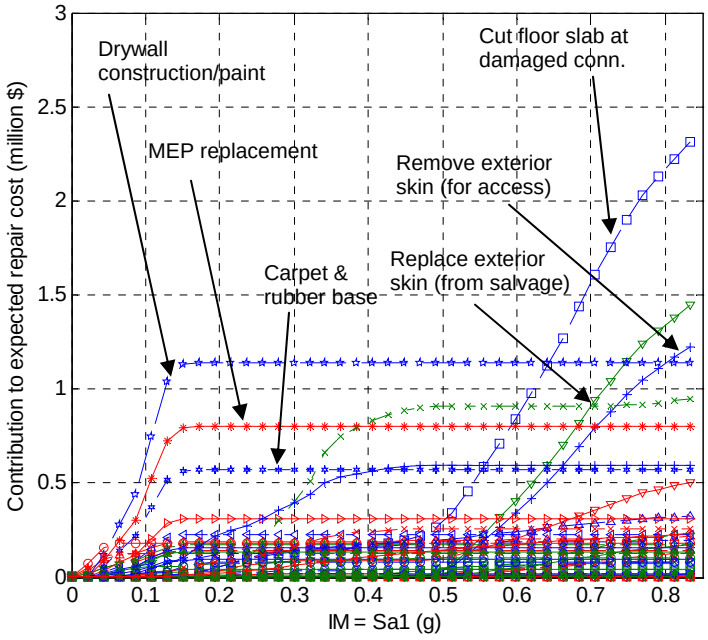

Fig. B.2 Disaggregation of total repair cost by repair quantity for nine-story SAC building with cladding type C1

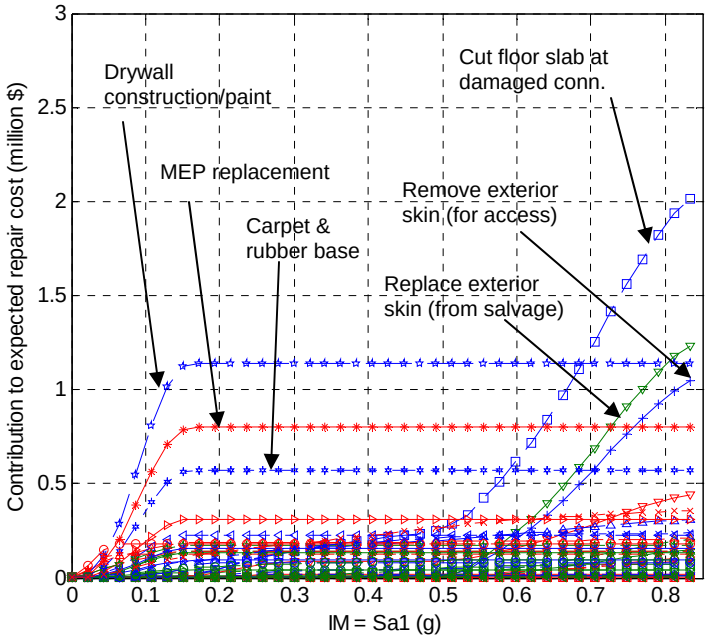

Fig. B.3 Disaggregation of total repair cost by repair quantity for nine-story SAC building with cladding type C2

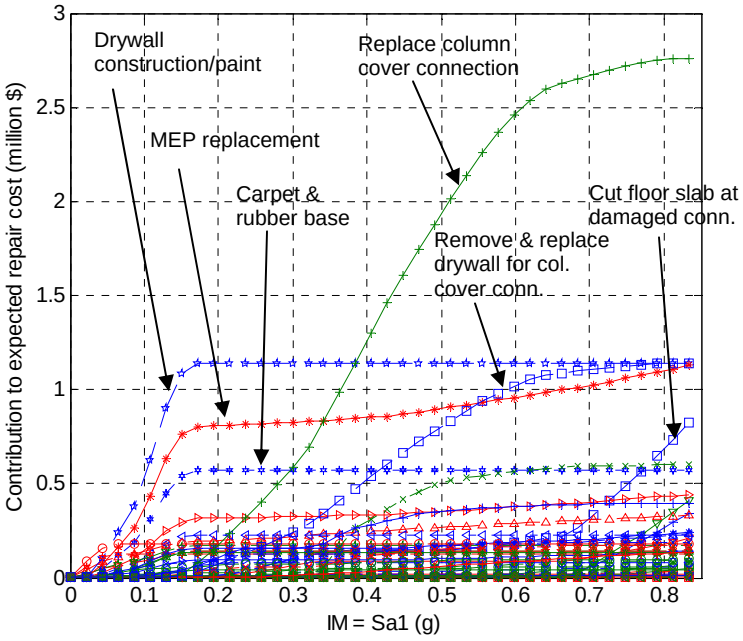

Fig. B.4 Disaggregation of total repair cost by repair quantity for nine-story SAC building with cladding type C3

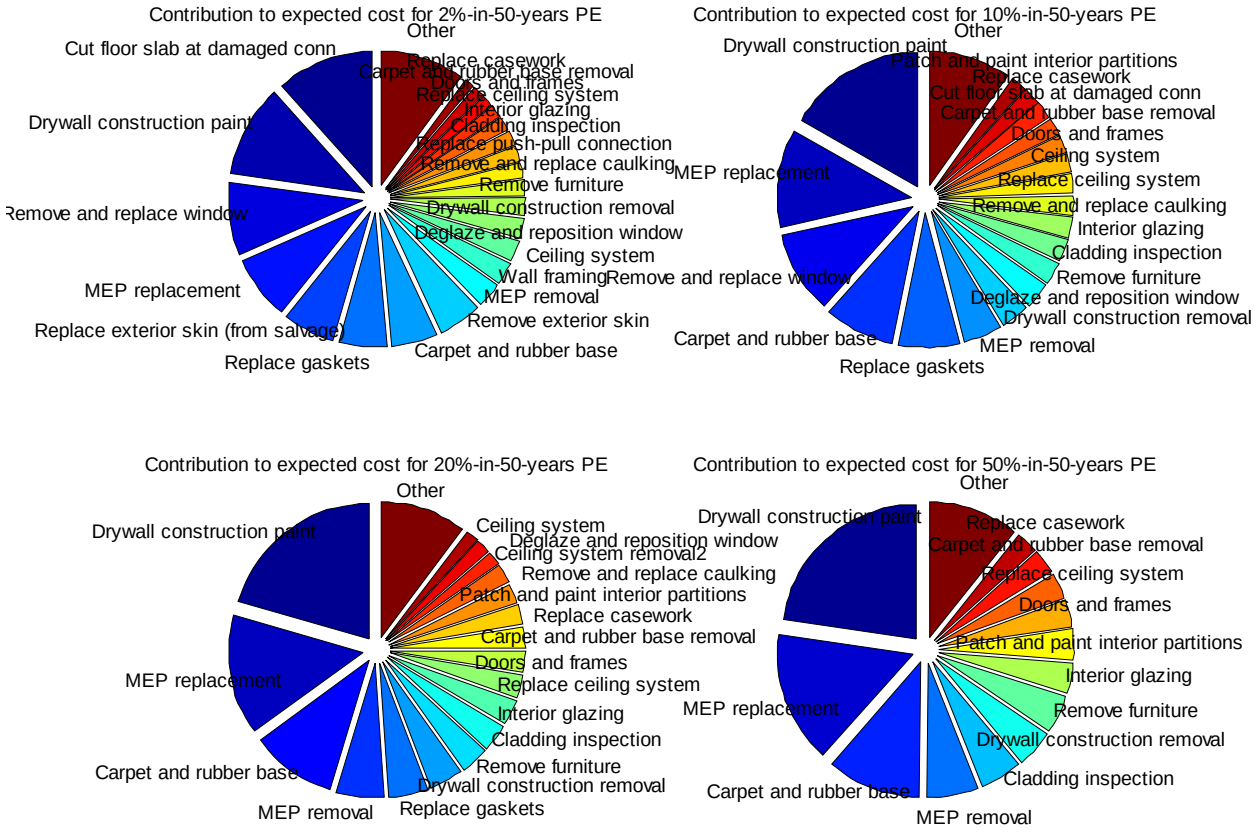

Fig. B.5 Disaggregation of total repair cost by repair quantity for nine-story SAC building with cladding type C1 for 4 discrete hazard levels

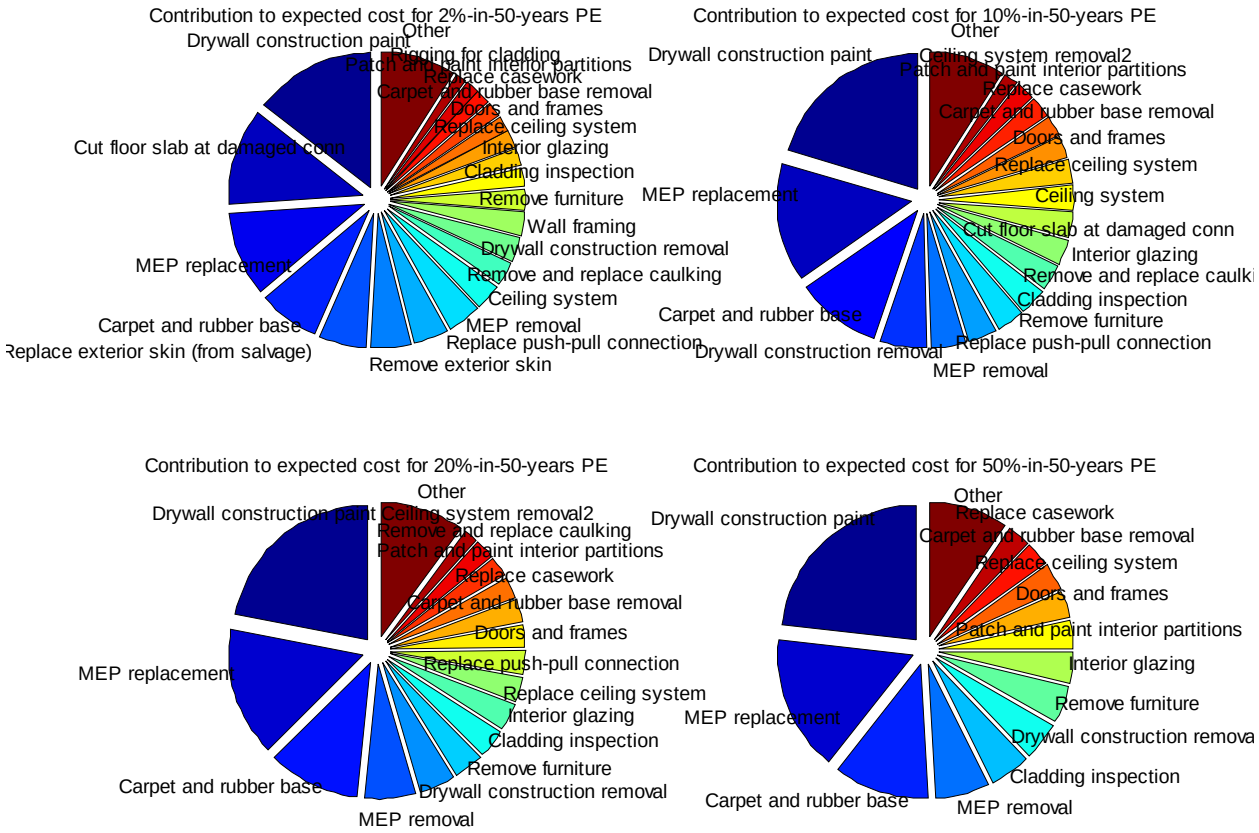

Fig. B.6 Disaggregation of total repair cost by repair quantity for nine-story SAC building with cladding type C2 for 4 discrete hazard levels

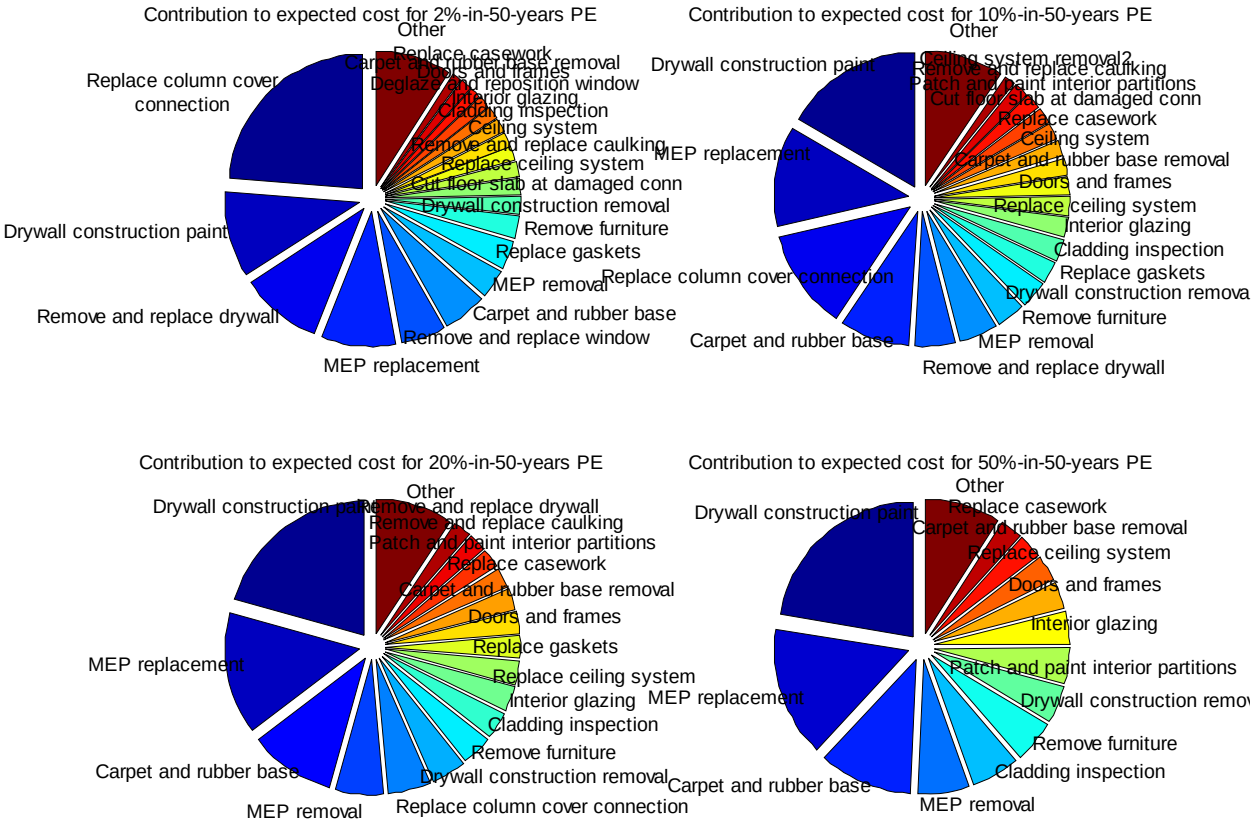

Fig. B.7 Disaggregation of total repair cost by repair quantity for nine-story SAC building with cladding type C3 for 4 discrete hazard levels

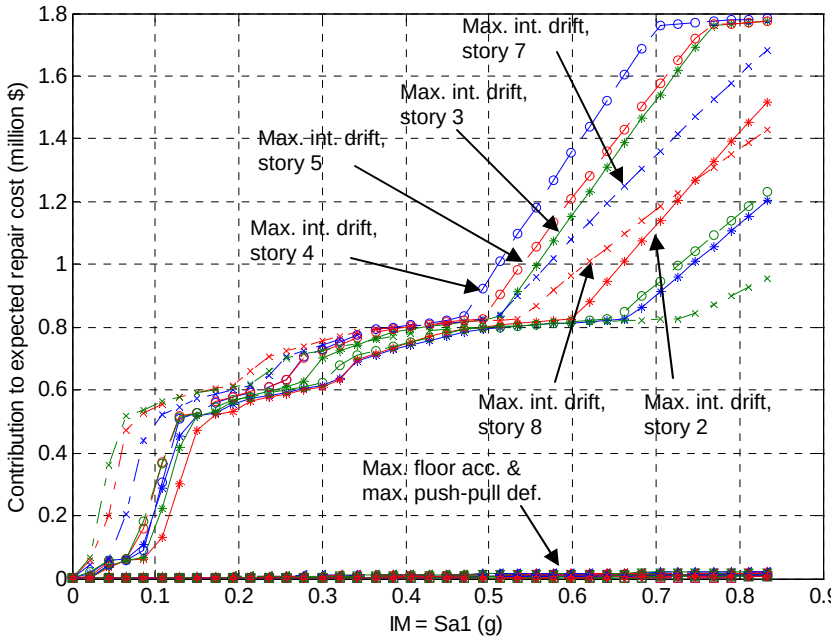

Fig. B.8 Disaggregation of total repair cost by performance group for nine-story SAC building with cladding type C1

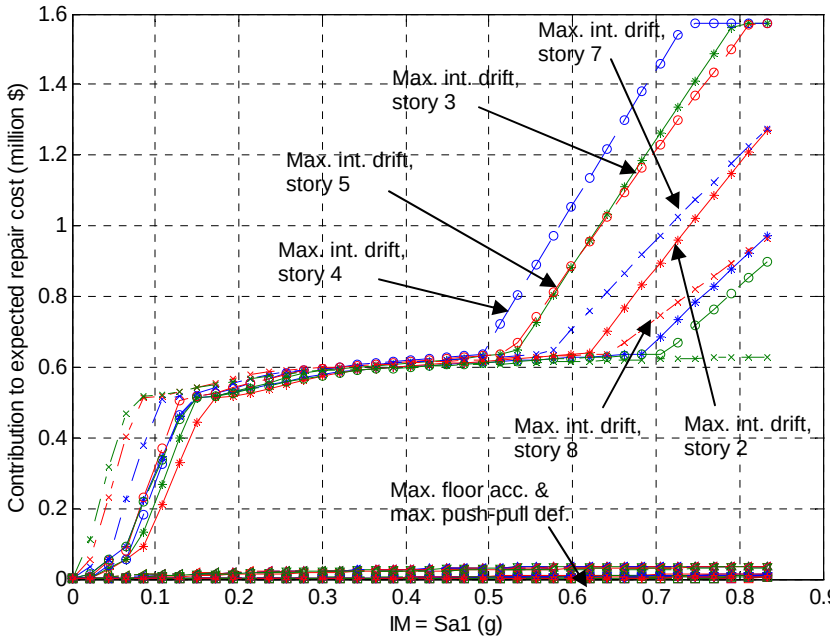

Fig. B.9 Disaggregation of total repair cost by performance group for nine-story SAC building with cladding type C2

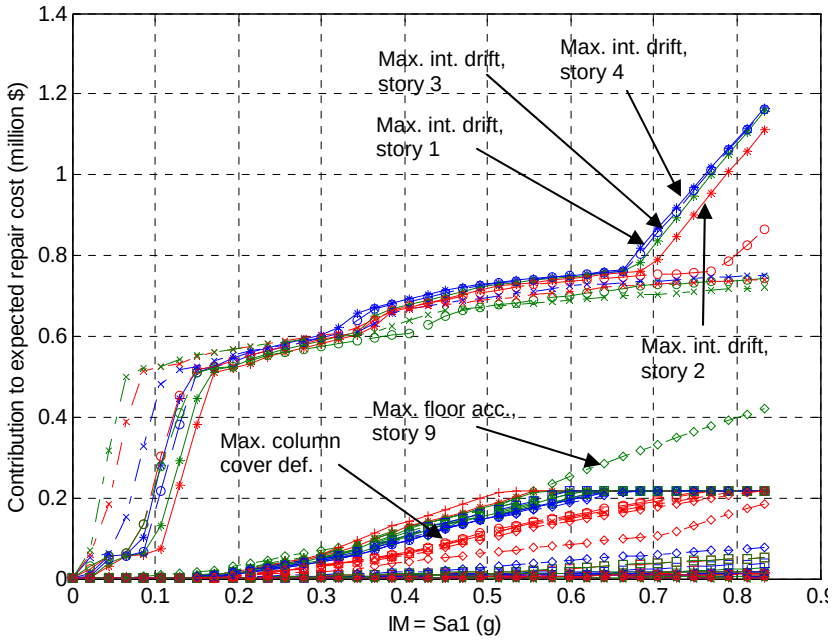

Fig. B.10 Disaggregation of total repair cost by performance group for nine-story SAC building with cladding type C3

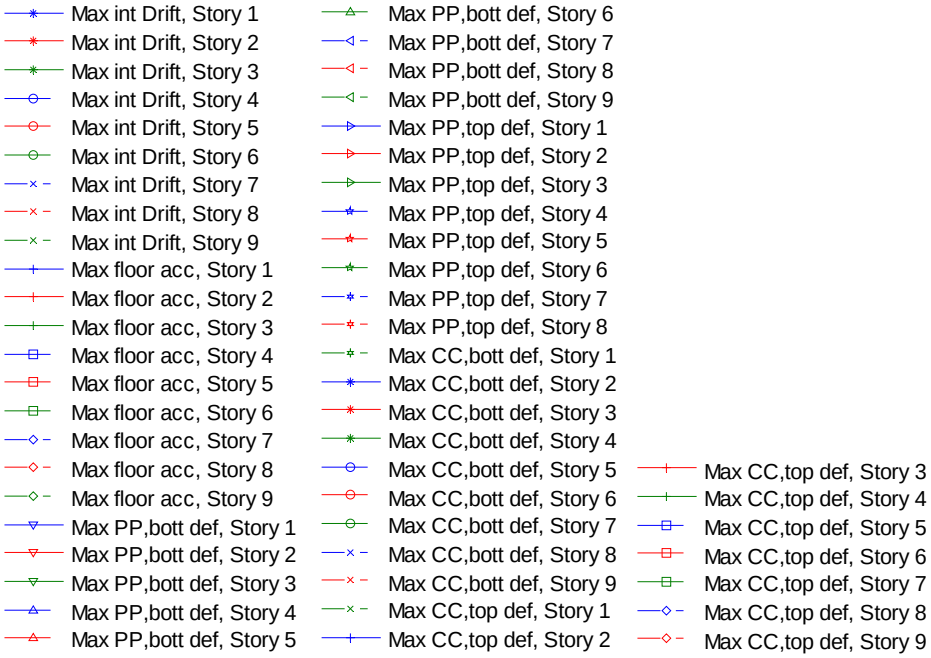

Fig. B.11 Legend for plots B.8, B.9, and B.10